LATERAL VARIATION IN UPPER MANTLE TEMPERATURE AND COMPOSITION BENEATH MID-OCEAN RIDGES INFERRED FROM SHEAR-WAVE PROPAGATION, GEOID, AND BATHYMETRY

BY

ANNE FRANCES SHEEHAN

B.S., UNIVERSITY OF KANSAS (1984)

SUBMITTED TO THE DEPARTMENT OF EARTH, ATMOSPHERIC, AND PLANETARY SCIENCES IN PARTIAL FULFILLMENT OF THE REQUIREMENTS FOR THE DEGREE OF

DOCTOR OF PHILOSOPHY

AT THE

MASSACHUSETTS INSTITUTE OF TECHNOLOGY

JUNE 1991

SIGNATURE OF AUTHOR Anne F. Sheehan
DEPARTMENT OF EARTH, ATMOSPHERIC, AND PLANETARY SCIENCES
MAY, 1991

CERTIFIED BY Sean C. Solomon
SEAN C. SOLOMON
THESIS SUPERVISOR

ACCEPTED BY Thomas H. Jordan
THOMAS H. JORDAN
DEPARTMENT HEAD

LATERAL VARIATION IN UPPER MANTLE TEMPERATURE AND COMPOSITION BENEATH MID-OCEAN RIDGES INFERRED FROM SHEAR-WAVE PROPAGATION, GEOID, AND BATHYMETRY

BY

ANNE FRANCES SHEEHAN

SUBMITTED TO THE DEPARTMENT OF EARTH, ATMOSPHERIC, AND PLANETARY SCIENCES ON MAY 28, 1991, IN PARTIAL FULFILLMENT OF THE REQUIREMENTS FOR THE DEGREE OF DOCTOR OF PHILOSOPHY IN GEOPHYSICS

ABSTRACT

Resolution of both the extent and mechanism of lateral heterogeneity in the upper mantle constrains the nature and scales of mantle convection. Oceanic regions are of particular interest as they are likely to provide our closest glimpse at the patterns of temperature anomalies and convective flow in the upper mantle because of their young age and simple crustal structure relative to continental regions. Our objectives in this thesis are to determine lateral variations in the seismic velocity and attenuation structure of the lithosphere and asthenosphere beneath the oceans, and to combine these seismological observations with the data and theory of geoid and bathymetry anomalies in order to test and improve current models for seafloor spreading and mantle convection. We concentrate on determining variations in mantle properties on a scale of about 1000 km, comparable to the thickness of the upper mantle. Seismic velocity, geoid, and bathymetry anomalies are all sensitive to variations in upper mantle density, and we formulate inversions to combine quantitatively these different data and search for a common origin. Variations in mantle density can be either of thermal or compositional origin and are presumably related to mantle convection and differentiation.

By means of a large data base of digital seismograms and waveform cross-correlation and spectral ratio techniques, we have measured SS-S differential travel time residuals and differential attenuation in order to determine lateral variations in upper mantle structure beneath the Mid-Atlantic Ridge and East Pacific Rise. Differential travel times of such phases as SS and S with identical source and receiver have the advantage that residuals are likely to be dominated by contributions from the upper mantle near the surface bounce point of the reflected phase (SS). Under this assumption, differential SS-S travel time residuals are mapped at the SS bounce points as a means of delineating lateral variations in mantle structure. After removing the signature of lithosphere age, we find evidence for long-wavelength variations in SS-S residuals along the Mid-Atlantic Ridge. The dominant wavelength of these variations is 1000 to 2000 km. These travel time anomalies correlate qualitatively with along-axis variations in bathymetry and geoid height. We formulate a joint inversion of travel time residual,

geoid height, and bathymetry under the assumption that all arise from variations in upper mantle temperature or bulk composition (parameterized in terms of Mg#). The inversion employs geoid and topography kernels which depend on the mantle viscosity structure. Inversion for temperature perturbations alone provides good fits to travel time and geoid data. The fit to topography, which is likely dominated by unmodeled crustal thickness variations, is not as good. The inversions for temperature favor the presence of a thin low viscosity layer in the upper mantle and temperature perturbations concentrated at depths less than 300 km. Compositional variations alone are unable to match the travel time and geoid or bathymetry data simultaneously. A joint inversion for temperature and composition provides good fits to both geoid and travel time anomalies. Temperature variations are ± 50 K and compositional variations are ± 0.5-3 % Mg# for models with the temperature variations uniformly distributed over the uppermost 300 km and the compositional variations either distributed uniformly over the same interval or concentrated at shallower depths. The magnitudes of these variations are consistent with the chemistry and geothermometry of dredged peridotites along the Mid-Atlantic Ridge.

Differential travel times of SS-S pairs in the east central Pacific show several differences from the north Atlantic. The most obvious difference is that the travel time residuals are significantly larger than in the Atlantic, even at a fixed age. The travel time - age relation is weaker in the Pacific, although this may be partially attributable to the fact that we have not sampled a large range of plate ages in the eastern Pacific. In the Atlantic our results are not consistent with the presence of a simple pattern of azimuthal anisotropy, while in the Pacific the data are consistent with the presence of weak anisotropy in the upper mantle. It has been suggested that anisotropy may be more pronounced at fast spreading rates than at slow spreading rates both in the lithosphere (due to a rate dependence of the mechanism for orienting olivine crystals in the lithosphere) and the asthenosphere (because the asthenospheric flow beneath fast moving plates is likely to take the form of a progressive simple shear which can induce a lattice preferred orientation of olivine crystals), and our results are consistent with this suggestion. There is substantial ambiguity in our anisotropy measurements for the Pacific, however, due to a poor sampling of azimuths, so that it is also possible that lateral heterogeneity rather than azimuthal anisotropy is producing the observed azimuthal pattern. Sampling at a more uniform distribution of azimuths should make this result less ambiguous, and as more seismic stations are deployed at new geographic locations our chances of resolving this issue will improve.

Inversion of travel time residuals, geoid, and bathymetry data for the eastern Pacific indicates that compositional variations alone are inadequate to match all of the data simultaneously, similar to our results for the north Atlantic. Temperature variations alone, however, produce significant variance reduction. The inversion solutions indicate excess temperature in the vicinity of the Galapagos hotspot in the range 50 - 150 K. Further analysis is needed to determine the effects of subduction zone structure and possible crustal thickening in the eastern Cocos plate region.

As a complement to the study of travel times, we have measured SS-S differential attenuation in the north Atlantic region. Mapping seismic Q in the upper mantle is an important tool for assessing mechanisms of lateral heterogeneity because the attenuation of seismic waves is sensitive to variations in temperature and to partial melting. Differential attenuation is positively correlated with SS-S travel time residual. Both differential attenuation and travel time residual decrease with increasing seafloor age. The age dependence of SS-S travel time residual can be explained entirely by the cooling of the oceanic lithosphere, i.e., contributions from the asthenosphere or from a mantle melt fraction are not required. On the assumption that plate cooling also dominates the

variation of differential attenuation with age, we derive an empirical Q^{-1}-temperature relation for the oceanic lithosphere. The variation of Q^{-1} with temperature that we derive is not as strongly dependent on temperature as that observed in laboratory studies. Systematic long-wavelength (1000-6000 km) variations in upper mantle differential attenuation are evident along the axis of the Mid-Atlantic Ridge. These variations correlate approximately with long-wavelength variations in shear wave travel time residuals and are attributed to along-axis differences in upper mantle temperature.

Thesis Supervisor: Sean C. Solomon
Title: Professor of Geophysics

ACKNOWLEDGEMENTS

There are many people to whom I owe thanks for their encouragement and support during my years at MIT. Since the hour is late, I am sure that I will leave someone out, so remind me next time we're both in Cambridge and maybe I'll take you to Toscanini's.

I thank Sean Solomon for agreeing to be my advisor and for taking my ideas seriously. I have appreciated his ability to listen and to ask good questions. Marcia McNutt supervised my generals paper on the Bermuda Swell, and has continued to show interest and provide advice on several aspects of the work presented in this thesis. I am grateful to Tom Jordan for his support during my early days in graduate school, and for his efforts at fostering a dynamic atmosphere for research on the 5th floor. Ted Madden and Brad Hager were my favorite faculty hockey stars, and in addition to their prowess on the ice, Ted was always willing to answer my questions on inverse theory, and Brad was helpful in explaining various aspects of geodynamics (and furnished me with all sorts of geoid coefficients). Fred Frey allowed me to sit in on his undergraduate geochemistry lectures (in my 5th year of graduate school), and patiently answered my questions.

Bob Woodward, Justin Revenaugh, Eric Bergman, and Ban-Yuan Kuo generously provided advice and subroutines for many seismological aspects of this thesis, and Anne Judge shared her codes for computing geoid and topography kernels. Lind Gee deserves a good citizenship award for her computing efforts for the common good, including setting up most of the digital seismic data retrieval software at MIT, of which I was a heavy user. Dave Krowitz also deserves credit in the computing category. We have been very fortunate to have someone as talented as Dave as our system manager. Libby Kurten and Katherine Ware shielded me from MIT's bureaucracy, and Marie Sénat kindly typed most of the references in this thesis.

One of this department's greatest resources is its students, and I have been lucky enough to go through graduate school with a talented and interesting group of people. Those who deserve special mention include Joanne Fredrich, William S. D. Wilcock (thanks also for drafting Figure 2.1), Geoff Abers, Steve Hickman, John Goff, Steve Shapiro, Jeanne Sauber, Peter Puster, Mark Murray, Greg Beroza, Carolyn Ruppel, Cecily Wolfe, Matt Cordery, Mike Bergman, Kurt Feigl, Randy Mackie, Sang-Mook Lee, and Jim Gaherty. I also thank all of the folks who took the time to captain the departmental intramural sports teams.

My housemates in Belmont (William Wilcock, Delaine Thompson, and Youssef Hashash) have provided me with a happy and friendly home during my last few years in graduate school. I've enjoyed our many late night chats, and occasional forays to Rock Meadow, the par course, and Rancatori's (Toscanini's Belmont cousin).

I thank my parents for their warmth and understanding during my long career as a student. Craig Jones provided me with an excuse to escape from MIT every now and then. I thank him for his encouragement and support, and for his continued patience.

This research was supported by the National Science Foundation, under grants EAR-8817173 and EAR-9004750, and by NASA, under grant NAG5-814. I thank John Woodhouse, Adam Dziewonski, and more recently, Göran Ekström for allowing me to access the digital data archives at Harvard University, and Bob Woodward for keeping the "daemons" running.

TABLE OF CONTENTS

Chapter 1

Introduction

It is important to measure lateral variations in the Earth's mantle because of the key role of this information in the formulation and testing of theories of the interior dynamics of the Earth. The mantle convection associated with the escape of heat from the Earth's interior gives rise to global tectonic activity, but the exact forms and scales of convection and the interaction of convective processes with the lithosphere are still controversial. Mid-ocean ridges are of particular interest as they are known to be sites of upwelling and elevated temperature. The excess temperatures have expressions in the seismic velocity and density fields. The focus of this study is to examine lateral variations in upper mantle properties near mid-ocean ridges on a scale of about 1000 km, comparable to the thickness of the upper mantle. The broad questions we seek to address include the following: What are the variations in mantle convection at this scale? Are they observable as anomalies in temperature-sensitive physical properties? Are such differences in temperature manifested as differences in melt production and thus in the chemistry of the mantle residuum? If so, are these compositional variations observable?

Learning about the large-scale structure of the Earth has become a multidisciplinary effort. Consequently in this thesis we adopt a multidisciplinary approach to the problem of resolving lateral variations in mantle properties at the 1000-km scale. Specifically we combine seismic data with geoid and bathymetry anomalies. It is

important when combining these different data to consider dynamic effects, possible compositional variations, and the spatial scales of convection.

Seismology has made great contributions to the resolution of lateral velocity differences in the mantle, and advances in techniques and a steady improvement in the capabilities of global seismic networks have greatly increased our knowledge of the Earth's interior. No longer can the Earth be treated as a rigid body possessing radial symmetry; large lateral variations have been observed in the upper mantle as well as in the crust from both regional and global studies. Global tomographic models such as M84C [*Woodhouse and Dziewonski*, 1984] utilize long-period surface waves to describe the Earth's upper mantle heterogeneity on a global scale, up to spherical harmonic degree and order 8 (λ= 5000 km). In this thesis we seek to examine lateral variations on a somewhat shorter scale (wavelengths of about 1000 to 5000 km). To do this we make use of body waves rather than surface waves, and rather than performing a global analysis we concentrate on ocean ridge environments.

The body waves used in this study are direct and surface-reflected long-period S waves. Differential travel times and attenuation are measured using SS and S wave pairs from the same source and station. Much progress has been made in resolving upper mantle heterogeneity through differential travel times [*Sipkin and Jordan*, 1976, 1980a; *Stark and Forsyth*, 1983; *Butler*, 1979; *Kuo et al.*, 1987; *Woodward and Masters*, 1991]. Among the advantages of differential rather than absolute times is that source and receiver effects are approximately common to both phases and are thus largely eliminated by differencing. If we assume that the lower mantle is relatively homogeneous and that the portions of the wave paths in the upper mantle are steep, the differential travel time anomaly is associated with upper mantle heterogeneity centered beneath the surface bounce point of the reflected (SS) phase. This technique is thus well suited to the investigation of horizontal variations in upper mantle structure.

Other data sensitive to variations in mantle properties at depth include oceanic bathymetry and geoid height. Variations in mantle density can be either of thermal or compositional origin and, like seismic velocity, are presumably related to mantle convection and differentiation. Geoid (or gravity) and topography have become the most commonly used tools for mapping out and constraining models of upper mantle convection [e.g., *Anderson et al.*, 1973, *McKenzie and Bowin*, 1976; *McKenzie*, 1977; *McKenzie et al.*, 1980, *Parsons and Daly*, 1983; *Buck and Parmentier*, 1986; *Craig and McKenzie*, 1986]. Several workers [*Dziewonski et al.*, 1977; *Nakanishi and Anderson*, 1984; *Tanimoto and Anderson*, 1984; *Stark and Forsyth*, 1983; *Dziewonski*, 1984; *Kuo et al.*, 1987] have noted correlations of geoid and travel time (or velocity structure) at a number of different wavelengths, although only a few [*Hager et al.*, 1985; *Hager and Clayton*, 1989; *Hager and Richards*, 1989] have combined observational seismology with geoid anomalies in a quantitative and dynamically consistent manner.

Since very different convective flows can produce the same geoid and surface topography, the inversion of these data alone for the thermal or compositional source function is nonunique. Because this inverse problem is not well posed, most studies have concentrated on forward modelling, i.e., varying the parameters of a simple model until a good fit to the data is achieved. With this approach, there is no guarantee that the set of parameters which give the best fit to the data is unique and that the correct solution has been isolated. Including seismic data provides additional constraints which are sufficient to allow us to formulate simple one-dimensional inversions.

In Chapter 2 we describe a comprehensive study of differential travel times in the north Atlantic region. We present details of the measurement procedure we use to obtain SS-S measurements from seismograms recorded by the GDSN network, as well as other aspects of the collection and reduction of these data. We examine the relationship of these measurements to such factors as seafloor age and upper mantle anisotropy, and we

examine the correlation with geoid and bathymetry. We develop techniques for quantitatively combining the observed travel time residuals with geoid and bathymetry anomalies in a joint inversion for upper mantle thermal and compositional variations. Since the inversion includes dynamic geoid and topography kernels which depend upon a given viscosity model, inversions can be carried out with a range of different viscosity models in order to determine which are the most consistent with the data. We invert separately and jointly for distributions of thermal perturbations and compositional variations which best produce the observed travel time, geoid, and bathymetry.

In Chapter 3 we examine differential attenuation between the phase pairs SS and S, with SS bounce points in the north Atlantic, and we examine the possible relations between Q_S^{-1} and the temperature of the upper mantle. Earlier studies with body waves suggest that the upper mantle beneath mid-ocean ridges should display a significantly greater than average level of S-wave absorption [e.g., *Molnar and Oliver*, 1969; *Solomon*, 1973]. We examine differential shear wave attenuation in the north Atlantic and its variation with lithosphere age, and we utilize thermal models to interpret the observations in terms of an empirical relation between differential attenuation and temperature. This work is a complement to the study of SS-S differential travel times presented in Chapter 2. The data show clear evidence for a decrease in Q_S^{-1} in the upper mantle with increasing plate age. There are also systematic along-axis variations in differential attenuation, and we address whether these variations might be the result of along-axis differences in the characteristic temperature of the upper mantle, such as those obtained from the inversions of travel time residuals, geoid, and bathymetry described in Chapter 2.

In Chapter 4 we examine SS-S differential travel times, geoid, and bathymetry in the region of the East Pacific Rise in the east-central Pacific. Comparision of the results from the East Pacific Rise with those from the Mid-Atlantic Ridge provides us with the

opportunity to compare and constrast upper mantle properties beneath fast and slow spreading ridges. Several authors [e.g., *Duschenes and Solomon*, 1977; *Stark and Forsyth*, 1983; *Zhang and Tanimoto*, 1990b] have found that shear wave velocities in the eastern Pacific are significantly lower than those observed in either the Atlantic or Indian Oceans. In addition, the presence of anisotropy has been found to be more pronounced in the Pacific upper mantle than in the Atlantic upper mantle [*Montagner and Tanimoto*, 1990], consistent with predictions of models of shear-induced alignment of olivine crystals [*McKenzie*, 1979; *Ribe*, 1989].

In Chapter 5 we discuss some conclusions of this thesis relating to the mechanisms of heterogeneity in the oceanic upper mantle. We raise several questions generated by the analyses in this work. Finally, we suggest directions for future research designed to help answer these questions. We feel that further application of the techniques developed in this thesis will allow constraints to be placed on upper mantle viscosity structure, the presence of partial melt, and the mechanisms of lateral heterogeneity on both global and regional scales. These techniques will allow the theories of mantle convection to be tested and sharpened with abundant and diverse data.

Chapter 2

Joint Inversion of Shear Wave Travel Time Residuals and Geoid and Depth Anomalies for Long-Wavelength Variations in Upper Mantle Temperature and Composition along the Mid-Atlantic Ridge

INTRODUCTION

Seismic velocity and density of upper mantle material are expected to be functions of temperature and composition. The delineation of long wavelength variations in these physical properties thus provide important constraints on mantle convection, crust-mantle differentiation, and mantle chemical heterogeneity. In this study we determine lateral variations in upper mantle temperature and composition along the Mid-Atlantic Ridge through the combined inversion of shear wave differential travel times, geoid height, and bathymetric depth anomalies.

The advent of seismic tomography has led to a number of three-dimensional maps of lateral variations in seismic velocity in the upper mantle, and several such models of the north Atlantic region have been developed, both as parts of global studies [e.g., *Woodhouse and Dziewonski*, 1984; *Nakanishi and Anderson*, 1984; *Tanimoto*, 1990] and through regional investigations of long-period surface waves [e.g., *Honda and Tanimoto*, 1987; *Mocquet et al.*, 1989; *Mocquet and Romanowicz*, 1990]. With surface wave

methods each wave samples the average vertical variation in upper mantle structure along its path, but because of the long wavelengths involved the inversion of phase or group velocity from many paths tends to smooth out lateral variations. Body wave travel times can provide independent information about upper mantle heterogeneity at potentially shorter horizontal scales than surface waves can resolve, and progress has been made in the determination of lateral heterogeneity in the north Atlantic through the use of both differential and absolute travel times of body waves [*Kuo et al.*, 1987; *Grand*, 1987, 1989].

The travel times used in this study are differential times of the body wave phase pair SS-S (Figure 2.1). Differential travel times of shear wave pairs are well suited to the study of upper mantle heterogeneity [*Sipkin and Jordan*, 1976, 1980a; *Stark and Forsyth*, 1983; *Butler*, 1979; *Kuo et al.*, 1987; *Woodward and Masters*, 1991] and have the advantage that source and receiver effects are approximately common to both phases and are thus largely eliminated by differencing. Under the assumption that the lower mantle is relatively homogeneous and that the portions of the wave paths in the upper mantle are steep, the differential travel time anomaly can be associated with upper mantle structure within a small volume centered beneath the surface bounce point of the reflected (SS) phase. This technique is thus well suited to the investigation of horizontal variations in structure, but the resolution of variations with depth is poor.

Oceanic bathymetry and geoid height data are sensitive to variations in mantle density at depth. Such variations can be either thermal or compositional in origin and, like seismic velocity, are presumably related to mantle convection and differentiation. Geoid (or gravity) and topography have become the most commonly used tools for mapping out and constraining models of upper mantle convection [e.g., *Anderson et al.*, 1973, *McKenzie and Bowin*, 1976; *McKenzie*, 1977; *McKenzie et al.*, 1980, *Parsons and Daly*, 1983; *Buck and Parmentier*, 1986; *Craig and McKenzie*, 1986]. In addition, measurement

of the admittance (the spectral ratio of geoid to topography) has been widely utilized to estimate the depth and mode of compensation of oceanic swells and plateaus [e.g., *Watts et al.*, 1985, *Cazenave et al.*, 1988; *Sandwell and MacKenzie*, 1989; *Sheehan and McNutt*, 1989]. Several workers [*Dziewonski et al.*, 1977; *Nakanishi and Anderson*, 1984; *Tanimoto and Anderson*, 1984; *Stark and Forsyth*, 1983; *Dziewonski*, 1984; *Kuo et al.*, 1987] have noted correlations of geoid and travel time (or velocity structure) at a number of different wavelengths, although only a few [*Hager et al.*, 1985; *Hager and Clayton*, 1989; *Hager and Richards*, 1989] have combined observational seismology with geoid anomalies in a quantitative and dynamically consistent manner.

In this study we present the first formal inversion of geoid, depth, and travel time anomaly data for lateral variations in upper mantle temperature and composition along the Mid-Atlantic Ridge. Given a distribution of temperature or density perturbations in the upper mantle, the forward problem of calculating differential travel time, geoid, and depth anomalies is straightforward. This forward problem forms the basis for a joint linear inversion of these three types of observations under the assumption that all arise from parameterized long-wavelength variations in upper mantle temperature or composition. Results of a set of inversions carried out under different assumptions regarding the depth extent of lateral heterogeneity and the mantle viscosity structure are compared with other constraints on variations in mantle temperature and degree of melt removal.

MEASUREMENT OF DIFFERENTIAL TRAVEL TIMES

The seismic data used in this study consist of long-period S and SS phases obtained from the Global Digital Seismic Network (GDSN) [*Peterson et al.*, 1976; *Peterson and Hutt*, 1982]; the Network of Autonomously Recording Seismographs (NARS), a linear broadband array in western Europe [*Nolet and Vlaar*, 1982]; and several

broadband stations from the global GEOSCOPE network [*Romanowicz et al.*, 1984]. A list of stations used in this study is presented in Table 2.1. We use only transversely polarized (SH) seismograms (rotated from N-S and E-W components) to avoid interference from the SKS phase and contamination from P-SV conversions at the base of the crust and other near-surface discontinuities. Recent work by *Gee and Jordan* [1989] suggests that travel times depend on the frequency band used in the analysis. In order to maintain a self-consistent data set for our study, additional processing is applied to data from the NARS and GEOSCOPE arrays in order to mimic the instrument response of the longer period GDSN stations. This processing allows us to measure travel times from a set of seismograms that all have essentially the same frequency response. Data from the NARS and GEOSCOPE arrays are decimated (with a low-pass antialiasing filter) to a common sampling interval of 1 s. The data are further filtered using a noncausal 3-point Butterworth filter [*Rader and Gold*, 1967] with a frequency bandpass of 0.01 - 0.20 Hz. This additional filtering greatly improves the signal-to-noise ratio of the SS phase.

A waveform cross-correlation method is utilized to determine the differential travel time between the phases S and SS [*Butler*, 1979; *Stark and Forsyth*, 1983; *Kuo et al.*, 1987]. The procedure involves the construction of a "synthetic" SS pulse from S and the evaluation of the cross-correlation function between the real and synthetic windowed SS phases (Figure 2.2). The synthetic SS pulse is created from S in the following manner. The S pulse is windowed and attenuated (with attenuation parameter $t^*= 3$ s) [*Grand and Helmberger*, 1984; *Kuo et al.*, 1987] to account for the additional time SS travels in the mantle, and then a $\pi/2$ phase shift (Hilbert transform) is applied to the attenuated S pulse to simulate the frequency-dependent phase shift which the SS wave undergoes at an internal caustic [*Choy and Richards*, 1975]. The differential time is obtained from the peak of the cross correlation between the synthetic SS constructed from the S wave and the real SS. The residual SS-S times are obtained by subtracting the observed differential time from that

predicted by the PREM Earth model [*Dziewonski and Anderson*, 1981] and correcting for Earth ellipticity [*Dziewonski and Gilbert*, 1976] and SS bounce point bathymetry. Our convention is that negative residuals are indicative of either early SS or late S.

Constant window lengths of 120 s are used for both the S and SS phases. In general, the observed differential travel times vary by as much as 1 s depending on how S and SS are windowed. Our modelling with synthetic seismograms indicates that emphasizing the onset of the SS waveform can lead to bias for bounce points in areas of oceanic sediments. The effect of sediments at long periods is to produce precursory arrivals from reflections at the base of the sediments and late arrivals from waves which travel through the low-velocity sediments and are reflected at the crust-water interface. The net effect, after convolving the crustal response with the long-period GDSN instrument response, is that the time center of the SS phase is effectively unchanged but the pulse is broadened both at the front and at the back. In our procedure the use of a constant window containing the entire SS pulse should yield differential travel times that are little affected by the presence of sediments.

DATA

The north Atlantic is an ideal area for conducting a differential travel time study in terms of the geographic distribution of available events and stations at suitable distances. The range in source-receiver separation was taken to be 55° to 86° to ensure separation of S and ScS at the longer distances and to avoid triplication in SS at shorter distances. The SS and S phases bottom from about 670 km to 2300 km depth. We performed a search over all earthquakes in the Harvard centroid moment tensor (CMT) catalog for the years 1977-1987 [*Dziewonski et al.*, 1981; *Dziewonski and Woodhouse*, 1983] and over all GDSN, NARS, and GEOSCOPE digital seismic stations in order to find event-station pairs of the

proper epicentral distance which provide SS bounce points in the North Atlantic region. Epicenters were obtained from the Bulletin of the International Seismological Centre (ISC) for events occurring before 1987 and from the "Preliminary Determination of Epicenters" of the U.S. National Earthquake Information Service (NEIS) for events occurring in 1987. The final distribution of sources and stations used to measure SS-S differential travel times is shown in Figure 2.3. The majority of data in this study comes from records of equatorial fracture zone earthquakes at North American and European stations, north and central Atlantic events at North American stations, Central American events at European stations, and Mediterranean and European earthquakes at North American stations.

This search yielded over 2000 event-station pairs with the proper epicentral separation. After winnowing the list because of station inoperation, poor signal to noise ratio for the phases of interest, and interfering events, the final data set consists of nearly 500 SS-S differential travel time residuals with bounce points in the north Atlantic (Figure 2.4). Uncertainties are determined for each measurement following the procedure outlined in Appendix 2.A. A tabulation of all residuals is given in Appendix I.

RESULTS

We interpret the variations in SS-S differential travel times in terms of lateral velocity variations within the crust and upper mantle beneath the surface reflection points of the SS wave path. *Kuo et al.* [1987] and *Woodward and Masters* [1991] tested the validity of this assumption by plotting absolute S and SS residuals against SS-S residuals. They found that S and SS-S residuals are uncorrelated while SS and SS-S residuals are strongly correlated, indicating that the assumption is justified. The validity of this assumption is further supported by the strong correlation of SS-S times with surface tectonic features in the vicinity of the SS bounce point. The residuals are further interpreted in terms of such

upper mantle processes as lithospheric aging, flow-induced anisotropy, and along-axis heterogeneity in mantle structure.

Lithospheric Aging

Cooling and thickening of the lithosphere should yield a tendency toward an increase in seismic velocity with increasing lithospheric age. A linear regression experiment was performed to examine the correlation of the SS-S residuals with seafloor age. A gridded map of seafloor ages was constructed for the north Atlantic from the magnetic anomalies of *Klitgord and Schouten* [1986] and ages assigned according to *Kent and Gradstein* [1986] and *Klitgord and Schouten* [1986]. The isochrons of *Sclater et al.* [1981] were used in a few regions which were not covered by the *Klitgord and Schouten* [1986] data set. To obtain a representative age value for the region spanning approximately one horizontal wavelength of the incident (SS) wave, an average seafloor age was estimated for a 1° x 1° box centered on each SS bounce point. To reduce scatter, measurements whose bounce point depths differed by more than 2500 m from the depth predicted by the *Parsons and Sclater* [1977] plate cooling model were excluded from the final age regression. Although each SS wave samples the upper mantle at a finite range of lithosphere ages, we expect that the different travel time anomalies contributed by the SS path segments on the younger and older sides of the bounce point approximately cancel so that the age at the SS bounce point is appropriate to the associated SS-S residual.

The SS-S residuals for the north Atlantic are consistent with the expectation of an increase in seismic velocity with seafloor age. For bounce points between 0° and 60°N latitude, the coefficient derived by linear regression of residual with square root of age is -0.68 ± 0.08 s $My^{-1/2}$ from 0 to 100 My, with a linear correlation coefficient of -0.85 (Figure 2.5). However, residuals from 60 - 90°N do not seem to be strongly correlated with lithospheric age. This may be due to the fact that this area is more tectonically

complicated than 'normal' oceanic lithosphere [e.g., *White*, 1988; *Zehnder and Mutter*, 1990], includes several ridge jumps, is in close proximity to continental regions, and does not closely follow the age-depth relation of *Parsons and Sclater* [1977]. Compared with the residuals for 0-60°N, those from 60-90°N are anomalously negative at young ages and anomalously positive at older ages. The slope of SS-S residual vs. square root of age for data from 0 to 60°N is smaller than that inferred from S delays of intraplate earthquakes in the Atlantic by *Duschenes and Solomon* [1977] (two-way S delay = -1.2 s $My^{-1/2}$) and that reported by *Kuo et al.* [1987] (-1 s $My^{-1/2}$). It is larger, however, than the global average obtained by *Woodward and Masters* [1991] (-0.51 s $My^{-1/2}$). We find that the residual-age relation is not constant over the entire north Atlantic, so that some of these variations in slope may reflect real geographic differences.

We may compare the variation of SS-S residual versus age with that due only to lithospheric cooling. For a lithospheric structure given by the plate cooling model of *Parsons and Sclater* [1977], we may convert temperature variations to differences in shear velocity v_s by adopting a value for $\partial v_s/\partial T$, which we take to be uniform and equal to -0.6 m/s K^{-1} [*McNutt and Judge*, 1990]. For a horizontal slowness typical of the teleseismic S and SS waves of this study (0.1375 s/km), the slope of the line best fitting the SS-S travel time delay versus age given by the plate cooling model over 0-100 My is then -0.64 ± 0.07 s $My^{-1/2}$, a result indistinguishable from the observed slope. This agreement indicates that the dependence of travel time residual on plate age can be explained entirely by lithospheric cooling.

The trend of the travel time residual versus lithospheric age relation changes at about 100 My. After 100 My, the residuals appear to flatten out (Figure 2.5), in the same sense as the plate cooling model of *Parsons and Sclater* [1977]. Such a pattern may reflect the unmodeled effect of increased sediment or crustal thickness, or, as suggested by *Parsons and Sclater* [1977] may be partially the result of secondary convection which

supplies heat to the base of the plate at older ages. To avoid possible biases associated with any of these effects we shall restrict our analysis to data with bounce points on lithosphere less than 100 My. To look for other systematic variations in the residuals, we correct for age by removing the linear relation shown by the solid line in Figure 2.5. This correction is effectively a normalization of residuals to 22-My-old lithosphere (the zero crossing of the regression line).

Anisotropy

Another systematic velocity variation that has been suggested as a possible contributor to residual SS-S travel times is azimuthal anisotropy. *Kuo et al.* [1987] examined this phenomenon in detail and concluded that alignment of olivine cystals in the asthenosphere created a significant pattern of azimuthal anisotropy in SS-S residuals measured in the Atlantic region. We have also searched for evidence of azimuthal anisotropy with our data set.

Backus [1965] and *Crampin* [1977] demonstrated, from the general form of body wave anisotropy in a weakly anisotropic medium, that the linear form of the azimuthal variation of velocity is given by

$$V^2 = A_0 + A_1 \cos 2\theta + A_2 \sin 2\theta + A_3 \cos 4\theta + A_4 \sin 4\theta \qquad (2.1)$$

where V is the body wave velocity, the A_n are linear functions of the elastic moduli, and θ is an azimuth, defined for our problem by the angle between the great circle path and the direction to geographic north measured at the SS bounce point. Equation (2.1) was further simplified by *Kuo et al.* [1987] and parameterized in terms of travel time residuals:

$$R = R_0 + R_1 \cos 2\theta + R_2 \sin 2\theta + R_3 \cos 4\theta + R_4 \sin 4\theta \qquad (2.2)$$

where R is the travel time residual and the R_n are constants. By fitting a function of this form to our age-corrected measurements we can determine if our data are consistent with the presence of anisotropy.

We have conducted several tests of azimuthal anisotropy with our travel time data. We performed least squares inversions to determine 2θ and 4θ patterns which provide best fits to the age-corrected SS-S residuals. The anisotropy indicated by our regression experiments differs significantly from the preferred model of *Kuo et al.* [1987] both in magnitude and in phase (Figure 2.6). Our results indicate that for the 2θ model the slow direction for SS-S is N4°W and the peak-to-peak magnitude of the effect is less than 1 s; for the 4θ model the slow directions are N32°W and N58°E and the magnitude is 2.5 s; for the joint 2θ and 4θ model the slow direction is N32°W and the magnitude is just under 3 s. *Kuo et al.* [1987] obtained a peak-to-peak variation with azimuth of 5-7 s and a slow direction at N13°W. The slowest residuals in the *Kuo et al.* [1987] study were from north-south paths, i.e., nearly along the ridge, and the fastest residuals were from northeast-southwest-trending paths with bounce points north of the Azores-Gibraltar plate boundary (an area noted to be anomalously fast in their study), so their reported anisotropy may have been at least partly the result of unmodelled upper mantle heterogeneity. Our inversion for a 2θ pattern of anisotropy provided a variance reduction of only 2%, compared with 20% for a 4θ pattern, and 22% for a combined 2θ and 4θ pattern. On the basis of these values of variance reduction and the number of free parameters involved, our results suggest that there is no single coherent pattern of upper mantle anisotropy in the north Atlantic. The latest anisotropic upper mantle models obtained from surface wave tomography [*Montagner and Tanimoto*, 1990] also show a complex pattern of anisotropy in the region. Any azimuthal anisotropy in the asthenosphere induced by plate motions in the north Atlantic may be heterogeneous because the three plates in the region are slow-moving and the return

flow is not closely related to plate divergence [*Hager and O'Connell*, 1979, 1981; *Parmentier and Oliver*, 1979].

Spatial Patterns of Age-corrected Residuals

After removal of the dependence on seafloor age, a plot of SS-S travel time residuals at the SS surface reflection point (Figure 2.7) shows several interesting features. Perhaps the most striking is that residuals in the western Atlantic north of about 35° N are on average nearly 4 s more negative than those to the south. This feature is also noticeable in Figure 2.4 but is more obvious after age-dependence is removed. A similar change at approximately this latitude was noted for SS-S residuals with bounce positions on the eastern side of the Mid-Atlantic Ridge by *Kuo et al.* [1987] and was attributed to a change in upper mantle structure across the Azores-Gibraltar plate boundary. The signal we observe is predominantly from data with bounce points on the western side of the ridge. A map view of the azimuthal distribution is shown in Figure 2.8 and serves as an aid to assess qualitively the geometry of wave paths to the south and north of 35°N. We examined the possibility that this signal may be from the Caribbean anomaly, a region of anomalously high velocity in the mantle between 600 and 1400 km depth beneath the Caribbean originally reported by *Jordan and Lynn* [1974] and further confirmed by *Grand* [1987]. If the first leg of the SS rays propagating to western Europe were to bottom in the high velocity Caribbean region, the result would be early SS-S residuals. This would produce a feature of opposite sign from that observed, so we discount it as an influence here. Another possible explanation for the long-wavelength signal could be azimuthal anisotropy, but the examination above of possible patterns of azimuthal anisotropy does not support this suggestion.

Another distinctive feature of the residuals in Figure 2.7 is a row of negative values which trends northwest to southeast along the trend of the New England Seamounts

and across the ridge to the vicinity of the Great Meteor Seamount. This feature comes from event-station pairs at a number of different azimuths and distances so cannot be attributed to a source or receiver effect. We do not observe distinctive anomalies in the vicinity of the Bermuda, Azores or Canary Islands hotspots. The data density is poor for the Bermuda region, however, and any signal associated with the Canary Islands may be obscured by the ocean-continent transition. Recently active hotspot islands might be expected to display strong positive (late) residuals, such as *Stewart and Keen* [1978] observed for PP-P residuals at the Fogo Seamounts. In contrast, *Woodward and Masters* [1991] found mostly negative (early) SS-S residuals in the vicinity of the Hawaiin hotspot, and *Jordan* [1979] and *Sipkin and Jordan* [1980b] have suggested that the net effect of hotspots may be to produce early arrivals because of the presence of high velocities in a depleted mantle residuum.

There is a systematic variation of SS-S residual with latitude, i.e., effectively along the direction of the Mid-Atlantic Ridge axis. Age-corrected SS-S residuals with SS bounce points on lithosphere younger than 100 My are shown versus latitude in Figure 2.9. The along-axis variations show a variety of scales, notably at wavelengths of about 1000 - 2000 km in the region from 15° to 35°N, and at about 6000 km wavelength from late (positive residuals) in the south (20-35°) to early (negative residuals) farther north (45-55°N). The largest of these variations are robust with respect to selective removal of portions of the data. The Iceland region appears as a local maximum (positive SS-S delay) on the profile, but the Azores hot spot does not have a distinct seismic signal.

JOINT INVERSION OF TRAVEL TIME RESIDUALS AND GEOID AND DEPTH ANOMALIES

Long-wavelength variations in shear wave velocity of the sort depicted in Figure 2.9 presumably are a consequence of some combination of variations in temperature and

composition of the upper mantle. Such lateral variations should also have signatures in other physical quantities measurable at these wavelengths, notably gravity (or geoid height) and topography (or residual bathymetry), because of the dependence of these quantities on bulk density. Travel time residuals, geoid anomalies, and residual depth anomalies are independent quantities dependent in different ways on temperature, bulk composition, and their variation with depth. We therefore seek a quantitative procedure for treating travel time residuals jointly with geoid and bathymetry data and in particular for a combined inversion of all three quantities for horizontal variations in upper mantle temperature and composition.

To ensure complementarity of data sets, bathymetry and geoid height values are obtained at each SS bounce point, and both are corrected for subsidence with seafloor age by means of the plate cooling model [*Parsons and Sclater*, 1977; *Parsons and Richter*, 1980]. In this manner we effectively normalize all observations to zero age. Bathymetric data are obtained from the corrected Digital Bathymetric Data Base (5' grid) [*U.S. Naval Oceanographic Office*, 1985]. Geoid data are taken from a combined set of Seasat and GEOS3 altimeter data [*Marsh et al.*, 1986]. Data north of 70° N were not included in the *Marsh et al.* [1986] data set due to the high probability of being over sea ice, so our analysis below is confined to latitudes less than 70°N. We find that the correlation of SS-S residuals with the low order geoid is negative, but that at high order the correlation is positive (Figure 2.10). This relationship may indicate a depth dependence of contributions to geoid and travel time (e.g., the long wavelength signal may be a lower mantle effect). Low degree harmonics are likely linked to deep-seated density heterogeneities and subducting slabs [*Hager*, 1984; *Hager et al.*, 1985]. Since we are interested in upper mantle processes, we filter out the long-wavelength component of the geoid by subtracting a reference field [*Lerch et al.*, 1979] expanded in spherical harmonics to degree and order 7 and tapered to degree and order 11. To provide a comparable bathymetric data set,

bathymetry is high-pass filtered (corner at 4000 km, cutoff at 6000 km) to remove long-wavelength trends. Along-axis profiles are constructed from the age-corrected and filtered geoid and bathymetry data.

Profiles of age-corrected travel time residuals, geoid, and bathymetry are compared in Figure 2.11. While qualitative correlations among profiles are apparent, we seek to quantify possible models of temperature and compositional variations that can match these observations. Oceanic bathymetry and geoid height are both sensitive to variations in mantle density at depth. Such variations can be either thermal or compositional in origin and, like seismic velocity, are presumably related to mantle convection and differentiation. For a given density change, the seismic signature of thermal and compositional heterogeneity are of opposite sign, so travel time residuals constitute key information for distinguishing between mechanisms of heterogeneity.

Inversion for Thermal Structure

We seek to formulate an inversion for the distribution of temperature anomalies T(x,z) (where x is along-axis and z is depth) that can produce the along-axis geoid, bathymetry, and travel-time anomalies shown in Figure 2.11. Topography and geoid kernels were calculated for prescribed models of viscosity for an incompressible Newtonian mantle with free slip at the surface and the core-mantle boundary. The convecting region is assumed to be overlain by a high-viscosity layer 40 km thick. We performed calculations both for a mantle of constant viscosity and for a mantle with a shallow low-viscosity layer. Topography and geoid anomalies depend on the viscosity structure, but the predicted travel times do not. Kernels were calculated using a method similar to that of *Richards and Hager* [1984] except that the solution was directly integrated across the layers instead of being obtained via propagator matrices [*McNutt and Judge*, 1990].

The inversion is best conducted in the horizontal wavenumber domain. The thermal anomalies $\Delta T(k,z)$ at depth are related to the predicted dynamic topography $h(k)$ for wavenumber k via an integral of the form

$$\Delta h\,(k) = \frac{\rho_0 \alpha}{\rho_0 - \rho_w} \int_{Z_{min}}^{Z_{max}} H\,(k,z)\,\Delta T\,(k,z)\,dz \qquad (2.3)$$

[*Parsons and Daly*, 1983] where α is the volumetric coefficient of thermal expansion, ρ_0 and ρ_w are the densities of the mantle and of water at standard temperature and pressure, and z_{min} and z_{max} are the upper and lower boundaries of the layer in which temperatures are allowed to vary. Table 2.2 contains a summary of the constants adopted here. The depth and wavenumber-dependent topography kernel $H(k,z)$ is calculated from the equations of continuity and motion given a set of boundary conditions, a viscosity model, and a constitutive relation between stress and strain [*Parsons and Daly*, 1983]. Similarly, the kernel $G(k,z)$ for the geoid relates the thermal anomalies to the geoid $N(k)$ via

$$\Delta N(k) = \frac{2\pi\Gamma\rho_0\alpha}{gk} \int_{z_{min}}^{z_{max}} G(k,z)\,\Delta T(k,z)\,dz \qquad (2.4)$$

[*Parsons and Daly*, 1983] where Γ is the gravitational constant, and g is the surface gravitational acceleration.

Sample geoid and topography kernels calculated for different wavenumbers and viscosity structures are shown in Figures 2.12 and 2.13. Cartesian kernels are used throughout this study because of their computational efficiency and straightforward application to Fourier transform techniques. We have compared extrema of the upper mantle portions of the geoid and topography kernels for a layered cartesian Earth and a spherical Earth for a number of wavelengths and different viscosity structures (Figure

2.13), and we note good agreement even at very long wavelengths (spherical harmonic order $\ell = 6$). This agreement suggests that the results presented here should be applicable to the spherical Earth without introducing unreasonably large errors.

Temperature perturbations at depth can be converted to a seismic velocity perturbation by assuming a value for the partial derivative of shear wave velocity with respect to temperature, $\partial v_s/\partial T$. The resulting two-wave travel time perturbation is given by

$$\Delta t\,(k) = 2\,\frac{\partial v_s}{\partial T}\int_{z_{min}}^{z_{max}} \frac{\Delta T\,(k, z)\,dz}{v_s(z)^2\,(1 - p^2 v_s(z)^2)^{1/2}} \qquad (2.5)$$

where $v_s(z)$ is from the reference shear velocity model [*Dziewonski and Anderson*, 1981] and p is the ray parameter, generally taken to be a representative value for the range of epicentral distances considered here. We use a value of -0.6 m/s K^{-1} for $\partial v_s/\partial T$. This value is higher than the values of *Anderson et al.* [1968] and *Kumazawa and Anderson* [1969] at standard temperature and pressure but is similar to the value of -0.62 m/s K^{-1} determined by *McNutt and Judge* [1990] by a least squares fit of Love-wave phase velocities to predicted temperature of the lithosphere. Such a value is consistent with the change in P-wave velocity with temperature, $\partial v_p/\partial T$ = -0.5 m/s K^{-1}, found from modeling wave propagation along subducting slabs [*Creager and Jordan*, 1986; *Fischer et al.*, 1988] if we assume that $\partial v_s/\partial T = 1.1\ \partial v_p/\partial T$ [*Woodhouse and Dziewonski*, 1984]. Partial melt would increase the value of $\partial v_s/\partial T$ [*Sleep*, 1974; *Sato and Sacks*, 1989], but simultaneous analysis of both shear and compressional differential travel times by *Woodward and Masters* [1991] indicates that significant partial melting is not required to explain the differential travel time residuals in the north Atlantic region.

The forward problem consists of calculating geoid, topography, and travel time residual profiles given a starting two-dimensional temperature structure T(x,z). The

inverse problem consists of finding a temperature structure that predicts (via equations 2.3 - 2.5) geoid, topography, and travel time profiles which best fit those observed. The familiar matrix equation $\mathbf{d} = \mathbf{A}\,\mathbf{m}$ is formed from discrete versions of equations 2.3 - 2.5. The data vector $\mathbf{d}$ consists of the topography, geoid, and travel time residuals, the model vector $\mathbf{m}$ contains the temperature variations for which we are solving, and the matrix $\mathbf{A}$ contains the coefficients and kernels which relate the data to the model. As a check on our procedure, we constructed a forward problem for geoid and topography and found good agreement with the modelling results of *McKenzie et al.* [1980].

The bathymetry, geoid, and travel time profiles of Figure 2.11 are interpolated to a constant spacing, demeaned, tapered at both ends with a 10% sine squared taper, and Fourier transformed. Since our profile extends from 10 to 72°N, the first and last 10% of the profile (10 - 16°N and 66 - 72°N) will be affected by the taper. The 3n x 1 data vector $\mathbf{d}$ is then constructed, using the complex (to retain both amplitude and phase) bathymetry, geoid, and travel time data sampled at n discrete wavenumbers:

$$\mathbf{d} = [\ \Delta h(k_1),\ldots,\Delta h(k_n),\Delta N(k_1),\ldots,\Delta N(k_n),\Delta t(k_1),\ldots,\ \Delta t(k_n)\ ]^T \qquad (2.6)$$

where T denotes transpose, and n in this case is equal to 5, representing the first 5 coefficients of the Fourier series expansion (wavelengths 7104 km, 3552 km, 2368 km, 1776 km, and 1420 km). For the case where temperature perturbations are constrained to be in a single layer, the n x 1 model vector $\mathbf{m}$ is given by

$$\mathbf{m} = [\ \Delta T(k_1),\ldots,\Delta T(k_n)]^T \qquad (2.7)$$

For the more general case of a multi-layer system, the nj x 1 model vector $\mathbf{m}$ is given by

$$\mathbf{m} = [\ \Delta T(k_1, z_1),\ldots,\Delta T(k_1, z_j),\ \Delta T(k_2,z_1),\ldots,\Delta T(k_2,z_j),\Delta T(k_n,z_1)\ldots,\Delta T(k_n,z_j)]^T \qquad (2.8)$$

where z_i is the layer index and j is the total number of layers. In this paper we perform inversions for single-layer models only. The "layers" of temperature variations are independent of the "layering" system of lid, low viscosity zone, and mantle which we use for the calculation of kernels, although major changes in viscosity would tend to segment ΔT as well. The temperature layering simply refers to that region bounded by z_{min} and z_{max} in the integrals of equations 2.1 - 2.3.

The 3n x n matrix A contains the coefficients and kernels that relate the temperature perturbations to the observations, which for the single-layer case is given by

$$\mathbf{A} = \begin{pmatrix}
\frac{\rho_0\alpha}{\rho_0-\rho_w}\sum_{z_{min}}^{z_{max}} H(k_1,z)\,\Delta z & 0 & \cdots & 0 \\
0 & \frac{\rho_0\alpha}{\rho_0-\rho_w}\sum_{z_{min}}^{z_{max}} H(k_2,z)\,\Delta z & \cdots & 0 \\
0 & 0 & \ddots & 0 \\
0 & 0 & \cdots & \frac{\rho_0\alpha}{\rho_0-\rho_w}\sum_{z_{min}}^{z_{max}} H(k_n,z)\,\Delta z \\
\frac{2\pi\Gamma\rho_0\alpha}{gk_1}\sum_{z_{min}}^{z_{max}} G(k_1,z)\Delta z & 0 & \cdots & 0 \\
0 & \frac{2\pi\Gamma\rho_0\alpha}{gk_2}\sum_{z_{min}}^{z_{max}} G(k_2,z)\Delta z & \cdots & 0 \\
0 & 0 & \ddots & 0 \\
0 & 0 & \cdots & \frac{2\pi\Gamma\rho_0\alpha}{gk_n}\sum_{z_{min}}^{z_{max}} G(k_n,z)\Delta z \\
2\frac{\partial v_s}{\partial T}\sum_{z_{min}}^{z_{max}} \frac{v_s(z)^{-2}}{(1-p^2v_s(z)^2)^{\frac{1}{2}}}\Delta z & 0 & \cdots & 0 \\
0 & 2\frac{\partial v_s}{\partial T}\sum_{z_{min}}^{z_{max}} \frac{v_s(z)^{-2}}{(1-p^2v_s(z)^2)^{\frac{1}{2}}}\Delta z & \cdots & 0 \\
0 & 0 & \ddots & 0 \\
0 & 0 & \cdots & 2\frac{\partial v_s}{\partial T}\sum_{z_{min}}^{z_{max}} \frac{v_s(z)^{-2}}{(1-p^2v_s(z)^2)^{\frac{1}{2}}}\Delta z
\end{pmatrix} \tag{2.9}$$

The matrix **A** contains both bathymetry and topography kernels and is thus viscosity dependent; i.e., a viscosity structure must be assumed. We solve the equation $\mathbf{d} = \mathbf{A}\,\mathbf{m}$ by least squares

$$\mathbf{m} = (\tilde{\mathbf{A}}\, \mathbf{R}_{dd}^{-1}\, \mathbf{A})^{-1}\, \tilde{\mathbf{A}}\, \mathbf{R}_{dd}^{-1}\, \mathbf{d} \tag{2.10}$$

where $\tilde{\mathbf{A}}$ is the complex conjugate transpose of the matrix **A**. Construction of the data covariance matrix $\mathbf{R}_{dd}$ is discussed in Appendix 2.B. Equation (2.10) is solved for the solution vector **m**, and variance reduction is calculated via

$$\text{variance reduction} = 1 - \frac{\widetilde{(\mathbf{d}-\mathbf{Am})}\, \mathbf{R}_{dd}^{-1}\, (\mathbf{d}-\mathbf{Am})}{\tilde{\mathbf{d}}\, \mathbf{R}_{dd}^{-1}\, \mathbf{d}} \tag{2.11}$$

The resulting model vector **m** is inverse Fourier transformed back to the spatial domain to produce an along-axis temperature profile. The solution **m** is also substituted into equations 2.3 - 2.5 to compare predicted geoid, bathymetry, and travel time residuals with those observed.

Six inversion experiments for temperature structure were performed (Tables 2.3 and 2.4). Table 2.4 contains spectral coefficients for both the observed data and the predicted models, and serves as a guide to how well the various spectral components of the data are being fit. Since the geoid and bathymetry kernels do not include any phase information (except that a sign change produces a 180° phase shift), large phase differences between components of the observed geoid and bathymetry would indicate that these components cannot simultaneously be well fit by our models. Inversions were carried out for two different viscosity models and for three different thicknesses of the layer in which lateral temperature variations were assumed to occur. Because topography and geoid anomalies depend only on the ratios of viscosity in different layers [*Richards and Hager*,

1984; *Robinson et al.*, 1987; *Hong et al.*, 1990], we set the dimensionless viscosity of the layer representing the bulk of the mantle to unity. In one viscosity model, termed the "constant viscosity mantle," a 40-km-thick high-viscosity lid overlies a unit viscosity mantle. We set the viscosity in the lid to 10^4, which effectively mimics rigid behavior. In a second model, a 160-km-thick low-viscosity zone is present beneath a 40-km-thick lid; the viscosity in the low-viscosity zone is a factor of 100 less than in the underlying mantle. The thickness of the layer of temperature perturbations was taken variously to extend from 0-150 km depth, 0-300 km depth, and 0-650 km depth. The matrix **A** is different for each of these cases, as it involves viscosity-dependent geoid and topography kernels and also a summation over depth.

Inversion results for the constant-viscosity-mantle cases are shown in Figure 2.14. The "observed" profile is actually a filtered version of the observations, containing only the wavelengths used in the inversion (1400 to 7100 km). Predicted profiles were calculated from equation 2.5. For these solutions, the long-wavelength fit to geoid is better than at short wavelengths. The fit to bathymetry is poor. The predicted magnitude of the SS-S residuals range from a factor of 5 too small for the 650-km-thick layer to a factor of about 1.5 too small for the 150-km-thick layer. Increasing the temperature variations to improve the fit to the SS-S residuals leads to predicted geoid variations that are too large. The highest total variance reduction and best fit for the constant-viscosity cases come when lateral variations are constrained to shallow (0-150 km) depth. The variance reduction is 25% for bathymetry, 79% for geoid, and 58% for travel times (Table 2.3). The total variance reduction is 53%. The variation in temperature is 180 K for the 150-km-thick layer, and only 60 K for the 300-km-thick layer.

Figure 2.15 shows inversion results for the models with a thin low-viscosity zone. A good fit to both geoid and travel time is found, although the alignment in phase of predicted and observed geoid is not as good as for the constant-viscosity case. The fit to

bathymetry is again poor. The total variance reduction for the 150-km-thick and 300-km-thick layers are both 57%, although the shallow model provides slightly higher variance reduction for bathymetry (27% for 0-150 km deep layer, 24% for 0-300 km deep layer) and the 300-km-thick-layer model provides higher variance reduction for geoid (79% for 0-150 km deep layer, 85% for 0-300 km deep layer). The variation in temperature for the 150-km-thick layer is 230 K and in the 300-km-thick layer is 110 K.

We have explored the hypothesis that the lack of correlation of predicted and observed topography is an indication that the source of variations in the geoid and travel time anomalies is deep. To test this hypothesis, we performed inversions with temperature variations restricted to deeper layers and found that fits to topography were still poor. It is possible that the bathymetric signal is dominated by crustal thickness variations which are not included in our calculation of dynamic topography. An assessment of such thickness variations is discussed further in Appendix 2.B.

Inversion for Compositional Variations

A possible alternative to along-axis variation in mantle temperature is lateral variation in bulk mantle composition, due perhaps to a variable extent of melt extraction or different degrees of mixing of compositionally distinct volumes of mantle material. The dynamical effects of compositionally induced density variations can be large [*O'Hara*, 1975; *Boyd and McCallister*, 1976; *Oxburgh and Parmentier*, 1977; *Sotin and Parmentier*, 1989]. The fraction of mantle potentially extractable as basaltic melt is thought to be 15-25% [e.g., *Green and Liebermann*, 1976]. Thus, for every volume of basalt removed from the mantle, a volume of residuum several times larger is left behind. The effect of basalt depletion is to increase the molar ratio Mg/(Mg + Fe) (or Mg#) in the residuum, which reduces the density and increases the seismic velocities [e.g., *Liebermann*, 1970; *Akimoto*, 1972]. For example, subtraction of 20 mole % olivine basalt from pyrolite can

decrease the density of the residuum by nearly 2%, equivalent to a thermal perturbation of nearly 500 K [*Jordan*, 1979]. Thus compositional changes need only be slight to produce effects on the order of 100 K, comparable to values obtained from the inversions for temperature variations. In this section we explore the effects of compositional variations parameterized in terms of the variation in the Mg# in the upper mantle along the ridge. Our motivation for parameterizing compositional variations simply in terms of Mg# is that differences in this quantity yield significant variations in seismic velocity and density, in contrast to most other measures of degree of melt extraction.

Partial derivatives of density and seismic velocity with respect to Mg# are obtained from *Akimoto* [1972]. These values were measured on a suite of samples ranging from pure forsterite (Mg_2SiO_4) to pure fayalite (Fe_2SiO_4). While these partial derivatives are at standard temperature and pressure, it is expected that a change to elevated temperature and pressure will have only a second order effect, since temperature and pressure corrections work in opposite directions [*Jordan*, 1979]. Above the solidus temperature, however, the amount and distribution of partial melt, which may depend strongly on composition and particularly volatile content, is important. The presence of melt is likely to have a larger effect on shear wave velocities than on bulk density. Calculations of melt migration, however, suggest that once created, melt segregates rapidly by a percolation mechanism [e.g. *Scott and Stevenson*, 1989], so that the melt fraction present in the mantle at any given time is probably small. Studies of mantle peridotites [*Johnson et al.*, 1990] also support the importance of fractional melting.

It is straightforward to convert equations (2.3) and (2.4) to relations between geoid or topography and a compositionally induced density perturbation by means of the relation

$$\Delta\rho = - \rho_0 \alpha \Delta T \qquad (2.12)$$

Compositional anomalies at depth yield a dynamic topography h(k) given by

$$\Delta h(k) = \frac{1}{\rho_0 - \rho_w} \frac{\partial \rho}{\partial Mg} \int_{z_{min}}^{z_{max}} H(k,z)\, \Delta Mg(k,z)\, dz \qquad (2.13)$$

where ΔMg represents the fractional change in the Mg#. Compositional anomalies yield a geoid anomaly

$$\Delta N(k) = \frac{2\pi\Gamma}{gk} \frac{\partial \rho}{\partial Mg} \int_{z_{min}}^{z_{max}} G(k,z)\, \Delta Mg(k,z)\, dz \qquad (2.14)$$

For a compositional perturbation at depth the resulting two-wave travel time perturbation is given by

$$\Delta t(k) = 2 \frac{\partial v_s}{\partial Mg} \int_{z_{min}}^{z_{max}} \frac{\Delta Mg(k,z)\, dz}{v_s(z)^2 \left(1 - p^2 v_s(z)^2\right)^{1/2}} \qquad (2.15)$$

Using equations (2.13) - (2.15), an inversion scheme similar to that used for thermal perturbations is formed. The solution vector now has the form

$$\mathbf{m} = [\Delta Mg(k_1), \ldots, \Delta Mg(k_n)]^T \qquad (2.16)$$

The data vector remains the same as in equation (2.6), while the matrix of coefficients, **A**, changes to reflect the relation between the data and mantle composition, rather than temperature, as outlined in equations (2.13) - (2.15).

The results of the inversions for compositional variations are summarized in Table 2.3 and in Figures 2.16 and 2.17. We are unable to match simultaneously both SS-S travel

time residuals and geoid and bathymetric anomalies with solely mantle compositional variations for either a constant viscosity mantle or one with a low viscosity zone. This is not surprising, as the travel times are for the most part positively correlated with geoid and bathymetry, but compositional variations (at least for the Mg_2SiO_4 - Fe_2SiO_4 system examined here) have an opposite effect on travel time and geoid-bathymetry.

For the constant viscosity case, the fit to the geoid is excellent, and the fit to bathymetry is slightly better than in the inversion for temperature. The fit to SS-S residuals is so poor that the variance reduction is negative for travel time. Large compositional changes would be required to affect travel times, whereas only small compositional changes are needed to produce significant density contrasts to match the geoid signal. The total variance reduction for the constant viscosity case does not vary greatly (from 32-33%) for compositional changes constrained to be over different depth intervals, though the variance reductions for individual data sets (bathymetry, geoid, travel time) vary significantly from model to model (see Table 2.3). The range in Mg# is about 1% if the variation is constrained to the depth range 0-150 km and only 0.1% for the 0-650 km depth range.

Figure 2.17 shows inversion results for the model with a low viscosity zone. A good fit to both geoid and bathymetry is found, although the alignment of predicted and observed geoid is not as good as in the constant viscosity case. The fit to bathymetry is the best of any models so far. The total variance reduction is still low (43 to 49%), due to the poor fit to travel times (negative variance reduction in all cases except the 0-650 km model). The range in Mg# is 2.4% if constrained to 0-150 km depth, 1.3% over 0-300 km depth, and 0.5% over 0-650 km depth.

Joint Inversion for Temperature and Composition

We next explore whether a combination of temperature and compositional

variations can provide a good match to the observed geoid, travel time, and bathymetry. Joint inversions provide improved fits to all data at the expense of introducing additional free parameters. For these inversions the data vector remains the same as in equation (2.6), the solution vector is modified to include both temperature and composition, and the matrix of coefficients, A, includes the effects of both temperature and composition. The matrix-building equations become, for example, for topography,

$$\Delta h(k) = \frac{\rho_0 \alpha}{\rho_0 - \rho_w} \int_{z_{min}}^{z_{max}} H(k,z)\, \Delta T(k,z)\, dz + \frac{1}{\rho_0 - \rho_w} \frac{\partial \rho}{\partial Mg} \int_{z_{min}}^{z_{max}} H(k,z)\, \Delta Mg(k,z)\, dz \quad (2.17)$$

which is simply a combination of equations (2.3) and (2.13). The new geoid equation comes from a combination of equations (2.4) and (2.14) and the travel time equation from a combination of equations (2.5) and (2.15). Cross terms, such as compositional changes induced by increases or decreases in temperature, are neglected.

The results for the joint inversion for temperature and composition are summarized in Table 2.3 and Figures 2.17 and 2.18. The travel time residuals are well-modeled in all cases, as are the geoid data. The topography is best fit for the case with a low viscosity zone. Resolution of the depth interval of the most important lateral variations is rather poor. The topography is fit marginally better for the case where temperature and compositional anomalies are constrained to be shallower than 300 km. For the constant viscosity mantle, the temperature variations range from 210 K, if constrained to 0-150 km depth, to 55 K if over 0-650 km depth; variations in Mg# range from 1.5% if over 0-150 km depth to 0.4% for 0-650 km depth. For the case with an upper mantle low viscosity zone, the temperature variations are similar to those in the constant viscosity case, but the variations in Mg# are larger, from over 2% for 0-150 km depth to nearly 1% for 0-650 km depth.

The travel time residuals are perfectly fit in the joint inversions for temperature and

composition (Table 2.3). This occurs because of the way the model parameters act in a similar manner on both geoid and bathymetry, producing a singular matrix if only geoid and bathymetry data are inverted for both temperature and composition. Undamped least squares always provides perfect solutions when the number of equations is equal to the number of unknowns unless the matrix to be inverted is singular. If we perform an inversion including only travel time and geoid data, we have the same number of equations as unknowns, the matrix is nonsingular, and we obtain perfect fits to both travel time and geoid. Similarly, if we perform an inversion of travel time and bathymetry data, we again obtain perfect fits to both data sets. If we perform an inversion of geoid and bathymetry data, however, we are unable to obtain solutions without applying damping. In the joint inversion of travel time, geoid, and bathymetry, we have more equations than unknowns and the inversion is overdetermined. However, the travel times are perfectly determined in this case because of the nonuniqueness inherent with geoid and bathymetry. We have performed undamped inversions with various weightings on the geoid, bathymetry, and travel time data, and in all cases the travel times remain perfectly fit.

We have also performed joint inversion for temperature and composition with Mg# variations constrained to be in the upper 50 km of the lithosphere so as to mimic compositional variations due solely to variable melt extraction at the ridge. Temperature perturbations were allowed to remain within the depth ranges adopted earlier. The results for this inversion are summarized in Table 2.3 and Figures 2.20 and 2.21. The variance reduction was similar for the constant viscosity case and for the model with a low viscosity zone. In general, the geoid is fit very well, the predicted amplitudes are a bit low for travel time residuals, and the topography fit is slightly out of phase. For the constant viscosity mantle, the range in temperature is 210 K over 0-150 km depth and 25 K over 0-650 km, while Mg# variations constrained to be confined to 0-50 km depth were over 5%. For the case with a low viscosity zone, the temperature variations were not dramatically different

from those in the constant viscosity case, and variations in Mg# were about 4.5%. The inversion solution shows high temperatures near 30°N and low temperatures in the region from 50-60°N. Iceland also appears to be underlain by high-temperature mantle. Going from south to north along the ridge, compositional variations indicate low Mg# in the vicinity of 20-30°N, high Mg# in the Azores region (40°N), low values near 50°N, and high values near 60°N.

DISCUSSION

The temperature and compositional variations in Figures 2.14-2.21 are broadly consistent with observed travel time, geoid, and bathymetry anomalies in the north Atlantic region. Temperature variations alone can account for most of the observed anomalies. In contrast, compositional variations alone cannot match all anomalies simultaneously. We infer that a component of the observed anomalies is due to long-wavelength variations in upper mantle temperature. Joint inversions for temperature and composition provide better fits than single-variable models, but at the expense of introducing additional free parameters.

It is difficult to select a 'best' model from the suite of inversions presented. The variance reductions in Table 2.3 serve as a guide, but independent criteria may allow us to reject some of the models, even those with high variance reductions. In particular, those models with large temperature variations (well in excess of 100 K) can be seriously questioned. Lateral temperature variations at upper mantle levels beneath oceanic ridges are thought to be no more than about 300 K globally [*Klein and Langmuir*, 1987], so a variation in temperature of 230 K (as in the inversion with a low-viscosity zone and a 150-km-thick layer of temperature perturbations) solely within a section of the north Atlantic is probably unreasonably large. Further, as *White and McKenzie* [1989] have noted,

relatively small increases in mantle temperature above values typical for the mid-ocean ridge are sufficient to cause large increases in melt production. Their models indicate that, for fixed bulk composition, an increase of 100 K above normal doubles the amount of melt while a 200 K increase can quadruple it. Such increased melt production should lead to approximately corresponding increases in crustal thickness. Variations in oceanic crustal thickness away from fracture zones, however, are generally thought to be small, with thicknesses typically 6-7 km and ranging from 4.5 to 8.5 km [*Spudich and Orcutt*, 1980; *White*, 1984; *Purdy and Detrick*, 1986]. In the joint inversion for temperature and composition, temperature variations if confined to 150 km depth are excessive (over 200 K) and if the variations extend over 0-650 km the fit to topography is poor, especially for the constant-viscosity mantle. On the basis of these results we prefer the models with temperature variations occurring over 0-300 km depth. For the constant viscosity mantle, the temperature variation is 110 K, and the variation in Mg# is 0.75%. For the case with an upper mantle low viscosity zone, the predicted temperature variation is 125 K, and the variation in Mg# is 1.1 %. The total variance reduction is greater in the model with a low viscosity zone.

Even a temperature variation of about 100 K is high for a mantle of constant composition, since we do not observe increased crustal thickness in regions that our models indicate have high temperatures. The assumption of approximately constant upper mantle composition warrants discussion. In particular, lateral variation in trace amounts of mantle volatiles may have a large effect on seismic velocity at a given temperature. The presence of even a slight amount of water, for instance, is sufficient to cause a significant decrease in the initial melting temperature of peridotite [*Wyllie*, 1971]. Estimates of volatile contents and their lateral variations in the north Atlantic region have been made from measurements of abundances of halogens, SiO_2, K_2O, and H_2O in basalts and from the volumes of vesicles in basalts [*Schilling et al.*, 1980, 1983; *Schilling*, 1986; *Michael*,

1988]. These studies indicate that Cl, Br, F, and H_2O contents increase toward the Azores and Iceland and that H_2O is two to three times more abundant in Mid-Atlantic Ridge basalts erupted over the Azores platform than at adjacent normal ridge segments. The effect of volatiles on density and shear wave velocity will be slight at subsolidus temperatures but can be major over the melting interval [*Goetze*, 1977]. The presence of melt will act to decrease significantly the seismic velocity [*Duschenes and Solomon*, 1977] and, to a lesser extent, lower the density of the mantle. To the extent that seismic velocity depends on proximity of the temperature to the solidus temperature [*Sato et al.*, 1988, 1989], volatile content can trade off with temperature in its effect on velocity at subsolidus conditions. Thus, variation in volatile content could lessen the variations in melt production implied by the inversion solutions.

Even without significant variations in volatile content, it is clearly an oversimplification to parameterize mantle composition in terms of only a single quantity. Further we have assumed that the partial derivatives of bulk density and seismic velocity with respect to Mg# that are those for olivine [*Akimoto*, 1972]. The work of *Jordan* [1979] indicates that these derivatives remain nearly constant for many different mantle compositions (i.e., pyrolite-type compositions with various amounts of olivine, orthopyroxene, clinopyroxene, spinel, and garnet), so the latter assumption is sound. However, at any given Mg#, orthopyroxene and clinopyroxene have lower velocities and are less dense than olivine, while garnet and spinel are seismically faster and denser than olivine [*Jordan*, 1979], so an increase in the weight percent of orthopyroxene and clinopyroxene or a decrease in the weight percent of garnet and spinel with respect to olivine in the mantle could counteract some of the temperature variations obtained under the assumption of effectively uniform mineralogy. Several studies [*Wood*, 1979; *Jaques and Green*, 1980; *Dick et al.*, 1984] have suggested that compositional variations in the mantle are plausible. Indeed a number of workers [e.g., *Davies*, 1984; *Allègre et al.*, 1984] favor

dynamic models for the mantle in which dispersed heterogeneities of various sizes and shapes are passively embedded in a continually mixed, convecting mantle. Variations in modal fractions of olivine, orthopyroxene, and clinopyroxene in peridotites recovered along the Mid-Atlantic Ridge have been reported in several studies [*Dick et al.*, 1984; *Michael and Bonatti*, 1985]. These variations are typically attributed to different degrees of melt extraction but could also be partially due to intrinsic upper mantle heterogeneity. For example, the relative fractions of olivine, clinopyroxene, and orthopyroxene indicated by *Michael and Bonatti* [1985] at 26°N and 30°N, if extended to depth, could counteract a portion of the temperature differences indicated by the inversion solutions for these regions.

Chemical analysis of dredged peridotites in the north Atlantic indicate a range of about 2.5% variation in Mg# [*Michael and Bonatti*, 1985]. This value is intermediate between what we find for models with compositional variations constrained to be shallow (4.5 to 6% variation) and those models with compositional variations in the same depth ranges as the thermal variations (1-2%). This suggests that compositional variations may be concentrated slightly shallower than the temperature variations. *Michael and Bonatti* [1985] present an along-axis profile of Mg# variations from dredged peridotites which can be compared with our calculated profile. The main feature in their profile is a zone of high values of Mg# in the Azores region, from 34-45°N, relative to the rest of the ridge, consistent with our modelling results. Their data sampling is too sparse to delineate other long-wavelength features. Their average value for 26°N also has a high Mg# relative to adjacent data. This is consistent with our observation of early SS-S travel times and low geoid in this region. This anomaly is of too short a wavelength (< 1000 km), however, to resolve in our inversions. We should note that comparisons merit caution, as small scale features, such as those due to ridge segmentation, can produce large differences in composition between peridotites over scales of tens of kilometers. In addition, dredged

peridotites are mostly from fracture zone environments, which may not be representative of typical ridge mantle [*Dick*, 1989].

On the SS-S residual profile the Iceland region appears as a local maximum (late SS) but the Azores hotspot does not show a distinct seismic signal. The inversion results for these two regions are also markedly different. The results of the joint inversion for temperature and composition predict a high Mg# in the Azores region while indicated temperatures are not anomalously high. At Iceland, in contrast, high temperatures dominate. Work by *Schilling* [1986] and *Bonatti* [1990] outlines the differences in geochemical signatures between the Azores and Iceland hot spots. These workers suggest that Iceland is a "traditional" plume hot spot, with a predominantly thermal origin, but that the Azores might be more aptly named a "wet spot" because of the presence of excess hydrous phases and the lack of a thermal anomaly. *Bonatti* [1990] suggests that because the Azores hotspot is rich in volatiles, enhanced melt production could occur with little or no increase in temperature. The high Mg# indicated in our inversions allows the region to be seismically fast (as we observe) but of low density (as geoid and bathymetry require). The results are consistent with the hypothesis that the Azores hot spot is not associated with a plume-like thermal anomaly. Inversion of surface wave dispersion data can potentially provide further tests of these ideas, but studies to date have yielded apparently conflicting results. Results of several such investigations [*Nakanishi and Anderson*, 1984; *Tanimoto*, 1990; *Zhang and Tanimoto*, 1990a] suggest that the Azores region is seismically slow at depths less than 300 km but a study utilizing 50-200-s-period Rayleigh waves by *Mocquet et al.* [1989] does not. These differences may be partially attributable to the differences in wave periods employed and mode of analysis from study to study. It may be possible that what appear to be low velocities at the Azores are a result of horizontal smoothing of the low velocities along the ridge and have little to do with the actual structure in the Azores region. None of these long-period surface wave studies resolve a distinctive anomaly at

Iceland. Clearly, more work is needed to resolve the upper mantle velocity structure of hot spot regions.

Bonatti [1990] has constructed profiles of the equilibrium temperature of dredged peridotites along the Mid-Atlantic Ridge axis from 0 to 60°N by means of two different geothermometers [*Wells*, 1977; *Lindsley*, 1983]. Comparison of these profiles with the along-axis temperature variations obtained from our inversions reveals a number of qualitative correlations as well as a few discrepancies. The range of temperature variations in the profile based on the *Lindsley* [1983] geothermometer is about 150 K, neglecting high values termed "anomalous." When the high values are included the range increases to 400 K. The profile utilizing the *Wells* [1977] geothermometer has a range of 100 K neglecting the anomalous values and 350 K including them. The highest temperatures in our inversions are near 30°N (Figures 2.18-2.19), a region showing a slight peak in Bonatti's temperature profile estimated according to *Lindsley* [1983] and a very weak rise in the profile utilizing the *Wells* [1977] geothermometer. There is a small dip in temperature at 26°N (a region which we find to be seismically fast) in the *Lindsley* [1983] and *Wells* [1977] profiles, but the difference may not be significant considering the error bars. *Bergman and Solomon* [1989] also found the upper mantle near 26°N to be seismically fast from an analysis of teleseismic P-wave travel time residuals from earthquakes in this region recorded by a local ocean-bottom seismic network. The lowest temperatures on the profiles of *Bonatti* [1990] are at 43°N. Temperatures from our inversion solutions are also low in this region, although the *Bonatti* [1990] profiles indicate an increase in temperature proceeding north from 43°N to 53°N, whereas our results favor continued low temperatures. Part of the difference between our results and the geochemical studies may be attributed to the fact that the depth sampled by basalts and peridotites is likely to be shallower than the layer thicknesses of most of our models. Assuming that the 6-km-thick oceanic crust was formed by 9 to 22 % partial melting of the mantle [*Klein and Langmuir,*

1987], then the volume of residual peridotite will extend from the base of the crust to somewhere between 30 and 70 km depth. The amount of depletion will vary with depth if we assume a fractional melting model. Our models with compositional variations confined to depths less than 50 km are most representative of shallow fractionation and differentiation.

Several improvements in future studies of the type presented here may be envisioned. Our models thus far have been limited to simply parameterized one-dimensional variations in temperature and composition within a single layer. It is likely that these lateral variations are not constant within a given layer and that there are two-dimensional lateral variations independent of lithospheric aging. The techniques outlined in this paper can be generalized to a multilayer system and to two-dimensional wavenumber (see equation 2.8), but we do not feel that the resolution of our data can justify more complicated models at this time. Kernels for seismic surface waves are strongly peaked in the upper mantle, and such data would provide a useful constraint in future models. The inclusion of surface wave data would help to distinguish between lithospheric and asthenospheric effects and may allow for two or more independently resolved layers. Extension of the modelling to three dimensions would permit an assessment of the degree to which mantle anomalies beneath the ridge extend off axis. Implicit in our age-correction is the assumption that the anomalous properties of the ridge mantle are steady state on a time scale of 100 My. Recent seafloor surveys and theoretical studies [e.g., *Pockalny et al.*, 1988; *Scott and Stevenson*, 1989] bring this assumption into question and suggest that at least on short time scales (< 1 My) and at slow spreading rates (as in the Atlantic) intermittent periods of melting and crustal formation may be separated by periods with little or no melt production. These temporation variations are likely to be averaged out, however, over the typical horizontal wavelength (100 km) of a long-period SS wave.

Another limitation of our models is that they depend on the assumed values of

several physical constants. It is straightforward, however, to estimate the effect of choosing different values. The viscosity structures we employ are also quite simple but have been chosen to represent two models widely invoked in other studies - a constant or nearly constant viscosity mantle [e.g., *Peltier*, 1989] and a mantle with a thin low viscosity layer [e.g., *Craig and McKenzie*, 1986; *Robinson et al.*, 1987]. The viscosity structure of the Earth may be temperature and pressure dependent or vary laterally, but we have not considered viscosity structures of this type. Nor have we modelled the effects of partial melting which could accompany the temperature variations we predict. The effect of retained melt on the physical properties of the mantle depends critically on the melt fraction and geometry, characteristics presently poorly known. *Sato et al.* [1988, 1989] downplay the importance of partial melt and suggest that most mantle seismic velocity anomalies can be explained by temperature variations at subsolidus conditions. The combined analysis of both shear and compressional differential travel times also suggest that significant partial melting is not required to explain the travel time residuals in the north Atlantic region [*Woodward and Masters*, 1991].

CONCLUSIONS

We have measured 500 SS-S differential travel times for paths in the north Atlantic region. The SS-S travel time residual decreases linearly with square root of age, in general agreement with the plate cooling model to an age of 80-100 My [*Parsons and Sclater*, 1977]. Azimuthal anisotropy is not clearly resolved, and the azimuthal patterns of our data are not consistent with the preferred upper mantle anisotropy model of *Kuo et al.* [1987] for the north Atlantic. An along-axis profile of age-corrected travel time residuals displays significant long-wavelength variations, notably at wavelengths of 1000-2000 km. The largest of these variations are robust with respect to selective removal of portions of the

data.

We have formulated a joint inversion of travel time residuals and geoid and bathymetric anomalies for lateral variation in upper mantle temperature and composition. On the basis of variance reduction, inversion for temperature favors the presence of an upper mantle low viscosity zone and temperature anomalies concentrated at depths less than 300 km. We are unable to match travel time residuals simultaneously with geoid and bathymetry solely with lateral variations in bulk composition (Mg#). Joint inversions for temperature and composition provide good fits to both travel time and and geoid regardless of viscosity structure or layer depth and thickness, but the best fits to bathymetry come from models with a low-viscosity zone and thermal or compositional variations confined to shallow depth. The Mg# variations predicted in the joint inversion for temperature and composition are comparable to those found by *Michael and Bonatti* [1985] in a study of dredged peridotites along the Mid-Atlantic Ridge and may be related to variations in melt production along the ridge.

The preferred inversion solutions have variations in upper mantle temperature along the Mid-Atlantic Ridge of about 100 K. For a constant bulk composition, such a temperature variation would produce about a 7 km variation in crustal thickness [*White and McKenzie*, 1989], larger than is generally observed [*Spudich and Orcutt*, 1980; *White*, 1984; *Purdy and Detrick*, 1986]. Introducing compositional variations as well as temperature variations in the inversions does not change the range of temperature appreciably. The presence of volatiles in the mantle can have a strong effect on temperatures required for melting, and variations in volatile content along the ridge may reduce the large variation in melt production implied by the lateral temperature variations indicated in our models.

APPENDIX 2.A: ESTIMATION OF ERRORS FOR SS-S DIFFERENTIAL TRAVEL TIMES

It is important to quantify the uncertainties in the differential travel time measurements. After cross-correlation, the "quality" of each individual SS-S measurement is rated and a grade is assigned. The cross correlation coefficient, which describes the degree of fit between the synthetic and real SS phases, is used as an objective aid in the assignment of quality. However, our final assignment of quality is largely subjective and based upon visual inspection of the "synthetic" SS, real SS, and cross correlogram, taking into account the sharpness of the arrivals and their alignment, the clarity of the seismogram, and the appearance of a single clear peak in the cross correlation function. An "A" quality grade indicates an excellent fit, "B" quality indicates good phase alignment but only a fair fit, and a "C" quality grade indicates a poor fit or some ambiguity as to phase alignment. In addition to A, B, and C grades, there were data that were rejected due to poor signal to noise ratio for either the S or SS phases.

Assuming that the uncertainty in an individual measurement comes from a combination of measurement error, unmodeled lower mantle structure, and epicentral error, we write, for example, for the measurement variance of an "A" quality datum:

$$\sigma_A^2 = \sigma_{Am}^2 + \sigma_{lm}^2 + \sigma_{epi}^2 \qquad (2.A1)$$

where σ_A is the total uncertainty, σ_{Am} is the measurement error, σ_{lm} is the uncertainty due to unmodeled lower mantle structure, and σ_{epi} is the epicentral error. We assume that σ_{lm} and σ_{epi} are the same for A, B, and C quality measurements, but the measurement error is obviously a strong function of data quality.

Effect of Epicentral Error

In general, epicentral errors affect the travel times only slightly. The events used in this study were well recorded by a large number of stations over a wide range of azimuths, and typical epicentral mislocations are probably less than 10 km (which would yield a differential travel-time error of 0.35 s at 75° distance). The travel times are even less sensitive to errors in focal depth; an error in depth of 25 km contributes only about 0.3 s to the SS-S residual. Using the rule of thumb that one standard deviation is about one half of the estimated extremes, we adopt $\sigma_{epi} = 0.75$ s as a conservative estimate of epicentral error.

Effect of Unmodelled Lower Mantle Heterogeneity

We estimate the likely magnitude of lateral variations in the shear wave velocity of the lower mantle from models of lower mantle heterogeneity in P wave velocity (such as model L02.56 of *Dziewonski* [1984]). The average variation in travel times of direct P waves bottoming in the lower mantle is in the range ± 0.5 s. Global tomographic studies by *Dziewonski and Woodhouse* [1987] indicate that the scaling ratio $(\delta V_s/V_s)/(\delta V_p/V_p) \approx 2$ in the lower mantle. Such a scaling is also suggested by comparison of lower mantle P wave models with the recent lower mantle S model of *Tanimoto* [1990]. Assuming such an S to P velocity anomaly scaling, the resulting variation in S wave arrival time contributed by the lower mantle would likely be about ± 1.5 s, a fraction of the observed range in SS-S residual. While the major features of lower mantle model L02.56 [*Dziewonski*, 1984] and the lower mantle portions of *Tanimoto's* [1990] model are for the most part similar, enough differences exist that the application of a lower mantle "correction" to our data might add more uncertainty than it removes. Further, absolute S-wave travel times do not show enough variance for us to suspect large lower mantle effects [e.g., *Randall*, 1971; *Girardin and Poupinet*, 1974; *Hart and Butler*, 1978; *Uhrhammer*,

1978, 1979], and the work of *Gudmundson et al.* [1990] indicates that most of the variance from the ISC tables is attributable to the shallow mantle, i.e., most of the Earth's heterogeneity is in the upper mantle and the lower mantle is fairly homogeneous. On the basis of the above information, we set $\sigma_{lm} = 0.5$ s for our study.

Measurement Error

As an objective means to obtain error estimates, we examine the scatter in A, B, and C quality picks in a small region. We measured the root mean square (rms) difference between travel time residuals of the same grade (A, B, or C) with bounce points separated by less than 80 km and with differences in path azimuth at the bounce point of less than 10°. An 80-km distance is less than the horizontal wavelength of SS (which is about 180 km at 25 s period) so we do not expect much contribution to the rms difference from actual lateral variations in structure. The rms difference for the 16 A quality residual pairs which were within 80 km of each other was 1.15 s. For B quality picks, an rms difference of 2.08 s was measured using 20 residual pairs, and for C quality picks 44 residual pairs yielded an rms difference of 2.96 s.

We interpret these estimates of the rms diffences as representing the average overall errors in the A, B, and C grade measurements. (Unmodelled lower mantle structure should be nearly identical for data with bounce points within 80 km and at similar azimuths). Under this interpretation we can write, for A-quality residuals,

$$\sigma_{Arms}^2 = \sigma_{Am}^2 + \sigma_{epi}^2 \qquad (2.A2)$$

Substituting values of σ_{Arms} and σ_{epi} into (A2) yields σ_{Am}= 0.87 s. Similarly, for B and C quality measurements, we find $\sigma_{Bm} = 1.94$ s and $\sigma_{Cm} = 2.86$ s. From (A1), the total uncertainty for A, B, and C quality is, respectively, $\sigma_A = 1.25$ s, $\sigma_B = 2.14$ s, and σ_C =

3.00 s.

In the weighted regression experiments the A, B, and C quality measurements are weighted inversely by their measurement variance.

APPENDIX 2.B: ERRORS IN THE ALONG-AXIS PROFILES AND CONSTRUCTION OF THE DATA COVARIANCE MATRIX

Errors in Bathymetry, Geoid, and Travel Time Profiles

Uncertainties in the along-axis profiles of geoid, bathymetry, and travel times are important information in the inversion. The gridded bathymetric data [*U.S. Naval Oceanographic Office*, 1985] include corrections for the deviation of water column acoustic velocity from the assumed value of 1500 m s^{-1}. The geoid data, provided in the form of a 0.25° x 0.25° grid [*Marsh et al.*, 1986], include corrections for orbit errors, instrument and atmospheric propagation effects, and solid Earth and ocean tides.

We have averaged the bathymetry and geoid height values within a 1° x 1° box centered at each SS bounce point. The averaging yields a representative value for a region over approximately one horizontal wavelength of the SS wave and acts to smooth out short-wavelength variations. Both bathymetry and geoid are corrected for subsidence with seafloor age, using the plate cooling model [*Parsons and Sclater*, 1977; *Parsons and Richter*, 1980]. Error introduced into depth and geoid anomalies by isochron mislocation is difficult to estimate precisely, but for an error in age of 2 My, depth and geoid errors at 80 My would be about 30 m and 0.2 m, respectively, while at 2 My, an error in age of 2 My would have a much larger affect, giving depth and geoid errors of 350 m and 0.3 m. The magnitude of this error highlights the importance of accurate age determination, especially at young ages.

The presence of oceanic sediments is another source of error. In the Atlantic Ocean, the sediment thickness increases regularly from less than 100 m along the Mid-Atlantic Ridge toward continental margins where it can exceed 1 km [*Ewing et al*, 1973; *Tucholke*, 1986]. A 1-km sediment thickness leads to corrections to residual depth and geoid of about 500 m and 0.3 m, respectively [*Cazenave et al.*, 1988; *Sheehan and*

McNutt, 1989]. On Atlantic lithosphere of 100 My age or less the sediment thickness is less than 500 m in most areas. Hence, neglecting the sediment loading correction should not be crucial in this region.

The along-axis profile of SS-S residual is a weighted moving average of 10 adjacent data points grouped by latitude, using the weights discussed in Appendix 2.A. The same weights and moving average are applied to geoid and bathymetry values at a given SS bounce point, even though bathymetry and geoid data are presumed to be of equal quality, in order that these profiles will be consistent with the SS-S residuals. The standard error of the mean values for SS-S residual ranges from 0.2 s to 1.6 s. For bathymetry the range of standard deviations from the mean value is from 24 to 370 m, and for geoid, 0.08 to 1.0 m. The largest variances in the bathymetry and geoid data come from the Iceland region (north of 60°N), and may be due to the more complicated tectonics of this region [*White*, 1988].

Before Fourier transforming, the along-axis profiles must be interpolated to a constant spacing. We use a simple linear interpolation scheme to estimate values at a 0.5° spacing. We estimate that the typical error in the interpolated data is comparable to that in the along-axis moving averages, which for bathymetry is on the order of 125 m, for geoid 0.4 m, and for travel time 1 s.

Effect of Crustal Thickness Variations

Our poor fit to topography in the inversion experiments can be at least partially attributed to unmodelled effects such as crustal thickness differences. Variations in oceanic crustal thickness about the typical value of 6-7 km [*Spudich and Orcutt*, 1980; *White*, 1984; *Purdy and Detrick*, 1986] are generally thought to be small at horizontal scales of 100 km and greater. However, the crust beneath the Azores plateau is estimated to be between 8 and 9 km thick [*Searle*, 1976; *Whitmarsh et al.*, 1982] and that beneath Iceland

is at least 8 to 14 km thick [*Bjornsson*, 1983]. By simple isostatic mass balance, the depth anomaly due to excess crustal thickness in the Azores region would be about 400 m, and at Iceland, 200 m to 1.6 km. In general, simple variations in crustal thickness are insufficient to produce a significant SS-S residual. For crustal and mantle S wave velocities of 3.5 and 4.4 km/s, a 2-km variation in crustal thickness would contribute less than 0.2 s to an SS-S differential travel time corrected for differences in bathymetry. However, at Iceland, where the crust is estimated to be as much as 14 km thick, the additional SS-S travel time could be up to 0.8 s.

Data Covariance Matrix

The data covariance matrix $\mathbf{R}_{dd}$ is of the form

$$\mathbf{R}_{dd} = \begin{pmatrix} \sigma_h(k_1)^2 & 0 & 0 & 0 & 0 & 0 & 0 & 0 & 0 \\ 0 & \dots & 0 & 0 & 0 & 0 & 0 & 0 & 0 \\ 0 & 0 & \sigma_h(k_n)^2 & 0 & 0 & 0 & 0 & 0 & 0 \\ 0 & 0 & 0 & \sigma_N(k_1)^2 & 0 & 0 & 0 & 0 & 0 \\ 0 & 0 & 0 & 0 & \dots & 0 & 0 & 0 & 0 \\ 0 & 0 & 0 & 0 & 0 & \sigma_N(k_n)^2 & 0 & 0 & 0 \\ 0 & 0 & 0 & 0 & 0 & 0 & \sigma_t(k_1)^2 & 0 & 0 \\ 0 & 0 & 0 & 0 & 0 & 0 & 0 & \dots & 0 \\ 0 & 0 & 0 & 0 & 0 & 0 & 0 & 0 & \sigma_t(k_n)^2 \end{pmatrix}$$

where σ_h^2, σ_N^2, and σ_t^2 are the nominal variances of the bathymetry, geoid, and travel time data, respectively. We may choose to construct the data covariance matrix not to reflect the true variance of the data but rather to allow weighting between the different data sets. In this way, the data covariance matrix can be altered to test the relative contributions of different data sets to the inversion results.

In all of our inversions, the covariance matrix is constructed to weight the three data sets approximately equally. For example, examination of Figure 2.11 indicates that at 3000-km wavelength the amplitude of the geoid signal is approximately 4 m, bathymetry 1 km, and travel time 2 s. Thus if a value of 1 m is chosen for σ_N, then a value of 0.5 s for σ_t and 0.25 km for σ_h should yield approximately equal weighting of data sets. The corresponding $1/\sigma^2$ values are then 1 for geoid, 4 for travel time, and 16 for bathymetry.

TABLE 2.1. Digital Seismograph Stations Used

Station Code	Network	Latitude (°N)	Longitude (°E)
ALQ	DWWSSN	34.942	-106.458
ANMO	SRO	34.946	-106.457
ANTO	SRO	39.869	32.794
BCAO	SRO	4.434	18.535
BER	DWWSSN	60.387	5.326
BOCO	SRO	4.587	-74.043
COL	DWWSSN	64.900	-147.793
GAC	CAN	45.70	-75.47
GDH	DWWSSN	69.250	-53.533
GRFO	SRO	49.692	11.222
JAS1	DWWSSN	37.947	-120.438
KBS	DWWSSN	78.917	11.924
KEV	DWWSSN	69.755	27.007
KONO	ASRO	59.649	9.598
LON	DWWSSN	46.750	-121.810
NE04	NARS	52.810	6.670
NE06	NARS	50.100	4.600
NE09	NARS	44.850	0.980
NE10	NARS	43.090	-0.700
NE11	NARS	41.480	-1.730
NE12	NARS	40.640	-4.160
NE13	NARS	38.690	-4.090
NE14	NARS	37.190	-3.600
NE15	NARS	50.810	5.780
NE16	NARS	45.763	3.103
NE17	NARS	39.881	-4.049
RSCP	RSTN	35.600	-85.569
RSNT	RSTN	62.480	-114.592
RSNY	RSTN	44.548	-74.530
RSON	RSTN	50.859	-93.702
RSSD	RSTN	44.120	-104.036
SCP	DWWSSN	40.795	-77.865
SSB	GEOSCOPE	45.280	4.540
TOL	DWWSSN	39.881	-4.049
WFM	GEOSCOPE	42.610	-71.490
ZOBO	ASRO	-16.270	-68.125

ASRO = Abbreviated Seismic Research Observatory Network
CAN = Canadian Seismic Network
DWWSSN = Digital World-Wide Standardized Seismograph Network
GEOSCP = Geoscope Network
NARS = Network of Autonomous Recording Seismographs
RSTN = Regional Seismic Test Network
SRO = Seismic Research Observatory Network

TABLE 2.2. Adopted Constants

Variable	Description	Value
α	volumetric coefficient of thermal expansion	2.5×10^{-5} K^{-1} (a)
ρ_0	average mantle density	3300 kg m^{-3}
ρ_w	density of seawater	1000 kg m^{-3}
Γ	gravitational constant	6.67×10^{-11} N m^{2}kg^{-2}
g	surface gravitational acceleration	9.8 m s^{-2}
$\partial v_S/\partial T$	thermal coefficient of shear velocity	-6.0×10^{-4} km/s K^{-1}
$\partial v_S/\partial Mg$	variation of shear velocity with Mg#	1.8×10^{-2} km/s/Mg# (b)
$\partial \rho/\partial Mg$	variation of density with Mg#	-12 kg/m^3/Mg# (b)
p	average SS ray parameter at 70°	0.1375 s/km

(a) *Stacey* [1977], *Duffy and Anderson* [1989]

(b) *Akimoto* [1972]

TABLE 2.3. Inversion Models and Variance Reduction

Model: Temperature variations only

Layer thickness	Viscosity structure	ΔT range	Variance reduction, % total	bathym	geoid	SS-S
0-150 km	cvm	180 K	53	25	79	58
0-150 km	lvz	230 K	57	27	79	66
0-300 km	cvm	60 K	47	21	85	41
0-300 km	lvz	110 K	57	24	85	65
0-650 km	cvm	20 K	41	14	91	25
0-650 km	lvz	33 K	49	17	83	51

Model: Compositional variations only

Layer thickness	Viscosity structure	ΔMg# range	Variance reduction, % total	bathym	geoid	SS-S
0-150 km	cvm	1.1	33	46	74	-9
0-150 km	lvz	2.4	44	75	76	-9
0-300 km	cvm	0.4	33	29	87	-6
0-300 km	lvz	1.3	43	73	73	-7
0-650 km	cvm	0.1	32	19	93	-3
0-650 km	lvz	0.5	49	65	86	+5

Model: Thermal and compositional variations in same layer

Layer thickness	Viscosity structure	ΔT range	ΔMg# range	Variance reduction, % total	bathym	geoid	SS-S
0-150 km	cvm	210 K	1.5	75	44	78	100
0-150 km	lvz	235 K	2.1	86	75	80	100
0-300 km	cvm	110 K	0.7	73	28	89	100
0-300 km	lvz	125 K	1.1	84	74	76	100
0-650 km	cvm	55 K	0.4	71	18	94	100
0-650 km	lvz	60 K	0.8	85	66	88	100

Model: Thermal inversion in layers as noted, compositional variations 0-50 km only

Layer thickness	Viscosity structure	ΔT range	ΔMg# range	Variance reduction, % total	bathym	geoid	SS-S
0-150 km	cvm	210 K	5.5	84	83	77	91
0-150 km	lvz	240 K	4.5	85	85	70	96
0-300 km	cvm	80 K	5.9	80	84	86	72
0-300 km	lvz	120 K	4.7	86	90	77	89
0-650 km	cvm	25 K	6.0	73	85	92	47
0-650 km	lvz	35 K	4.6	75	82	73	71

cvm = constant viscosity mantle
lvz = mantle with low viscosity zone

TABLE 2.4. Spectral Coefficients of Travel Time, Geoid, and Bathymetry Data and of Inversion Solutions

Spectral Coefficients of Observations

Wavelength,	Bathymetry		Geoid		SS	
km	amp	phase	amp	phase	amp	phase
7104	0.97	-0.61	4.39	1.70	3.53	0.99
3552	3.25	-1.59	2.15	-1.08	2.73	-1.81
2368	3.25	2.12	0.85	-2.99	1.42	-1.12
1776	1.63	0.64	0.58	0.96	1.55	-3.00
1421	0.52	-1.32	0.23	-1.70	0.84	-2.62

Spectral Coefficients of Models (from Inversion)

Inversion for temperature variations only

Constant Viscosity Mantle, 0-150 km

Wavelength,	Bathymetry		Geoid		SS		Temperature	
km	amp	phase	amp	phase	amp	phase	amp	phase
7104	1.90	1.36	3.70	1.36	2.05	1.36	3.48	1.36
3552	1.82	-1.49	3.32	-1.49	1.98	-1.49	3.36	-1.49
2368	0.49	2.71	0.83	2.71	0.53	2.71	0.91	2.71
1776	0.30	1.68	0.48	1.68	0.33	1.68	0.56	1.68
1421	0.35	-2.13	0.54	-2.13	0.40	-2.13	0.68	-2.13

Mantle with Low Viscosity Zone, 0-150 km

Wavelength,	Bathymetry		Geoid		SS		Temperature	
km	amp	phase	amp	phase	amp	phase	amp	phase
7104	2.06	1.32	3.34	1.32	2.25	1.32	2.91	1.32
3552	2.55	-1.59	2.25	-1.59	2.97	-1.59	3.84	-1.59
2368	0.48	2.46	0.21	2.46	0.61	2.46	0.79	2.46
1776	0.39	2.44	0.14	2.44	0.52	2.44	0.67	2.44
1421	0.48	-2.26	0.21	-2.26	0.67	-2.26	0.86	-2.26

Constant Viscosity Mantle, 0-300 km

Wavelength,	Bathymetry		Geoid		SS		Temperature	
km	amp	phase	amp	phase	amp	phase	amp	phase
7104	1.27	1.49	4.41	1.49	1.31	1.49	3.54	1.49
3552	1.12	-1.41	3.41	-1.41	1.18	-1.41	3.20	-1.41
2368	0.35	2.84	0.94	2.84	0.38	2.84	1.03	2.84
1776	0.22	1.55	0.54	1.55	0.25	1.55	0.69	1.55
1421	0.26	-2.12	0.56	-2.12	0.31	-2.12	0.83	-2.12

Mantle with Low Viscosity Zone, 0-300 km

Wavelength,	Bathymetry		Geoid		SS		Temperature	
km	amp	phase	amp	phase	amp	phase	amp	phase
7104	1.52	1.44	4.21	1.44	1.62	1.44	2.26	1.44
3552	2.42	-1.59	2.27	-1.59	3.02	-1.59	4.23	-1.59
2368	0.15	1.94	0.07	-1.20	0.23	1.94	0.33	1.94
1776	0.39	3.11	0.39	-0.03	0.74	3.11	1.03	3.11
1421	0.30	-2.45	0.27	0.69	0.65	-2.45	0.91	-2.45

Constant Viscosity Mantle, 0-650 km

Wavelength,	Bathymetry		Geoid		SS		Temperature	
km	amp	phase	amp	phase	amp	phase	amp	phase
7104	0.73	1.58	4.57	1.58	0.71	1.58	3.27	1.58
3552	0.65	-1.33	3.15	-1.33	0.68	-1.33	3.13	-1.33
2368	0.23	2.98	0.93	2.98	0.28	2.98	1.27	2.98
1776	0.16	1.59	0.53	1.59	0.21	1.59	0.98	1.59
1421	0.20	-2.16	0.57	-2.16	0.30	-2.16	1.39	-2.16

Mantle with Low Viscosity Zone, 0-650 km

Wavelength,	Bathymetry		Geoid		SS		Temperature	
km	amp	phase	amp	phase	amp	phase	amp	phase
7104	0.83	1.56	4.57	1.56	0.85	1.56	1.85	1.56
3552	1.33	-1.46	3.39	-1.46	1.73	-1.46	3.79	-1.46
2368	0.08	-3.02	0.01	-3.02	0.15	-3.02	0.34	-3.02
1776	0.36	-3.09	0.40	0.05	0.99	-3.09	2.16	-3.09
1421	0.20	-2.54	0.27	0.61	0.70	-2.54	1.54	-2.54

Inversion for compositional variations only

Constant Viscosity Mantle, 0-150 km

Wavelength,	Bathymetry		Geoid		SS		Composition	
km	amp	phase	amp	phase	amp	phase	amp	phase
7104	1.41	1.68	2.74	1.68	0.31	-1.47	2.78	1.68
3552	1.48	-1.27	2.69	-1.27	0.33	1.87	2.93	-1.27
2368	1.18	2.39	2.01	2.39	0.27	-0.75	2.36	2.39
1776	0.83	0.66	1.34	0.66	0.19	-2.48	1.69	0.66
1421	0.24	-1.19	0.37	-1.19	0.06	1.96	0.50	-1.19

Mantle with Low Viscosity Zone, 0-150 km

Wavelength,	Bathymetry		Geoid		SS		Composition	
km	amp	phase	amp	phase	amp	phase	amp	phase
7104	1.46	1.67	2.36	1.67	0.33	-1.47	1.41	1.67
3552	2.35	-1.35	2.06	-1.35	0.56	1.79	2.42	-1.35
2368	3.07	2.19	1.31	2.19	0.80	-0.96	3.45	2.19
1776	1.87	0.56	0.66	0.56	0.52	-2.58	2.23	0.56
1421	0.46	-0.90	0.20	-0.90	0.13	2.24	0.57	-0.90

Constant Viscosity Mantle, 0-300 km

Wavelength,	Bathymetry		Geoid		SS		Temperature	
km	amp	phase	amp	phase	amp	phase	amp	phase
7104	1.04	1.68	3.61	1.68	0.22	-1.46	3.15	1.68
3552	0.89	-1.22	2.70	-1.22	0.19	1.92	2.76	-1.22
2368	0.64	2.51	1.72	2.51	0.14	-0.63	2.05	2.51
1776	0.51	0.70	1.24	0.70	0.12	-2.44	1.72	0.70
1421	0.16	-1.25	0.36	-1.25	0.04	1.89	0.58	-1.25

Mantle with Low Viscosity Zone, 0-300 km

Wavelength,	Bathymetry		Geoid		SS		Composition	
km	amp	phase	amp	phase	amp	phase	amp	phase
7104	1.20	1.68	3.33	1.68	0.26	-1.46	1.15	1.68
3552	2.25	-1.34	2.10	-1.34	0.58	1.80	2.51	-1.34
2368	2.72	2.01	1.37	-1.13	0.88	-1.13	3.84	2.01
1776	0.88	0.37	0.89	-2.78	0.35	-2.78	1.51	0.37
1421	0.28	-0.22	0.25	2.93	0.12	2.93	0.54	-0.22

Constant Viscosity Mantle, 0-650 km

Wavelength,	Bathymetry		Geoid		SS		Composition	
km	amp	phase	amp	phase	amp	phase	amp	phase
7104	0.65	1.69	4.03	1.69	0.13	-1.45	2.95	1.69
3552	0.53	-1.18	2.58	-1.18	0.12	1.97	2.61	-1.18
2368	0.37	2.63	1.46	2.63	0.09	-0.51	2.04	2.63
1776	0.34	0.72	1.14	0.72	0.09	-2.42	2.14	0.72
1421	0.12	-1.24	0.34	-1.24	0.04	1.90	0.84	-1.24

Mantle with Low Viscosity Zone, 0-650 km

Wavelength,	Bathymetry		Geoid		SS		Temperature	
km	amp	phase	amp	phase	amp	phase	amp	phase
7104	0.72	1.69	3.96	1.69	0.15	-1.45	0.52	1.69
3552	1.04	-1.22	2.67	-1.22	0.28	1.92	0.97	-1.22
2368	3.29	2.12	0.38	2.12	1.32	-1.02	4.55	2.12
1776	0.84	0.32	0.94	-2.83	0.48	-2.83	1.65	0.32
1421	0.24	0.13	0.33	-3.01	0.18	-3.01	0.61	0.13

Inversion for both temperature and compositional variations

Constant Viscosity Mantle, 0-150 km

Wavelength,	Bathymetry		Geoid		SS		Temperature		Composition	
km	amp	phase	amp	phase	amp	phase	amp	phase	amp	phase
7104	1.59	1.59	3.10	1.59	3.53	0.99	3.60	1.04	2.61	-2.58
3552	1.65	-1.33	3.01	-1.33	2.73	-1.81	2.88	-1.76	1.59	0.69
2368	1.10	2.42	1.88	2.42	1.42	-1.12	1.12	-1.20	2.89	2.21
1776	0.74	0.75	1.19	0.75	1.55	-3.00	1.33	-3.07	2.56	0.35
1421	0.27	-1.46	0.41	-1.46	0.84	-2.62	0.81	-2.56	0.86	0.15

Mantle with Low Viscosity Zone, 0-150 km

Wavelength,	Bathymetry		Geoid		SS		Temperature		Composition	
km	amp	phase	amp	phase	amp	phase	amp	phase	amp	phase
7104	1.70	1.57	2.76	1.57	3.53	0.99	3.59	1.05	1.63	-2.63
3552	2.84	-1.42	2.50	-1.42	2.73	-1.81	3.13	-1.74	0.96	-0.49
2368	2.92	2.21	1.25	2.21	1.42	-1.12	0.63	-1.32	3.74	2.15
1776	1.62	0.67	0.57	0.67	1.55	-3.00	1.10	3.09	2.65	0.45
1421	0.52	-1.37	0.22	-1.37	0.84	-2.62	0.83	-2.47	0.67	-0.32

Constant Viscosity Mantle, 0-300 km

Wavelength,	Bathymetry		Geoid		SS		Temperature		Composition	
km	amp	phase	amp	phase	amp	phase	amp	phase	amp	phase
7104	1.10	1.64	3.82	1.64	3.53	0.99	3.59	1.03	3.05	-2.41
3552	0.95	-1.26	2.91	-1.26	2.73	-1.81	2.80	-1.78	2.18	1.05
2368	0.60	2.55	1.62	2.55	1.42	-1.12	1.26	-1.17	2.26	2.19
1776	0.46	0.78	1.12	0.78	1.55	-3.00	1.42	-3.04	2.25	0.30
1421	0.18	-1.49	0.40	-1.49	0.84	-2.62	0.83	-2.58	0.87	0.26

Mantle with Low Viscosity Zone, 0-300 km

Wavelength,	Bathymetry		Geoid		SS		Temperature		Composition	
km	amp	phase	amp	phase	amp	phase	amp	phase	amp	phase
7104	1.30	1.63	3.60	1.63	3.53	0.99	3.52	1.04	1.88	-2.48
3552	2.75	-1.41	2.57	-1.41	2.73	-1.81	3.18	-1.73	1.03	-0.55
2368	2.56	2.01	1.29	-1.13	1.42	-1.12	0.55	-1.10	4.01	2.01
1776	0.61	0.50	0.61	-2.64	1.55	-3.00	1.25	-3.06	1.97	0.30
1421	0.21	-1.13	0.19	2.01	0.84	-2.62	0.80	-2.51	0.68	0.00

Constant Viscosity Mantle, 0-650 km

Wavelength,	Bathymetry		Geoid		SS		Temperature		Composition	
km	amp	phase	amp	phase	amp	phase	amp	phase	amp	phase
7104	0.67	1.67	4.15	1.67	3.53	0.99	3.57	1.01	3.27	-2.28
3552	0.55	-1.21	2.71	-1.21	2.73	-1.81	2.78	-1.79	2.43	1.18
2368	0.35	2.67	1.38	2.67	1.42	-1.12	1.32	-1.16	1.89	2.17
1776	0.31	0.80	1.02	0.80	1.55	-3.00	1.46	-3.04	2.03	0.28
1421	0.13	-1.52	0.38	-1.52	0.84	-2.62	0.84	-2.58	0.82	0.28

Mantle with Low Viscosity Zone, 0-650 km

Wavelength,	Bathymetry		Geoid		SS		Temperature		Composition	
km	amp	phase	amp	phase	amp	phase	amp	phase	amp	phase
7104	0.75	1.66	4.10	1.66	3.53	0.99	3.67	1.02	1.65	-2.31
3552	1.16	-1.28	2.97	-1.28	2.73	-1.81	3.02	-1.76	0.90	0.83
2368	3.25	2.14	0.38	2.14	1.42	-1.12	0.20	-2.03	4.30	2.12
1776	0.52	0.48	0.58	-2.67	1.55	-3.00	1.28	-3.08	1.64	0.30
1421	0.11	-0.96	0.15	2.18	0.84	-2.62	0.84	-2.53	0.53	0.09

Joint inversion for Temperature and Composition,
Composition variations constrained to be shallow

Constant Viscosity Mantle, 0-150 km

Wavelength,	Bathymetry		Geoid		SS		Temperature		Composition	
km	amp	phase	amp	phase	amp	phase	amp	phase	amp	phase
7104	0.38	2.41	3.49	1.37	3.75	1.28	3.95	1.30	2.64	-1.97
3552	2.10	-1.32	3.36	-1.48	1.77	-1.70	2.36	-1.61	0.66	-0.52
2368	2.63	2.22	1.20	2.51	1.87	-1.19	1.31	-1.33	3.42	2.11
1776	1.62	0.57	0.65	1.16	1.52	-2.96	1.22	-3.09	2.34	0.39
1421	0.40	-0.93	0.49	-1.93	0.73	-2.70	0.76	-2.57	0.66	-0.06

Mantle with Low Viscosity Zone, 0-150 km

Wavelength,	Bathymetry		Geoid		SS		Temperature		Composition	
km	amp	phase	amp	phase	amp	phase	amp	phase	amp	phase
7104	0.65	1.87	2.98	1.35	3.90	1.22	3.65	1.25	2.89	-2.05
3552	2.91	-1.42	2.47	-1.46	2.67	-1.80	3.07	-1.72	1.08	-0.59
2368	2.39	2.26	1.84	2.24	1.18	-1.07	0.57	-1.24	3.20	2.21
1776	1.30	0.75	1.13	0.58	1.44	-3.01	1.12	3.12	2.21	0.47
1421	0.49	-1.50	0.29	-1.07	0.82	-2.61	0.83	-2.48	0.56	-0.33

Constant Viscosity Mantle, 0-300 km

Wavelength,	Bathymetry		Geoid		SS		Temperature		Composition	
km	amp	phase	amp	phase	amp	phase	amp	phase	amp	phase
7104	0.83	-1.93	4.57	1.48	2.66	1.43	3.93	1.45	2.56	-1.76
3552	1.80	-1.33	3.37	-1.41	0.70	-1.56	1.84	-1.47	0.89	-1.19
2368	2.94	2.17	0.91	2.88	1.81	-1.20	1.80	-1.34	3.49	2.09
1776	1.79	0.52	0.57	1.46	1.31	-2.91	1.46	-3.06	2.25	0.41
1421	0.42	-0.72	0.55	-2.05	0.59	-2.78	0.90	-2.61	0.61	-0.13

Mantle with Low Viscosity Zone, 0-300 km

Wavelength,	Bathymetry		Geoid		SS		Temperature		Composition	
km	amp	phase	amp	phase	amp	phase	amp	phase	amp	phase
7104	0.54	-2.22	4.27	1.44	3.15	1.38	3.22	1.40	3.32	-1.83
3552	2.86	-1.42	2.53	-1.47	2.65	-1.79	3.62	-1.71	1.16	-0.69
2368	2.54	2.22	1.84	2.25	0.65	-0.80	0.09	0.50	3.02	2.24
1776	1.29	0.80	1.37	0.44	0.99	-2.99	0.88	3.04	1.82	0.62
1421	0.57	-1.64	0.34	-0.24	0.64	-2.58	0.86	-2.42	0.49	-1.10

Constant Viscosity Mantle, 0-650 km

Wavelength,	Bathymetry		Geoid		SS		Temperature		Composition	
km	amp	phase	amp	phase	amp	phase	amp	phase	amp	phase
7104	1.22	-1.66	4.75	1.57	1.57	1.54	3.34	1.56	2.19	-1.62
3552	1.84	-1.39	3.04	-1.33	0.09	-0.64	1.39	-1.28	1.40	-1.42
2368	3.12	2.15	0.83	3.13	1.64	-1.19	2.42	-1.35	3.60	2.09
1776	1.86	0.51	0.54	1.55	1.17	-2.88	2.03	-3.04	2.23	0.43
1421	0.43	-0.67	0.55	-2.07	0.54	-2.81	1.38	-2.62	0.58	-0.22

Mantle with Low Viscosity Zone, 0-650 km

Wavelength,	Bathymetry		Geoid		SS		Temperature		Composition	
km	amp	phase	amp	phase	amp	phase	amp	phase	amp	phase
7104	1.16	-1.70	4.75	1.55	1.80	1.52	2.70	1.54	2.97	-1.65
3552	1.94	-1.31	3.44	-1.45	1.27	-1.64	3.25	-1.55	1.13	-1.01
2368	2.40	2.26	1.86	2.23	1.09	-1.04	0.99	-1.21	3.32	2.23
1776	1.27	0.80	1.33	0.47	1.15	-3.00	1.88	3.07	1.88	0.64
1421	0.56	-1.63	0.32	-0.37	0.70	-2.58	1.63	-2.44	0.56	-1.28

0-150 km, 0-300 km, 0-650 km = depths over which temperature or composition is allowed to vary

amp = relative spectral amplitude. The amplitudes of both observed and predicted data profiles are normalized by dividing by the average spectral amplitude of the observed profile. The amplitudes of model parameters are normalized by dividing by the average spectral amplitude of the parameter profile.

phase = phase in radians

Figure Captions

Figure 2.1. Schematic paths of S and SS phases. For the range of epicentral distances considered in this study the bottoming depth for S ranges from 1450 to 2370 km, and for SS from 670 to 900 km.

Figure 2.2. An example of the measurement of SS-S differential travel time for the event of December 24, 1985 (10 km focal depth), at GDH (63° epicentral distance). (a) "Synthetic" SS pulse generated from S. The S pulse is windowed and attenuated to account for the additional time that SS travels in the mantle ($t^* = 3$ s), and a $\pi/2$ phase shift is applied. (b) Windowed SS wave pulse. (c) Cross-correlation of the trace in (b) with that in (a). The differential travel time residual is -5.04 s.

Figure 2.3. Distribution of earthquakes (triangles) and seismograph stations (circles) used to measure SS-S differential travel times. Stations are from the GDSN, NARS, and GEOSCOPE digital arrays. Earthquakes are from the Harvard CMT catalogue (generally $m_b > 5.0$) from the years 1977-1987. Lambert equal area projection with pole of projection at 45°N, 40°W.

Figure 2.4. (a) Map view of SS-S residuals relative to PREM [*Dziewonski and Anderson*, 1981], corrected for Earth ellipticity and seafloor bathymetry. Residuals are plotted at the SS bounce point. The size of each symbol scales linearly with magnitude of the residual. Lambert equal area projection with pole of projection at 40°N, 60°W. Negative residuals

indicate either early SS or late S. Plate boundaries are from *DeMets et al.* [1990].

(b) Same as (a) but including data only for SS bouncepoints on lithosphere younger than 100 My.

Figure 2.5. SS-S travel time residual versus square root of seafloor age for data from 0-60°N. Each plotted point represents the weighted mean of 14 adjacent data points. Weights are constructed from variances determined as discussed in Appendix A. Horizontal and vertical bars are standard errors of the means of the travel time residuals and $(age)^{1/2}$. Linear regression yields a slope of -0.68 ± 0.08 s/ $(My)^{1/2}$ for a 0-100 My age range (solid line) or -0.76 ± 0.09 s/ $(My)^{1/2}$ for a 0-80 My range (dashed line).

Figure 2.6. Age-corrected SS-S residual (see text) versus azimuth θ. Each plotted point represents the weighted mean of 10 adjacent data points. The solid curve shows the best-fitting 4θ variation derived from these data. The dashed curve shows the preferred model of *Kuo et al.* [1987], which corresponds to an alignment of the *a* axis of olivine in the approximate direction N13°W.

Figure 2.7. (a) Map view of age-corrected SS-S residuals.

(b) Same as (a) but including data only with SS bounce points on lithosphere younger than 100 My.

Figure 2.8. Map view of the distribution of sampling azimuths. Lines indicate the wave path azimuth at the SS bounce point. Mercator projection.

Figure 2.9. Age-corrected SS-S residual versus latitude along the Mid-Atlantic Ridge from 10 to 90°N. The residuals shown are moving averages (such that each point is used twice) of 12 adjacent data points. Bounce points on lithosphere of age 0-100 My are used. The approximate locations of several fracture zones (Fifteen-Twenty, Kane, Atlantis, Oceanographer, and Charlie-Gibbs, denoted by abbreviations) and of the Iceland and Azores hotspots are indicated.

Figure 2.10. Linear correlation, by highest harmonic degree removed from the geoid, of observed SS-S residual with geoid height measured at the corresponding SS bounce point. Both travel time and geoid residuals are age-corrected. First the raw [*Marsh et al.*, 1986] geoid data are correlated with SS-S residuals and a slope and correlation coefficient determined. Then a geoid reference field [*Lerch et al.*, 1979] up to degree and order 2 (with taper to degree and order 6) is calculated and removed from the geoid data, the slope and correlation coefficient with SS-S calculated, and so on for higher harmonic degrees ℓ removed from the geoid data, with appropriate tapers (up to $\ell + 4$). (a) Linear correlation coefficient between geoid and SS-S residuals vs. highest harmonic degree and order removed from the geoid. (b) Slope of the correlation between geoid and SS-S data, as a function of highest harmonic degree and order removed from the geoid. Extra points at degree and order 10 are obtained by using different tapers (no taper, taper to $\ell = 14$, and taper to $\ell = 15$).

Figure 2.11. Comparative plots of age-corrected (a) bathymetry, (b) geoid, and (c) SS-S

residual along the Mid-Atlantic Ridge, 10-65°N. Bathymetry and geoid have been high-pass filtered (see text). All of the residuals shown are moving averages of 10 adjacent data points. Bounce points from lithosphere of age 0-100 My are used, except that data from the Labrador Sea region are omitted.

Figure 2.12. Upper mantle portion of the kernels for geoid and topography at two wavelengths $\lambda = 2\pi/k$ for two viscosity models. The convecting region in both models is overlain by a high-viscosity layer 40 km thick, with viscosity 10^4 that of the underlying mantle.

(a) High-viscosity lid is underlain by a mantle of uniform viscosity and other physical parameters.

(b) High-viscosity lid is underlain by a zone extending to a depth of 200 km having a viscosity equal to 0.01 that of the underlying mantle.

Figure 2.13. Upper mantle portion of the kernels for geoid and topography at two wavelengths in spherical versus cartesian coordinates. The convecting region is overlain by a high-viscosity layer 40 km thick in each of two models for viscosity structure.

(a) Underlying mantle is of uniform viscosity. Cartesian kernels are for 4000 km wavelength (solid lines) and spherical kernels are for $\ell = 10$ (dashed lines).

(b) High-viscosity lid is underlain by zone extending to 200 km depth having a viscosity equal to 0.01 that of the underlying mantle. Cartesian kernels are for 4000 km wavelength and spherical kernels are for $\ell = 10$.

(c) Same as (a) but with Cartesian kernels for 6667 km wavelength and

spherical kernels for $\ell = 6$.

(d) Same as (b) but with Cartesian kernels for 6667 km wavelength and spherical kernels for $\ell = 6$.

Figure 2.14. Results of combined inversion of geoid, bathymetry, and SS-S travel time residuals for upper mantle temperature variations. The viscosity structure is taken to consist of a 40-km-thick high-viscosity lid overlying a constant-viscosity halfspace.

(a) Three solutions for along-axis temperature variations: Dotted line: Temperature perturbations constrained to be uniform over 0-150 km depth. Long-dashed line: Temperature perturbations constrained to be uniform over 0-300 km depth. Short-dashed line: Temperature perturbations constrained to be uniform over 0-650 km depth.

(b) Observed (solid line) and predicted along-axis profiles of SS-S travel time residual. The "observed" profile is actually a filtered version of the observations, containing only the wavelengths used in the inversion (1400 to 7100 km). Predicted profiles were calculated from equation 5. Line types correspond to those of the temperature models.

(c) Observed and predicted along-axis geoid profiles. Same treatment as in (b).

(d) Observed and predicted along-axis bathymetry profiles. Same treatment as in (b).

Figure 2.15. Same as Figure 2.14 except for that the viscosity structure includes a zone extending from the base of the lid to a depth of 200 km with a viscosity equal to 0.01 that of the underlying mantle.

Figure 2.16. Results of combined inversion of geoid, bathymetry, and SS-S travel time residuals for variations in upper mantle composition (Mg#). The viscosity structure is taken to consist of a 40-km-thick high-viscosity lid overlying a constant-viscosity halfspace.

(a) Three solutions for along-axis composition variations: Dotted line: Composition perturbations constrained to be uniform over 0-150 km depth. Long-dashed line: Composition perturbations constrained to be uniform over 0-300 km depth. Short-dashed line: Composition perturbations constrained to be uniform over 0-650 km depth.

(b) Observed (solid line) and predicted along-axis profiles of SS-S travel time residual.

(c) Observed and predicted along-axis geoid profiles.

(d) Observed and predicted along-axis bathymetry profiles.

Figure 2.17. Same as Figure 2.16 except for that the viscosity structure includes a zone extending from the base of the lid to a depth of 200 km with a viscosity equal to 0.01 that of the underlying mantle.

Figure 2.18. Results of combined inversion of geoid, bathymetry, and SS-S travel time residuals for both upper mantle temperature and composition variations. The viscosity structure is taken to consist of a 40-km-thick high-viscosity lid overlying a constant-viscosity halfspace.

(a) Three solutions for along-axis temperature variations: Dotted line: Composition perturbations constrained to be uniform over 0-150 km depth. Long-dashed line: Composition perturbations constrained to be

uniform over 0-300 km depth. Short-dashed line: Composition perturbations constrained to be uniform over 0-650 km depth.
(b) Three solutions for along-axis composition variations: Dotted line: Composition perturbations constrained to be uniform over 0-150 km depth. Long-dashed line: Composition perturbations constrained to be uniform over 0-300 km depth. Short-dashed line: Composition perturbations constrained to be uniform over 0-650 km depth.
(c) Observed (solid line) and predicted along-axis profiles of SS-S travel time residual.
(d) Observed and predicted along-axis geoid profiles.
(e) Observed and predicted along-axis bathymetry profiles.

Figure 2.19. Same as Figure 2.18 except for that the viscosity structure includes a zone extending from the base of the lid to a depth of 200 km with a viscosity equal to 0.01 that of the underlying mantle.

Figure 2.20. Same as Figure 2.18 but compositional variations constrained to be from 0-50 km depth only.

Figure 2.21. Same as Figure 2.19 but compositional variations constrained to be from 0-50 km depth only.

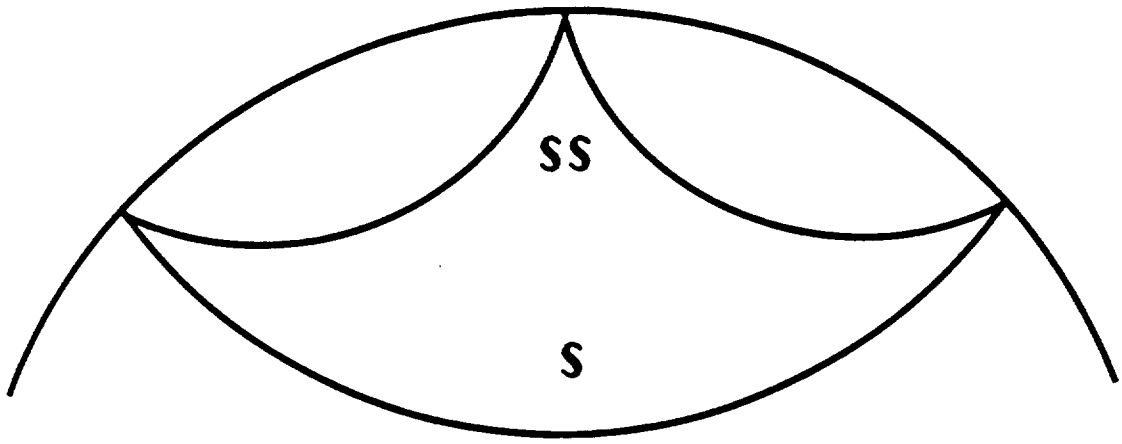

Figure 2.1

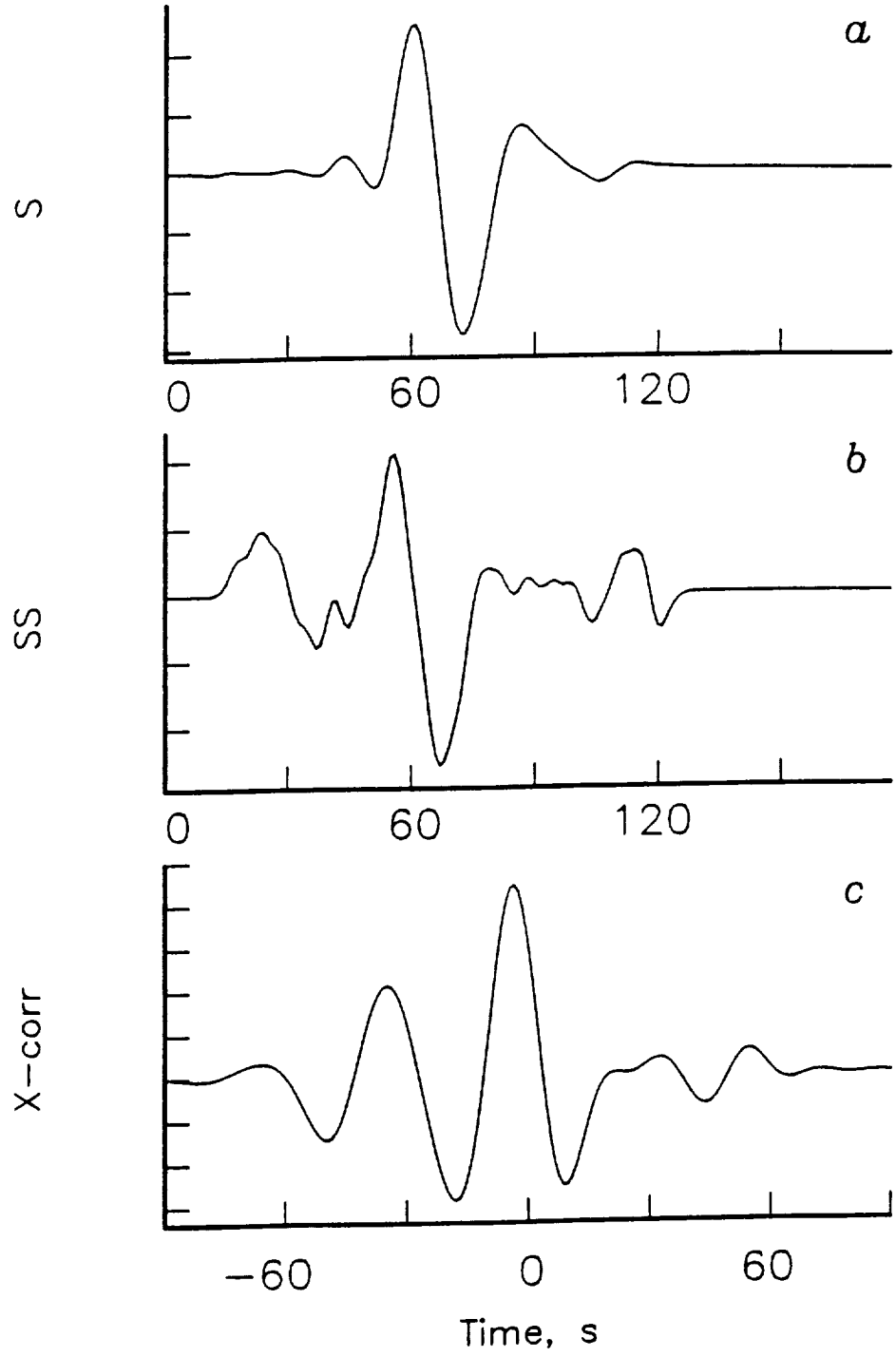

Figure 2.2

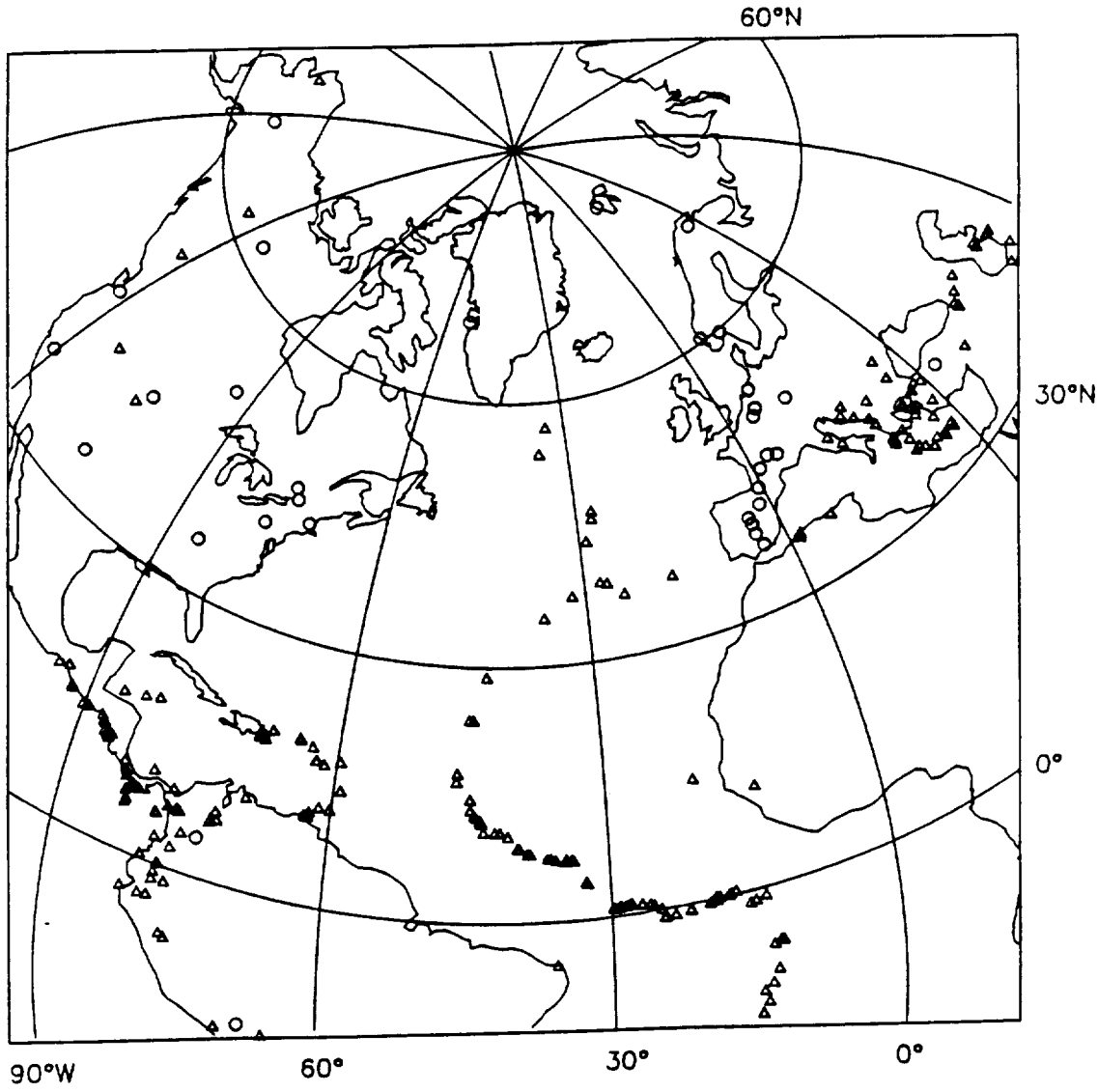

Figure 2.3

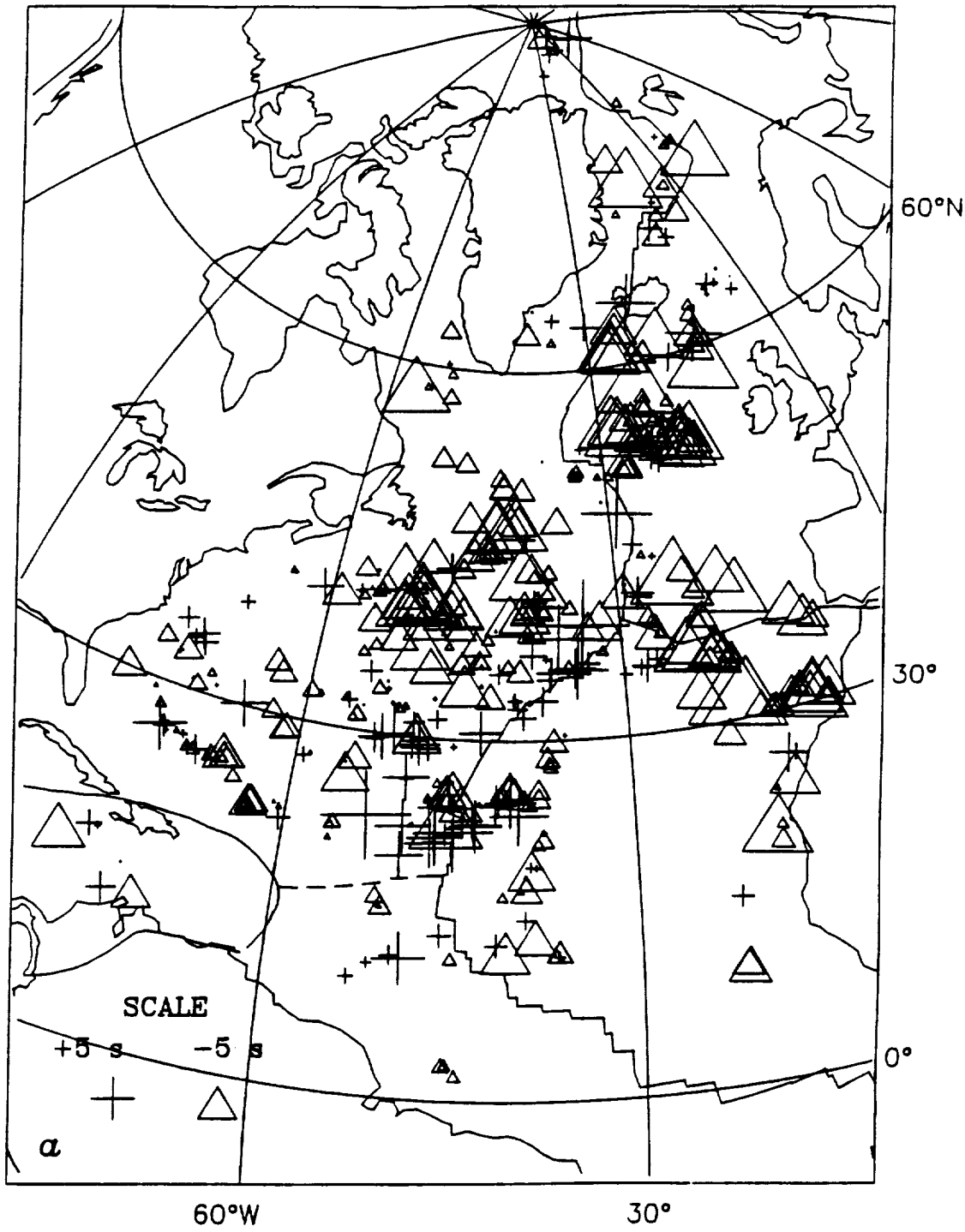

Figure 2.4a

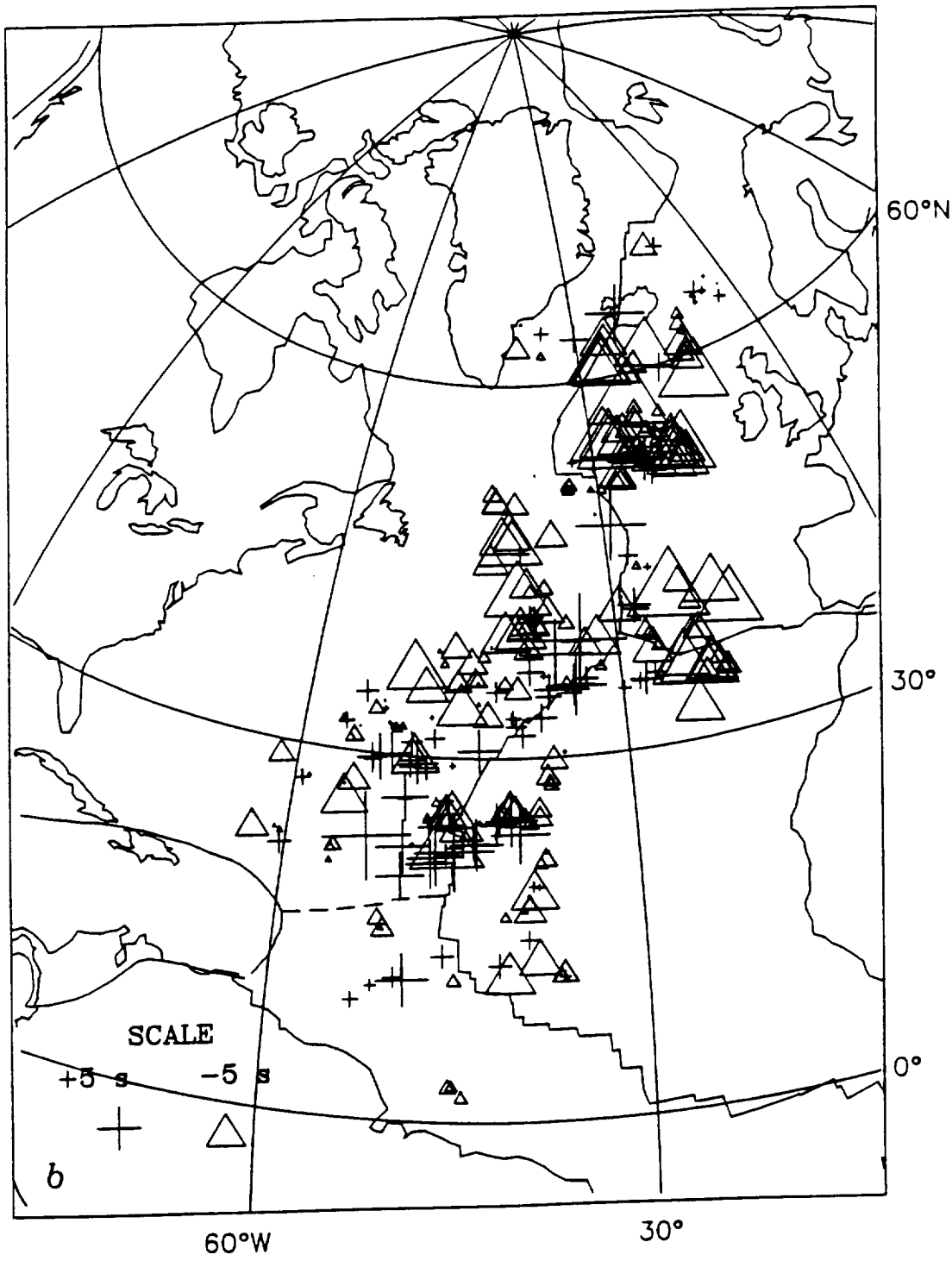

Figure 2.4b

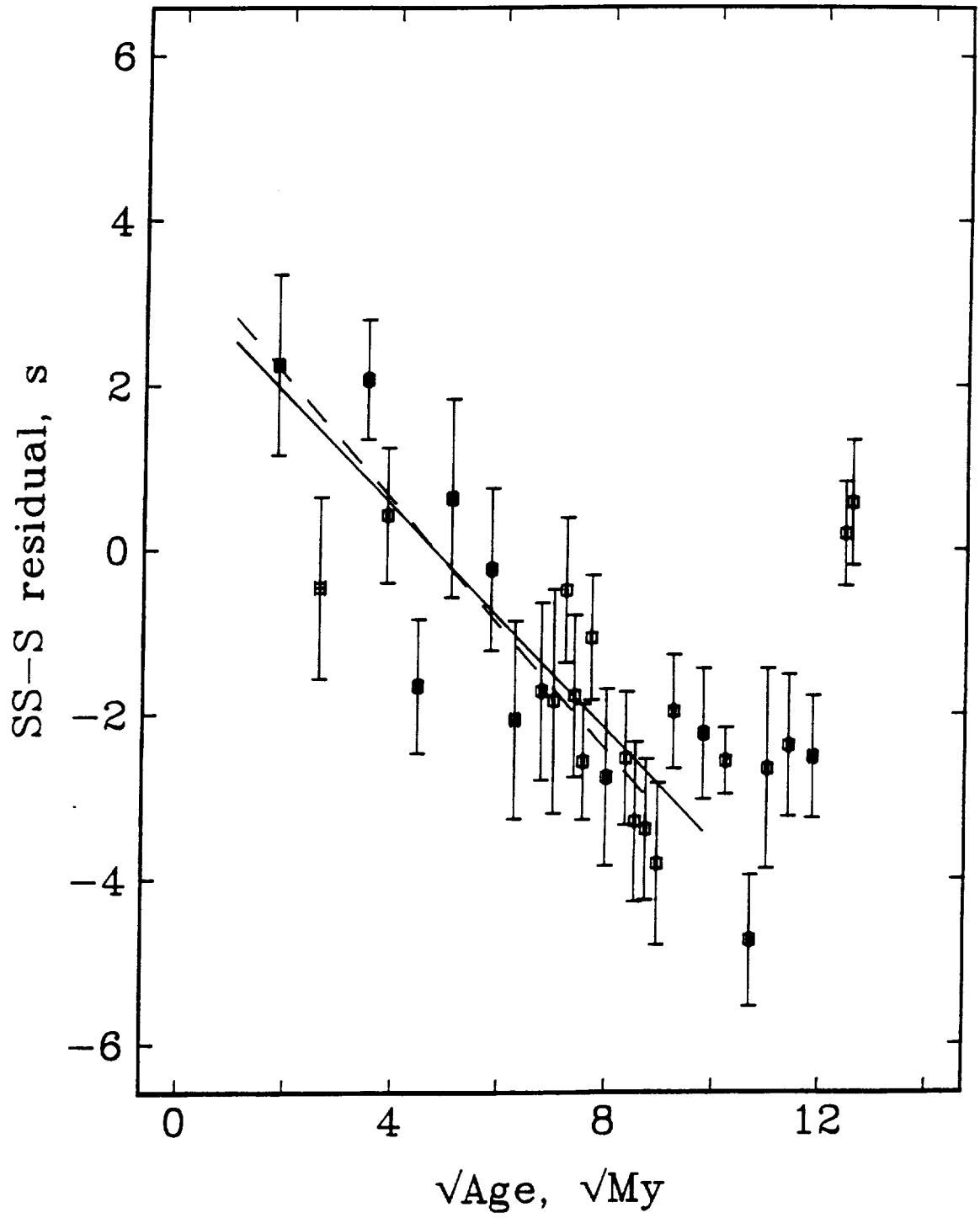

Figure 2.5

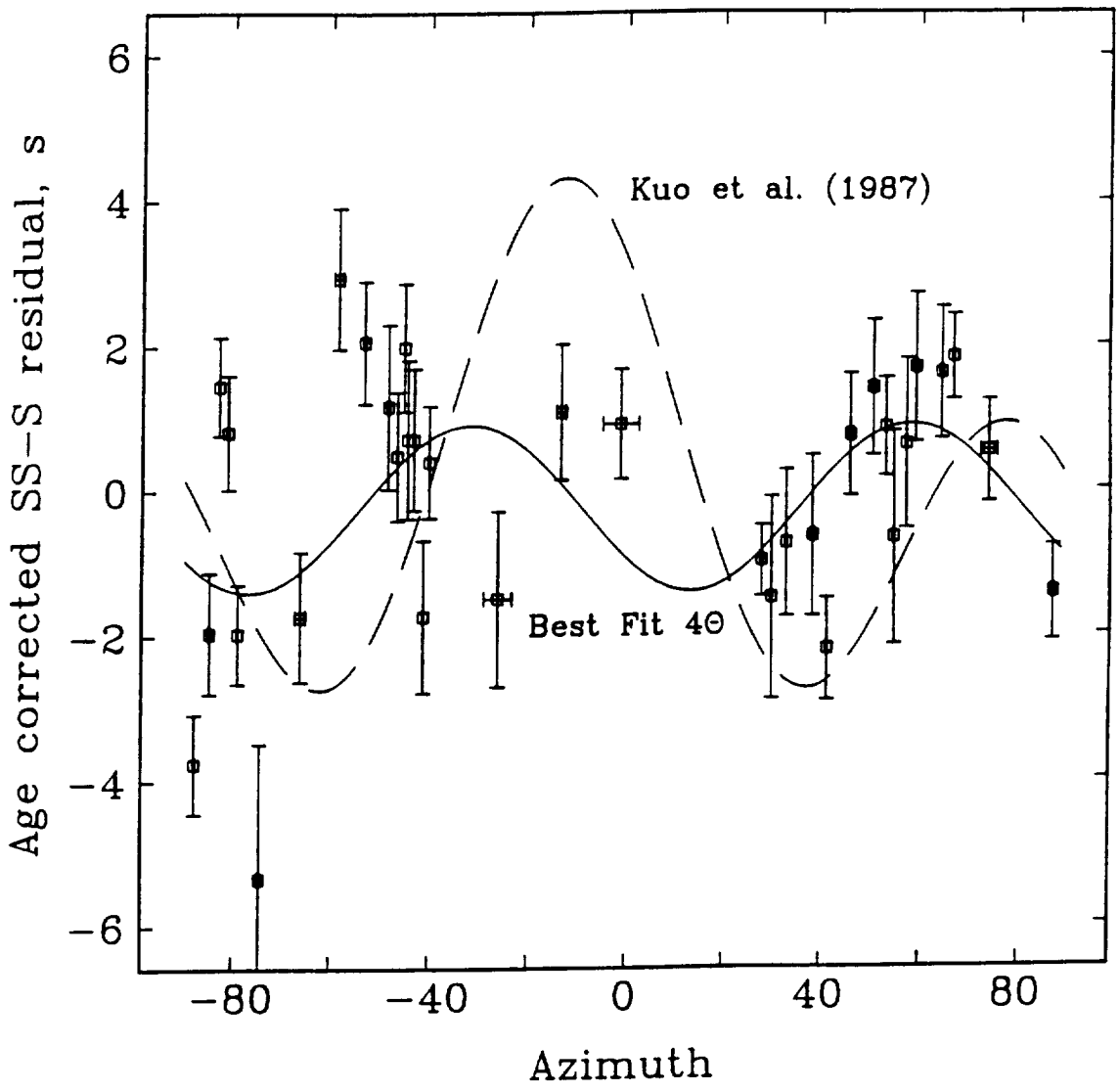
Age corrected SS−S residual, s
6
4
2
0
−2
−4
−6
−80
−40
0
40
80
Azimuth
Kuo et al. (1987)
Best Fit 4Θ

Figure 2.6

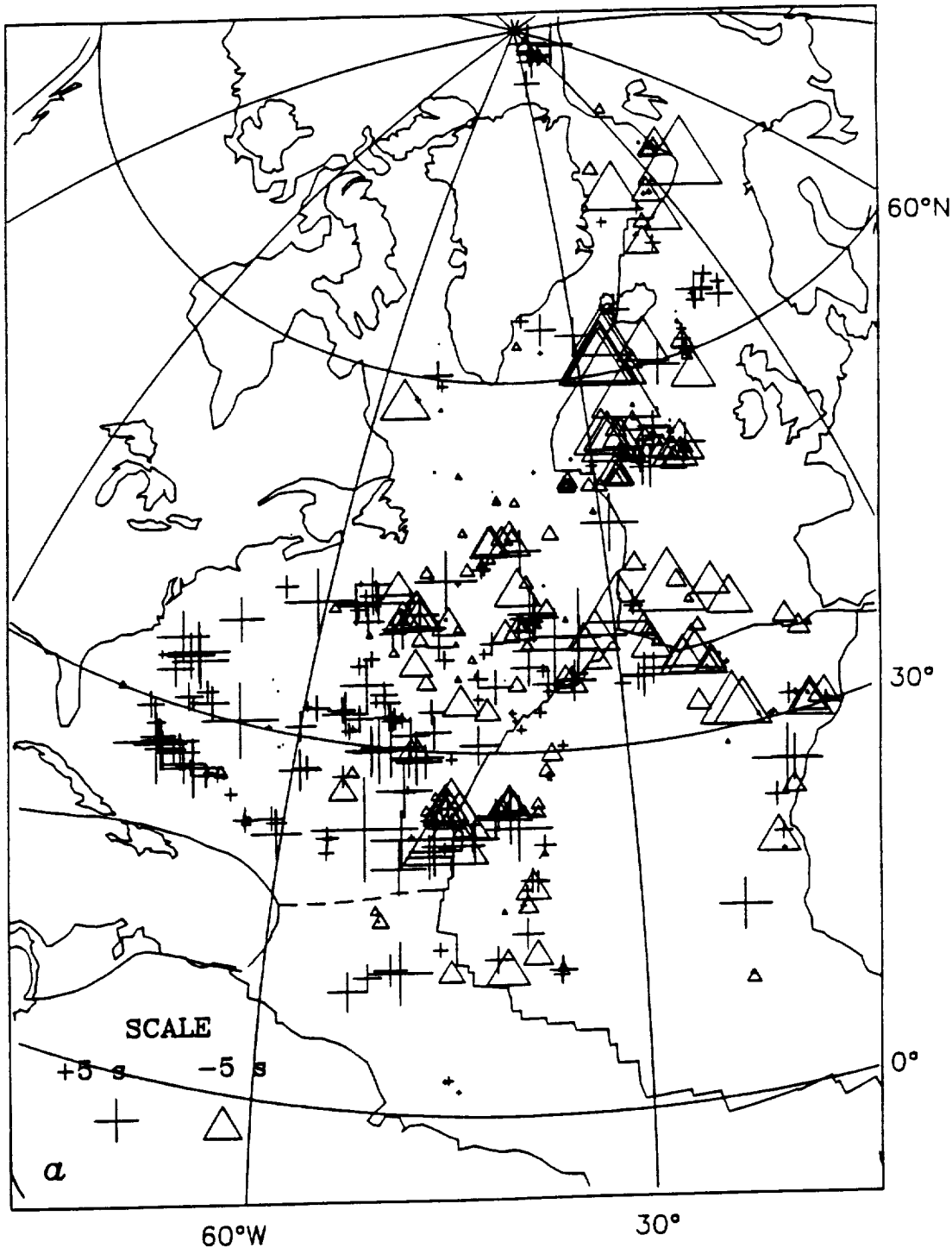

Figure 2.7a

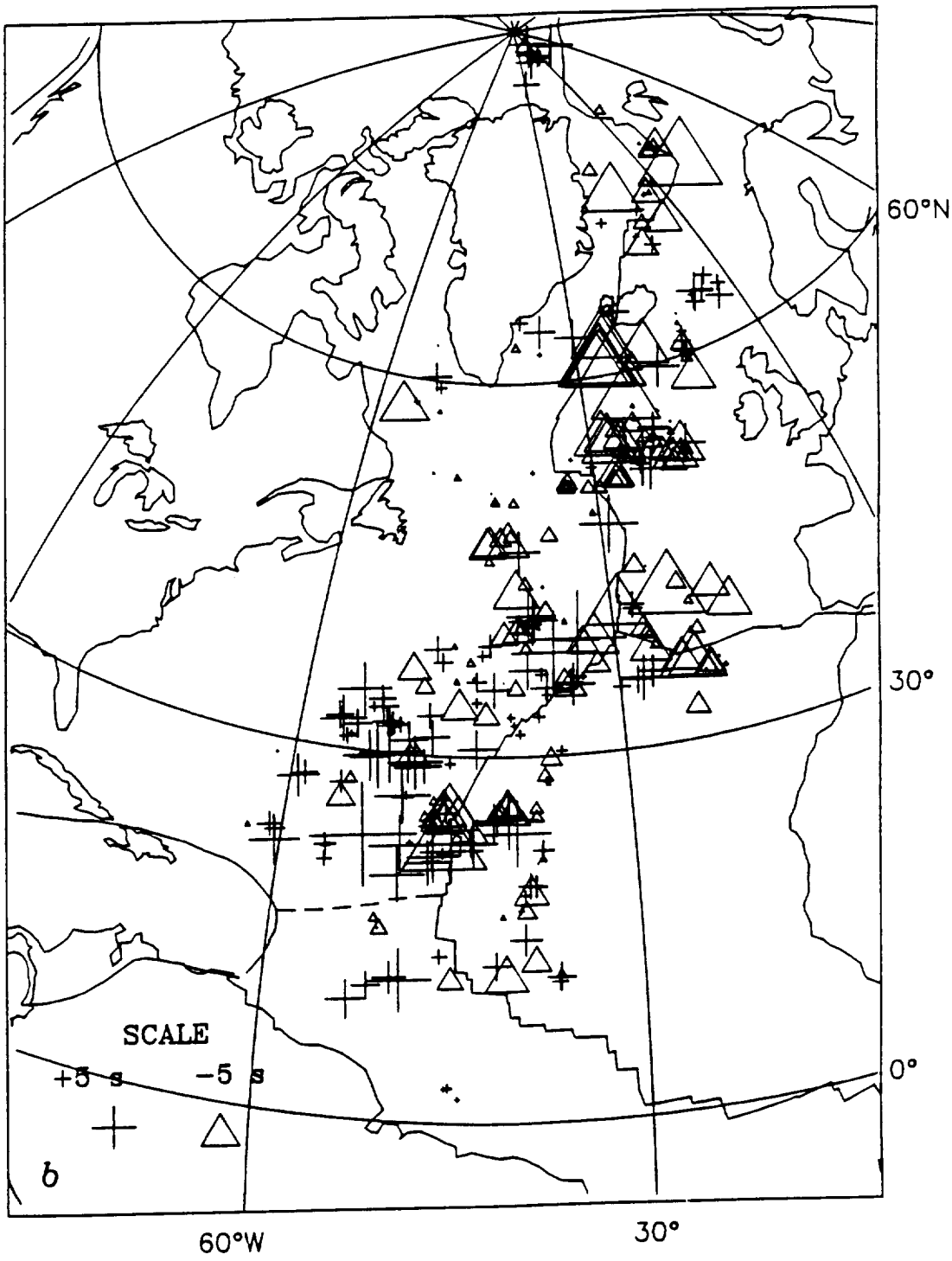

Figure 2.7b

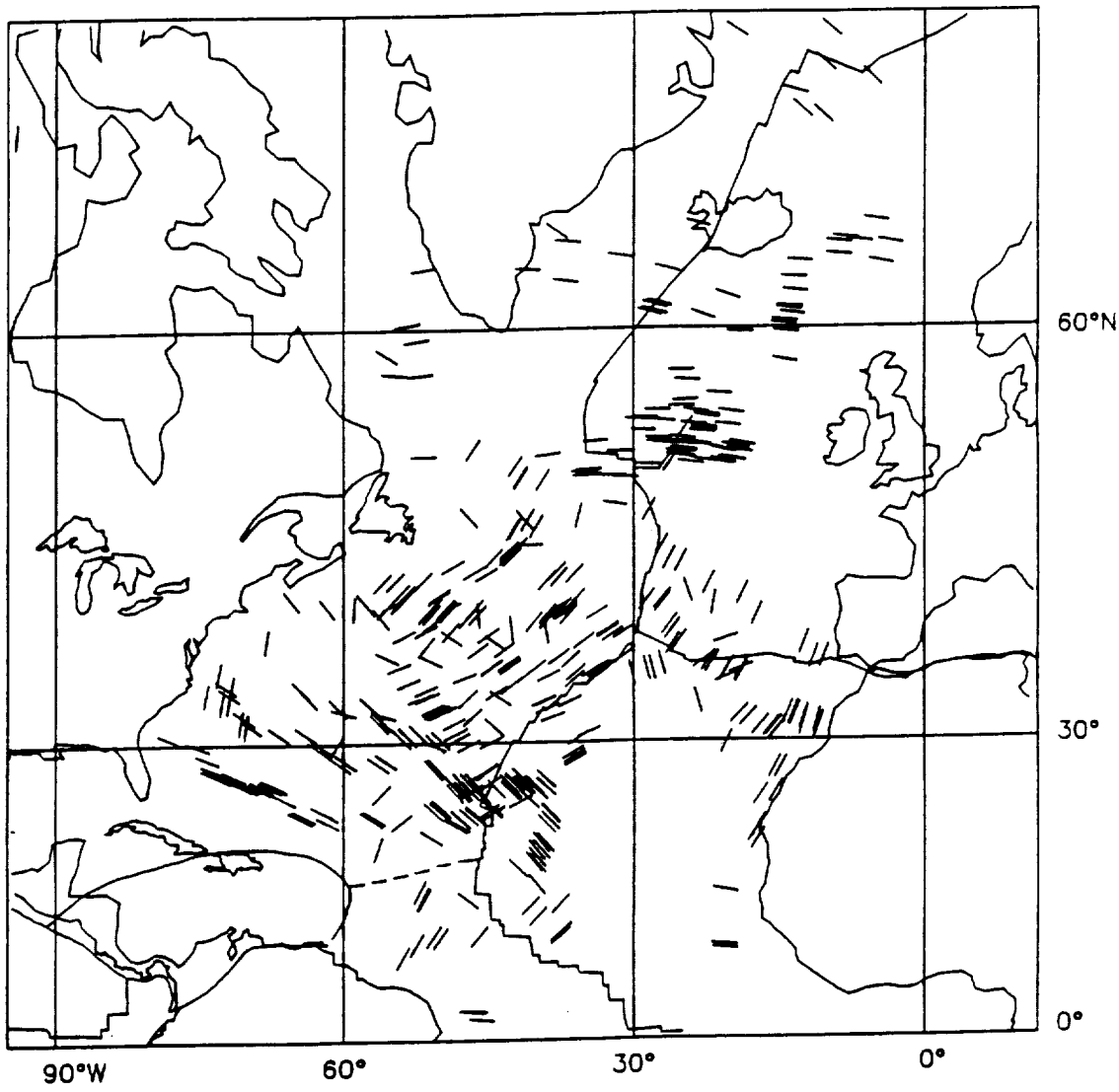

Figure 2.8

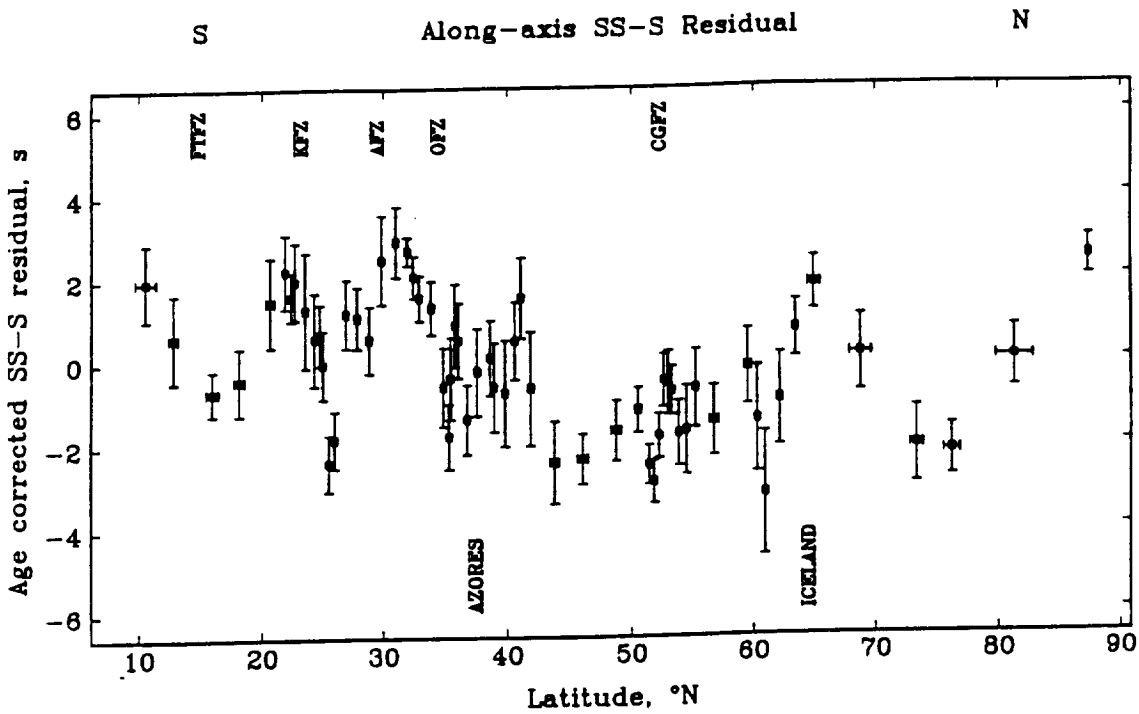
S
Along-axis SS-S Residual
N
FTFZ
KFZ
AFZ
OFZ
CGFZ
AZORES
ICELAND
Age corrected SS-S residual, s
6
4
2
0
-2
-4
-6
10
20
30
40
50
60
70
80
90
Latitude, °N

Figure 2.9

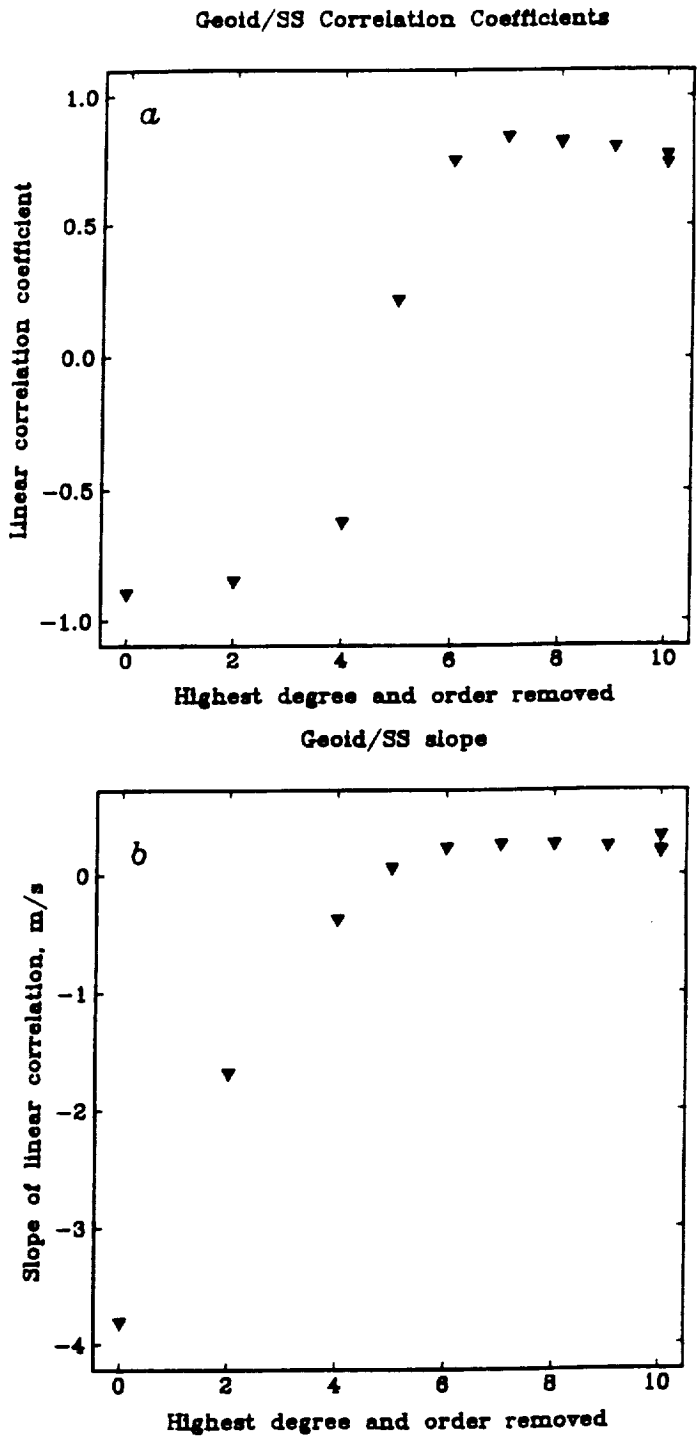
Geoid/SS Correlation Coefficients
a
Linear correlation coefficient
1.0
0.5
0.0
−0.5
−1.0
0
2
4
6
8
10
Highest degree and order removed
Geoid/SS slope
b
Slope of linear correlation, m/s
0
−1
−2
−3
−4
0
2
4
6
8
10
Highest degree and order removed

Figure 2.10

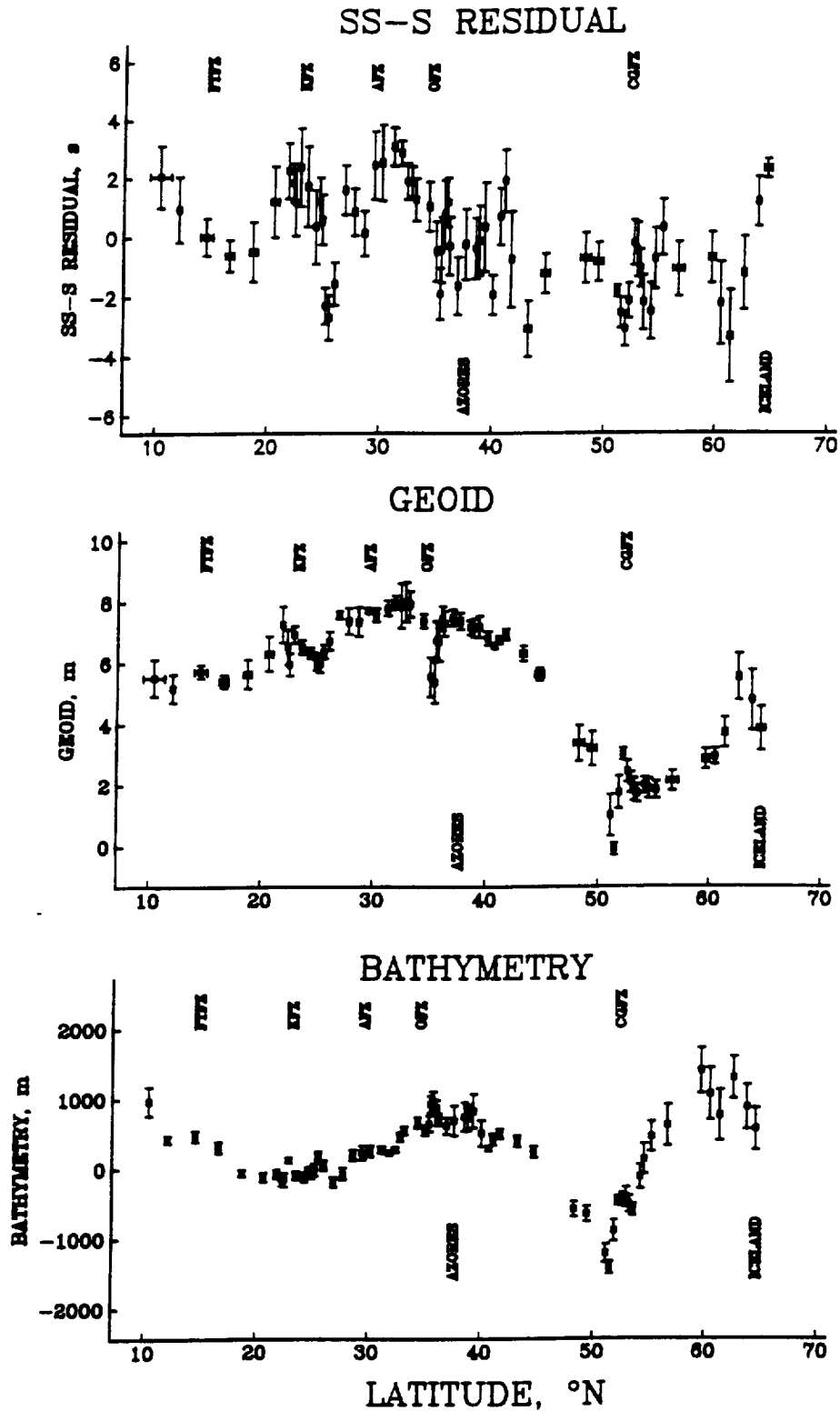
SS–S RESIDUAL
SS–S RESIDUAL, m
6
4
2
0
−2
−4
−6
10
20
30
40
50
60
70
AZORES
ICELAND
GEOID
GEOID, m
10
8
6
4
2
0
BATHYMETRY
BATHYMETRY, m
2000
1000
0
−1000
−2000
LATITUDE, °N

Figure 2.11

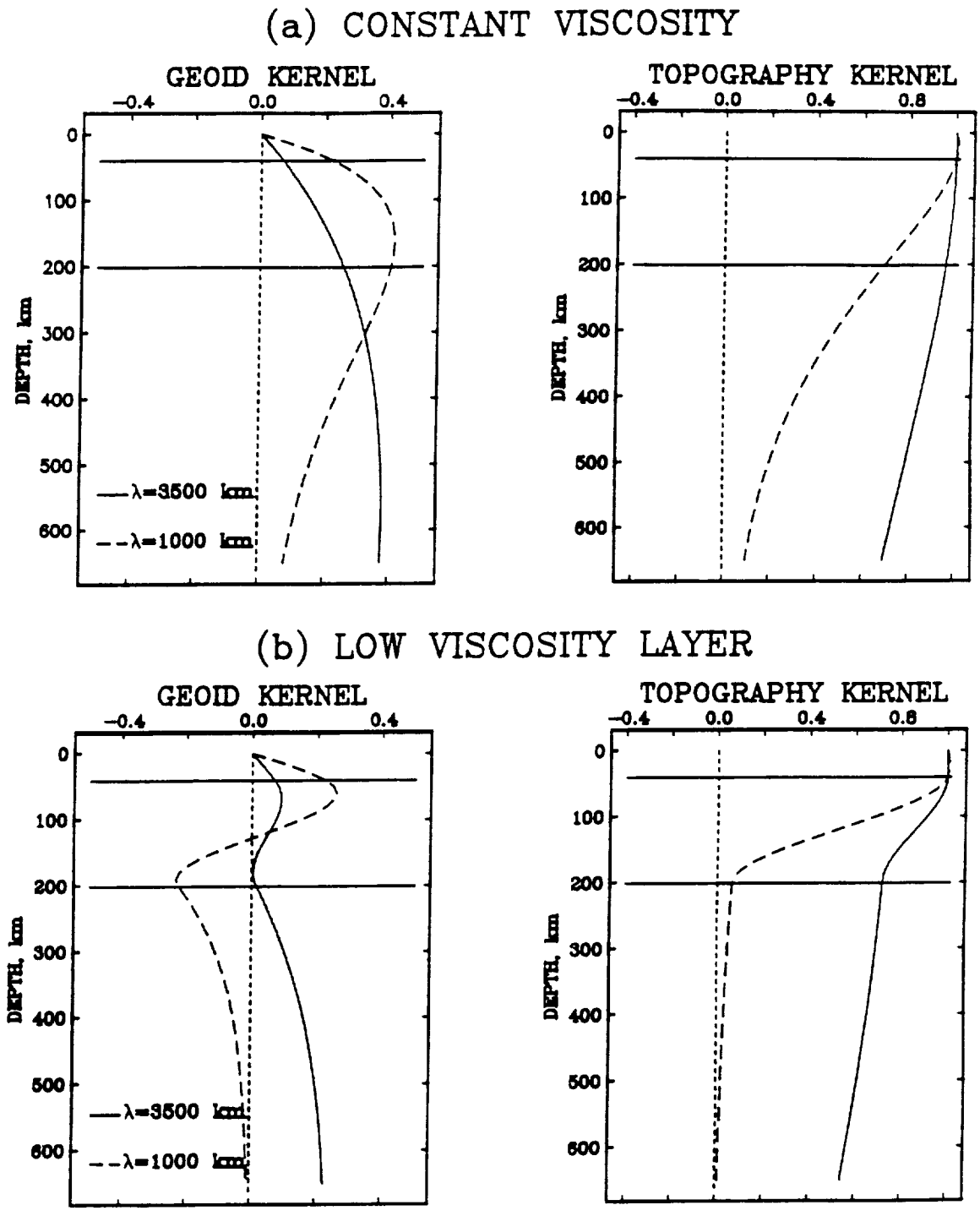
(a) CONSTANT VISCOSITY
GEOID KERNEL
TOPOGRAPHY KERNEL
−0.4
0.0
0.4
0.8
0
100
200
300
400
500
600
DEPTH, km
λ=3500 km
λ=1000 km
(b) LOW VISCOSITY LAYER
GEOID KERNEL
TOPOGRAPHY KERNEL
λ=3500 km
λ=1000 km

Figure 2.12

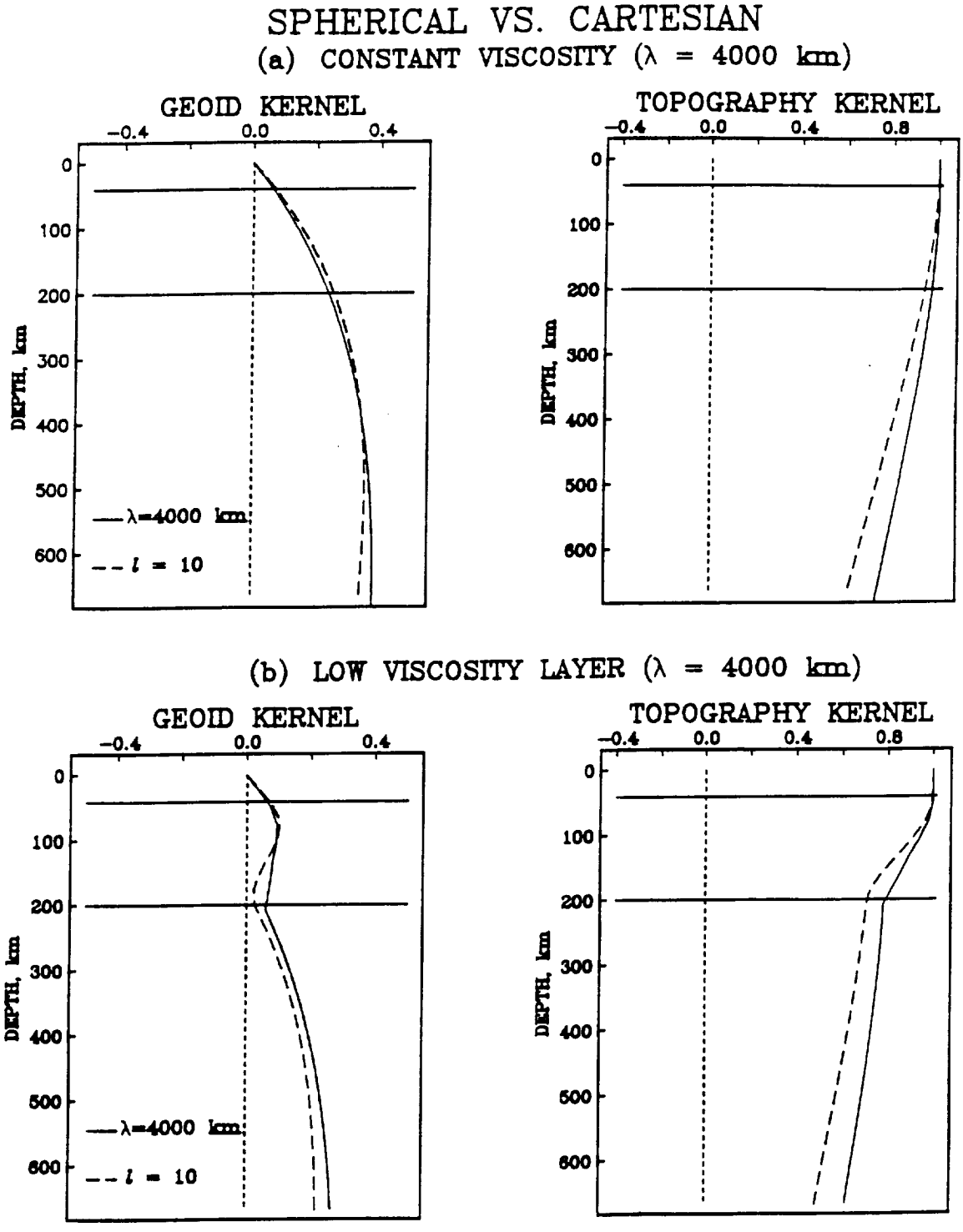

Figure 2.13a,b

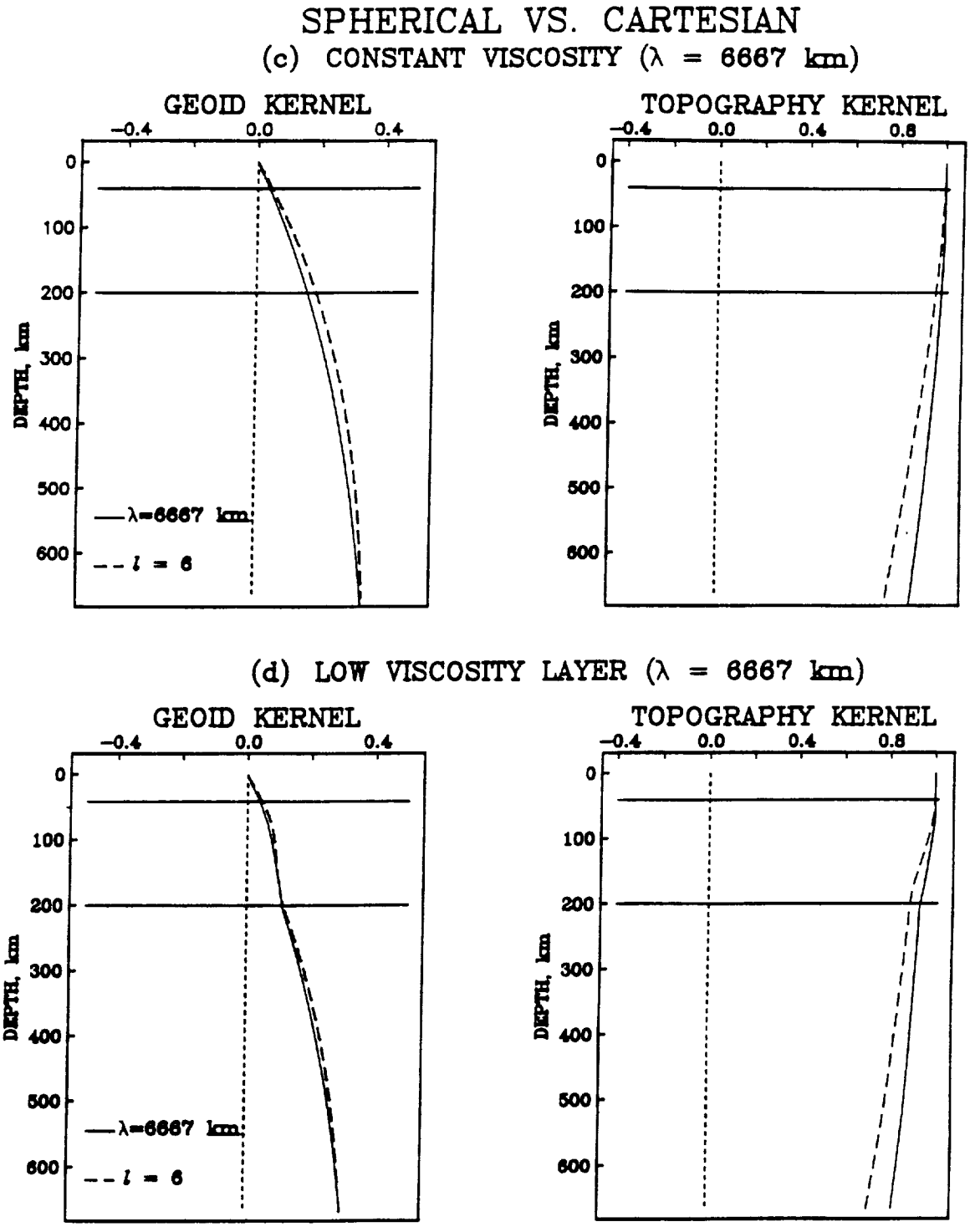

Figure 2.13c,d

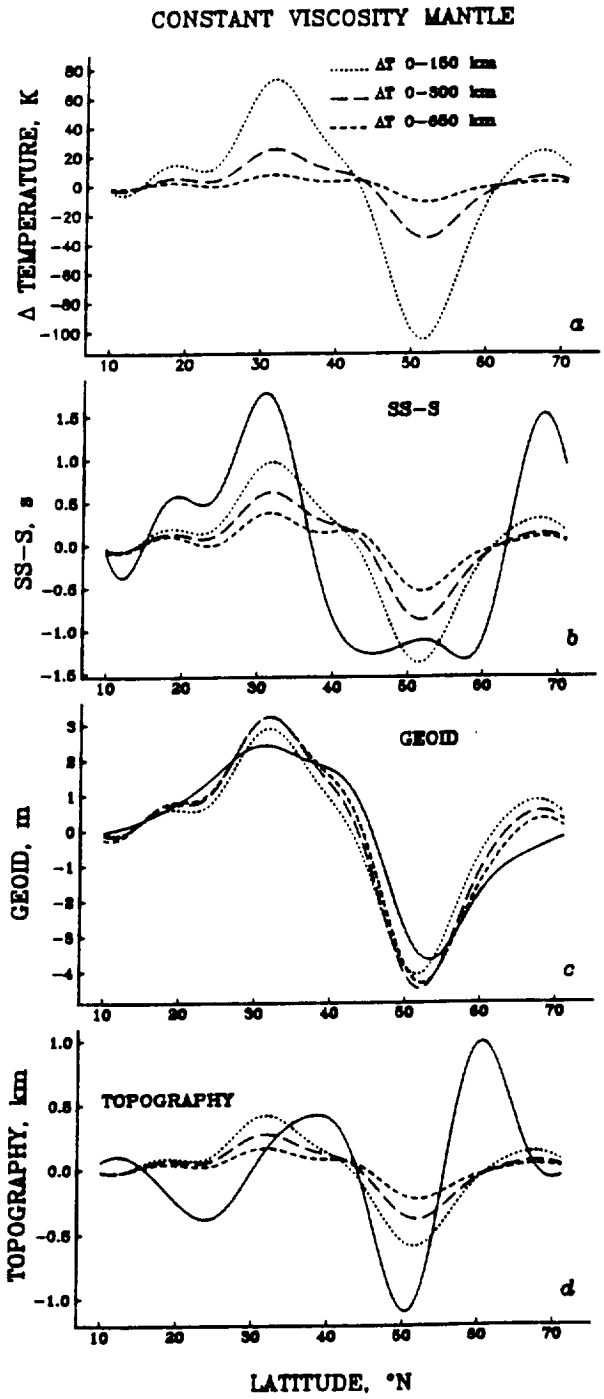
CONSTANT VISCOSITY MANTLE
ΔT 0–150 km
ΔT 0–300 km
ΔT 0–650 km
Δ TEMPERATURE, K
a
SS–S
SS–S, s
b
GEOID
GEOID, m
c
TOPOGRAPHY
TOPOGRAPHY, km
d
LATITUDE, °N

Figure 2.14

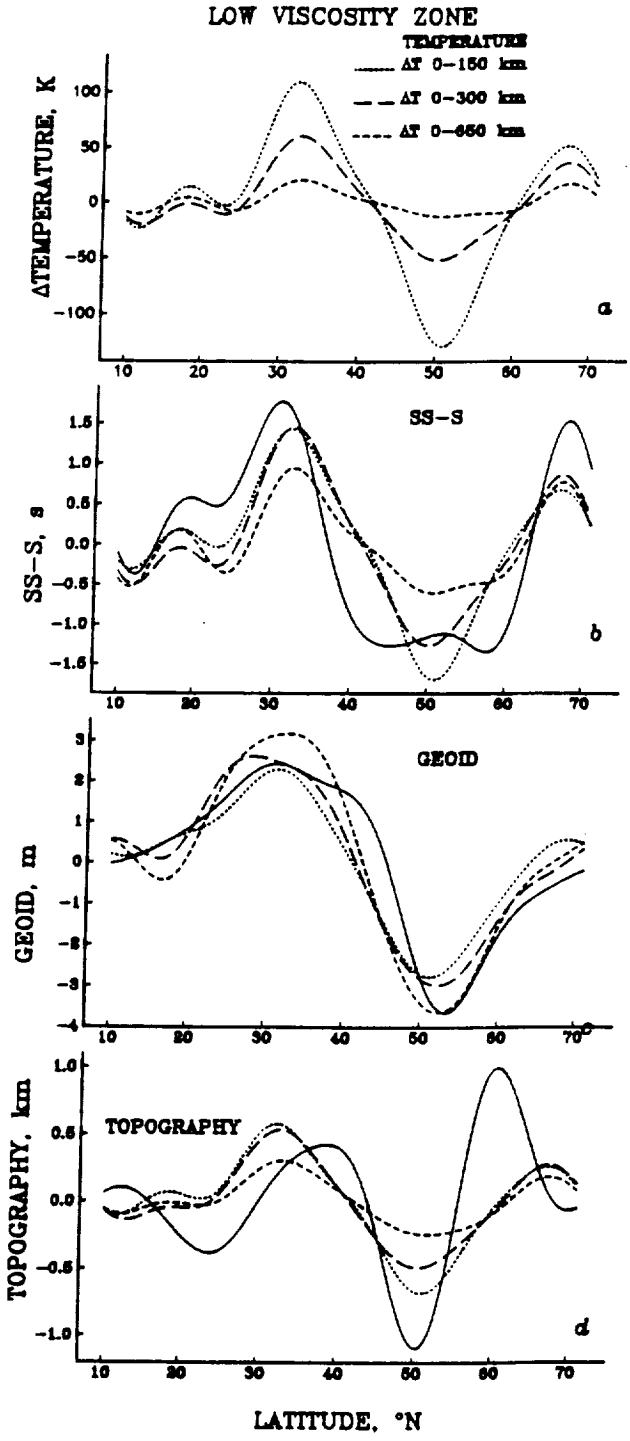
LOW VISCOSITY ZONE
TEMPERATURE
ΔT 0–150 km
ΔT 0–300 km
ΔT 0–650 km
ΔTEMPERATURE, K
a
SS–S
SS–S, s
b
GEOID
GEOID, m
TOPOGRAPHY
TOPOGRAPHY, km
d
LATITUDE, °N

Figure 2.15

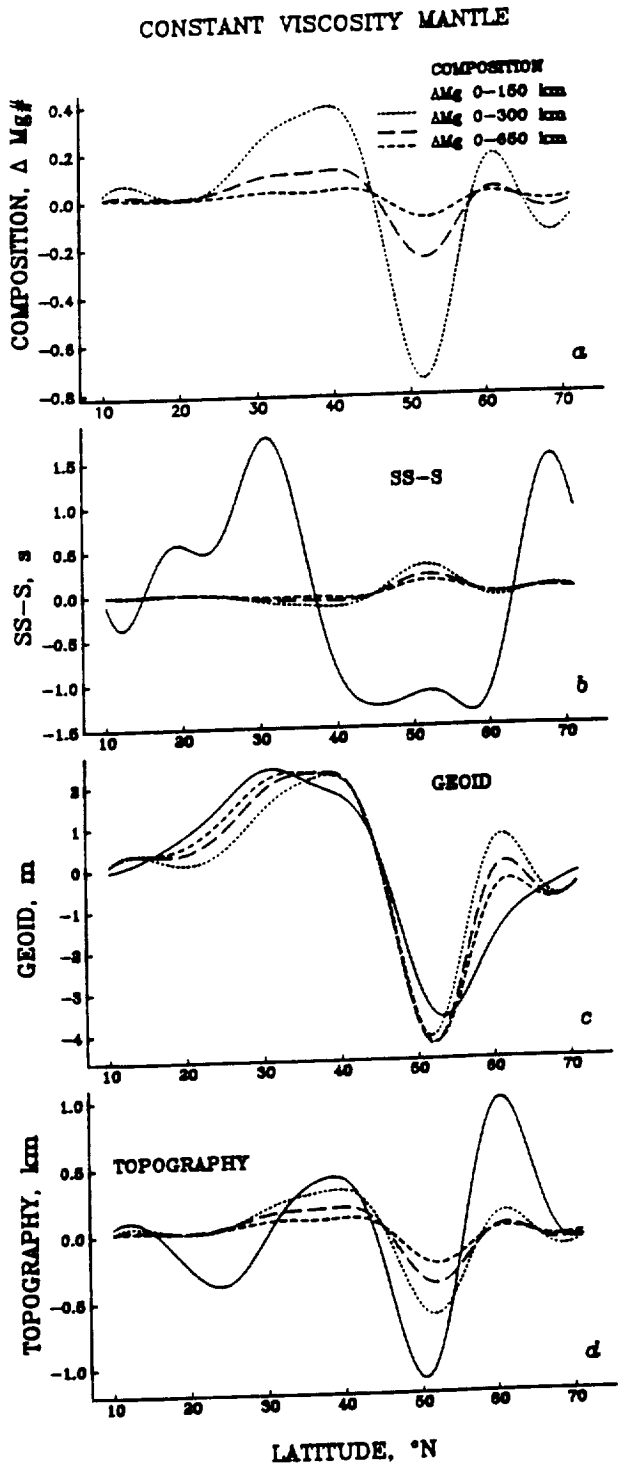
CONSTANT VISCOSITY MANTLE
COMPOSITION
ΔMg 0–150 km
ΔMg 0–300 km
ΔMg 0–650 km
COMPOSITION, Δ Mg#
a
SS–S
SS–S, s
b
GEOID
GEOID, m
c
TOPOGRAPHY
TOPOGRAPHY, km
d
LATITUDE, °N

Figure 2.16

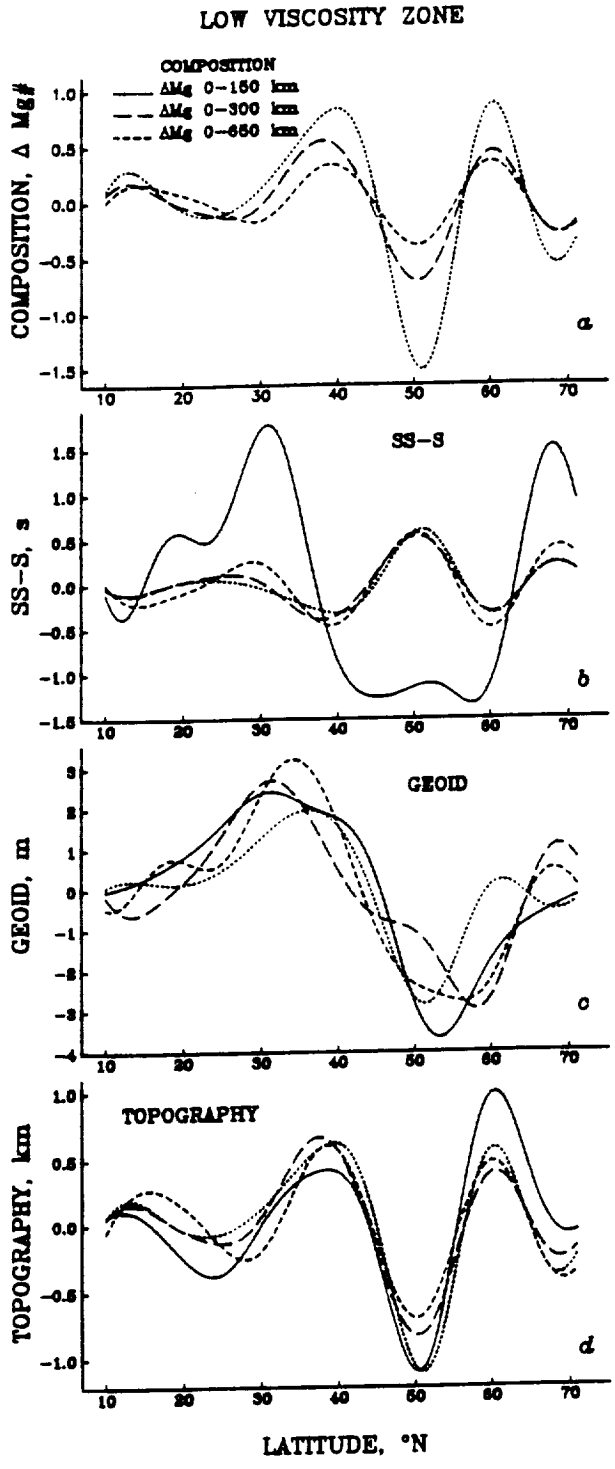
LOW VISCOSITY ZONE
COMPOSITION
ΔMg 0–150 km
ΔMg 0–300 km
ΔMg 0–650 km
COMPOSITION, Δ Mg#
a
SS–S
SS–S, s
b
GEOID
GEOID, m
c
TOPOGRAPHY
TOPOGRAPHY, km
d
LATITUDE, °N

Figure 2.17

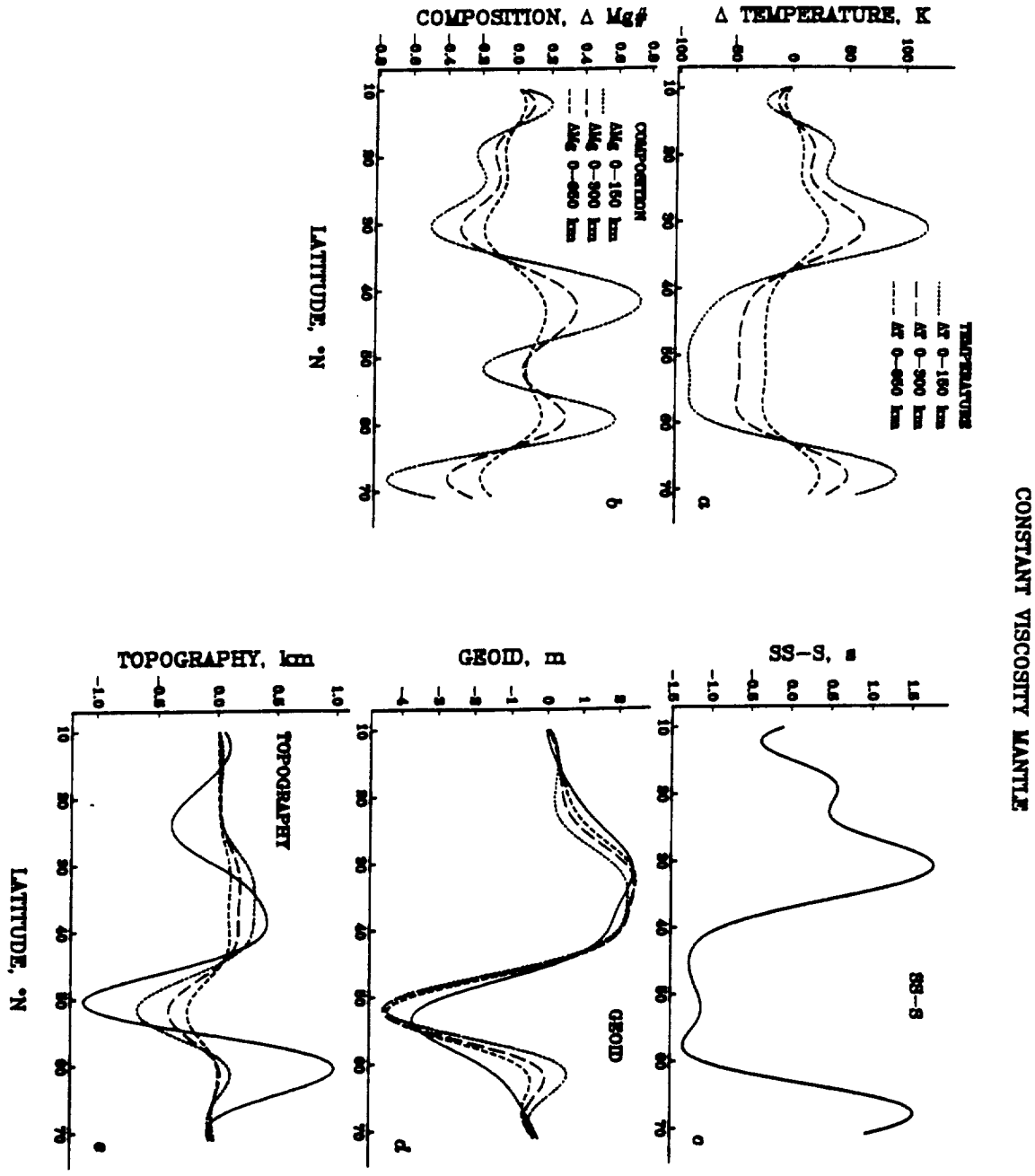
CONSTANT VISCOSITY MANTLE
Δ TEMPERATURE, K
COMPOSITION, Δ Mg#
LATITUDE, °N
TEMPERATURE
ΔT 0–150 km
ΔT 0–300 km
ΔT 0–660 km
COMPOSITION
Δ Mg 0–150 km
Δ Mg 0–300 km
Δ Mg 0–660 km
a
b
SS–S, s
GEOID, m
TOPOGRAPHY, km
LATITUDE, °N
SS–S
GEOID
TOPOGRAPHY
c
d
e

Figure 2.18

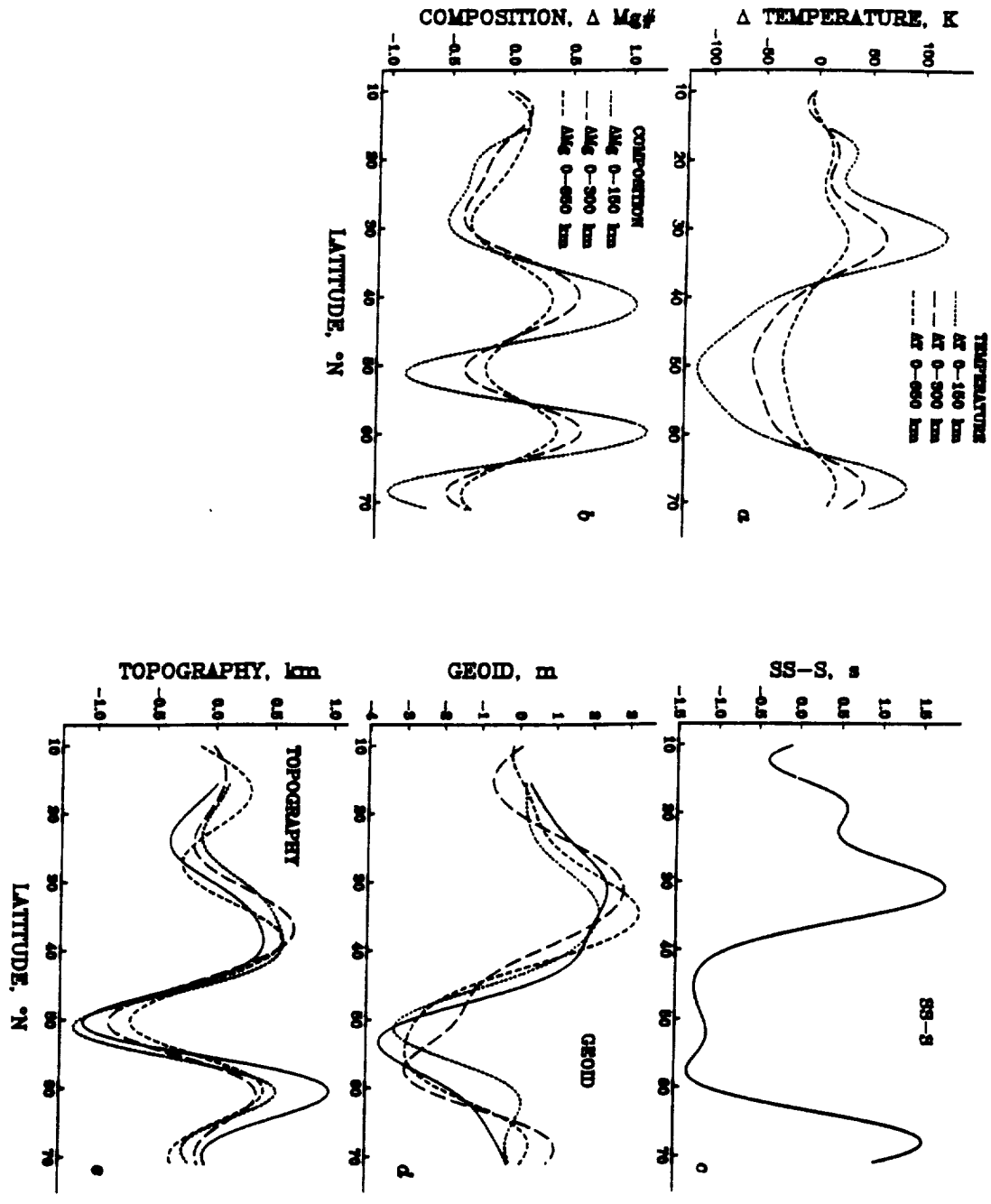
LOW VISCOSITY ZONE
Δ TEMPERATURE, K
COMPOSITION, Δ Mg#
SS−S, s
GEOID, m
TOPOGRAPHY, km
LATITUDE, °N
TEMPERATURE
COMPOSITION
SS−S
GEOID
TOPOGRAPHY

Figure 2.19

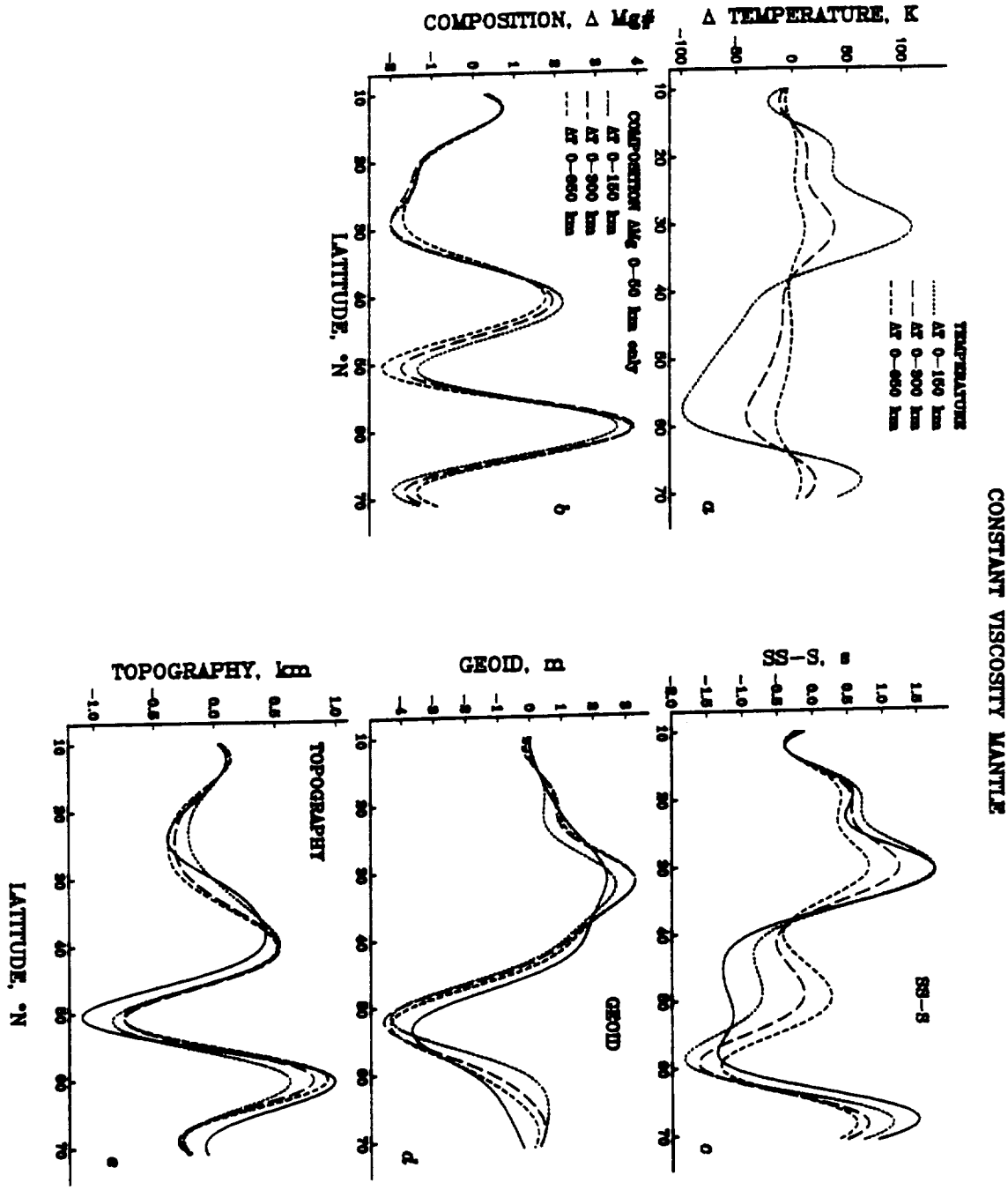
CONSTANT VISCOSITY MANTLE
Δ TEMPERATURE, K
COMPOSITION, Δ Mg#
SS−S, s
GEOID, m
TOPOGRAPHY, km
LATITUDE, °N
TEMPERATURE
COMPOSITION Δ Mg# 0−50 km only
SS−S
GEOID
TOPOGRAPHY
a
b
c
d
e

Figure 2.20

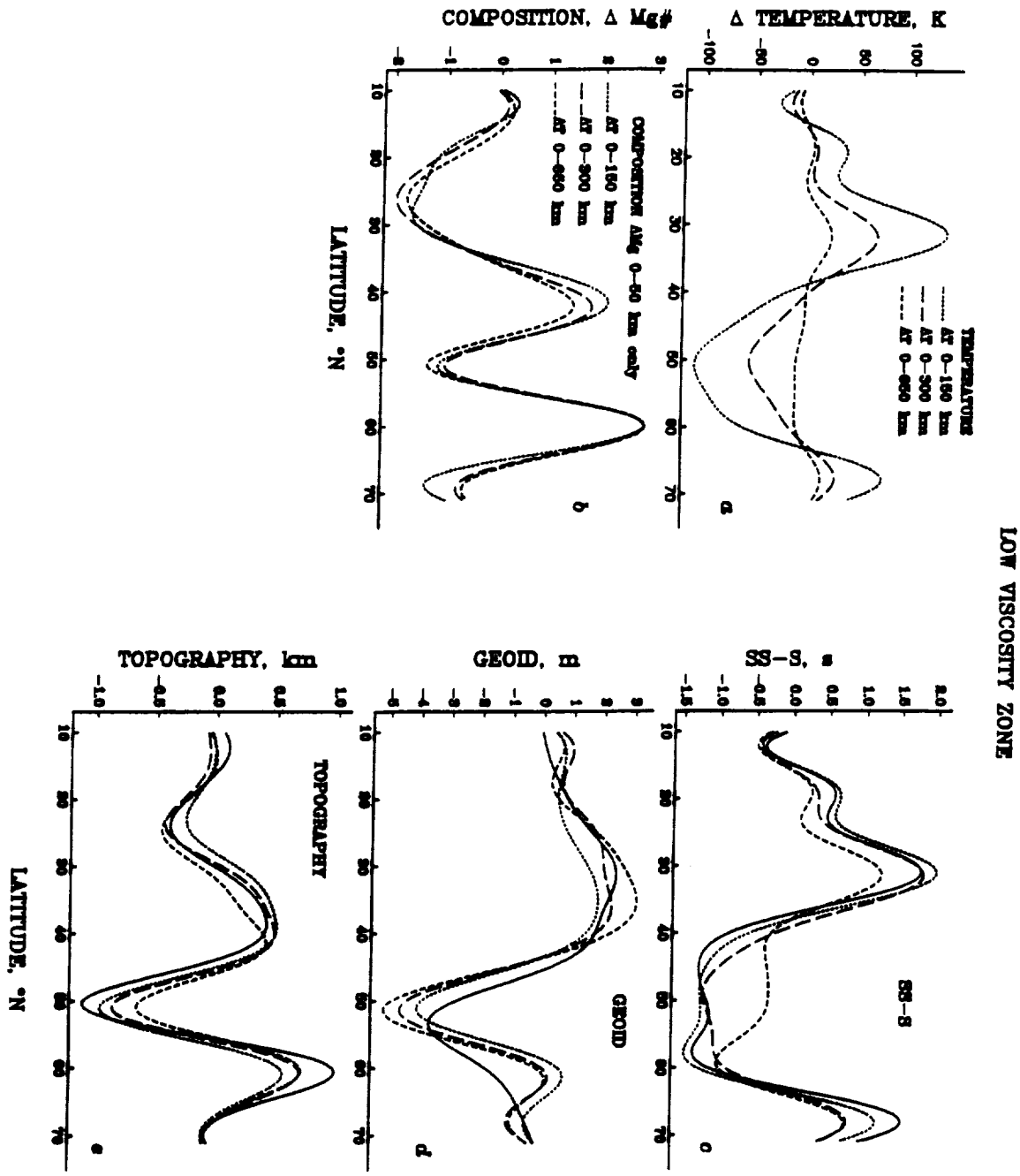
LOW VISCOSITY ZONE
Δ TEMPERATURE, K
COMPOSITION, Δ Mg#
SS−S, s
GEOID, m
TOPOGRAPHY, km
LATITUDE, °N
TEMPERATURE
COMPOSITION
GEOID
SS−S
TOPOGRAPHY

Figure 2.21

Chapter 3

Differential Shear Wave Attenuation and Its Lateral Variation in the North Atlantic Region

INTRODUCTION

The rate of attenuation of seismic waves provides important information complementary to that provided by seismic velocities. Seismic attenuation can be strongly affected by variations in the physical state and temperature field of the Earth's interior. Recent analysis of global variations in Q structure using long-period surface waves suggests that the most significant variations are confined to the upper mantle low-velocity, low-Q zone [*Ritzwoller et al.*, 1989] and that the main contributors to these variations are the mid-ocean ridges (M.H. Ritzwoller, pers. comm., 1989). Earlier studies with body waves suggest that the upper mantle beneath mid-ocean ridges should display a significantly greater than average level of S-wave absorption [e.g., *Molnar and Oliver*, 1969; *Solomon*, 1973]. A more detailed analysis of mantle attenuation beneath ridges and its variation with lithospheric age would do much to sharpen the inferences from global models and to assess whether the observed lateral variations reflect differences in the percentage of partial melt [*Ritzwoller et al.*, 1989] or only in temperature.

There is considerable difficulty in relating laboratory experiments on seismic properties to propagation characteristics in the mantle because of differences in pressure

and temperature conditions beetween the two environments. Moreover, most laboratory experiments are conducted at frequencies much greater than those in the seismic wave band. Direct quantitative measurement of variations in Q in the Earth are therefore important. In this paper we present measurements of differential shear wave attenuation in the north Atlantic and its variation with lithosphere age, and we utilize thermal models to interpret the observations in terms of an empirical relation between differential attenuation and temperature. Our approach is to measure the spectral amplitude ratio of long-period SS and S waves and to attribute variations in this ratio to differential attenuation of the SS waves in the upper mantle near the bounce points of these surface-reflected phases. This work is a complement to our study of SS-S differential travel times in the north Atlantic [*Sheehan and Solomon*, 1991; Chapter 2]. *Sipkin and Jordan* [1980b] and *Revenaugh and Jordan* [1987] used the ScS phase as an effective tool to map lateral variations in Q_{ScS}, which measures the vertically-averaged Q of the entire mantle. The SS-S differential attenuation measurement does not sample the significant lateral heterogeneity at the base of the mantle [*Dziewonski*, 1984] as does multiple ScS. Such measurements thus provide an important complement to ScS studies and can serve to isolate the upper mantle contribution to Q. The SS path segment in the upper mantle is not as nearly vertical as ScS, but many more paths are possible for SS because shallow sources can be employed, in contrast to ScS_n, for which deep sources are normally required to avoid interference from surface waves. The most important result of this study is the documentation of an increase in Q_S in the upper mantle with increasing plate age. We also examine along-axis variations in differential attenuation, and we test whether they might be produced by along-axis variations in temperature, such as those derived from the inversion of along-axis variations in SS-S travel times, geoid, and bathymetry [*Sheehan and Solomon*, 1991; Chapter 2].

MEASUREMENT OF DIFFERENTIAL ATTENUATION

The seismic data used in this study consist of long-period S and SS phases recorded at digital stations in the Global Digital Seismic Network (GDSN) [*Peterson et al.*, 1976; *Peterson and Hutt*, 1982], the Network of Autonomously Recording Seismographs (NARS), [*Nolet and Vlaar*, 1982], and the GEOSCOPE network [*Romanowicz et al.*, 1984]. We use only transversely polarized (SH) seismograms (rotated from N-S and E-W components) to avoid interference from the SKS phase and contamination from P-SV conversions at the base of the crust and other near-surface discontinuities.

A spectral ratio method is utilized to determine the differential attenuation between the phases SS and S [e.g., *Teng*, 1968; *Schlue*, 1981]. The spectral amplitude A of an S-phase can be written as the product of terms for source $A_0(\omega,\theta,\phi)$, instrument $A_i(\omega)$, crustal layering at the source $A_{cs}(\omega)$ and receiver $A_{cr}(\omega)$, and geometrical spreading G and attenuation t* along the path, as

$$A(\omega) = A_0(\omega,\theta,\phi)\, A_i(\omega)\, A_{cs}(\omega)\, A_{cr}(\omega)\, G \exp(-\pi f t^*) \qquad (3.1)$$

where

$$t^* = \int_{path} \frac{ds}{Q(s)\, V(s)} \qquad (3.2)$$

and Q and V are the quality factor and wave velocity along the path *s*. For a given source and station, the SS phase will have the same values of A_0, A_i, A_{cs}, A_{cr} as the S phase, so taking the natural logarithm of the amplitude ratio,

$$\ln (A_{SS}/A_S) = -\pi f (t^*_{SS} - t^*_S) = - \pi f \delta t^* \qquad (3.3)$$

where the differential attenuation $\delta t^* = t^*_{SS} - t^*_S$. Thus an estimate of δt^* may be obtained from the negative of the slope of the log of the amplitude ratio.

In practice, the digital long-period seismograms are rotated, and the transverse (SH) component is windowed to isolate the S and SS pulses (Figure 3.1a). Constant window lengths of 100 s are used for both the S and SS phases. A Kaiser-Bessel [*Harris*, 1978] taper with $\alpha = 3$ (the parameter α controls the width of the central window versus the sidelobe amplitude) is applied to each windowed pulse. This taper is an effective tool for reducing amplitudes at the front and the tail of the window and acts to reduce the effects of signals not associated with the phase of interest. We find that it is crucial to form narrow windows around the S and SS pulses, as the differential attenuation values can vary by as much as 1 s depending on how S and SS are windowed. The amplitude spectrum of the isolated phase is then obtained for the frequency band 0.01 to 0.15 Hz. The log of the amplitude spectrum is calculated and then smoothed by taking running averages over a 0.04-Hz band (Figures 3.1b-c). An amplitude ratio spectrum (Figure 3.1d) is formed by subtracting the log spectrum of the S phase (Figure 3.1b) from that of the SS pulse (Figure 3.1c). The log amplitude ratio spectrum is smoothed by a moving average (0.02 Hz wide) before a linear fit is derived. In general the amplitude ratios decrease systematically with frequency over the approximate band 0.01 to 0.08 Hz but above a frequency between 0.07 and 0.11 Hz the amplitude ratios tend to increase. We attribute this increase to noise in both the S and SS phases. We measure the slope of the log amplitude ratio spectrum between a constant lower frequency of 0.016 Hz and three different upper frequencies: 0.08, 0.095, and 0.11 Hz. The upper frequency cutoff that gives the most negative (steepest) slope is that used to calculate δt^*. Choosing the steepest

slope may bias us toward large values of δt^*, but our motivation is to obtain the most robust measure of attenuation and to avoid the part of the spectrum where the slope is likely to be susceptible to noise. Uncertainties involved with the measurement of δt^* are discussed further in Appendix 3.A.

As an alternative technique for measuring differential attenuation we have also constructed stacks of amplitude ratio spectra for groups of SS-S pairs. Stacks are constructed by calculating a mean value of ln (A_{SS}/A_S) with corresponding standard error at each frequency. A single slope is measured for the stacked spectrum, over the frequency band 0.016 to 0.10 Hz. If we were to retain the use of variable cutoffs with the spectra going into the stacks the high frequency values of ln (A_{SS}/A_S) would not have a contribution from each seismogram and would therefore not be representative of all of the seismograms included in the stack. Since we choose a single cutoff frequency of 0.10 Hz instead of picking the steepest slope, the values of δt^* from the stacks are consistently lower than those measured individually. However, we find that the trends observed using stacked data are nearly identical to those obtained from the individual measurements. The analysis presented in the remainder of the paper is based on individual measurements.

DATA

The north Atlantic region has a good distribution of events and stations at suitable epicentral distances. Source-receiver separations were restricted to lie in the range 55° to 86° to ensure clear separation of S and ScS at greater distances and to avoid triplication in SS at shorter distances. The SS and S phases bottom in the mantle between about 670 km and 2300 km depth. Digital seismograms selected for spectral analysis are from the travel time study of *Sheehan and Solomon* [1991]; see also Chapter 2. The distribution of sources and stations used to measure SS-S attenuation is shown in Figure 3.2. The

majority of data used in this study comes from equatorial fracture zone earthquakes recorded at North American and European stations, north and central Atlantic events recorded at North American stations, Central American events recorded at European stations, and Mediterranean and European earthquakes recorded in North America. The data set consists of over 150 δt^* values with SS bounce points in the north Atlantic (Figure 3.3). A tabulation of all δt^* values is given in Appendix II.

RESULTS

Contributions to δt^* can arise from any portion of the wave path. It is expected, however, that δt^* will be controlled primarily by the upper mantle, where values of Q^{-1} are known to be large and variable [*Solomon*, 1972; *Sipkin and Jordan*, 1980b] and where seismic velocity and other physical properties also show significant lateral variation. We interpret the variations in δt^* in terms of lateral variation in Q within the crust and upper mantle beneath the surface reflection points of the SS wave path. The validity of this assumption is supported by the correlation, discussed further below, of δt^* with surface tectonic features (and with sediment thickness) in the vicinity of the SS bounce point. In addition, the δt^* values correlate with the SS-S travel time residuals (Figure 3.4), and regression experiments by *Kuo et al.* [1987] and *Woodward and Masters* [1991] have shown that the SS-S travel time residuals can be attributed to lateral variations in upper mantle structure in the vicinity of the SS bounce point. The δt^* values are further interpreted in terms of such upper mantle processes as lithospheric aging and along-axis heterogeneity in mantle structure.

Epicentral Distance Dependence

The value of δt^* increases with epicentral distance Δ (Figure 3.5). Presumably this effect is at least partly due to the S phase being increasingly less attenuated relative to SS as a greater fraction of its path is in the high-Q deep mantle [*Brune*, 1977]. A simple correction for epicentral distance Δ was made by fitting a straight line, $\delta t^* = (0.054 \pm 0.019)\,\Delta - 0.265$, to the observed values of δt^* versus Δ (Figure 3.5). The slope of this line is in approximate agreement with the predictions of several radial Q models [*Anderson and Hart*, 1978; *Anderson and Given*, 1982] (Figure 3.6). The form of the correction for epicentral distance dependence applied to the individual measurements is

$$\delta t^*_{corr} = \delta t^*_{old} - (b\,\Delta + a) + \delta t^*_{av} \qquad (3.4)$$

where $b = 0.054$, $a = -0.265$, and $\delta t^*_{av} = 3.67$ is the mean of all values of δt^*. Application of this correction does not substantially affect the relation between δt^* and travel times (Figure 3.7).

Lithospheric Aging

Cooling and thickening of the lithosphere should yield a tendency toward decreasing seismic attenuation with increasing lithospheric age. A linear regression experiment was performed to examine the correlation of δt^* with seafloor age. To obtain a representative age value for the region spanning approximately one horizontal wavelength of the incident (SS) wave, an average seafloor age was estimated for a 1° by 1° box centered on each SS surface bounce point [*Sheehan and Solomon*, 1991]. Measurements from zones with sediment thickness in excess of 1 km were excluded from the final age regression to avoid potentially large contributions from the low-Q sediments. Although the SS wave samples the upper mantle over a range of ages, we expect that the differential attenuation

contributed by the SS path segments on the younger and older sides of the bounce point approximately cancel so that the age at the SS surface bounce point is representative.

The δt^* values for the north Atlantic are consistent with the expectation of a decrease in attenuation with increasing seafloor age. The slope derived by linear regression of δt^* with square root of age is -0.20 ± 0.07 s $My^{-1/2}$ from 0 to 100 My, with a linear correlation coefficient of -0.97 (Figure 3.8a). This slope is consistent with observations of increasing Q_S with lithosphere age [*Canas and Mitchell*, 1981; *Sipkin and Jordan*, 1980b; *Revenaugh and Jordan*, 1987]. The trend of decreasing attenuation with increasing seafloor age is in the same sense as that for SS-S travel times for this region [*Sheehan and Solomon*, 1991] (Figure 3.8b).

To look for other systematic variations in the differential attenuation measurements, we correct for age t by removing the linear relation shown by the dashed line in Figure 3.8a. The form of the age correction for the individual measurements is

$$\delta t^*_{corr} = \delta t^*_{old} - (b\, t^{1/2} + a) + \delta t^*_{av} \qquad (3.5)$$

where $b = -0.20$, $a = 4.71$, and $\delta t^*_{av} = 3.42$ is the average of all data after application of equation 3.4.

Spatial Patterns of Age-corrected δt^*

After removal of the age-dependence of δt^*, we may then search for systematic variations along the Mid-Atlantic Ridge. Such variations are seen in SS-S differential travel times and are attributable to along-axis differences in upper mantle temperature and composition [*Sheehan and Solomon*, 1991; Chapter 2]. A north-south profile of δt^* values, constructed with averages of 10 adjacent data points grouped by latitude, is shown in Figure 3.9. In order to maintain consistency with our earlier travel time study [*Sheehan*

and Solomon, 1991] and to avoid possible biases associated with deviations from the simple plate cooling model, the along-axis δt^* profile is constructed using data with bounce points on lithosphere less than 100 My in age. Systematic variations of δt^* are evident with latitude, i.e., along the direction of the Mid-Atlantic Ridge axis. The along-axis variations show a variety of scales, notably at wavelengths of about 1000 - 2000 km in the region from about 15 to 35°N, and at about 6000 km wavelength from large δt^* (high attenuation, low Q) in the south (20-35°N) to lesser δt^* (low attenuation, high Q) farther north (45-60°N). These variations are qualitatively similar to the along-axis pattern of travel time residuals [*Sheehan and Solomon*, 1991; Chapter 2] and are also plausibly the result of thermal or compositional variations along the axis of the Mid-Atlantic Ridge.

VELOCITY AND Q AS FUNCTIONS OF LITHOSPHERIC TEMPERATURE

Because of the strong temperature dependence of both shear wave velocity and attenuation, the most straightforward hypothesis to explain the variations of SS-S travel time residual and differential attenuation with age is that both variations are due entirely to lateral variation in the thermal structure of the lithosphere, i.e., cooling of the oceanic plate. We have tested this hypothesis against the observed SS-S travel time delays as a function of age by means of the plate cooling model of *Parsons and Sclater* [1977]. Geotherms for different ages, according to this model, are shown in Figure 3.10. Temperature perturbations ΔT can be converted to a seismic velocity perturbation by assuming that velocity varies linearly with ΔT and adopting a value for the partial derivative of shear wave velocity with respect to temperature, $\partial V_s/\partial T$. The resulting two-way travel time perturbation, as a function of horizontal wave number k, is given by

$$\Delta t\,(k) = 2\,\frac{\partial V_S}{\partial T}\int_{z_{min}}^{z_{max}} \frac{\Delta T(k,z)\,dz}{V_S(z)^2\,(1 - p^2 V_S(z)^2)^{1/2}} \qquad (3.6)$$

where $V_S(z)$ is from the reference shear velocity model [*Dziewonski and Anderson*, 1981], z is depth, p is the ray parameter, generally taken to be a representative value (0.1375 s/km) for the range of epicentral distances considered here, and z_{min} and z_{max} are the upper and lower boundaries of the region of significant lateral variations in temperature. We choose 50 My as a reference age, so that temperature anomalies are obtained by subtracting the geotherm at 50 My from the geotherm at an arbitrary age t : $\Delta T_t(z) = T_t(z) - T_{50}(z)$. We use a value of -0.6 m s^{-1} K^{-1} for $\partial V_S/\partial T$. This value is a factor of 1.5 higher than the experimental values of *Anderson et al.* [1968] and *Kumazawa and Anderson* [1969] for olivine at standard temperature and pressure but is comparable to the value of -0.62 m s^{-1} K^{-1} determined by *McNutt and Judge* [1990] by a least squares fit of Love-wave phase velocities to a temperature model for the lithosphere.

The SS-S travel time delays predicted by the plate cooling model (Figure 3.11) are in excellent agreement with observed values (Figure 3.8b). The slope derived by linear regression of observed SS-S residual with square root of age is -0.68 ± 0.08 s $My^{-1/2}$ for bounce points between 0° and 60°N latitude and for ages between 0 and 100 My, with a linear correlation coefficient of -0.85 (Figure 3.8b). The value obtained using only that subset of the travel time data in common with the differential attenuation measurements is -0.74 ± 0.10 s $My^{-1/2}$. For comparison, the slope calculated from the plate cooling model for 0-100 My age is -0.64 ± 0.01 s $My^{-1/2}$. The trend of the travel time residual versus age flattens out at about 80 to 100 My for both the observed and predicted residuals. These results support the hypothesis that most, if not all, of the dependence of travel time residual on plate age is due to plate cooling and does not require an additional contribution from below the lithosphere.

We next compare the age dependence of the observed δt^* values with lithospheric temperatures predicted by the plate cooling model. Specifically, we infer possible Q^{-1}-temperature relations through the simultaneous use of the observed δt^*-age relation and geotherms as functions of lithospheric age as predicted by *Parsons and Sclater* [1977]. Assuming that the differential attenuation δt^* arises solely from the upper mantle portion of the SS path, we can express δt^* as

$$\delta t^* = 2 \int_{path} \frac{dz}{Q_S(z)\, V_S(z)\, (1-p^2 V_S^2(z))^{1/2}} \qquad (3.7)$$

where Q_S and V_S are the shear wave Q and velocity along the path, respectively, and p is the ray parameter.

We choose to parameterize Q further in terms of temperature, following the Arrhenius law

$$Q^{-1} = A^{-1} \exp\left[-E / (R\, T(z))\right] \qquad (3.8)$$

where the constant E is an activation energy and R is the gas constant. Substituting this relation into equation 3.7, we obtain

$$\delta t^* = 2 \int_{path} \frac{dz}{A\, e^{E/RT(z)}\, V_S(z)\, (1-p^2 V_S^2(z))^{1/2}} \qquad (3.9)$$

Thus an estimate of δt^* can be obtained by integration, given a velocity model, a geotherm, and the constants A and E. From t^* and T(z) at a number of lithospheric ages, we can formulate an inversion for the parameters A and E by taking the derivatives of δt^* with respect to the model parameters and solving for perturbations to initial estimates of A

and E that minimize the difference between observed and calculated values of δt^*. The use of a constant activation energy might not be appropriate, as there may be several processes acting to produce the observed attenuation, each with its own activation energy. Despite these drawbacks, it is useful to try to parameterize Q in this way as it allows us to test whether or not a single thermally activated process can describe the observations.

Since differential travel time versus age is well modelled if temperature variations are confined to the lithosphere, we solve for Q as a function of temperature in the lithosphere only. We assume a constant value of Q for the asthenosphere; specifically we adopt a value of 130 for Q in the depth range 125 - 500 km, which is the average value for this region given in the PREM Q model [*Dziewonski and Anderson*, 1981]. This asthenospheric contribution to δt^* obtained from integrating equation 3.7 over the depth range 125 to 500 km is approximately 1.7 s.

The inversion for constants A and E indicates that equation 3.8 and the assumption that lateral temperature varitiations are confined to the lithosphere provide a good fit to observed values of δt^* (Figure 3.12). The best fitting values of A and E are 1.67 and 35 kJ mol^{-1}, respectively.

We also tested whether the laboratory-derived Q-temperature relation of *Sato and Sacks* [1989] also matches the observed δt^* values. From equations (1) and (2) of *Sato and Sacks* [1989] and assuming $Q_P/Q_S = 2.25$, we obtain

$$Q_S^{-1} = 2.25 \left[3.5 + \frac{P(z)}{0.073} \right] \exp \left\{ -g \left[\frac{T_m(z)}{T(z)} - a \right] \right\} \qquad (3.10)$$

where P(z) is pressure as a function of depth z, T_m is the solidus temperature, $T(z)/T_m(z)$ is the homologous temperature, and g and a are piecewise constant functions of T/T_m. We substitute this relation into equation 3.7 and integrate over depth to estimate the lithospheric contribution to δt^* (Figure 3.12). Including the asthenospheric contribution

to t* would add a constant of about 1.7 s to the plotted δt^* values. The variation of t* versus age predicted by equation 3.10 is much greater than that observed.

We also examined several other parameterizations of Q_S^{-1} in an attempt to assess the importance of pressure and homologous temperature dependence. A best fit for the parameterization $Q^{-1} = A^{-1} \exp [-c\, T_m(z)/T(z)]$ produced constants of 2.86 for A and 2.05 for c, and an equally good fit to the observed t* values as that obtained using equation 3.8. The parameterization $Q^{-1} = [A + b\, P(z)]^{-1} \exp [-c\, T_m(z)/T(z)]$ proved to be more problematic, as we were inverting for three parameters (A, b, and c) with a limited amount of data, and strong tradeoffs between these different parameters contribute to a nonuniqueness in the solution. We were able to obtain good fits to the data using widely different values of A, b, and c, and we had difficulty converging to physically reasonable solutions. For example, the values 2,1, and 1.7 for A, b, and c produce an rms misfit of 0.12 s, whereas the values 3.5×10^{-2}, -7.7×10^{-3}, and 7.61 for A, b, and c produce an rms misfit of only 0.08 s. We would not expect a negative pressure dependence on Q as this last relation predicts, as Q generally increases with depth in the Earth. Some form of pressure dependence is warranted to avoid Q values that are too low at depth. A parameterization in terms of an activation volume will be attempted in a future study.

Predicted distributions of Q_S versus depth obtained using the different Q-temperature parameterizations are shown in Figure 3.13 for two different lithospheric ages. The *Sato and Sacks* [1989] relation predicts Q values which are in general higher (except at very young ages) than the parameterizations more consistent with our data. The three Q_S profiles shown as dashed lines are all nearly equally consistent with our δt^* observations versus age.

DISCUSSION

The differences between the Q^{-1}-temperature relations we derived for oceanic lithosphere and those reported from laboratory measurements warrant discussion. The Q^{-1}-temperature relation of *Sato et al.* [1989] was obtained from laboratory measurements of P wave attenuation in peridotite at high temperature and pressure (but ultrasonic frequencies). *Sato and Sacks* [1989] argue that relationships between Q and temperature at ultrasonic frequencies can be extrapolated to the seismic band on the basis of the observed frequency independence of Q at ultrasonic frequencies and the prediction of reasonable mantle temperatures with their model. Their model actually tends to underpredict mantle temperatures, and to account for this difference they invoke a relation $Q_P'/Q_P = 1.7$ to 2.5 where Q_P' and Q_P are quality factors of compressional waves for seismic and laboratory studies, respectively. Thus, they suggest that seismic Q will be a factor of about 2 greater than laboratory Q. We find that our seismically derived Q^{-1}-temperature relation predicts smaller relative variations in upper mantle Q^{-1} resulting from a given temperature difference than predicted by the experimentally obtained relations. Many factors could contribute to these discrepancies, including differences in frequency, pressure, temperature, and mineralogy. It is likely that different mechanisms for Q operate under these different conditions, each process having its own activation energy. Possible mechanisms for Q include partial melting, viscous grain boundary migration, and dislocation motion [e.g., *Guegen et al.*, 1981]. The observation that laboratory Q scales with homologous temperature [*Sato and Sacks*, 1989] is purely empirical. We have found that the δt^* values predicted by the *Sato and Sacks* [1989] relation can vary significantly upon application of slightly different solidus temperatures. For example, we found that the δt^* versus age relation predicted from the *Sato and Sacks* [1989] relation and employing the *Wyllie* [1971] dry peridotite solidus differed significantly from that

predicted using the *Takahashi* [1986] dry peridotite solidus. This effect is most pronounced at temperatures near to and exceeding the solidus.

We have not included the possibility of a small degree of melt fraction on δt^*. The influence of partial melt on seismic attenuation depends on the melt fraction and the geometry of its distribution [*Cooper and Kohlstedt*, 1986]. Melt affects velocities through a direct effect on the elastic moduli and a dispersive effect of relaxation or attenuation. The volume fraction and geometrical distribution of any melt in the mantle, however, are not known. *Sato et al.* [1989] and *Kampfmann and Berckhemer* [1985] downplay the importance of the melt phase on anelasticity, at least for temperatures not significantly above the solidus, and instead suggest that variations in temperature alone are sufficient to produce observed Q variations in the Earth. In their experiments with peridotite *Sato et al.* [1989] find that there is no large change in Q on first melting but rather a steady change with temperature. *Kampfmann and Berckhemer* [1985] similarly observe no large effect at slightly super-solidus temperatures. However, the *Kampfmann and Berkhemer* [1985] samples included significant melt, so it is difficult to separate clearly the effects of melt from those due solely to temperature. *Goetze* [1977] suggests that extrapolated laboratory creep data on unmelted olivines are compatible with geophysical evidence regarding the rheology of the upper mantle. *Solomon* [1973] reported a narrow (no wider than 100 km and shallower than 50 to 150 km deep) zone of low Q centered along the Mid-Atlantic Ridge axis, which he attributed to the presence of partial melt, and *Molnar and Oliver* [1969] found that S_n does not propagate efficiently in the immediate vicinity of the Mid-Atlantic Ridge, consistent with the presence of a narrow low-Q zone at the ridge. The observations in this work lack the resolution to discern the presence of such a narrow low-Q feature, but our data are consistent with the hypothesis that low Q beneath young oceanic lithosphere is due simply to elevated temperature.

The values that we obtain for Q^{-1} averaged over depth in the lithosphere are high, with Q^{-1} values ranging from 0.016 to 0.033 (Q= 30 to 60), with the range in Q^{-1} values associated with the range of lithospheric ages from 0-100 My. This range is consistent with the values (Q^{-1} = 0.018 to 0.052, Q =19 to 55) found for Q^{-1} in the upper 220 km beneath the Lau back-arc spreading center [*Flanagan and Wiens*, 1990], but higher than the value of 0.014 for Q^{-1} (Q = 70) at depths between 75 and 150 km beneath the East Pacific Rise region obtained by *Ding and Grand* [1987]. The *Ding and Grand* [1987] study did not report Q^{-1} values for depths shallower than 75 km. *Canas and Mitchell* [1981] examined attenuation of Rayleigh waves in the north Atlantic and determined Q^{-1} as a function of depth and age; their Figures 6 and 7 can be compared with our Figure 3.13. They found that a low-Q zone is prominent in the upper mantle of all regions younger than 65 My in age but that such a zone is poorly developed in other regions. The Q^{-1} values in their low-Q zone range from approximately 0.010 to 0.020 (Q = 50 to 100).

We may also estimate the average difference in Q^{-1} between S and SS in the upper mantle by means of the simple equation of δt^* to the product of differential travel time and average Q^{-1}, where the travel time is the differential travel time of SS and S and t^* has the value of δt^*. We obtain Q^{-1} = 0.012 (Q = 82). This value likely represents an average Q^{-1} across the oceanic upper mantle (0-650 km). This value is consistent with the average upper mantle Q^{-1} value of 0.012 (Q = 82) obtained in a study of multiple ScS waves by *Revenaugh and Jordan* [1987]. Thus our δt^* measurements are consistent with other observations of seismic attenuation in the lithosphere and asthenosphere in general and of low Q near active spreading centers in particular.

As a further test of our Q^{-1}-temperature relation, we take the upper mantle temperature variations obtained from the inversion of SS-S differential travel time residuals, geoid, and bathymetry along the axis of the Mid-Atlantic Ridge [*Sheehan and Solomon*, 1991; Chapter 2] and predict the corresponding pattern of δt^* along the ridge

axis. In Figure 3.14 we compare the observed pattern of along-axis variations in δt^* with those produced assuming the Q^{-1}-temperature relation from equation 3.8. The predicted value of δt^* is obtained from equation 3.9, where T(z) is the sum of the *Parsons and Sclater* [1977] geotherm at a reference age and the average differential temperature ΔT obtained from the inversion. Below the lithosphere, T(z) is obtained by adding ΔT to an adiabatic temperature gradient. We found that the predicted δt^* variations depend on the choice of reference geotherm. To obtain an average representative δt^* variation for the range of lithospheric ages that we sample, we calculate δt^* using the geotherm for each of the seven ages of the data groups in Figure 3.12, and we perform an arithmetic average to obtain the final δt^*. Along-axis profiles were calculated for all four Q-temperature relations examined in this study.

Fits between the observed and predicted profiles of δt^* shown in Figure 3.14 are not as good as we might have expected after a visual inspection of the apparent qualitative correlation between travel time and δt^*. We obtain variance reductions of about 25% for the models shown. A large part of the misfit in phase is due to an offset in the latitude at which the peak residuals in travel time and δt^* are observed in the vicinity of 30°N. Both the observed and predicted δt^* profiles indicate low attenuation in the region near 50°N. If the observed δt^* profile had been included in the inversion it is likely that a better fit could have been obtained for the δt^* data but at the expense of the fits to the geoid, travel time, and bathymetry profiles. The along-axis δt^* profiles obtained using the *Sato and Sacks* [1989] Q-temperature relation are somewhat different (Figure 3.15), with relative variations in δt^* larger than the observed.

Profiles of δt^* were also constructed from temperature variations obtained from the joint inversion of travel time, geoid, and bathymetry for both temperature and composition [*Sheehan and Solomon*, 1991; Chapter 2]. These temperature profiles are influenced more strongly by the travel time residuals (relative to geoid and bathymetry) than are those

produced by the inversion for temperature only. No attempt has been made to include a compositional dependence of Q^{-1}, so the model δt^* values are those predicted from the thermal perturbations only. We find that the δt^* profiles predicted from these temperature variations are generally in somewhat better agreement with the δt^* observations than those constructed using the temperature perturbations resulting from the inversion for temperature variations only.

CONCLUSIONS

We have measured SS-S differential attenuation δt^* in the north Atlantic region from about 150 wave pairs. After correcting δt^* for epicentral distance we find that δt^* decreases with increasing seafloor age. We do not observe evidence for a narrow region of very low Q along the axis of the Mid-Atlantic Ridge as reported by *Solomon* [1973], although this may be due to the limited spatial resolution of the long-period shear waves utilized in our study.

We have derived empirical Q^{-1}-temperature relations by comparing measurements of δt^* with values predicted under the assumptions that δt^* variations arise from lithospheric cooling and that the temperature structure as a function of lithospheric age is that given by the plate cooling model [*Parsons and Sclater*, 1977]. The Q^{-1}-temperature relation that best fits our observations predicts smaller variations of $Q^{-1}$with temperature, especially at young ages, than the Q-temperature relation of *Sato and Sacks* [1989] derived from laboratory measurements of Q_P^{-1} in a spinel lherzolite at ultrasonic frequencies. Systematic variations of δt^* along the axis of the Mid-Atlantic Ridge are also seen. These variations are broadly consistent with the along-axis variations in temperature derived from an inversion of differential travel time residuals and geoid and bathymetry anomalies. Theoretical along-axis profiles of δt^* are constructed from the along-axis variations

derived in Chapter 2 of this thesis and the Q-temperature relation derived here.

APPENDIX 3.A: ESTIMATION OF ERRORS FOR SS-S DIFFERENTIAL ATTENUATION (δt^*)

It is important to quantify the uncertainties in the measurements from individual and stacked spectra of δt^*. After windowing and calculating spectra, the "quality" of each individual δt^* measurement is rated and a grade is assigned. Our assignment of quality is largely subjective and based upon visual inspection of the waveforms and amplitude spectra of S and SS waves, and of samples of noise background, taking into account the clarity of the seismogram and shape of the amplitude spectral ratio. An "A" quality grade indicates that both S and SS pulses are well above the noise level and the amplitude spectral ratio shows a smooth decrease with frequency. "B" quality indicates good signal to noise ratios but an amplitude spectral ratio not as smooth, and a "C" quality grade indicates lower signal to noise ratios or log spectral ratios poorly fit by a straight line. In addition to A, B, and C grades, there were data that were rejected because of a poor signal to noise ratio for either the S or SS phase, or an irregular spectral ratio.

As an objective means to obtain estimates of error, we examine the scatter in measurements of various quality within a small region. We measured the root mean squared (rms) difference between δt^* of the same grade (A, B, or C) with bounce points separated by less than 100 km and with differences in path azimuth at the bounce point of less than 10°. A 100-km distance is less than the horizontal wavelength of SS (which is about 180 km at 25 s period), so we do not expect much contribution to the rms difference from lateral variation in structure. The rms difference for 8 residual pairs of A quality which were within 100 km of each other was 3.4 s. For B quality picks, an rms difference of 3.8 s was measured using 17 residual pairs, and for C quality picks 20 residual pairs yielded an rms difference of 3.3 s. The rms values are strongly affected by a few outliers, so rms values were also calculated without these estimates. The resulting

rms values were 1.9 s for 6 A-quality δt^* pairs, 2.8 s for 13 B-quality pairs, and 2.6 s for 17 C-quality pairs. Part of the reason that the rms values for the C-quality data are less than those for the B-quality measurements is that the mean values of the first group of measurements are smaller and thus the rms differences are also smaller. The C-quality measurements are often smaller because of increased noise at high frequencies which results in a flattening of the slope of the spectral amplitude ratios.

Because of the bias of C-quality estimates towards low values of δt^*, we use the estimates of the rms differences only as an approximate guide for estimating the average overall errors in the A-, B-, and C-grade measurements. Our final choice of measurement errors used for relative weighting of the differently graded measurements is $\sigma_A = 1.9$ s, $\sigma_B = 2.7$ s, and $\sigma_C = 3.5$ s. In the weighted regression experiments the A-, B-, and C-quality measurements are weighted inversely by their measurement variance.

Figure Captions

Figure 3.1. An example of the measurement of SS-S differential attenuation for the event of December 24, 1985, at GDH. (a) Displacement seismogram with S and SS phases windowed. (b) Natural log of the amplitude spectrum of the S phase. (c) Natural log of the amplitude spectrum of the SS phase. (d) Natural log of the ratio of the amplitude spectra of the SS and S phases. Solid line is a least squares fit to the ratio from 0.01 to 0.08 Hz.

Figure 3.2. Distribution of earthquakes (triangles) and seismograph stations (circles) used to measure SS-S differential attenuation. Stations are from the GDSN, NARS, and GEOSCOPE digital networks. Earthquakes are from the Harvard CMT catalogue (generally $m_b > 5.0$) from the years 1977-1987. Lambert equal-area projection with the pole of projection at 45°N, 40°W.

Figure 3.3. Distribution of SS bounce points. Map projection as in Figure 3.2.

Figure 3.4. SS-S differential attenuation (δt^*) versus SS-S travel time residual. Each point represents the weighted mean of 38 data points adjacent in SS-S residual (x-axis). Weights are constructed from variances as discussed in Appendix 3.A. Horizontal and vertical bars are standard errors of the means. Linear regression yields a slope of 0.10 ± 0.04.

Figure 3.5. SS-S differential attenuation versus epicentral distance. Each point represents the weighted mean of 38 points adjacent in epicentral distance

(x-axis). Horizontal and vertical bars are standard errors of the means. Linear regression yields a slope of 0.05 ± 0.02 s/ degree (line).

Figure 3.6. Comparison of observed SS-S differential attenuation versus epicentral distance with predictions from several radial Q models [*Anderson and Hart*, 1978; *Anderson and Given*, 1982].

Figure 3.7. Distance-corrected SS-S differential attenuation (δt^*) versus SS-S travel time residual. Each point represents the weighted mean of 38 adjacent data points. Linear regression yields a slope of 0.09 ± 0.04.

Figure 3.8. (a) Distance-corrected SS-S differential attenuation (δt^*) versus square root of seafloor age. Each point represents the weighted mean of 38 adjacent data points. Horizontal and vertical bars are standard errors of the means. Linear regression yields a slope of -0.20 ± 0.07 s/ $(My)^{1/2}$ for an age range of 0-100 My (solid line).

(b) SS-S travel time residuals versus square root of seafloor age in the north Atlantic, from *Sheehan and Solomon* [1991]. Each point represents the weighted mean of 14 adjacent data points. Horizontal and vertical bars are standard errors of the means. Linear regression yields a slope of -0.68 ± 0.08 s/ $(My)^{1/2}$ for a 0-100 My age range (solid line) or -0.76 ± 0.09 s/ $(My)^{1/2}$ for a 0-80 My range (dashed line).

Figure 3.9. (a) SS-S differential attenuation, corrected for epicentral distance and lithospheric age, versus latitude along the Mid-Atlantic Ridge, 10-70°N. Values shown are moving averages (such that each point is used twice) of

12 adjacent data points from lithosphere of age 0-100 My. See the text for data reduction procedures. The location of the Iceland and Azores hotspots are indicated.

(b) Age-corrected SS-S travel time residual versus latitude along the Mid-Atlantic Ridge, 10-70°N. The residuals shown are moving averages of 10 adjacent data points from lithosphere of age 0-100 My.

Figure 3.10. Geotherms at several different lithospheric ages predicted by the plate cooling model of *Parsons and Sclater* [1977]. Solidus for peridotite (dashed line) after *Takahashi* [1986].

Figure 3.11. SS-S differential travel time residual versus plate age, as predicted by the plate cooling model at a number of discrete ages. Linear regression yields a slope of -0.64 ± 0.01 s/ $My^{1/2}$ for a 0-100-My age range (solid line). Note that a 50-My age corresponds to zero residual by convention.

Figure 3.12. Observed (solid circles, with error bars) and predicted (triangles and squares) δt^* values versus age. Triangles show δt^* values for the lithospheric portion of the SS wave path calculated assuming plate cooling geotherms, the *Takahashi* [1986] peridotite solidus, and the Q-temperature relation of *Sato and Sacks* [1989]. Squares indicate δt^* values for entire upper mantle (0-500 km) portion of the SS wave path from nonlinear iterative inversion of the observed δt^* versus age data for the constants A and E in the Q-temperature relation $Q^{-1} = A^{-1} \exp [-E / RT(z)]$. This relation is assumed to hold over 0-125 km depth; a constant Q of 130 is assumed for 125-500 km depth.

Figure 3.13. (a) Q_S versus depth ($\log_{10}$ scale) at a lithospheric age of 20 My, calculated from nonlinear least squares inversion of observed δt^* versus age assuming different parameterizations of Q in terms of temperature and pressure (dashed lines), and from forward modelling with the *Sato and Sacks* [1989] Q-temperature relation (solid line). Middle dashed line, $Q^{-1} = 0.6 \exp [-35/RT(z)]$. Short dashed line, $Q^{-1} = 0.35 \exp [-2.05 T_m(z)/T(z)]$. Long dashed line, $Q^{-1} = [2.0 + P(z)]^{-1} \exp [-1.7 T_m(z)/T(z)]$.
(b) Same as (a) but at 73 My age.

Figure 3.14. Observed (solid line) and predicted (dashed lines) δt^* along the Mid-Atlantic Ridge, 10-70°N. "Observed" profile is actually a filtered version of the observations, containing only the wavelengths 1400 to 7100 km for comparison with the along-axis pattern of temperature variations inferred from a joint inversion of travel-time residuals, geoid heights, and residual bathymetry [*Sheehan and Solomon*, 1991; Chapter 2]. The predicted δt^* profiles are calculated assuming one of the Q^{-1}-temperature relations derived in this study ($Q^{-1} = A^{-1} \exp [-E/RT]$) and the upper mantle temperature variations from models of *Sheehan and Solomon* [1991]; see also Chapter 2. Two of the predicted profiles were calculated using the temperature profiles [*Sheehan and Solomon*, 1991; Chapter 2] for models with temperature variations constrained first to be in the upper 150 km, then in the upper 300 km; the viscosity structure includes a high viscosity lid over a constant-viscosity mantle. The other predicted profiles were calculated from the temperature variations of *Sheehan and Solomon*

[1991] in which a joint inversion is performed for variations in both temperature and composition in the upper 150 km, and then upper 300 km for the same viscosity model. Mean values have been subtracted from both the observed and model profiles.

Figure 3.15. Observed (solid line) and predicted (dashed lines) δt^* along the Mid-Atlantic Ridge, 10-70°N. The predicted δt^* profiles are calculated assuming the *Sato and Sacks* [1989] Q-temperature relation (equation 3.10) and the upper mantle temperature variations from models of *Sheehan and Solomon* [1991]; see also Chapter 2. Two of the predicted profiles were calculated using the temperature profiles [*Sheehan and Solomon*, 1991; Chapter 2] for models with temperature variations constrained to be in the upper 150 km, then in the upper 300 km; the viscosity structure includes a high viscosity lid over a constant-viscosity mantle. The other predicted profiles were calculated from the temperature variations of *Sheehan and Solomon* [1991] in which a joint inversion is performed for variations in both temperature and composition in the upper 150 km, and then upper 300 km for the same viscosity model.

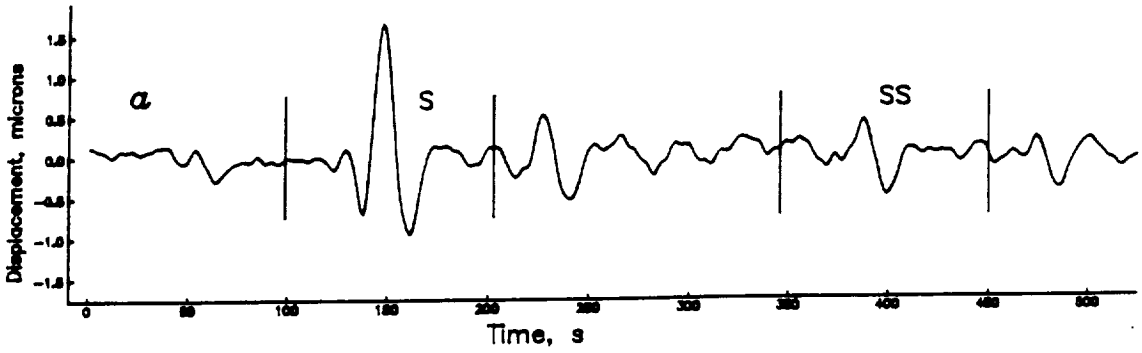

Figure 3.1a

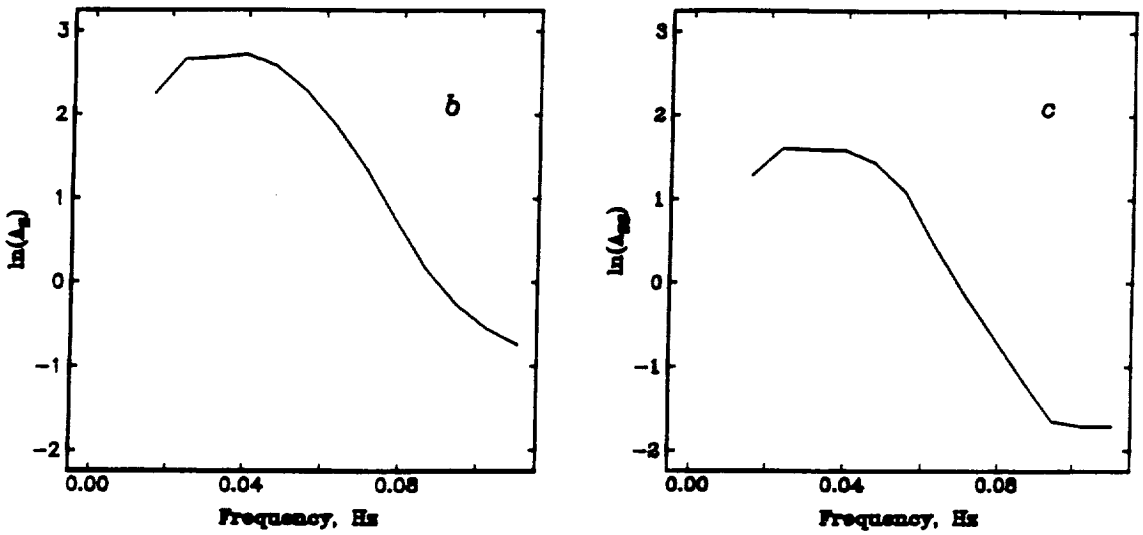

Figure 3.1bc

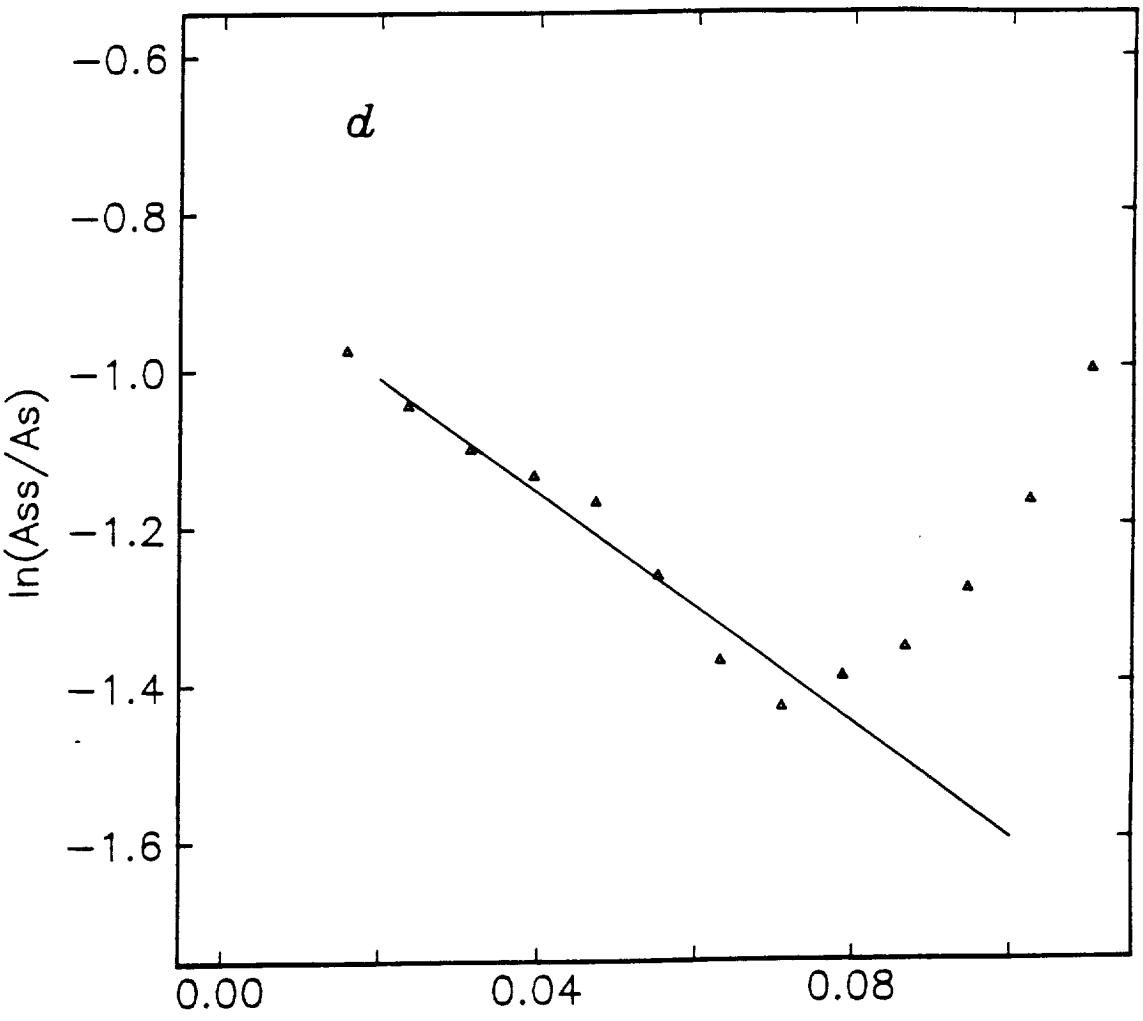

Figure 3.1d

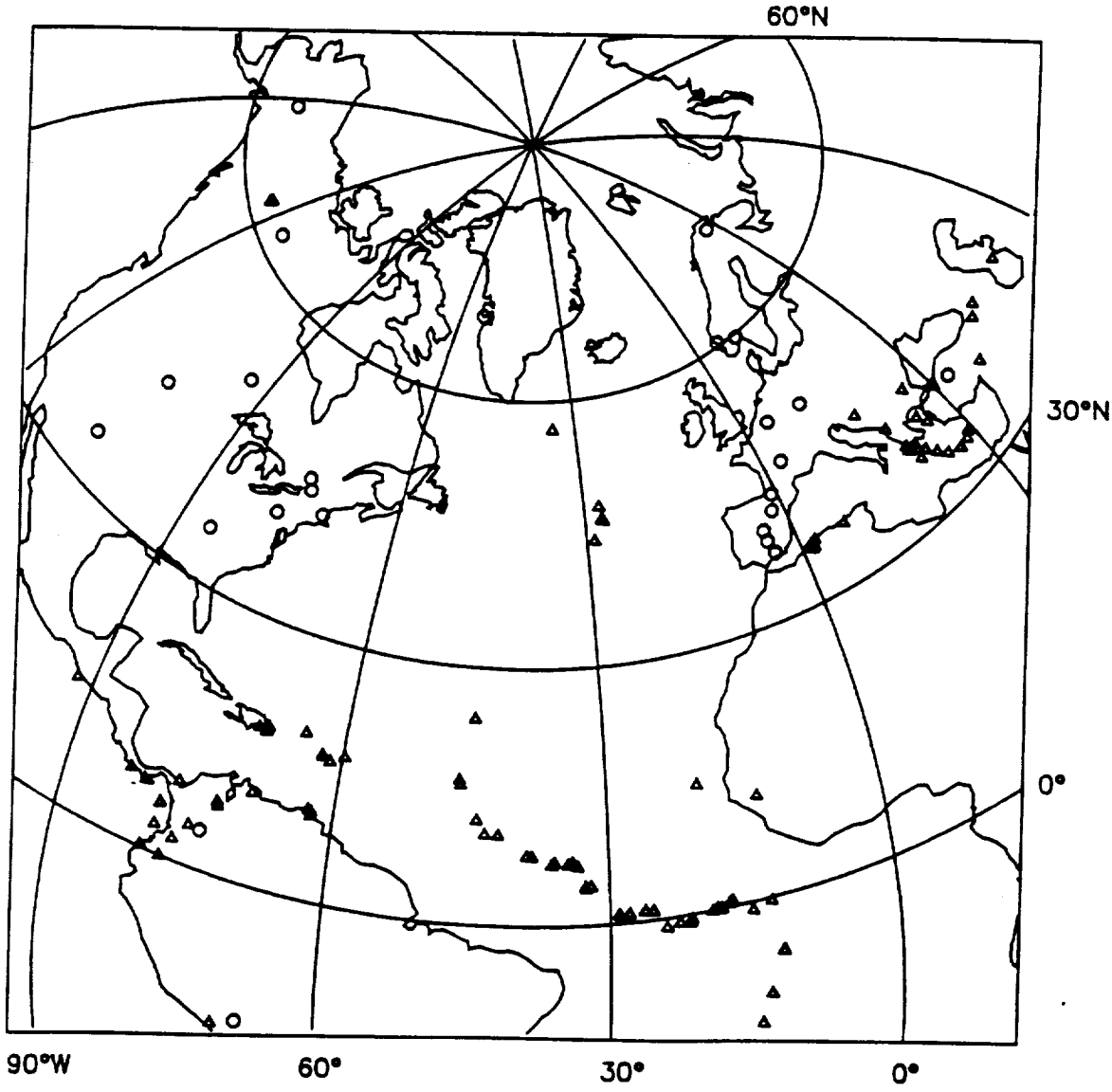

Figure 3.2

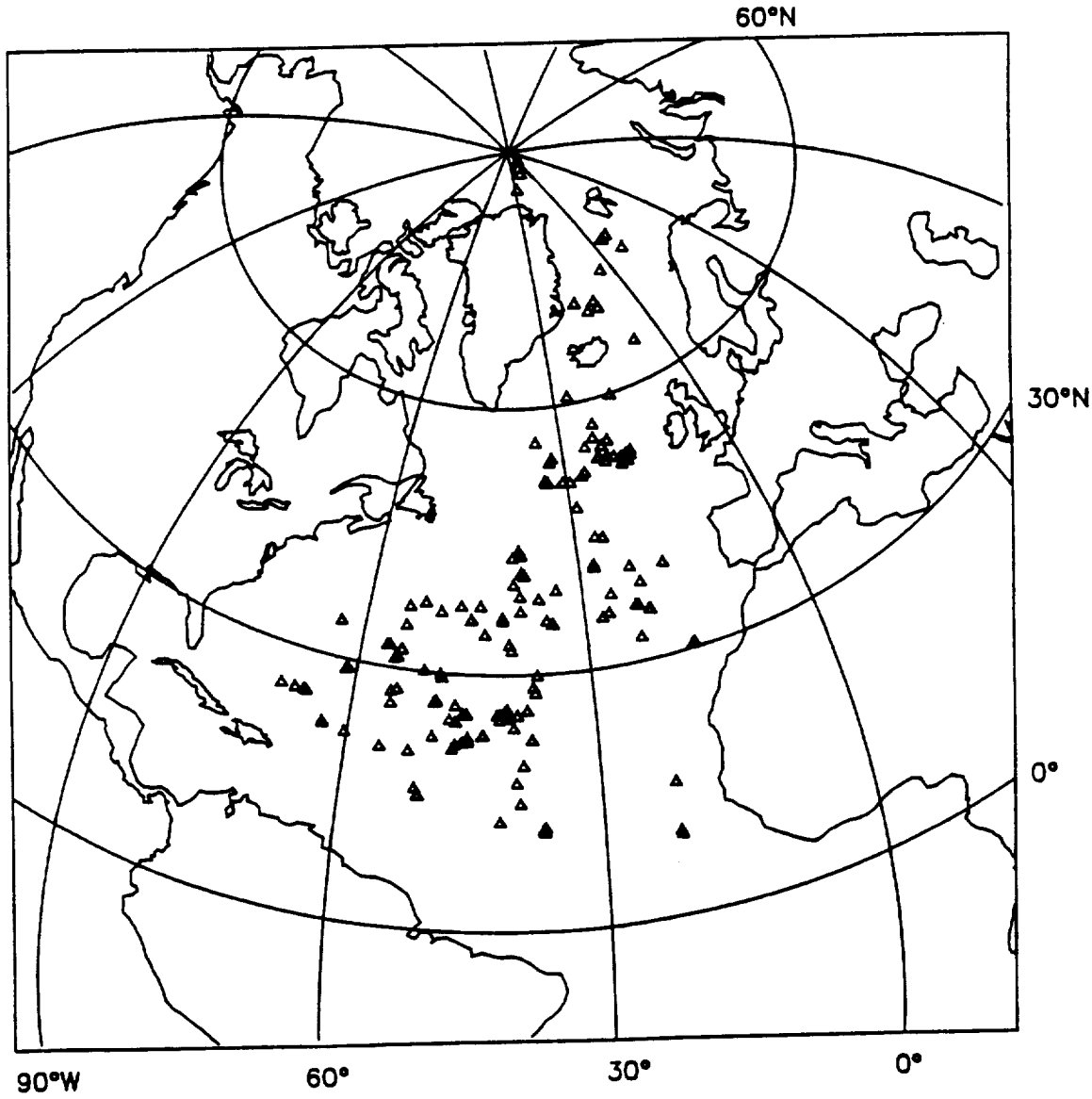

Figure 3.3

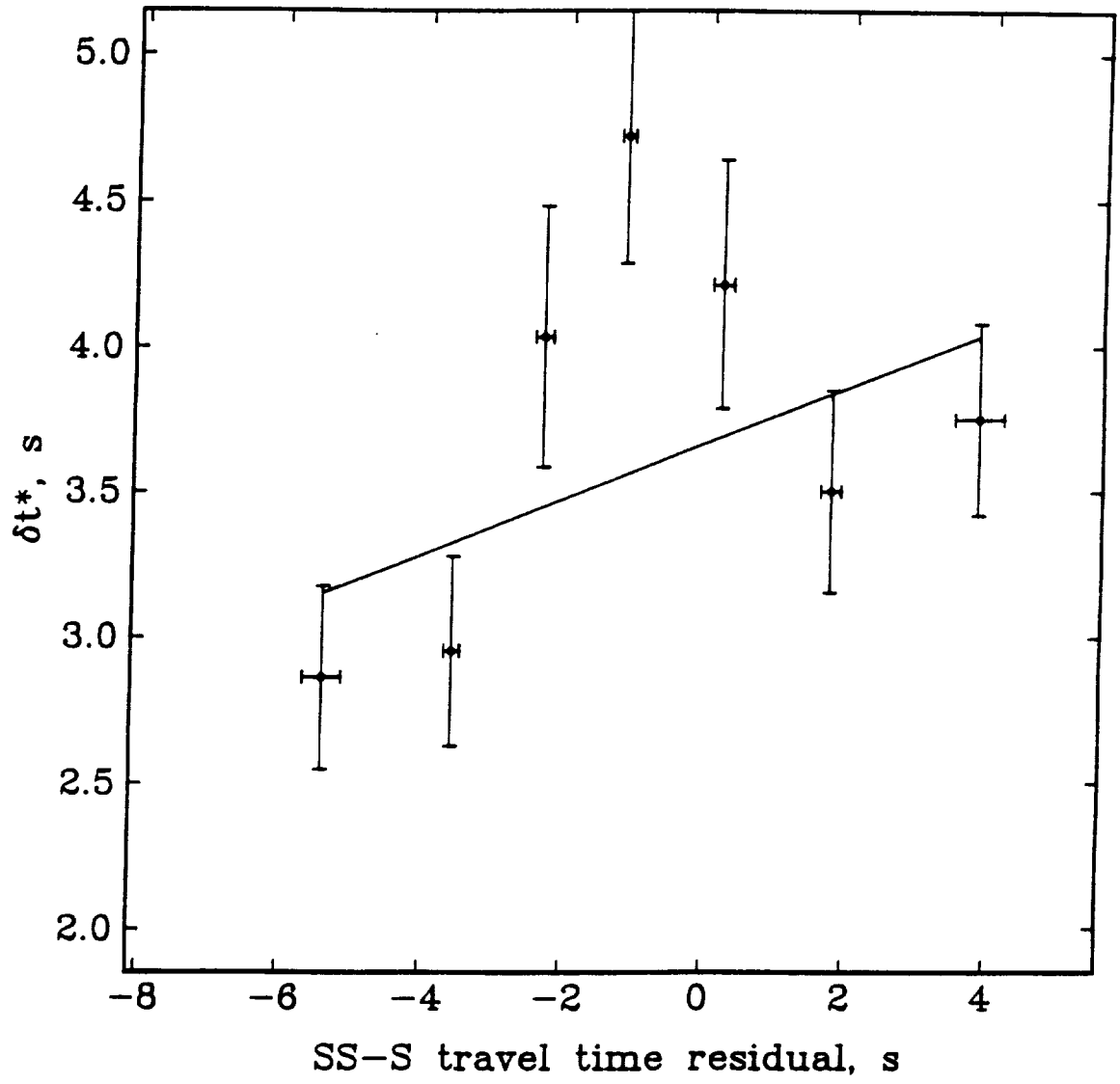

Figure 3.4

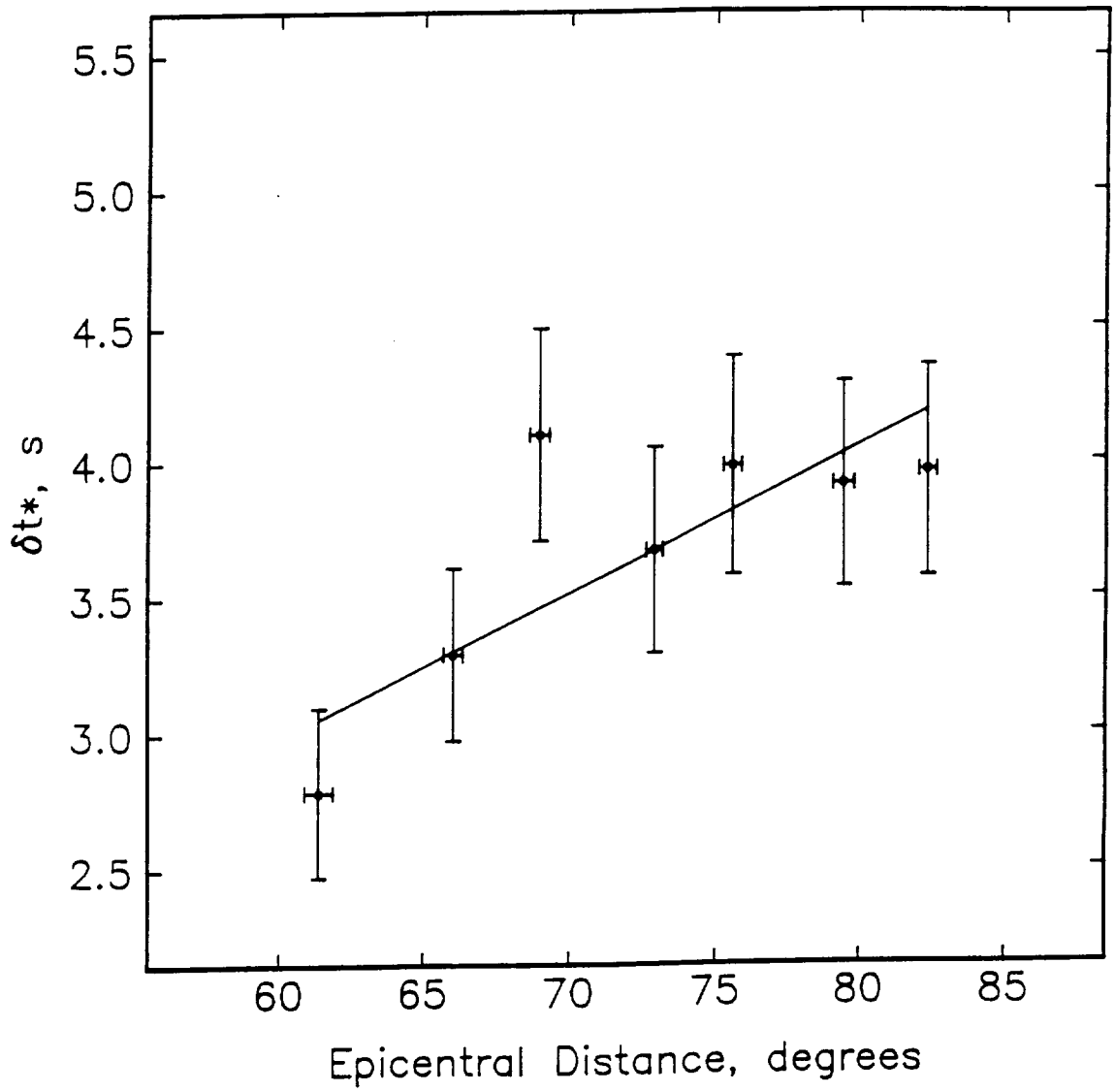
5.5
5.0
4.5
4.0
3.5
3.0
2.5
δt*, s
60
65
70
75
80
85
Epicentral Distance, degrees

Figure 3.5

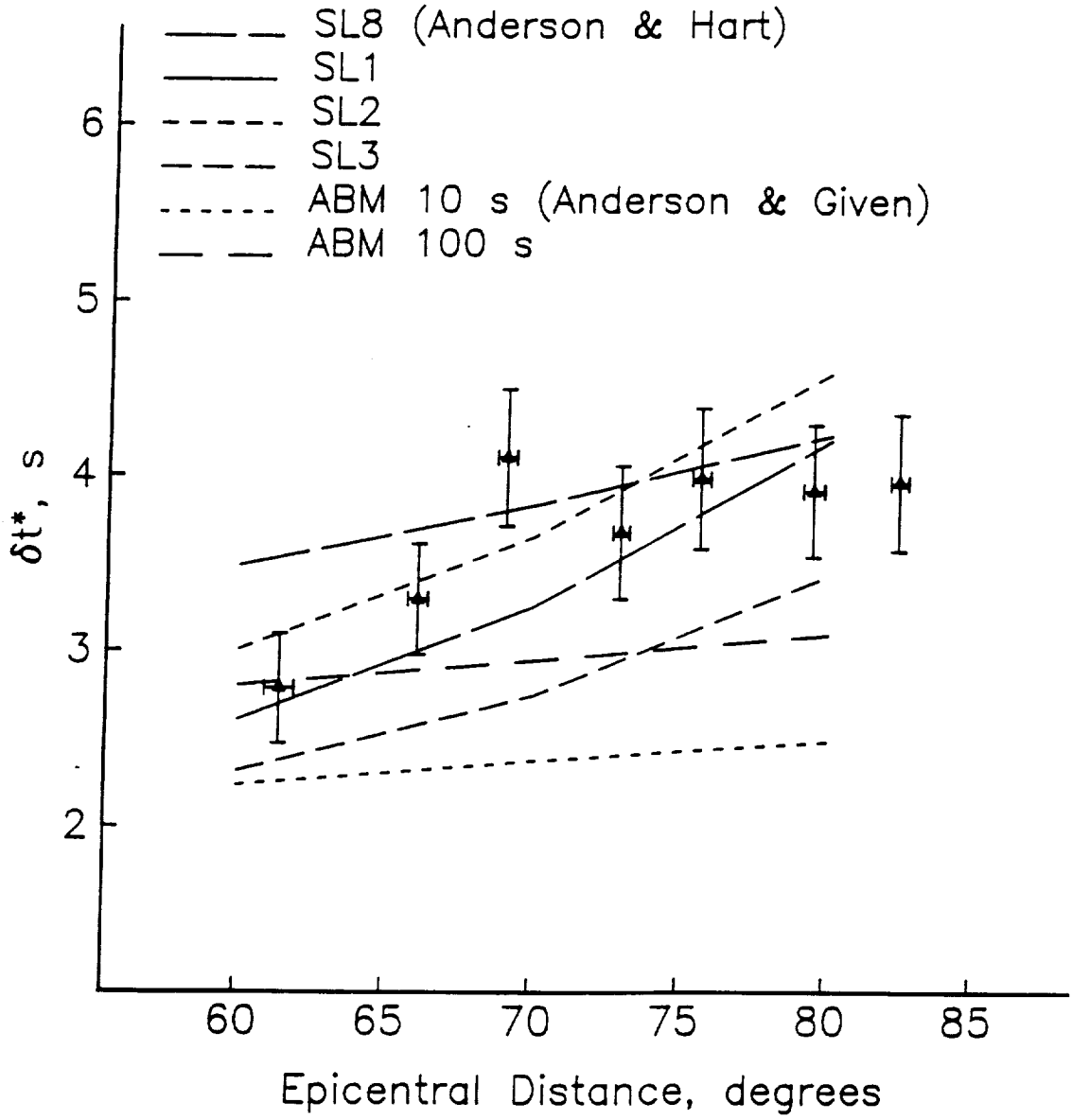
SL8 (Anderson & Hart)
SL1
SL2
SL3
ABM 10 s (Anderson & Given)
ABM 100 s
δt*, s
2
3
4
5
6
60
65
70
75
80
85
Epicentral Distance, degrees

Figure 3.6

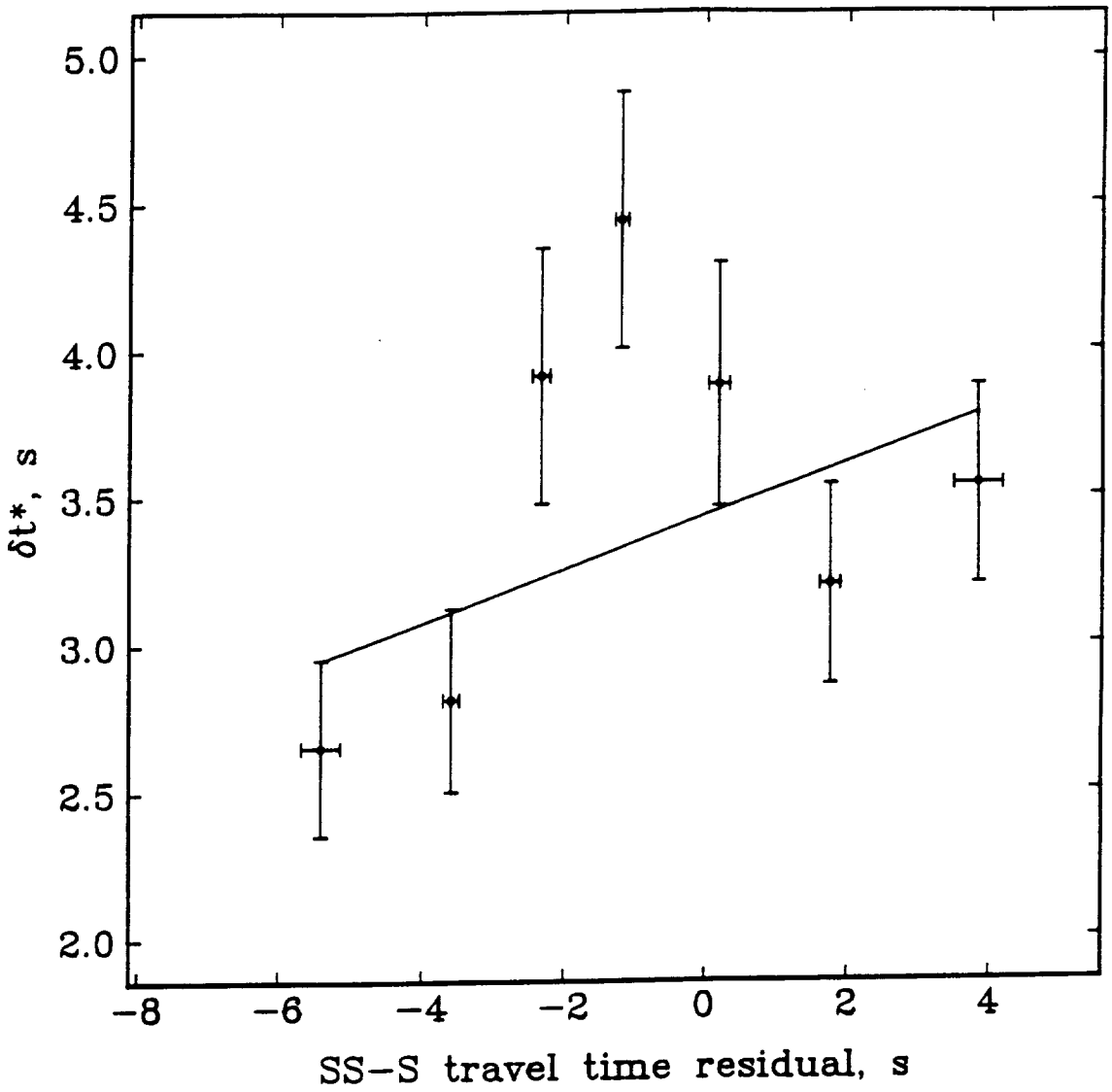

Figure 3.7

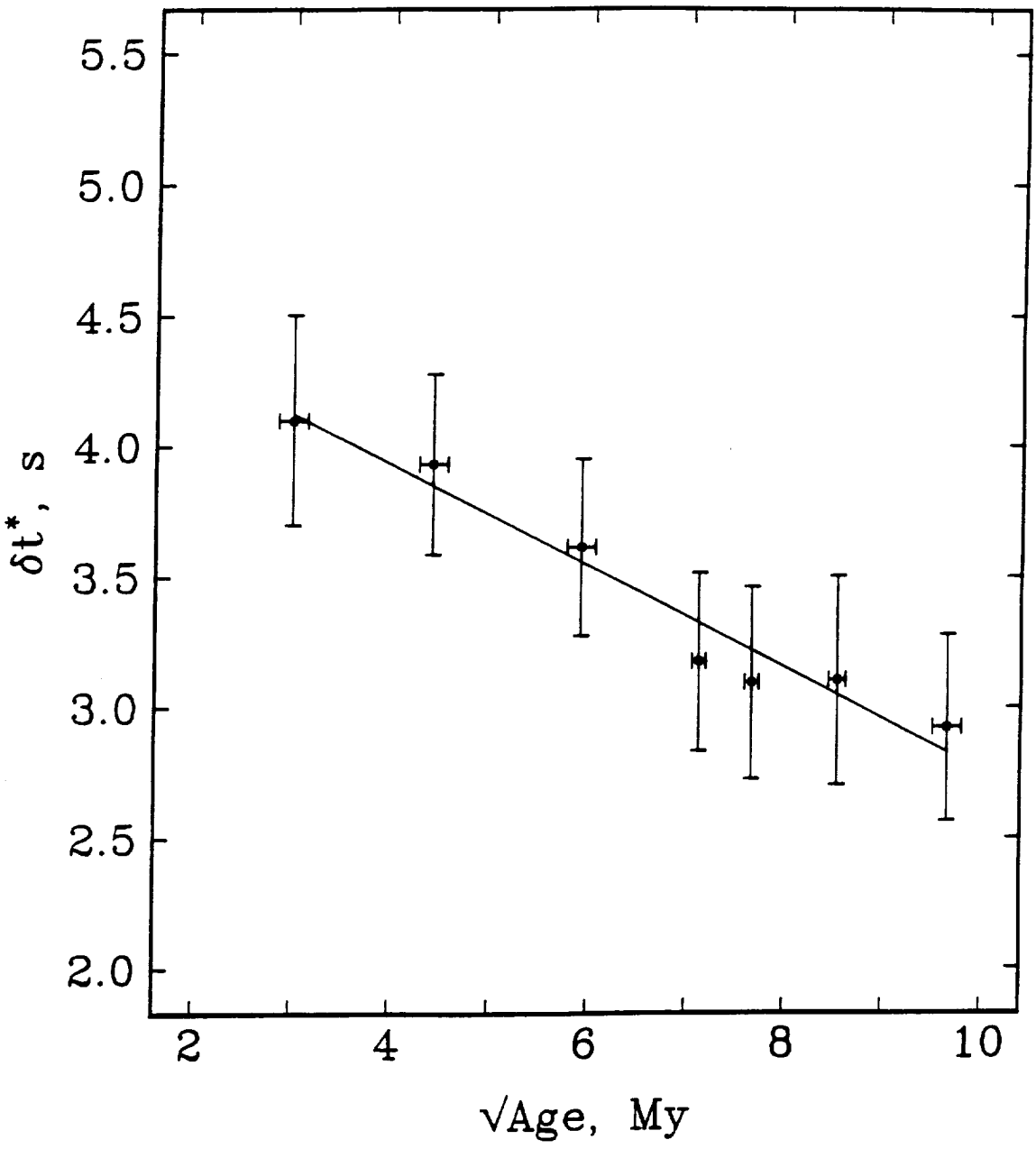

Figure 3.8a

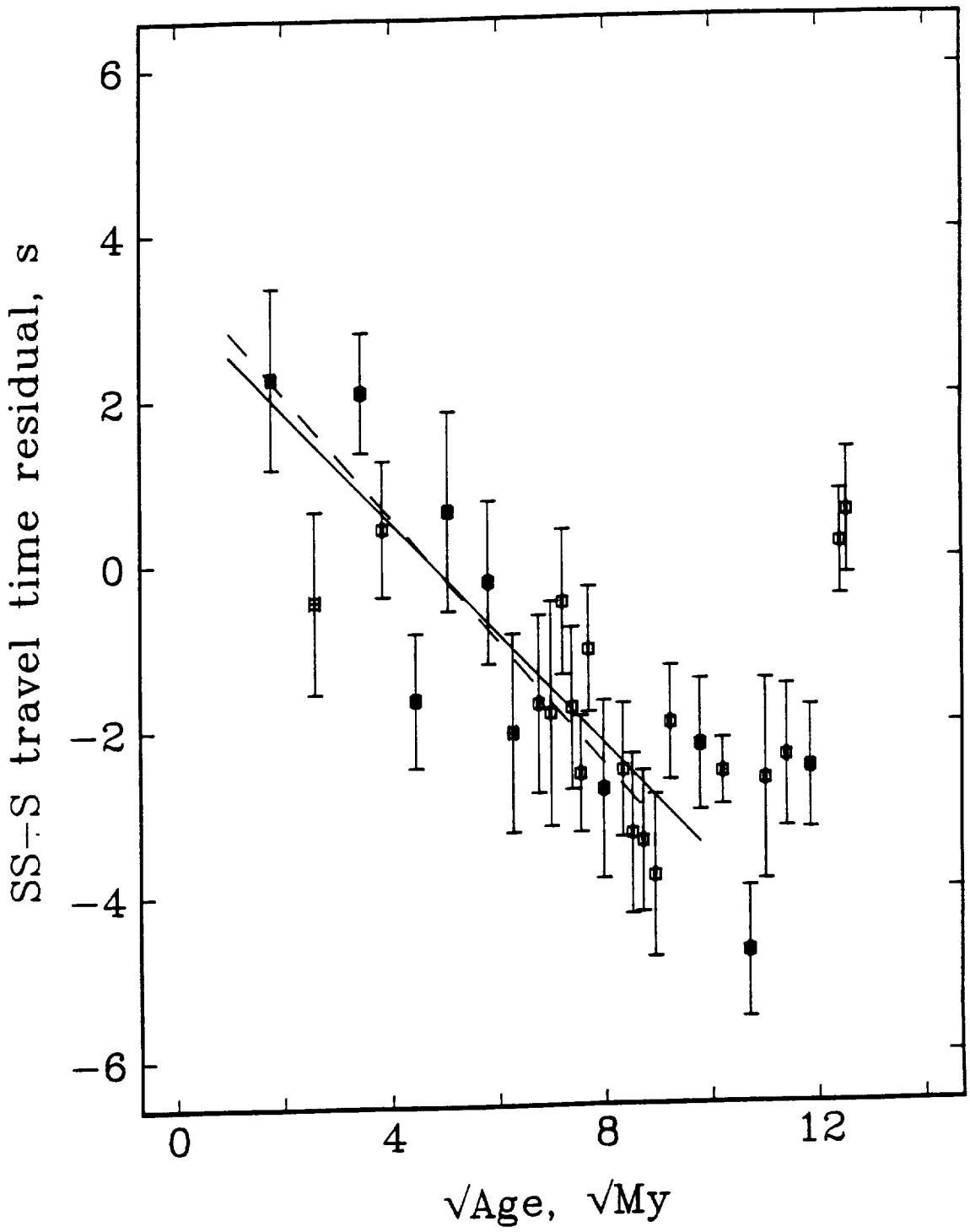

Figure 3.8b

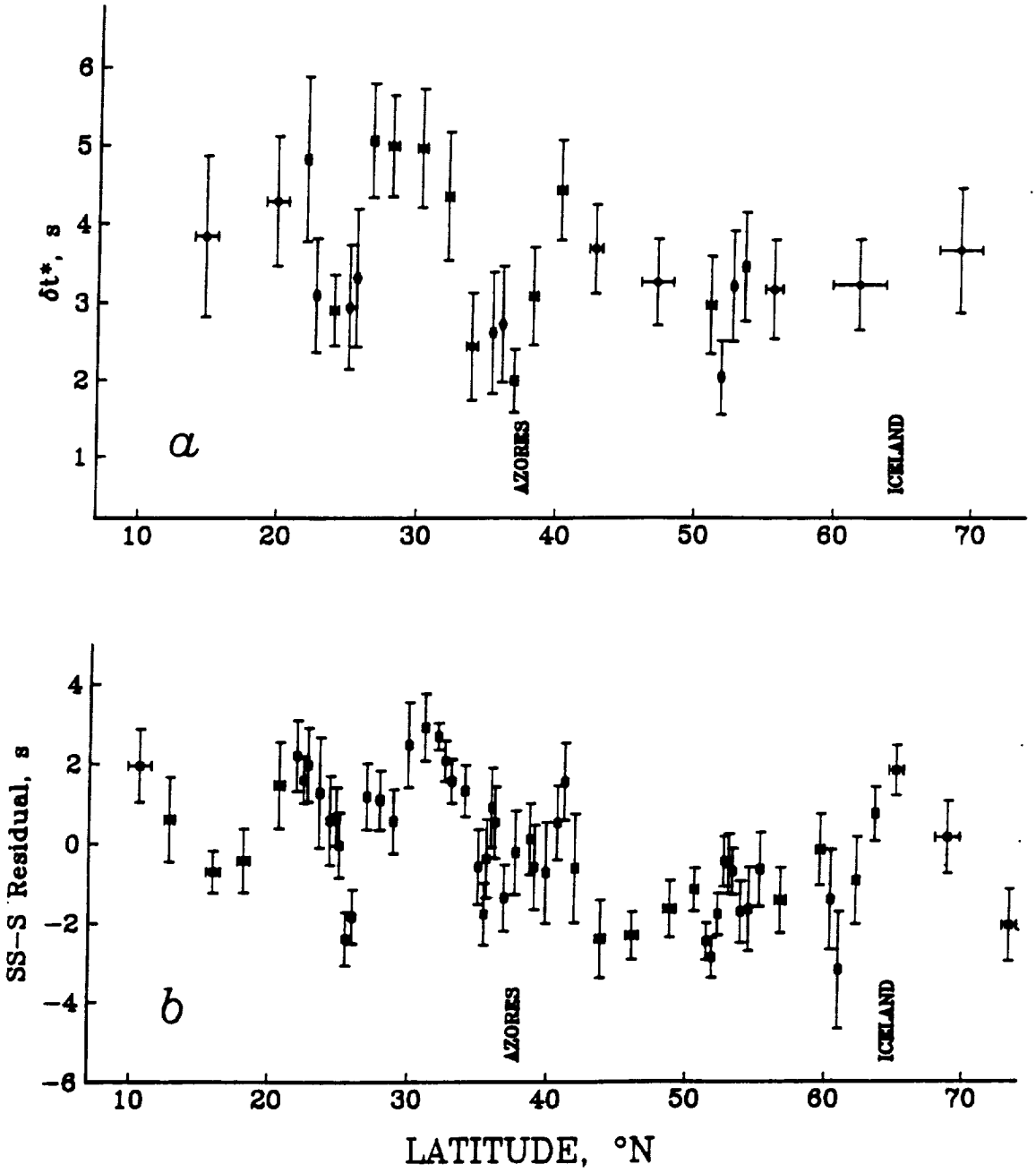
δt*, s
a
AZORES
ICELAND
SS−S Residual, s
b
AZORES
ICELAND
LATITUDE, °N

Figure 3.9

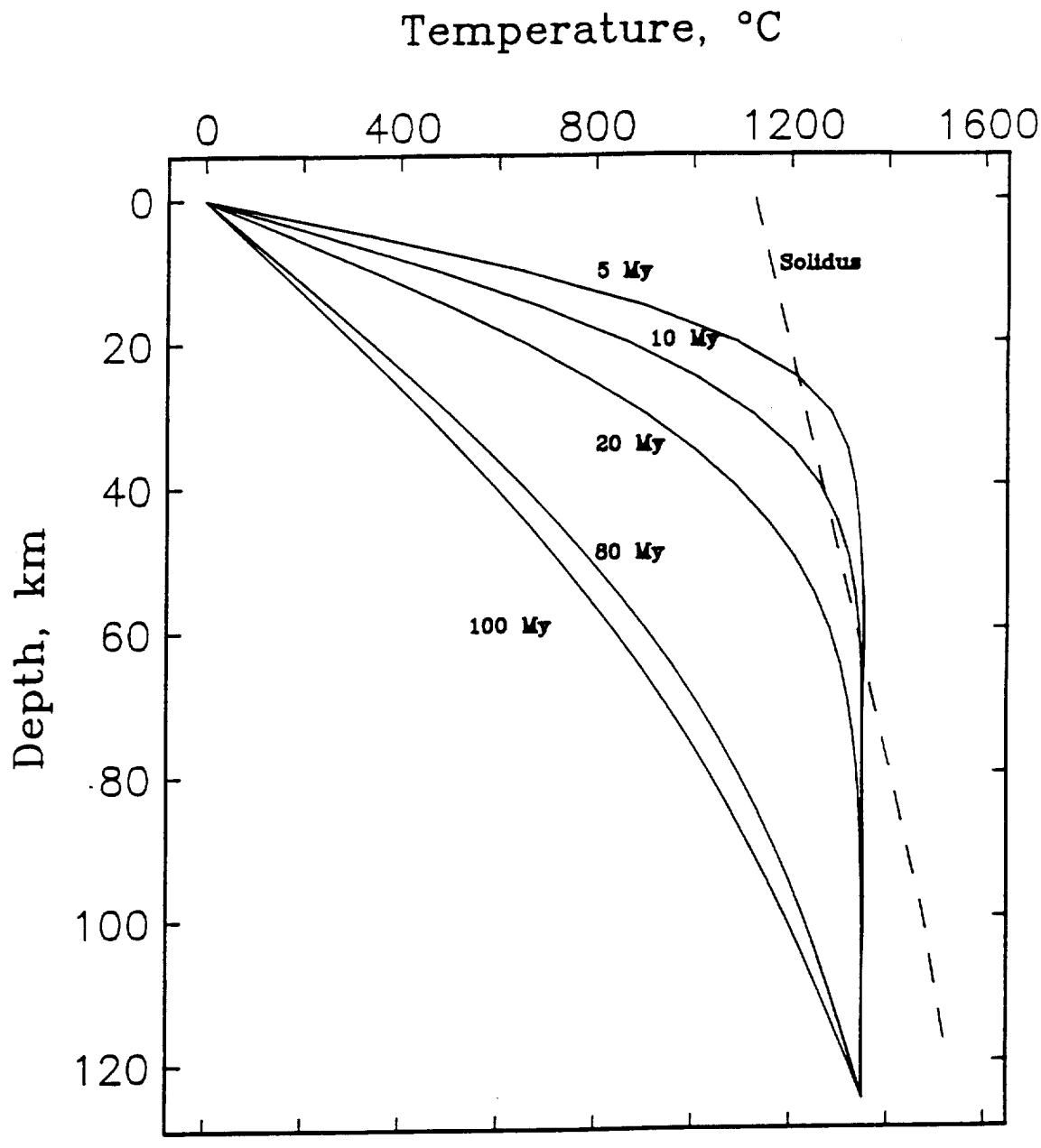
Temperature, °C
0
400
800
1200
1600
Depth, km
0
20
40
60
80
100
120
5 My
10 My
20 My
80 My
100 My
Solidus

Figure 3.10

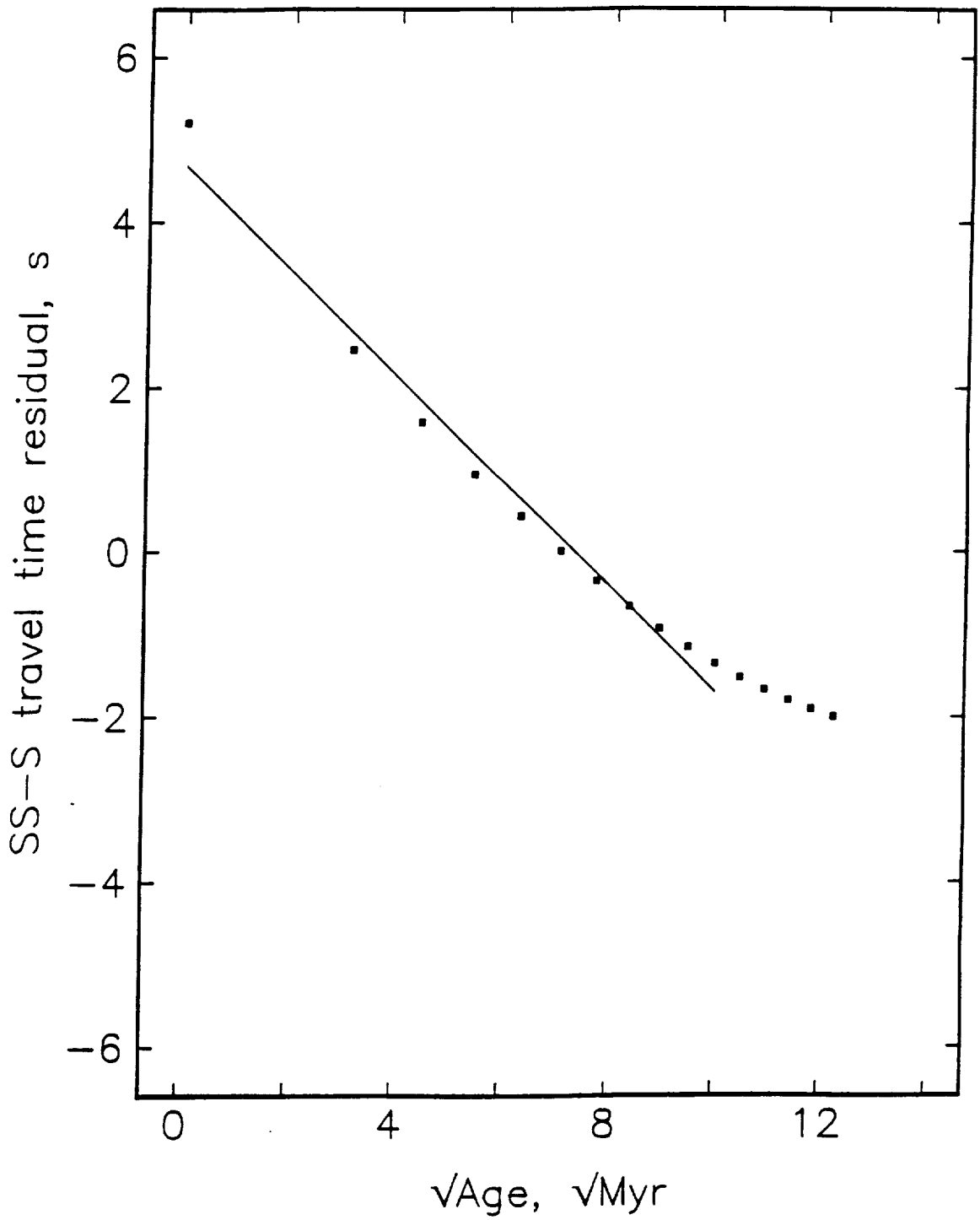

Figure 3.11

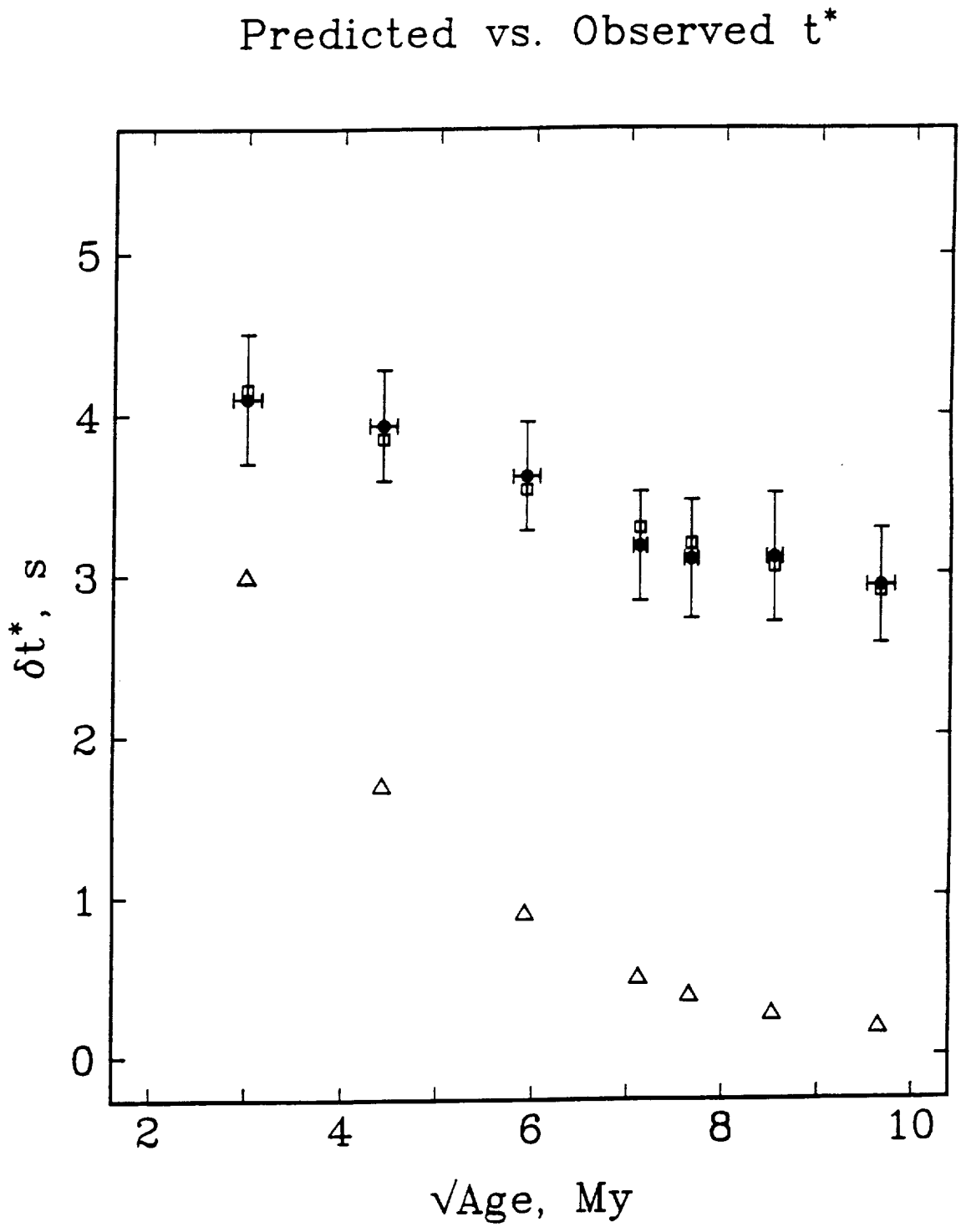

Figure 3.12

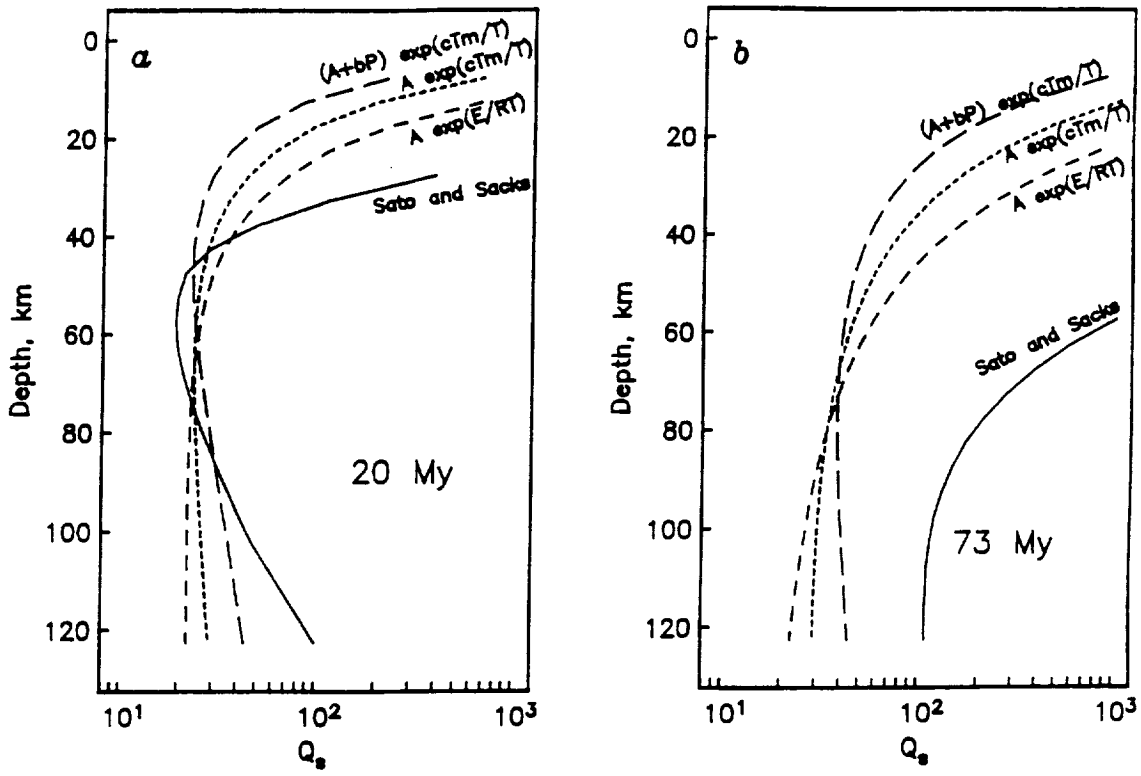
a
(A+bP) exp(cTm/T)
A exp(cTm/T)
A exp(E/RT)
Sato and Sacks
20 My
Depth, km
0
20
40
60
80
100
120
10^1
10^2
10^3
Q_s
b
(A+bP) exp(cTm/T)
A exp(cTm/T)
A exp(E/RT)
Sato and Sacks
73 My
Depth, km
Q_s

Figure 3.13

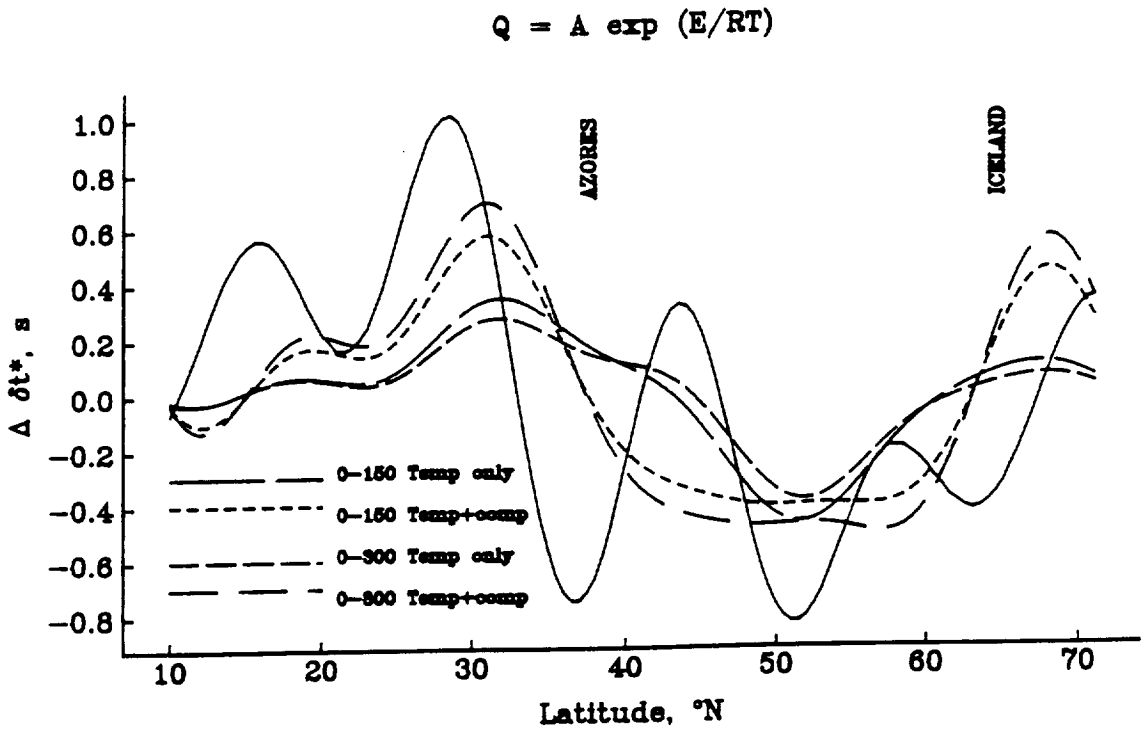
Q = A exp (E/RT)
AZORES
ICELAND
Δ δt*, s
1.0
0.8
0.6
0.4
0.2
0.0
−0.2
−0.4
−0.6
−0.8
0–150 Temp only
0–150 Temp+comp
0–300 Temp only
0–300 Temp+comp
10
20
30
40
50
60
70
Latitude, °N

Figure 3.14

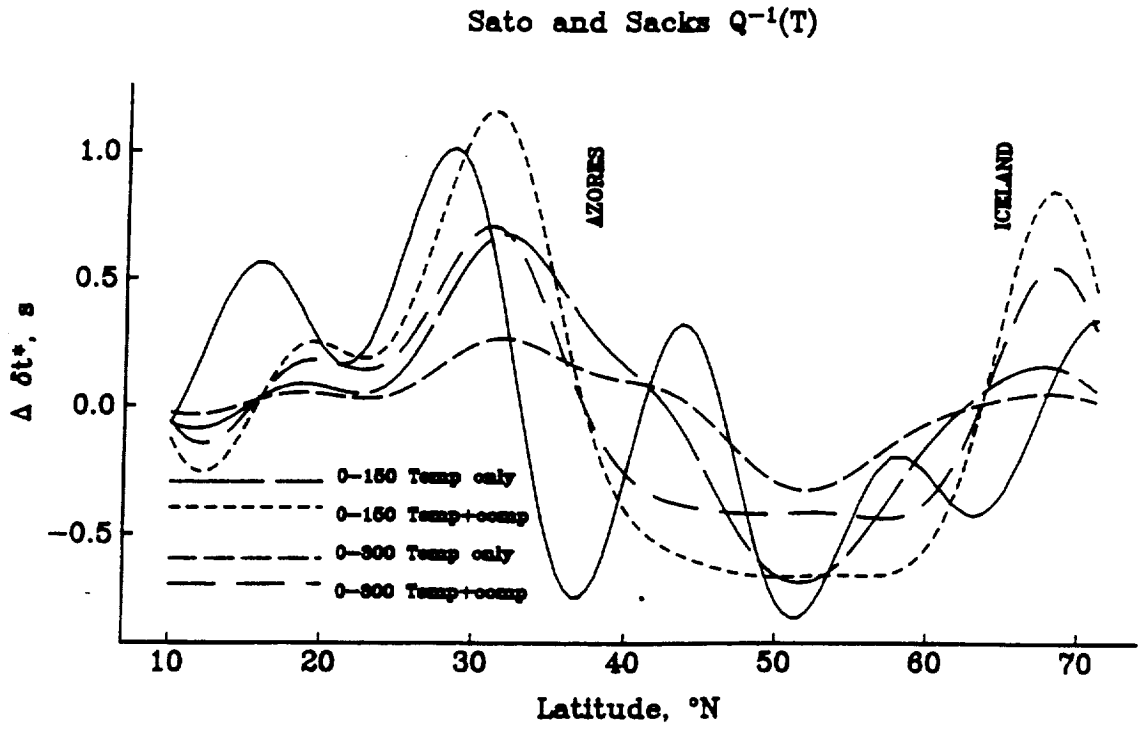
Sato and Sacks $Q^{-1}(T)$
1.0
0.5
0.0
−0.5
Δ δt*, s
AZORES
ICELAND
0–150 Temp only
0–150 Temp+comp
0–300 Temp only
0–300 Temp+comp
10
20
30
40
50
60
70
Latitude, °N

Figure 3.15

CHAPTER 4

UPPER MANTLE STRUCTURE IN THE VICINITY OF THE EAST PACIFIC RISE INFERRED FROM SHEAR WAVE DIFFERENTIAL TRAVEL TIMES, GEOID, AND BATHYMETRY

INTRODUCTION

The formation and evolution of the lithosphere and the interaction of mantle convection with the surface plates can, in principle, be constrained by the determination of variations in shear wave velocity in the upper mantle. Oceanic regions, and in particular, mid-ocean ridge systems, are most amenable to examination of the processes which drive the plates due to their simple crustal structure and young age relative to the continents. In this chapter we investigate lateral variations in the velocity structure beneath the East Pacific Rise by measuring differential travel times for the phase pair SS-S, and relate these variations in travel time to depth and geoid anomalies in the region. Body wave methods are well suited for resolving lateral variations in upper mantle structure at relatively short (<1000 km) wavelengths. Differential travel times of shear wave phase pairs, in particular, are an effective tool in the study of upper mantle heterogeneity [*Sipkin and Jordan*, 1976, 1980a; *Stark and Forsyth*, 1983; *Butler*, 1979; *Kuo et al.*, 1987; *Woodward and Masters*, 1991; *Sheehan and Solomon*, 1991] and have the advantage that source and receiver effects are approximately common to both phases and are thus largely eliminated by differencing. In addition, use of differential travel times eliminates any

absolute timing errors. Differential times also have the ability to constrain structural variations in regions of the world where there are no sources or receivers. Under the assumptions that the lower mantle is relatively homogeneous and that the paths in the upper mantle are reasonably steep, the differential travel time anomaly can be associated with upper mantle structure in the vicinity of the surface bounce point of the reflected (SS) phase.

A number of previous studies have brought important contributions to our understanding of upper mantle properties of the eastern Pacific. Surface wave dispersion studies in the Pacific Ocean region [e.g., *Leeds*, 1975, *Forsyth*, 1975, *Yu and Mitchell*, 1979; *Nishimura and Forsyth*, 1985, 1988, 1989; *Zhang and Tanimoto*, 1990b] show a clear relationship between the age of the seafloor and the seismic properties of the mantle. *Woodward and Masters* [1991], in a global study of SS-S and PP-P differential travel times, found the east Pacific region to be particularly slow. In the present study, we use shear wave differential travel time residuals, in combination with geoid and bathymetry data, to elucidate further the structure of the east Pacific region. Our data set allows us to search for velocity anomalies associated with the East Pacific Rise and with the Galapagos Spreading Center and Galapagos hotspot. In addition, we can compare the results from this intermediate to fast spreading ridge system with our earlier study of the northern Mid-Atlantic Ridge, a slow spreading ridge system [*Sheehan and Solomon*, 1991]. Several authors [e.g., *Stark and Forsyth*, 1983; *Zhang and Tanimoto*, 1990b, *Woodward and Masters*, 1991] have found that shear wave velocities in the east Pacific are significantly slower than those observed in either the Atlantic or Indian Oceans. In addition, the presence of anisotropy has been found to be more pronounced in the Pacific upper mantle than in the Atlantic upper mantle [*Montagner and Tanimoto*, 1990] as is predicted by models for flow-induced orientation of mantle olivine crystals [*McKenzie*, 1979; *Ribe*, 1989]. *Woodward and Masters* [1991] found that their Pacific data were consistent with

the presence of weak anisotropy, although they suggested that lateral heterogeneity could also have produced the observed azimuthal pattern. They did not resolve significant azimuthal variations in the Atlantic portion of their data set.

Our analysis technique, developed in Chapter 2, involves the use of shear wave differential travel time residuals in combination with geoid and bathymetry data . The combination of geoid (or gravity) data with seismic data is an effective way to determine Earth structure on scales ranging from global [*Hager and Richards*, 1989; *McNutt and Judge*, 1990] to local [*Lines et al.*, 1988; *Lees and VanDecar*, 1991]. Several authors [*Watts et al.*, 1985; *Haxby and Weissel*, 1986] have suggested that bathymetry and especially gravity (or geoid) data in the central and east Pacific regions show evidence for small-scale (wavelength of a few hundred kilometers) convection. With our combined data set and analysis we can search for evidence of small scale convection with the added constraint of shear wave travel times.

GEOLOGIC SETTING

The East Pacific Rise lies to the west of Central and South America and stretches over 6000 km from the Juan Fernandez triple junction at 34°S to the Gulf of California. Segments of the East Pacific Rise spread at rates as high as 162 mm/yr (full spreading rate) at about 20°S (Figure 4.1). In comparison, spreading rates on the Mid-Atlantic Ridge range from just 5 to 40 mm/yr. The East Pacific Rise separates the large Pacific plate on the west from the Nazca and Cocos plates on the east. The triple junction between these three plates lies at 2°N, 102°W. The Cocos plate is bounded on the west by the East Pacific Rise, on the south by the Galapagos Spreading Center, and on the northeast by the Middle America Trench. The Cocos plate includes the aseismic Cocos Ridge, which trends NNE from 1°N, 90°W to 7°N, 84°W. A related feature is the Carnegie Ridge on

the Nazca Plate from 0°N, 90°W to 0°N, 82°W. A rough-smooth bathymetric boundary is located at a distance of about 250 km to the west of the Cocos and Carnegie Ridges. The Cocos plate is shallower and its gravity is higher than that predicted by plate cooling models [*Parsons and Sclater*, 1977; *Parsons and Richter*, 1980]. Spreading rates on the north-south spreading Galapagos Spreading Center average around 70 mm/yr [*Macdonald*, 1989]. The Galapagos hotspot, just south of the Galapagos Spreading Center at about 100°W longitude, is a site of active volcanism. *Monnereau and Cazenave* [1988] found that the geoid-to-topography ratio in the region of this hotspot is not consistent with that found for swells in the center of a plate. They attributed this difference to the proximity of the Galapagos hotspot to the Galapagos Spreading Center.

DATA

Travel Time Data

The east Pacific was chosen as the study area because the very high spreading rates on the East Pacific Rise offer an interesting complement to our study of the slow-spreading Mid-Atlantic Ridge (Chapter 2) and because there is a convenient distribution of earthquake sources and digital seismic stations to allow for a sufficiently dense sampling of SS bounce points. We performed a search over all earthquakes in the Harvard centroid moment tensor (CMT) catalog for the years 1980-1987 [*Dziewonski et al.*, 1981; *Dziewonski and Woodhouse*, 1983] supplemented by a listing of intraplate earthquakes not included in the CMT catalog (E. A. Bergman, personal communication, 1991) and over all GDSN digital seismic stations in order to find event-station pairs of the proper epicentral distance which provide SS bounce points in the East Pacific Rise region. Searches were also performed to find event-station pairs recoverable using the GEOSCOPE broadband stations in the time periods for which we have data (January to

December of 1986 and January to May of 1988). The range in source-receiver separation was taken to be 55° to 86° to ensure separation of S and ScS at the longer distances and to avoid triplication in SS at shorter distances. A list of stations used in this study is presented in Table 4.1. We use only transversely polarized (SH) seismograms (rotated from N-S and E-W components) to avoid interference from the SKS phase and contamination from P-SV conversions at the base of the crust and other near-surface discontinuities. Epicenters were obtained from the "Preliminary Determination of Epicenters" of the U.S. National Earthquake Information Service (NEIS) for all events. The final distribution of sources and stations used to measure SS-S differential travel times is shown in Figure 4.2. Our study area extends from 25°S to 30°N latitude and 140°W to 80°W longitude, and includes a dense sampling of the Cocos plate. The majority of data in this study comes from records of southern East Pacific Rise, Chile Rise, and Peru-Chile subduction zone earthquakes recorded at North American stations. Other data include Peru-Chile and Middle America trench events recorded at Hawaiian stations, Hawaiian events and events from western North America recorded at South American stations (BOCO and ZOBO), Central and North American earthquakes recorded at the DWWSSN station AFI (Afiamalu, Western Samoa), intraplate events on the Nazca plate propagating to North America and Hawaii, and central Pacific intraplate events propagating to North American stations.

This search yielded over 1500 event-station pairs with the proper epicentral separation. Data with SS bounce points on regions of thick sediments (> 0.5 km) and thick crust off the coast of Central America [*Ludwig and Houtz*, 1979; *Winterer*, 1989] were omitted. After winnowing the list because of station inoperation, poor signal to noise ratio for the phases of interest, and interfering events, the final data set consists of over 600 SS-S differential travel time residuals with bounce points in the east Pacific (Figure 4.3). A total of 21 digital stations (Table 4.1) and 342 different earthquakes

(Table 4.2) were used in the final analysis. Uncertainties for each measurement are adopted from the analysis in Chapter 2, Appendix 2.A. A tabulation of all residuals is given in Appendix III.

Bathymetry Data

Bathymetric data are obtained from the corrected Digital Bathymetric Data Base (5' grid) (DBDB5C) [*U.S. Naval Oceanographic Office*, 1985]. DBDB5C data are corrected for the deviation of water column acoustic velocity from the generally assumed value of 1500 m s^{-1}. We obtain an average depth value for each SS surface bounce point by averaging all of the bathymetric data within a 1° x 1° square centered on each point.

The bathymetry of the East Pacific Rise region is shown in Figure 4.3. The rise axis is marked by depths generally shallower than 3000 m. To the west of the rise the seafloor depth gradually increases with increasing age of the seafloor. At the western edge of the map the depth is about 5000 m. To the east of the East Pacific Rise, however, the bathymetry does not closely follow simple depth-age relations and is complicated by the presence of the Galapagos hotspot and by the Middle America subduction zone. The depth along the crest of the Galapagos Spreading Center, about 2500 m, is generally shallower than that of the East Pacific Rise.

Geoid Data

Geoid data are taken from a combined set of Seasat and GEOS3 altimeter data [*Marsh et al.*, 1986]. The sea surface elevations are referenced to the IUGG 1980 Geodetic Reference System defined by an Earth semimajor axis of 6,378,137 m and a flattening coefficient of 1/298.257 [*Moritz*, 1980]. The mean sea surface is presented in the form of a 0.25° grid. The data have been corrected for orbit errors, instrument and atmospheric propagation effects, and solid Earth and ocean tides. Since we are only

interested in signatures related to upper mantle processes, we attempt to remove from the data all other effects. Therefore, we retain only the components of the field with wavelengths less than about 6000 km by subtracting the observed field up to degree and order 7 assuming the GEM-T2 coefficients [*Marsh et al.*, 1990] for the spherical harmonic expansion of the Earth's geoid and tapering the spectrum to degree and order 11 to avoid truncation effects [*Sandwell and Renkin*, 1988] (Figure 4.4). The geoid field over the East Pacific Rise and Cocos plate is characterized by positive anomalies over the East Pacific Rise that fall off gradually with increasing plate age to the west. To the east of the rise, however, the geoid does not follow the simple relation predicted by the plate cooling model [*Parsons and Richter*, 1980] but rather is characterized by positive values over much of the Cocos plate and a large positive anomaly presumably related to the slab subducting under Central America [*Hager*, 1984]. The Galapagos hotspot is marked by a short (400 km) wavelength geoid high superimposed on a northwest-southeast-trending regional field with a low of -4 m.

METHOD

Data processing procedures and the waveform cross-correlation technique for estimating differential travel time are as in Chapter 2.

RESULTS

Spatial Pattern of SS-S Residuals

The SS-S residuals are shown plotted at the SS bounce point in Figure 4.5. Much scatter is observed, and a clear signal associated with the rise is not obvious. The residuals far to the west of the rise (from longitude 130° to 140°W) are more negative

(earlier SS) than the residuals in close vicinity to the rise, but a gradual decrease from slow at the rise to fast off the rise is not apparent. Residuals to the south of the Galapagos Spreading Center tend to be less by 1 or 2 s than those from bounce points to the north of the Galapagos Spreading Center. The values of the SS-S residuals with bounce points on the Cocos plate vary widely, though some coherent patterns emerge. There are groups of early and late residuals with a characteristic wavelength of approximately 1200 km, patterns which are made more obvious when the data are smoothed and gridded. The residuals in the vicinity of the Galapagos hotspot are positive. Positive residuals are also found about 100-200 km to the northeast of the Galapagos hotspot.

Lithospheric Aging

Cooling and thickening of the lithosphere should yield a tendency toward an increase in seismic velocity with increasing lithospheric age. A linear regression experiment was performed to examine the correlation of the SS-S residuals with seafloor age. First a gridded map of seafloor ages was constructed for the East Pacific Rise from a compilation of data from several sources. Gridded age data from the map of *Larson et al.* [1985] were provided by S. C. Cande (personal communication, 1991). Since these data only included the age range of 0 - 6 My in our study area, we had to supplement them with data from other sources. These additional sources included digitized isochrons from *Sclater et al.* [1981] and magnetic anomalies from *Klitgord and Mammerickx* [1982], *Atwater* [1989], and *Atwater and Severinghaus* [1989] and from the tectonic map of the *Circum-Pacific Map Project* [1981]. The magnetic isochrons are assigned ages according to the polarity reversal time scales of *Kent and Gradstein* [1986] and *Berggren et al.* [1985]. Plate age is not well determined on parts of the Cocos plate due to its proximity to the magnetic equator [*Schouten*, 1971], and thus no ages have been assigned to such areas [*Atwater and Severinghaus*, 1989]. We place constraints on seafloor age in such regions lacking

identified isochrons by assuming symmetric spreading and using the ages from isochrons at an equal distance on the opposite side of the rise.

To obtain a reprsentative age value for the region spanning approximately one horizontal wavelength of the incident (SS) wave, an average seafloor age was estimated for a 1° x 1° box centered on each SS bounce point. To reduce scatter, measurements whose bounce point depths differed by more than 1200 m from the depth predicted by the regional depth-age relation were excluded from the age regression.

The SS-S residuals for the East Pacific Rise are shown plotted against the square root of seafloor age in Figure 4.6a. The solid line represents the linear travel time - age$^{1/2}$ relation derived from the data, but the figure indicates that the data are not well fit by a straight line. The age dependence derived in Chapter 2 for the plate cooling model is shown as a dashed line. The predicted slope is consistent with the longest wavelength trends in the data and suggests that perhaps there is an age dependence to the travel times but that several other competing processes are also contributing. The observed SS-S residuals increase from 0 to 2.5 My$^{1/2}$ partly because the Galapagos hotspot region is slow but not on zero-age lithosphere. Large positive residuals at 4.5 My$^{1/2}$ include SS bounce points off the coast of Central America, perhaps due to unmodeled sediments or increased crustal thickness.

We have calculated the "effective age" of the lithosphere by taking the depth and estimating the age of seafloor of that depth predicted by the plate cooling model. This procedure is consistent with the "lithospheric rejuvenation" hypothesis of *Menard and McNutt* [1982]. The term "rejuvenation" refers to the observation that many midplate swells cool and subside at the same rate as normal (younger) lithosphere at the same depth. Thus, thermal rejuvenation appears to produce lithosphere with many of the properties of normal lithosphere of a younger age. The Galapagos hotspot and the shallow Cocos and Carnegie ridges, for example, are regions of anomalously shallow

depth in our study area, and are presumably related to some sort of heating event. For other anomalously shallow regions included in this study (such as the majority of the Cocos plate), the mechanism for shoaling is less clear. The slope of the SS-S travel time residual versus square root of predicted age is -0.26 ± 0.04 s/My$^{1/2}$ for the age range 0-33 My (Figure 4.6b). This value is at least of the same sign as the relation predicted by plate cooling and with that observed in the Atlantic (Chapter 2), but the magnitude of the slope is still significantly lower than expected from the model.

To look for other systematic variations in the residuals, we correct for age by removing the linear dependence on square root of age predicted by the plate cooling model, approximately -0.7 s My$^{-1/2}$ (Chapter 2). This value for slope is also in good agreement with observations in the north Atlantic but admittedly is steeper than what we have observed with our limited range of east Pacific data. Future work is warranted to study further the relation between travel time and plate age in the east Pacific.

The travel time residuals in the region of the East Pacific Rise are about 2 s larger at a given bounce point age than those in the Atlantic. Part of this difference may be due to the fact that since the Mid-Atlantic Ridge is slow spreading the zone of lithosphere of young age is extremely narrow, whereas in the fast spreading Pacific it extends over a much greater width. So even if the age at two SS surface reflection points is the same in both of these studies, the upper mantle portion of the path in the Atlantic region will include a greater proportion of older lithosphere than the Pacific region. The magnitude of this effect would be about 1 s at young lithospheric ages (0-15 My) and less at older ages.

Anisotropy

Another systematic velocity variation that has been suggested as a possible contributor to residual SS-S travel times is azimuthal anisotropy. As noted in Chapter 2, the SS-S data from the north Atlantic do not show a consistent anisotropic effect. We

performed least squares inversions on the age-corrected SS-S residuals from the Pacific to determine best-fitting 4θ patterns. The anisotropy indicated by our regression experiments differs significantly from those found in the Atlantic. Our results indicate that for the 4θ fit to the SS-S residuals uncorrected for age the slow directions for SS-S are N44°W and N46°E and the peak-to-peak magnitude of the effect is 2.7 s (Figure 4.7a); for the 4θ model fit to the age-corrected SS-S data the slow directions are N48°W and N42°E and the magnitude is 3.4 s (Figure 4.7b). Our inversion for a 4θ pattern of anisotropy provided a variance reduction of 36% for both the uncorrected and the age-corrected SS-S residuals, a reduction that is significant considering the number of free parameters involved.

These results should be interpreted with caution, however, as our modelled azimuthal pattern may be partly the result of unmodelled upper mantle heterogeneity, and we lack data at many azimuths. The 4θ model fits the data well in the azimuth range -40° to +20°, but the fit is not good at -45° (where we have a peak in the predicted 4θ pattern), and the correlation of model to data is also poor in the vicinity of the +45° peak. The azimuthal distribution of the data is shown in Figure 4.8. Inspection of Figure 4.8 indicates that the distribution of azimuths is not uniform, and that data of a given azimuth tend to be clumped together geographically. Thus it is difficult to determine whether the observed azimuthal signal is due to anisotropy or due simply to the geographic distribution of lateral heterogeneity. The majority of the data at east-west azimuths come from Central American events propagating to Hawaii, with bounce points in the region 20°N, -120°E. The data at north-south azimuths come predominantly from Chile Rise events propagating to North America. Most of these residuals are negative (early) and contribute to the negative trough in the azimuthal patterns (Figures 4.7a, b). The data most inconsistent with the 4θ model come from the azimuth N60°W. These data are mainly from bounce points west of the rise on seafloor of approximately 50 Myr age.

Spatial Pattern of Age-corrected Residuals

A plot of age-corrected SS-S travel time residuals at the SS surface reflection point (Figure 4.9) shows several interesting features. The pattern of alternating fast and slow residuals, with a characteristic wavelength of 1200 km, is still visible in the Cocos plate region. The Galapagos hotspot is marked by positive residuals. The residuals south of the Galapagos Spreading Center are for the most part more negative than those to the north. Residuals in the region 15°-30°N, 115°-130°W are positive. Far from the rise, at 130°-140° W longitude, the residuals show much scatter. Residuals along the coast of Central America are positive.

ANALYSIS OF PROFILES

The sparse sampling of our data does not permit us to contruct a profile along the axis of the rise as was performed for the north Atlantic in Chapter 2. However, we have been able to construct several profiles across the East Pacific Rise and Galapagos Spreading Center which allow us to examine more closely the relation of the observations to plate age, and, after removal of the age dependence, to analyze anomalies orthogonal to the ridge. The locations of the profiles are shown in Figures 4.3 and 4.4.

Profiles of SS-S travel time, geoid, and bathymetry values were constructed by searching for all SS surface bounce points lying within 250 km (or 200 km for Profile 2) of the profile line and then applying a weighted averaging scheme to produce a single value every 50 km. To ensure complementarity of data sets, bathymetry and geoid height values are obtained at each SS bounce point, and all are corrected for cooling and subsidence with seafloor age. In this manner we effectively normalize all observations to zero age. The age correction for SS-S travel time data (-0.7 s $My^{-1/2}$) was given in an earlier section. The age corrections for depth and geoid are described below.

The age correction for depth is based on an empirical depth-age relationship from *Schroeder* [1984], which accounts for the thermal subsidence of oceanic lithosphere away from spreading centers, and is appropriate for this part of the Pacific. The *Schroeder* [1984] age-depth relation is $d(t) = 2967 - 305\ t^{1/2}$, where d is depth in meters and t is time in My. We also examined depth anomalies obtained using the *Parsons and Sclater* [1977] depth-age relation, which was determined using depth data from outside of this area. The general trends observed using the *Parsons and Sclater* [1977] relation are not markedly different from those obtained using the *Schroeder* [1984] relation, but we prefer the *Schroeder* [1984] relation as more appropriate for this region.

The geoid-age correction is done in two different ways. In the first method the theoretical geoid-age relation from the plate cooling model [*Parsons and Richter*, 1980] is removed to obtain the geoid anomaly. The second method, after *Hager* [1983], takes into account the fact that we have already removed the low order signal from the geoid. *Hager* [1983] made use of a global regionalization of plate ages [*Mauk*, 1977] and calculated the predicted effect of plate cooling on the geoid. The predicted field was then expanded in spherical harmonics up to degree and order 20. Our geoid-age correction after *Hager* [1983] then consists of the following: we remove the full predicted field up to degree and order 20, and then add the low order field (up to degree and order 7) back in. This prevents us from removing the low order part of the geoid-age dependence twice (empirically by the low degree and order reference geopotential field, and explicitly with the theoretical geoid-age relationship). This is especially critical in the very fast-spreading region of the Pacific included in this study, as the geoid-age dependence is dominated by the low order signal. This sort of correction is not critical in the slow-spreading Atlantic, where the geoid-age correction is dominated by wavelengths less than 4000 km, shorter than those removed to obtain our residual geoid [*Cazenave et al.*, 1986].

Error introduced into depth and geoid anomalies by isochron mislocation is difficult

to estimate precisely, but for an error in age of 2 My, depth and geoid errors at 80 My would be about 30 m and 0.2 m, respectively, while at 2 My, an error in age of 2 My would have a much larger effect, giving depth and geoid errors of 350 m and 0.3 m. The magnitude of this error highlights the importance of accurate age determination, especially at young ages. The age correction is relatively more important for bathymetric data than for the geoid, because the largest broad-scale variations in seafloor depth results from lithospheric cooling effects, unlike the geoid.

Profile 1, East Pacific Rise south of triple junction

Profile 1 starts to the west of the East Pacific Rise on seafloor approximately 45 My in age, passes over the ridge just south of the equator at 0.5 °S, 103.5 °W, and continues to the east of the rise to approximately 92 °W (Figure 4.3, 4.4). Figure 4.10a shows the seafloor age along the profile, with the rise axis marked by a line. The geoid high (Figure 4.10b) is centered to the west of the rise and is asymmetric, characterized by a steeper gradient over the east flank of the rise than to the west. The bathymetry (Figure 4.10c) correlates well with plate age, with the bathymetric high centered at the rise and a gentle slope to the west. The SS-S travel time residuals along the profile are shown in Figure 4.10d. The data along this profile are all at similar azimuths (approximately N-S), so azimuthal anisotropy can be discounted as a source of the variations. The travel time residuals of Profile 1 do not show a strong correlation with age. In fact, the rise is marked by a local minimum in the travel time residuals, with larger residuals (later arrivals) immediately to the east and the west of the rise. This pattern is similar to the one found by *Schlue* [1981] in a study of SS-S differential attenuation in the same region. To the west of the rise the residuals decrease gradually, with short wavelength signals superimposed. To the east of the rise the residuals drop off rapidly with age, in a manner similar to the geoid signal, but then increase again at about 700 km east of the rise axis.

Figure 4.10e shows the residual geoid signal after correcting for plate cooling with the method of *Hager* [1983]. In comparison, the geoid corrected according to the method of *Parsons and Richter* [1980] is shown in Figure 4.10f, and the higher order geoid (reference field up to degree and order 10 removed) is shown in Figure 4.10i. The high order geoid does not have an age correction applied, as we assume that the age dependence is dominated by the low order signal [*Cazenave et al.*, 1986]. This predicted dominance of the low-order geoid-age signal leads to a very small geoid-age correction if only the high order portions of the predicted field are removed (Figure 4.10e). The age-correction in Figure 4.10f reduces the geoid bulge in the immediate vicinity of the rise, but since the geoid data far to the west of the rise show little age dependence, the age-correction increases the geoid signal and produces a positive anomaly of about 4 m. The geoid to the east of the rise still falls off with distance, as it did before the age-correction was applied, but the slope is more gradual in the residual profile. The age-corrected bathymetry (Figure 4.10g) is marked by a large negative residual with a width of about 700 km at the rise axis, indicating that the rise is 400 m deeper than predicted by the plate cooling model. Positive depth anomalies of approximately 200 m are found on the east and west flanks of the rise axis. This steep residual at the rise axis is produced using either the *Parsons and Sclater* [1977] or the *Schroeder* [1984] depth-age relation and was also found by *Menard and Dorman* [1977]. The age-corrected travel time residual profile slopes monotonically from west to east, with a full range of 6 s. A short-wavelength residual low at the rise is also present in this profile and in the high order geoid profile (Figure 4.10i) but is not readily apparent in the lower order geoid profiles in Figures 4.10e and 4.10f.

Profile 2, across the Galapagos Spreading Center

Profile 2, approximately orthogonal to the Galapagos Spreading Center, starts to the south of the spreading center at 5°S, passes to the east of the Galapagos hotspot at 1°S,

and crosses the Galapagos Spreading Center at 1°N, 89°W. The profile continues north of the spreading center onto the Cocos plate, stopping near the Middle America Trench at 8.7°N, 87.3°W. A comparison of the bathymetry for profiles 1 and 2 shows their very different character. In profile 1, the area west of the rise increased gently up to the rise, whereas in profile 2 bathymetry (Figure 4.11c) is much more variable and seems to be strongly affected by the Galapagos hotspot and the Middle America Trench and less related to simple plate cooling. Because Profile 2 crosses the most tectonically disturbed area, it is expected to present the most difficulty for application of simple plate cooling models. Once again, data on this profile are all of similar azimuth (approximately N20°W) so the effects of azimuthal anisotropy on the shear wave travel time residuals can be neglected. We observe a positive correlation between both the age-corrected residual depth (4.11g) and travel time residual (Figure 4.11h) profiles. The geoid signal is dominated by a monotonic increase from south to north of about 12 m (Figures 4.11b,e,f), a pattern which is presumably at least partially related to the Middle America subduction zone. *Hager* [1984] has suggested that the signal of subducting slabs is strong up to degree and order 9. It is therefore worth examining the high-order geoid (Figure 4.11i) as we are mainly interested in processes unrelated to subduction. The high-order geoid shows some correlation with the bathymetry and travel time, mainly at long wavelengths and in the vicinity of the Galapagos hotspot. The Galapagos Spreading Center appears in the middle of a south-to-north, negatively sloping feature on the bathymetry, travel time, and high-order geoid.

Profile 3, East Pacific Rise north of triple junction

Profile 3 stretches from 10°N, 131°W to 9°N, 86°W, crossing over the East Pacific Rise at 9.5°N, 103.5°W. To the west of the rise the depth (Figure 4.12c) increases gradually with age. The geoid (Figure 4.12b) rolls off steeply on the west side of the rise

and increases slightly at a distance of about 1200 km from the rise axis. The SS-S travel time residuals are low (comparatively early) at the rise axis, but in the region from 300 km to 2500 km to the west of the rise, the residuals follow the predicted relation between age and travel time residual. The data to the east of the rise are all located on the Cocos plate, and, after initially decreasing with age to the east of the rise, increase significantly as the coast of central America is approached. The depth anomaly (Figure 4.12g) west of the East Pacific Rise is near zero and shows little deviation from the depth predicted by *Schroeder* [1984]. The main feature in the age-corrected depth and travel time anomaly profiles [Figures 4.12g and 4.12h] is the region of high values at the eastern end of the profile. The geoid profiles [Figures 4.12e, f, and i] are not well correlated with the travel time and bathymetry.

Profile 4, East Pacific Rise north of triple junction

Profile 4 stretches WNW - ESE from 23°N, 127°W to 7°N, 83°W, crossing over the East Pacific Rise at approximately 13.5°N, 104°W. As with the other E-W profiles (profiles 1 and 3) the bathymetry (Figure 4.13c) and travel time residuals (Figure 4.13d) follow the predicted age dependence to the west of the rise, whereas the residual geoid (Figure 4.13b) falls off more steeply than predicted to the west and then increases about 1300 km west of the rise axis. For this profile the travel time residuals are relatively large (late) at the rise axis, as expected from plate cooling models, but contrary to observations in the previous profiles. The travel time, geoid, and bathymetry all fall off steeply to the east of the rise and then increase as the Central American coastline is approached. The age-corrected residuals of Profile 4 do not differ markedly from those of Profile 3. The fact that the travel time residuals (Figures 4.13d, h) increase at the eastern end of the profile and then decrease sharply as the shallowest depths on the bathymetry profile are reached might be partly due to an inaccurate bathymetric correction to the travel times.

Inversion Experiments

Inversion experiments were conducted to assess whether the geoid, topography, and travel time anomalies presented in Profile 2 can be explained by reasonable variations in temperature and/or composition in the upper mantle. Profile 2 was singled out for further analysis in order to search for thermal and/or compositional variations related to the Galapagos hotspot, and also because of the qualitative correlation between bathymetry and travel time at a variety of wavelengths (700 - 1500 km). The geoid, admittedly, is problematic in this region due to the signal from the Middle American subduction zone. A total of 24 inversions were run, with various combinations of inversion parameters (temperature and/or composition), the thickness of the layer in which temperatures or composition were allowed to vary (0-150 km, 0-300 km, or 0-650 km), viscosity structures (constant viscosity mantle or mantle with a shallow low-viscosity zone), and geoid corrections. Results of the inversion experiments are summarized in Table 4.3 and Figures 4.14-4.21.

We find that compositional variations alone (parameterized in terms of Mg#) are inadequate to model simultaneously the geoid, travel time, and bathymetry observations. Temperature variations alone provide reasonably good fits to the data, with variance reductions ranging from 66% for the model with a low viscosity zone and temperatures constrained to vary only over the depth range 0-300 km, to 72% for the model with a low viscosity zone and temperature perturbations confined to the depth range 0-150 km. For the latter model, the range of predicted temperature variations is high (± 150°C), so the models with temperatures constrained to extend deeper are more reasonable, as they predict smaller temperature variations and thus lesser differences in melt production and crustal thickness. The most interesting feature in the Profile 2 inversions is the Galapagos hotspot region, marked by slow SS-S travel times, shallow topography, and a slight geoid

high. The other dominant feature in the profile is a long-wavelength southward slope, especially strong in the geoid, which may be partially due to the Middle American subduction zone. In an attempt to remove the slab signature, we also carried out temperature inversions using the high-order geoid (reference field up to degree and order 10 removed). The high-order geoid is of much smaller amplitude than the low-order geoid, and we had to adjust our data covariance matrix to ensure proper weighting between the various data. The fits with the high-order geoid were worse than those with the low-order geoid, as only a small temperature variation in the upper mantle was required to fit the geoid but this variation was insufficient to match the observed travel time residual and bathymetry. It may be worthwhile to remove the slab signal from the geoid explicitly.

DISCUSSION

We found that the SS-S differential travel time is about 2 s larger in the Pacific at a given seafloor age than in the north Atlantic. The Pacific has been found to be seismically slower at a given age than the Atlantic (or Indian Ocean) in a number of studies [*Stark and Forsyth*, 1983; *Zhang and Tanimoto*, 1990b; *Woodward and Masters*, 1991]. In addition, heat flow in the Pacific is higher than in the Atlantic [*Chapman and Pollack*, 1975], suggesting that there may be some differences in the thermal structure beneath these two ridges or that there are differences in the fraction of heat flow carried by hydrothermal circulation.

Observations of upper mantle anisotropy in the Pacific have been reported in many surface wave studies [e.g., *Forsyth*, 1975; *Schlue and Knopoff*, 1977; *Tanimoto and Anderson*, 1984, 1985; *Cara and Leveque*, 1988; *Nishimura and Forsyth*, 1988, 1989; *Montagner and Tanimoto*, 1990], and the lithospheric portion of this signal has been

attributed to the preferential alignment of olivine crystals with their a-axis parallel to the fossil direction of plate motion. *Nishimura and Forsyth* [1989] and *Cara and Leveque* [1988] have suggested that deep-seated (sub-lithospheric) anisotropy is related to the direction of present shear rather than the fossil seafloor spreading direction. In general, for fast-moving oceanic plates, the direction of horizontal shear in the underlying asthenosphere is expected to be similar to that of absolute plate motion [*Hager and O'Connell*, 1979].

Our study area encompasses a large range of absolute plate motions, as three plates are involved. Not surprisingly, surface wave studies also show a range of anisotropy patterns in the region. The study of *Montagner and Tanimoto* [1990] shows anisotropy in the region with the fast axis for Rayleigh waves at N80°E in the Cocos plate, approximately east-west in the Nazca plate, and approximately N80°W in the very eastern part of the Pacific Plate (within our study area). The absolute plate motion vectors from *Gripp and Gordon* [1990] have azimuths of approximately N35°E for the Cocos plate, N90°E for the Nazca plate, and N75°W for the Pacific plate. Our azimuthal distribution of data and corresponding 4θ models are consistent with alignment of the olivine *a* axis at either N45°W or N45°E. The olivine *a* axis direction is slow for SH incident at an angle of 45° from the vertical (similar to the incidence angles of SS waves in this study), though fast for horizontally propagating P. Since most of our bounce points lie on the Cocos plate, it is not surprising that our results are most consistent with the absolute motion of this plate.

Synthesizing the results on anisotropy from Chapter 2 and the east Pacific, there is not a significant pattern of anisotropy in the slow spreading north Atlantic, but there may be significant anisotropy in the faster spreading east Pacific. Travel time data at a better distribution of azimuths on the Cocos plate would help us to distinguish between upper mantle anisotropy and lateral heterogeneity as the mechanism of our observed azimuthal

distribution in travel time residuals. *McKenzie* [1979] and *Ribe* [1989] have suggested that anisotropy in both the lithosphere and the asthenosphere will not be as pronounced beneath slow spreading ridges as at fast spreading ridges for several reasons. In the lithosphere at slow spreading rates the crystals freeze in too quickly to be affected by strains which at fast spreading rates can produce a preferred alignment. In the asthenosphere, the lattice preferred orientation of olivine crystals is suggested to become aligned with the flow direction when the flow is progressive simple shear, which is likely to occur in the asthenosphere beneath a fast spreading ridge.

We have performed inversions of travel time, geoid, and bathymetry along a profile orthogonal to the Galapagos Spreading Center and just to the east of the Galapagos hotspot. The results of our inversions indicate that compositional variations alone are inadequate to produce the observed variations in travel time, geoid, and bathymetry, but that several different parameterizations of temperature variations produce generally good fits to the data (variance reductions are approximately 70%, see Table 4.3). The predicted excess temperature anomaly at the Galapagos hotspot ranges from 50° to 150°C. We also observe a long wavelength signal attributed to the slab subducting along the Middle America Trench. Our techniques have not been designed to deal with the strong lateral viscosity contrasts that a slab would presumably produce. Further work is needed to remove the slab signal from our geoid anomalies.

Several authors [*Watts et al.*, 1985, *Haxby and Weissel*, 1986] have argued for the presence of small scale convection in the central and eastern Pacific. *Haxby and Weissel* [1986] observed linear gravity anomalies of wavelength 150 to 500 km oriented orthogonal to the ridge. Their observations were from an area to the south and west of our study area, so a direct comparison is not possible. They suggest that these anomalies mark the locus of longitudinal convective rolls aligned by shear imparted by a fast moving plate [*Richter and Parsons*, 1975]. A denser sampling of data along the axis of the East

Pacific Rise might allow us to test this theory, but our present sampling is inadequate. In addition, even a 500-km-wavelength signal might be smaller than we can resolve with teleseismic techniques. *Stark and Forsyth* [1983] found a periodic variation of 640-km wavelength in shear wave travel time residuals in the Indian Ocean, and they used this result to argue for the presence of linear convective rolls in the upper mantle in that region.

CONCLUSIONS

We have measured 600 SS-S differential travel times for paths in the East Pacific Rise region. The SS-S travel time residuals are only weakly correlated with seafloor age. The travel time - age correlation is stronger if rather than using the actual plate age we use the age predicted by the depth of the seafloor at the SS bounce point.

We have examined the azimuthal distribution of the SS travel time residuals, and although not conclusive, our results are consistent with the presence of anisotropy in our study area. The sense of anisotropy is consistent with the fast axis of olivine oriented approximately parallel to the absolute plate motion vector for the Cocos plate. It is also possible that lateral heterogeneity rather than azimuthal anisotropy is producing our observed azimuthal pattern. Sampling at a more uniform distribution of azimuths should make this result less ambiguous, and as more seismic stations are deployed at new geographic locations our chances of resolving this issue improves.

We note several differences between the north Atlantic and the east Pacific. The most obvious difference is that the Pacific travel time residuals are significantly larger than those for the Atlantic, even at a fixed age. The travel time - age relation is weaker in the Pacific, though this may be partially attributable to the fact that we do not sample a large range of plate ages in the Pacific. In the Atlantic our results are not consistent with the presence of a simple pattern of azimuthal anisotropy, while in the Pacific our data are

consistent with the presence of weak anisotropy in the upper mantle. It has been suggested that anisotropy may be more pronounced at fast spreading rates than at slow spreading rates due to a rate-dependence of the mechanism for orienting olivine grains, and our results are consistent with this suggestion. There is substantial ambiguity in our Pacific anisotropy measurements, however, due to a poor sampling of azimuths.

We have applied a joint inversion of travel time residuals, geoid, and bathymetric anomalies for lateral variation in upper mantle temperature and composition to a north-south profile orthogonal to the Galapagos Spreading Center. We find that compositional variations alone are inadequate to match all of the data simultaneously. Temperature variations alone, however, significantly reduce the variance in all of the data. The models predict excess temperature in the vicinity of the Galapagos hotspot in the range of 50° to 150°C. Further analysis is needed to remove the effects of slab structure and possible crustal thickening in the east Cocos plate region.

TABLE 4.1. Digital seismograph stations used.

Station	Network†	Latitude, °N	Longitude, °E
AFI	DWWSSN	-13.910	-171.777
ALQ	DWWSSN	34.942	-106.458
ANMO	SRO	34.946	-106.457
BOCO	SRO	4.587	-74.043
CMB	DWWSSN	38.035	-120.385
COL	DWWSSN	64.900	-147.793
GAC	CAN	45.70	-75.47
HON	DWWSSN	21.322	-158.008
JAS	DWWSSN	37.947	-120.438
JAS1	DWWSSN	37.947	-120.438
KIP	GEOSCP	21.420	-158.022
LON	DWWSSN	46.750	-121.810
RSCP	RSTN	35.600	-85.569
RSNT	RSTN	62.480	-114.592
RSNY	RSTN	44.548	-74.530
RSON	RSTN	50.859	-93.702
RSSD	RSTN	44.120	-104.036
SCP	DWWSSN	40.795	-77.865
SCZ	GEOSCP	36.600	-121.400
WFM	GEOSCP	42.610	-71.490
ZOBO	ASRO	-16.270	-68.125

† Network abbreviations as in Table 2.1

TABLE 4.2 Earthquakes used in this study.

Year	Month	Day	Hour	Min	Sec	Depth, km	m_b	Lat., °N	Long., °E
1980	1	14	21	51	1.8	14	5.6	-33.19	-69.46
1980	1	20	1	3	33.2	33	5.0	-22.73	-114.20
1980	1	24	19	0	9.5	11	5.3	37.85	-121.82
1980	1	27	16	38	1.1	10	5.7	-35.38	-105.87
1980	1	28	16	59	22.9	33	5.3	-44.96	-76.11
1980	2	14	14	7	1.6	45	5.3	-31.77	-71.42
1980	3	29	6	41	50.5	33	5.6	-43.08	-75.20
1980	3	29	17	49	10.9	33	5.2	-37.93	-73.50
1980	4	9	8	17	55.1	10	5.5	-31.65	-67.48
1980	4	9	19	56	26.0	10	5.5	-44.61	-80.10
1980	4	14	23	57	27.6	100	5.4	-21.29	-68.73
1980	5	2	19	9	7.8	163	5.4	-24.13	-66.94
1980	5	26	18	41	36.8	62	6.0	-19.36	-69.29
1980	5	30	16	56	22.2	33	5.3	-23.11	-70.93
1980	6	9	3	28	18.9	5	5.6	32.22	-114.99
1980	6	11	14	21	18.9	35	5.5	-32.72	-71.65
1980	6	16	5	45	6.9	87	5.5	-22.03	-68.47
1980	7	13	6	20	30.3	103	5.6	-33.47	-70.15
1980	8	3	3	0	49.7	151	5.3	-35.25	-69.99
1980	8	3	13	42	35.4	10	5.1	-35.58	-104.63
1980	9	2	22	18	41.6	10	5.0	-26.79	-112.92
1980	9	26	20	26	34.8	10	4.9	-35.90	-102.94
1980	11	8	21	35	43.1	103	5.4	-24.34	-67.65
1980	12	11	18	15	3.5	80	6.1	-21.27	-68.15
1980	12	20	20	26	47.2	571	5.2	-24.37	-63.42
1981	1	7	16	26	42.5	37	5.5	-23.75	-70.62
1981	1	7	20	31	12.1	10	5.1	-49.91	-114.14
1981	3	2	21	19	56.0	246	5.1	-22.64	-65.99
1981	3	23	19	28	10.7	46	5.8	-33.66	-71.89
1981	3	26	18	4	44.7	138	5.8	-19.37	-68.96
1981	4	1	18	3	36.5	554	5.9	-27.31	-63.32
1981	4	6	14	34	1.3	88	5.3	-35.37	-71.05
1981	4	16	22	5	53.0	33	5.1	-20.16	-70.70
1981	5	17	17	4	58.0	33	5.4	-27.22	-71.83
1981	5	24	11	44	3.5	10	5.2	-22.16	-114.20
1981	6	1	19	50	13.3	330	5.0	-20.49	-65.19
1981	6	4	7	39	40.4	33	5.1	-34.20	-78.83
1981	6	10	4	6	10.2	10	4.8	-35.80	-102.17
1981	6	16	5	41	49.1	76	5.4	-21.49	-68.34
1981	6	21	10	30	1.1	36	5.2	-20.26	-70.45
1981	6	22	17	53	21.3	24	5.1	-13.17	-74.52
1981	7	10	18	2	4.9	10	5.2	-37.22	-95.37
1981	7	18	11	15	18.1	246	5.0	-22.68	-66.24
1981	7	28	3	3	21.6	43	5.5	-41.57	-73.20
1981	8	17	2	18	59.9	37	5.5	14.52	-93.77
1981	8	21	22	52	40.6	10	5.1	-26.51	-114.76
1981	8	22	23	47	41.4	10	5.2	-35.83	-103.30
1981	9	6	16	43	19.9	10	5.4	-36.17	-100.70

1981	9	19	11	40	56.9	30	5.6	-39.08	-74.81
1981	9	20	10	48	20.3	234	5.1	-23.08	-66.63
1982	1	21	21	52	41.0	10	5.5	19.22	-155.60
1982	1	21	22	29	13.0	13	5.5	19.20	-155.57
1982	2	10	20	38	3.5	226	5.9	-22.79	-66.66
1982	3	22	21	44	9.3	126	5.1	-19.88	-68.74
1982	4	18	11	30	55.3	10	5.9	-28.16	-114.07
1982	4	19	11	54	27.5	250	5.3	-22.60	-66.02
1982	5	3	7	26	2.5	107	5.5	-23.47	-68.81
1982	5	17	2	39	26.1	10	5.0	-35.35	-103.84
1982	5	27	1	39	19.5	10	5.3	-13.38	-111.62
1982	5	29	3	26	58.7	116	5.2	-22.35	-68.37
1982	5	29	17	22	24.4	47	5.1	-24.99	-70.25
1982	6	1	4	14	15.3	32	6.1	-41.63	-74.99
1982	6	5	0	17	0.3	33	5.4	-43.10	-75.21
1982	6	15	1	20	35.2	10	5.2	-36.52	-98.65
1982	7	11	2	13	37.7	39	5.3	-16.65	-73.21
1982	8	5	9	16	41.3	40	5.4	-26.68	-70.66
1982	8	23	21	35	5.9	10	5.1	-29.04	-111.78
1982	8	27	3	56	49.0	10	5.5	-35.52	-104.61
1982	9	9	6	40	21.4	10	5.0	-35.55	-102.42
1982	9	26	4	2	6.6	10	5.2	-42.70	-82.26
1982	10	24	10	43	41.1	35	5.4	-22.27	-70.08
1982	10	25	22	26	4.4	11	5.4	36.32	-120.51
1982	10	26	3	24	30.6	69	5.6	-29.67	-71.26
1982	10	31	6	3	4.5	97	5.3	14.15	-90.19
1982	11	18	20	39	51.2	160	5.5	-31.25	-65.86
1982	12	9	1	41	37.6	10	5.6	-29.01	-112.66
1982	12	31	1	35	35.2	130	5.3	-21.39	-68.05
1982	12	31	3	47	22.4	67	5.8	-21.05	-68.46
1983	1	10	9	17	32.8	98	5.6	-21.85	-68.32
1983	1	10	12	32	21.9	559	5.8	-27.30	-63.39
1983	1	13	9	23	47.9	10	5.6	-35.81	-102.63
1983	1	18	2	22	54.7	10	5.0	-49.74	-114.83
1983	1	23	6	0	52.9	10	4.2	-17.90	-96.78
1983	1	23	16	36	38.7	10	5.6	-37.28	-95.24
1983	1	24	8	17	38.6	45	6.3	16.18	-95.15
1983	1	26	4	43	18.7	10	5.7	-49.75	-115.12
1983	1	28	23	11	5.8	10	5.2	-36.23	-100.97
1983	2	1	4	22	51.1	102	5.2	-23.03	-68.80
1983	2	15	23	21	6.9	202	5.0	-22.97	-66.50
1983	2	25	22	49	54.7	146	5.9	-18.27	-69.44
1983	2	28	22	44	19.5	10	5.3	-43.98	-79.06
1983	3	2	7	7	41.4	64	5.5	-11.60	-77.83
1983	4	3	2	50	0.7	33	6.5	8.73	-83.12
1983	4	7	19	29	14.9	34	5.4	8.00	-82.69
1983	4	12	12	7	54.6	107	6.5	-4.89	-78.18
1983	5	2	23	42	37.9	12	6.2	36.24	-120.30
1983	5	7	1	7	22.7	51	5.4	-28.01	-70.79
1983	5	9	10	58	26.7	33	5.8	-40.87	-74.84
1983	5	9	15	53	2.7	36	5.5	8.28	-82.93
1983	5	23	0	54	11.6	110	5.5	-19.14	-69.15
1983	6	11	3	9	54.0	2	5.4	36.26	-120.47
1983	6	17	11	33	16.4	10	5.5	-36.45	-97.44
1983	7	3	17	14	23.2	33	5.7	9.66	-83.64
1983	7	9	7	40	50.9	10	5.3	36.24	-120.41
1983	7	12	3	39	27.2	10	5.2	23.89	-108.37

1983	7	21	7	11	33.1	127	5.5	-22.30	-68.53
1983	7	22	2	39	55.3	7	6.0	36.22	-120.40
1983	7	31	10	26	0.2	10	6.0	-20.14	-126.87
1983	8	20	8	30	34.1	10	5.3	-36.25	-101.54
1983	8	21	18	58	19.2	10	5.4	-28.78	-112.65
1983	8	31	8	50	37.2	10	5.3	-29.57	-111.84
1983	9	1	20	1	46.7	110	5.9	-17.58	-69.98
1983	9	9	16	30	55.4	9	5.4	19.33	-155.12
1983	9	14	0	47	4.7	37	5.4	-36.42	-73.08
1983	9	21	10	27	56.7	112	5.3	-18.98	-69.12
1983	9	24	15	51	57.7	10	5.5	-41.85	-83.61
1983	10	4	18	52	12.9	18	6.4	-26.62	-70.77
1983	10	6	15	1	48.4	20	5.5	-26.72	-70.91
1983	10	9	11	25	42.2	33	5.9	-26.26	-70.59
1983	10	12	3	39	39.0	22	5.7	8.06	-82.72
1983	10	16	9	59	45.8	66	5.7	-23.84	-70.21
1983	10	21	8	14	18.2	117	5.5	-30.64	-69.11
1983	10	24	0	36	6.7	55	5.6	-12.96	-76.75
1983	11	9	1	57	50.3	10	5.4	-36.13	-100.04
1983	11	16	16	13	0.0	11	6.3	19.43	-155.45
1983	11	17	10	39	30.9	575	5.4	-28.20	-63.22
1983	11	22	14	20	58.8	23	6.3	0.42	-79.94
1983	11	23	8	12	15.0	54	5.1	-15.09	-75.55
1983	11	25	9	23	27.8	33	5.3	24.25	-108.80
1983	11	26	20	18	23.5	10	5.6	7.38	-82.26
1983	11	26	23	29	8.9	10	5.3	-44.37	-80.15
1983	11	28	19	10	7.0	19	5.6	-44.95	-76.01
1983	11	29	2	55	15.7	10	4.8	-49.75	-114.54
1983	12	2	3	9	5.6	69	5.9	14.05	-91.94
1983	12	21	12	5	6.0	604	6.3	-28.23	-63.20
1983	12	23	22	56	6.9	33	5.3	-27.54	-71.46
1984	1	1	22	8	10.2	228	5.4	-22.61	-66.02
1984	1	6	15	1	34.6	103	5.4	-23.92	-68.65
1984	1	16	12	27	13.8	10	5.9	-30.00	-112.29
1984	1	26	19	30	57.3	58	5.3	-12.35	-76.93
1984	2	3	8	29	47.7	33	5.7	-29.46	-71.13
1984	2	9	4	31	18.5	41	5.4	-14.16	-76.23
1984	3	1	19	21	24.6	10	5.5	-4.65	-106.05
1984	3	4	22	34	24.0	33	5.4	-26.55	-70.70
1984	3	11	13	42	56.5	10	5.7	-26.64	-108.41
1984	4	13	5	54	52.1	10	4.8	-24.90	-112.11
1984	4	19	8	28	53.0	31	5.5	-31.80	-71.90
1984	5	7	14	9	13.3	137	5.6	-27.82	-66.64
1984	5	9	23	56	9.5	119	5.6	-34.14	-70.27
1984	5	10	9	51	2.3	10	5.1	-36.25	-98.75
1984	5	16	3	44	56.4	139	5.4	-27.17	-67.04
1984	5	25	13	20	23.9	31	5.5	-42.62	-75.13
1984	6	11	2	5	33.8	45	6.2	-30.72	-71.21
1984	6	18	11	20	18.2	121	5.8	-15.73	-72.48
1984	6	20	19	56	42.8	160	5.4	-23.98	-66.97
1984	7	2	4	50	42.6	35	5.8	16.76	-98.51
1984	7	24	4	49	45.3	34	5.6	-25.79	-70.52
1984	7	30	21	32	59.7	79	5.0	13.34	-90.07
1984	8	12	11	51	40.9	101	5.6	-24.36	-69.25
1984	8	26	5	2	7.9	16	5.4	15.91	-95.30
1984	8	28	10	4	24.6	10	5.3	-4.53	-105.87
1984	8	31	19	46	3.9	119	5.3	16.10	-93.34

1984	9	5	22	27	54.3	10	5.5	-25.51	-116.06
1984	9	6	20	34	25.8	10	5.0	30.65	-113.93
1984	9	12	21	56	28.2	10	5.0	19.88	-116.02
1984	9	28	10	40	24.1	10	6.0	-31.63	-110.89
1984	10	10	5	43	51.0	10	5.1	-4.59	-105.51
1984	10	13	17	18	14.2	31	6.1	15.06	-94.24
1984	11	8	6	32	55.9	42	5.3	-30.67	-71.36
1984	12	10	10	22	4.8	56	5.4	-14.86	-75.33
1984	12	11	23	22	20.6	122	5.6	-22.84	-68.80
1984	12	31	13	0	31.8	174	5.5	-23.06	-66.91
1985	1	18	15	0	8.3	82	5.8	-29.41	-70.71
1985	1	26	3	7	2.5	38	6.1	-33.15	-68.54
1985	2	14	8	30	55.6	123	5.6	-23.85	-67.75
1985	2	21	18	53	8.5	33	4.7	-33.28	-71.72
1985	2	21	21	52	56.5	33	5.3	-20.72	-70.37
1985	2	24	2	7	31.2	10	5.1	-32.25	-110.95
1985	3	3	22	47	6.9	33	6.9	-33.15	-71.98
1985	3	4	0	32	21.4	33	6.0	-33.23	-71.76
1985	3	4	6	6	57.8	33	5.4	-33.58	-71.86
1985	3	4	13	49	29.6	33	4.9	-33.95	-71.96
1985	3	4	15	1	6.2	33	6.1	-33.84	-71.32
1985	3	4	19	3	7.2	33	5.3	-32.75	-71.60
1985	3	5	9	8	54.6	33	5.4	-34.24	-71.72
1985	3	7	0	54	56.9	33	5.5	-33.01	-72.14
1985	3	12	8	23	15.3	33	5.3	-33.10	-72.16
1985	3	17	10	41	37.9	33	5.9	-32.66	-71.56
1985	3	19	4	1	6.5	33	5.9	-33.28	-71.76
1985	3	23	13	45	19.3	33	5.4	-34.28	-72.11
1985	3	23	14	36	57.0	33	5.6	-33.30	-72.22
1985	3	24	16	16	33.0	33	5.4	-34.35	-72.13
1985	3	25	5	14	33.2	33	6.1	-34.34	-72.28
1985	3	30	13	47	28.7	33	5.0	-45.46	-76.40
1985	4	3	13	6	19.8	33	5.7	-32.62	-71.61
1985	4	9	1	56	58.6	33	6.3	-34.17	-71.54
1985	4	15	4	41	50.5	33	5.0	-33.53	-72.02
1985	4	19	17	43	10.3	66	5.3	11.93	-86.56
1985	4	28	2	53	44.1	60	5.0	-33.07	-71.49
1985	4	28	8	30	32.6	33	6.0	-39.70	-75.61
1985	5	4	12	47	10.5	10	4.7	16.66	-113.53
1985	5	6	7	33	58.7	10	5.1	-36.37	-98.86
1985	5	17	2	44	7.8	33	5.1	-34.28	-72.46
1985	5	18	16	59	13.3	111	5.4	-19.20	-69.12
1985	5	19	7	7	46.2	33	5.2	-33.88	-72.30
1985	5	19	18	9	15.4	39	5.9	-30.24	-71.28
1985	6	2	16	26	58.0	33	5.4	-37.80	-73.59
1985	6	3	2	45	32.1	70	5.1	13.13	-90.18
1985	6	9	18	46	30.1	33	5.0	-33.25	-71.97
1985	6	10	15	37	3.3	180	5.8	-28.11	-67.19
1985	6	11	11	12	28.8	33	5.1	-32.48	-71.68
1985	6	14	13	14	14.9	33	5.5	-40.74	-74.92
1985	6	23	6	55	23.7	178	5.5	-24.06	-67.10
1985	7	5	15	22	38.1	33	5.0	-33.38	-72.17
1985	7	6	8	33	7.1	43	5.1	-33.36	-72.12
1985	7	7	11	25	12.0	32	5.4	-32.88	-72.00
1985	7	10	5	6	33.1	10	5.3	-38.63	-91.65
1985	7	11	20	31	13.9	33	5.2	-32.93	-72.00
1985	7	17	13	53	2.2	50	5.4	-32.65	-71.42

1985	7	27	16	26	45.5	10	5.4	-26.94	-113.41
1985	8	4	4	54	1.9	23	5.5	-44.89	-75.45
1985	8	6	2	29	44.0	10	4.8	-41.25	-85.78
1985	8	12	0	4	50.9	33	5.5	-38.42	-73.49
1985	8	19	7	53	48.0	33	5.3	-15.04	-75.60
1985	8	20	12	21	5.9	33	4.7	-33.75	-72.19
1985	8	21	11	26	28.8	61	6.1	-9.21	-78.91
1985	8	27	10	44	34.6	197	5.2	-21.46	-67.45
1985	9	1	8	28	21.3	10	4.9	-39.02	-91.61
1985	9	19	13	17	47.8	33	7.0	18.18	-102.57
1985	9	21	1	37	13.8	33	6.3	17.82	-101.67
1985	10	8	9	47	21.9	222	5.5	-23.05	-66.43
1985	10	12	20	29	24.5	75	5.2	13.19	-89.63
1985	10	29	15	2	27.1	33	5.6	18.17	-102.55
1985	10	31	21	49	20.0	595	5.8	-28.75	-63.19
1985	11	12	3	34	19.8	10	5.4	-36.25	-98.02
1985	11	17	20	50	50.9	10	5.1	-25.16	-112.33
1985	11	24	9	28	23.6	10	4.7	-7.69	-148.00
1985	11	27	15	59	2.6	10	9.9	-7.90	-148.60
1985	11	29	4	2	11.3	521	5.3	-22.76	-63.62
1986	1	7	16	37	47.8	10	4.9	-13.34	-111.59
1986	1	12	14	0	55.4	10	5.0	-35.97	-102.20
1986	1	26	7	48	22.9	30	5.7	-27.12	-70.87
1986	2	9	23	32	11.7	86	5.0	-36.13	-71.27
1986	2	20	9	16	2.4	33	5.7	-21.15	-70.11
1986	3	22	16	56	50.9	10	5.3	-4.45	-104.82
1986	3	26	7	4	49.8	33	5.1	-34.10	-72.10
1986	4	9	18	10	52.9	199	5.2	-22.96	-66.67
1986	4	30	14	9	39.7	116	5.5	-18.35	-69.70
1986	5	10	12	2	1.7	10	5.6	-37.04	-94.03
1986	6	5	9	1	15.6	10	5.2	-36.30	-97.37
1986	6	19	17	18	58.1	10	4.9	-36.12	-100.69
1986	6	24	23	53	32.6	10	4.7	-36.10	-100.47
1986	6	27	1	22	53.0	10	4.7	-19.30	-126.20
1986	6	30	22	52	12.0	62	5.2	11.22	-86.09
1986	7	2	20	45	50.5	10	5.6	-26.72	-114.35
1986	7	13	13	47	8.0	5	5.6	33.02	-117.79
1986	7	18	0	21	38.7	10	4.9	-19.80	-126.50
1986	7	28	20	29	1.5	32	5.1	-33.38	-72.13
1986	8	1	14	9	24.9	10	5.5	-35.89	-103.75
1986	8	13	4	11	41.1	10	5.4	5.84	-82.40
1986	8	21	17	1	28.5	10	5.0	-8.90	-109.47
1986	9	25	6	15	53.7	10	5.3	22.90	-108.07
1986	10	5	7	21	37.5	10	5.3	-23.72	-112.03
1986	10	5	13	15	45.6	10	5.4	-23.62	-112.02
1986	10	24	2	42	50.9	50	5.4	-25.41	-70.15
1986	11	23	1	39	25.9	126	6.4	-3.36	-77.47
1986	11	28	20	34	52.5	33	4.6	-45.12	-76.67
1986	12	5	1	45	37.4	10	5.2	-36.27	-97.53
1987	1	4	17	52	36.6	10	5.5	5.92	-82.67
1987	1	14	9	38	56.7	10	5.1	-49.92	-113.59
1987	2	14	15	44	15.9	10	5.4	-45.71	-75.99
1987	2	25	10	42	45.5	171	5.1	-27.94	-67.06
1987	3	5	9	17	0.0	27	6.5	-24.49	-70.17
1987	3	6	1	54	50.7	14	6.1	0.13	-77.67
1987	3	6	4	10	41.9	12	6.5	0.15	-77.83
1987	3	14	20	18	37.6	10	5.4	-38.89	-92.19

1987	3	15	6	3	3.1	33	5.1	-24.30	-70.55
1987	3	22	3	23	57.7	42	5.9	-24.08	-70.08
1987	3	23	20	47	57.2	33	4.9	-34.07	-72.23
1987	4	8	17	42	36.0	49	5.1	11.66	-86.36
1987	5	10	15	16	20.2	160	5.6	-30.91	-65.42
1987	5	12	16	12	42.1	121	5.4	-21.79	-68.32
1987	5	14	16	4	26.5	29	5.6	-5.62	-81.39
1987	5	15	13	49	14.2	10	5.5	-49.98	-115.23
1987	5	19	12	56	25.0	39	5.6	-30.33	-71.59
1987	5	23	5	1	8.1	41	5.2	-20.19	-70.71
1987	6	9	22	46	11.7	10	5.2	-35.24	-106.68
1987	6	11	5	8	52.8	33	5.0	-20.51	-70.61
1987	6	15	6	23	8.9	44	5.5	-12.46	-76.73
1987	6	19	19	0	8.3	119	5.4	-21.37	-68.38
1987	6	27	9	9	5.5	61	5.9	-14.13	-76.08
1987	7	6	1	6	7.5	10	6.3	-27.02	-108.25
1987	7	8	11	50	14.6	10	6.1	-26.97	-108.20
1987	7	9	4	7	34.3	64	5.2	-20.48	-68.74
1987	7	15	7	16	13.6	67	6.0	17.56	-97.18
1987	7	17	1	57	38.7	10	5.4	1.52	-85.30
1987	7	21	13	27	13.2	10	5.2	-36.29	-97.24
1987	7	22	8	23	3.7	98	5.2	15.76	-93.44
1987	7	29	15	22	33.0	141	5.4	-28.87	-67.17
1987	8	4	15	4	40.4	38	5.8	-40.46	-73.10
1987	8	6	15	15	34.7	10	5.6	-5.40	-105.02
1987	8	8	15	48	57.4	82	6.4	-19.19	-70.14
1987	8	9	8	24	20.0	10	5.0	-35.23	-103.95
1987	8	13	15	23	11.4	74	6.1	-17.83	-71.08
1987	8	15	9	34	47.7	104	5.1	-23.10	-68.57
1987	8	15	18	4	22.1	32	6.3	-28.15	-70.89
1987	8	21	23	0	52.5	10	5.3	23.85	-108.77
1987	8	24	6	9	43.2	33	5.1	-20.15	-70.58
1987	8	26	13	1	23.0	10	5.1	-37.27	-95.22
1987	9	8	2	58	52.8	25	5.4	6.52	-82.55
1987	9	11	0	34	51.8	128	5.4	-22.32	-68.36
1987	9	11	4	2	3.1	95	5.1	-31.46	-70.73
1987	9	18	8	43	25.9	71	5.6	-24.41	-69.10
1987	9	19	9	21	41.7	35	5.1	-14.97	-75.66
1987	9	19	21	18	25.9	69	5.7	-9.19	-79.07
1987	9	22	13	43	39.7	23	6.1	-0.96	-78.09
1987	9	22	16	21	38.5	33	5.8	-1.08	-78.11
1987	10	3	3	35	6.1	119	5.8	-18.22	-69.31
1987	10	4	8	15	17.8	45	5.4	10.74	-85.94
1987	10	6	14	39	54.6	10	5.2	-35.78	-101.02
1987	10	7	0	51	37.0	117	5.6	-23.07	-68.12
1987	10	20	21	10	59.9	10	5.3	0.91	-87.09
1987	10	21	6	11	33.3	10	5.4	-23.10	-114.48
1987	10	21	23	25	51.7	76	5.4	-21.14	-69.69
1987	10	27	21	58	17.7	616	5.9	-28.73	-62.96
1987	10	31	5	11	17.0	66	5.1	-25.88	-69.80
1987	10	31	8	52	30.8	33	5.4	-6.98	-80.57
1987	11	6	18	47	34.9	538	5.8	-22.84	-63.63
1987	11	9	17	46	21.0	62	5.4	-22.07	-69.47
1987	11	17	3	40	8.9	76	5.8	12.57	-86.98
1987	12	3	11	4	32.1	60	5.6	-21.40	-68.26
1987	12	8	14	47	59.3	10	5.6	-32.59	-112.16
1987	12	28	8	16	21.3	52	6.0	-28.08	-70.61

1988	1	19	7	30	29.7	21	6.3	-24.75	-70.60
1988	2	5	14	1	2.2	33	6.2	-24.77	-70.37
1988	2	6	18	3	53.6	285	6.0	-18.04	-66.96
1988	2	22	19	13	17.4	71	5.9	-20.93	-69.80
1988	3	28	18	36	26.4	10	5.7	-36.03	-102.81
1988	3	30	23	50	56.2	37	5.8	-24.91	-70.41
1988	4	12	23	19	57.3	54	6.1	-17.32	-72.40
1988	5	5	10	4	13.5	10	6.1	-26.91	-113.39
1988	5	5	22	32	48.1	10	5.5	-26.76	-113.70

TABLE 4.3. Inversion Models and Variance Reduction

Model: Temperature variations only — Variance reduction, %

Layer thickness	Viscosity structure	ΔT range	total	bathym	geoid	SS-S
0-150 km	cvm	415 K	71	57	72	76
0-150 km	lvz	560 K	72	59	51	92
0-300 km	cvm	175 K	69	55	75	70
0-300 km	lvz	285 K	66	63	28	96
0-650 km	cvm	85 K	70	47	76	74
0-650 km	lvz	155 K	70	54	46	93

Model: Compositional variations only — Variance reduction, %

Layer thickness	Viscosity structure	ΔMg# range	total	bathym	geoid	SS-S
0-150 km	cvm	1.7	35	50	90	-12
0-150 km	lvz	2.7	23	69	52	-15
0-300 km	cvm	0.7	37	44	95	-9
0-300 km	lvz	2.0	23	23	44	7
0-650 km	cvm	0.3	37	34	96	-6
0-650 km	lvz	1.8	35	-6	69	25

Model: Thermal and compositional variations in same layer — Variance reduction, %

Layer thickness	Viscosity structure	ΔT range	ΔMg# range	total	bathym	geoid	SS-S
0-150 km	cvm	525 K	1.9	89	57	90	100
0-150 km	lvz	555 K	1.9	81	78	58	100
0-300 km	cvm	275 K	1.1	89	51	94	100
0-300 km	lvz	290 K	1.9	75	87	37	100
0-650 km	cvm	140 K	0.6	89	43	95	100
0-650 km	lvz	160 K	1.5	84	72	69	100

Model: Temperature variations only, high-order geoid — Variance reduction, %

Layer thickness	Viscosity structure	ΔT range	total	bathym	geoid	SS-S
0-150 km	cvm	80 K	30	18	62	27
0-150 km	lvz	275 K	47	52	5	67
0-300 km	cvm	35 K	29	12	78	22
0-300 km	lvz	195 K	43	59	-10	55
0-650 km	cvm	20 K	30	10	83	26
0-650 km	lvz	80 K	23	31	-46	56

cvm = constant viscosity mantle
lvz = mantle with low viscosity zone

Figure Captions

Figure 4.1. Location map of the East Pacific Rise, after *Macdonald* [1989]. Spreading centers, transform faults, propagating rifts, and overlapping spreading centers are shown.

Figure 4.2. Distribution of earthquakes (triangles) and seismograph stations (circles) used to measure SS-S differential travel times. Stations are from the GDSN and GEOSCOPE digital arrays. Earthquakes are from the Harvard CMT catalogue (generally $m_b > 5.0$) from the years 1980-1988, and from a listing of intraplate events from the years 1980-1987 (E. A. Bergman, personal communication, 1991). Plate boundaries are from *DeMets et al.* [1990]. Lambert equal area projection with pole of projection at 5°N, -110°W.

Figure 4.3. Bathymetric map of East Pacific Rise and Cocos plate region, from DBDB5C [*U.S. Naval Oceanographic Office*, 1985]. Contour interval 1000 m. Straight lines show location of profiles examined in this study.

Figure 4.4. Residual geoid map for East Pacific Rise and Cocos plate region, derived from gridded altimetric data of *Marsh et al.* [1986] with the low order (to degree and order 7, tapered to degree and order 11) portion of GEM-T2 reference field [*Marsh et al.*, 1990] removed. Contour interval 2 m. Straight lines show location of profiles examined in this study.

Figure 4.5. Map view of SS-S residuals relative to PREM [*Dziewonski and Anderson*, 1981], corrected for Earth ellipticity and seafloor bathymetry. Residuals are

plotted at the SS bounce point. The size of each symbol scales linearly with the magnitude of the residual. A mean of +4.15 s has been removed from the data for plotting purposes. Negative residuals indicate early SS (or late S). Plate boundaries are from *DeMets et al.* [1990]. Mercator projection.

Figure 4.6. (a) SS-S travel time residual versus square root of seafloor age. Each plotted point represents the weighted mean of 25 adjacent data points. Horizontal and vertical bars are standard errors of the means of the travel time residuals and $(age)^{1/2}$. Linear regression yields a slope of -0.01 ± 0.08 s/ $(My)^{1/2}$ for a 0- 50 My age range (solid line). Age dependence of travel time residual predicted by the plate cooling model is shown as a dashed line.

(b) SS-S travel time residual versus the square root of the age predicted by the plate cooling model [*Parsons and Sclater*, 1977] for the given depth. Each plotted point represents the weighted mean of 25 adjacent data points. Linear regression yields a slope of -0.26 ± 0.04 s/ $(My)^{1/2}$ for a 0-33 My age range (solid line). Age dependence of travel time residual predicted by the plate cooling model is shown as a dashed line.

Figure 4.7. (a) SS-S residual versus azimuth θ. Each plotted point represents the weighted mean of 25 adjacent data points. The solid curve shows the best-fitting 4θ variation derived from these data.

(b) Age-corrected SS-S residual (see text) versus azimuth θ. Each plotted point represents the weighted mean of 25 adjacent data points. The solid curve shows the best-fitting 4θ variation derived from these data.

Figure 4.8. Map view of sampling azimuths. Lines indicate the wave path azimuth at the SS bounce point. Mercator projection.

Figure 4.9. Map view of age-corrected SS-S residuals. Residuals are plotted at the SS bounce point. The size of each symbol scales linearly with magnitude of the residual.

Figure 4.10. Profile 1 across the East Pacific Rise south of the Pacific-Cocos-Nazca triple junction. (a) Seafloor age at SS bounce points. Data corresponding to SS bounce points of "A" and "B" quality are designated by crosses. "C" quality data are designated by small dots. The rise axis is marked by a straight line. (b) Bathymetry at SS bounce points (see Figure 4.3). (c) Residual geoid at SS bounce points (see Figure 4.4). (d) SS-S travel time residuals. (e) Age corrected geoid, using the method of *Hager* [1983]. (f) Age corrected geoid, using the method of *Parsons and Richter* [1980] (g) Age corrected bathymetry, using the method of *Parsons and Sclater* [1977]. (h) Age corrected SS-S travel time residuals (see text). (i) High-order portion of the geoid (GEM-T2 reference field to degree and order 10 removed). No age correction applied. The residuals shown in b - i are weighted moving averages (such that each point is used twice) of 4 adjacent data points.

Figure 4.11. Profile 2, across the Galapagos Spreading Center. See Figure 4.10 for explanation. Location nearest present Galapagos hotspot marked with an asterisk.

Figure 4.12. Profile 3 across the East Pacific Rise north of the Pacific-Cocos-Nazca triple junction. See Figure 4.10 for explanation.

Figure 4.13. Profile 4 across the East Pacific Rise north of the Pacific-Cocos-Nazca triple junction. See Figure 4.10 for explanation.

Figure 4.14. Results of combined inversion of geoid, bathymetry, and SS-S travel time residuals for upper mantle temperature variations along Profile 2. The viscosity structure is taken to consist of a 40-km-thick high-viscosity lid overlying a constant-viscosity halfspace. Location nearest Galapagos hotspot marked with an asterisk.
(a) Three solutions for lateral temperature variations: Dotted line: Temperature perturbations constrained to be uniform over 0-150 km depth. Long-dashed line: Temperature perturbations constrained to be uniform over 0-300 km depth. Short-dashed line: Temperature perturbations constrained to be uniform over 0-650 km depth.
(b) Observed (solid line) and predicted profiles of SS-S travel time residual. The "observed" profile is actually a filtered version of the observations, containing only the wavelengths used in the inversion (850 to 5000 km). Line types correspond to those of the temperature models.
(c) Observed and predicted geoid profiles. Same treatment as in (b).
(d) Observed and predicted bathymetry profiles. Same treatment as in (b).

Figure 4.15. Results of combined inversion of geoid, bathymetry, and SS-S travel time residuals for upper mantle temperature variations along Profile 2. The viscosity structure includes a zone extending from the base of the high-

viscosity lid to a depth of 200 km with a viscosity equal to 0.01 that of the underlying mantle. Other aspects as in Figure 4.14.

Figure 4.16. Results of combined inversion of geoid, bathymetry, and SS-S travel time residuals for variations in upper mantle composition (Mg#). The viscosity structure is taken to consist of a 40-km-thick high-viscosity lid overlying a constant-viscosity halfspace.
(a) Three solutions for lateral composition variations: Dotted line: Composition perturbations constrained to be uniform over 0-150 km depth. Long-dashed line: Composition perturbations constrained to be uniform over 0-300 km depth. Short-dashed line: Composition perturbations constrained to be uniform over 0-650 km depth.
(b) Observed (solid line) and predicted profiles of SS-S travel time residual.
(c) Observed and predicted geoid profiles.
(d) Observed and predicted bathymetry profiles.

Figure 4.17. Results of combined inversion of geoid, bathymetry, and SS-S travel time residuals for variations in upper mantle composition (Mg#). The viscosity structure includes a zone extending from the base of the high-viscosity lid to a depth of 200 km with a viscosity equal to 0.01 that of the underlying mantle. Other aspects as in Figure 4.16.

Figure 4.18. Results of combined inversion of geoid, bathymetry, and SS-S travel time residuals for both upper mantle temperature and composition variations. The viscosity structure is taken to consist of a 40-km-thick high-viscosity lid overlying a constant-viscosity halfspace.

(a) Three solutions for lateral temperature variations: Dotted line: Composition perturbations constrained to be uniform over 0-150 km depth. Long-dashed line: Composition perturbations constrained to be uniform over 0-300 km depth. Short-dashed line: Composition perturbations constrained to be uniform over 0-650 km depth.
(b) Three solutions for lateral composition variations: Dotted line: Composition perturbations constrained to be uniform over 0-150 km depth. Long-dashed line: Composition perturbations constrained to be uniform over 0-300 km depth. Short-dashed line: Composition perturbations constrained to be uniform over 0-650 km depth.
(c) Observed (solid line) and predicted profiles of SS-S travel time residual.
(d) Observed and predicted geoid profiles.
(e) Observed and predicted bathymetry profiles.

Figure 4.19. Results of combined inversion of geoid, bathymetry, and SS-S travel time residuals for both upper mantle temperature and composition variations. The viscosity structure includes a zone extending from the base of the high-viscosity lid to a depth of 200 km with a viscosity equal to 0.01 that of the underlying mantle. Other aspects as in Figure 4.18.

Figure 4.20. Results of combined inversion of high-order geoid (see Figure 4.10i), bathymetry, and SS-S travel time residuals for upper mantle temperature variations along Profile 2. The viscosity structure is taken to consist of a 40-km-thick high-viscosity lid overlying a constant-viscosity halfspace. Other aspects as in Figure 4.14.

Figure 4.21. Results of combined inversion of high-order geoid (see Figure 4.10i), bathymetry, and SS-S travel time residuals for upper mantle temperature variations along Profile 2. The viscosity structure includes a zone extending from the base of the high-viscosity lid to a depth of 200 km with a viscosity equal to 0.01 that of the underlying mantle. Other aspects as in Figure 4.15.

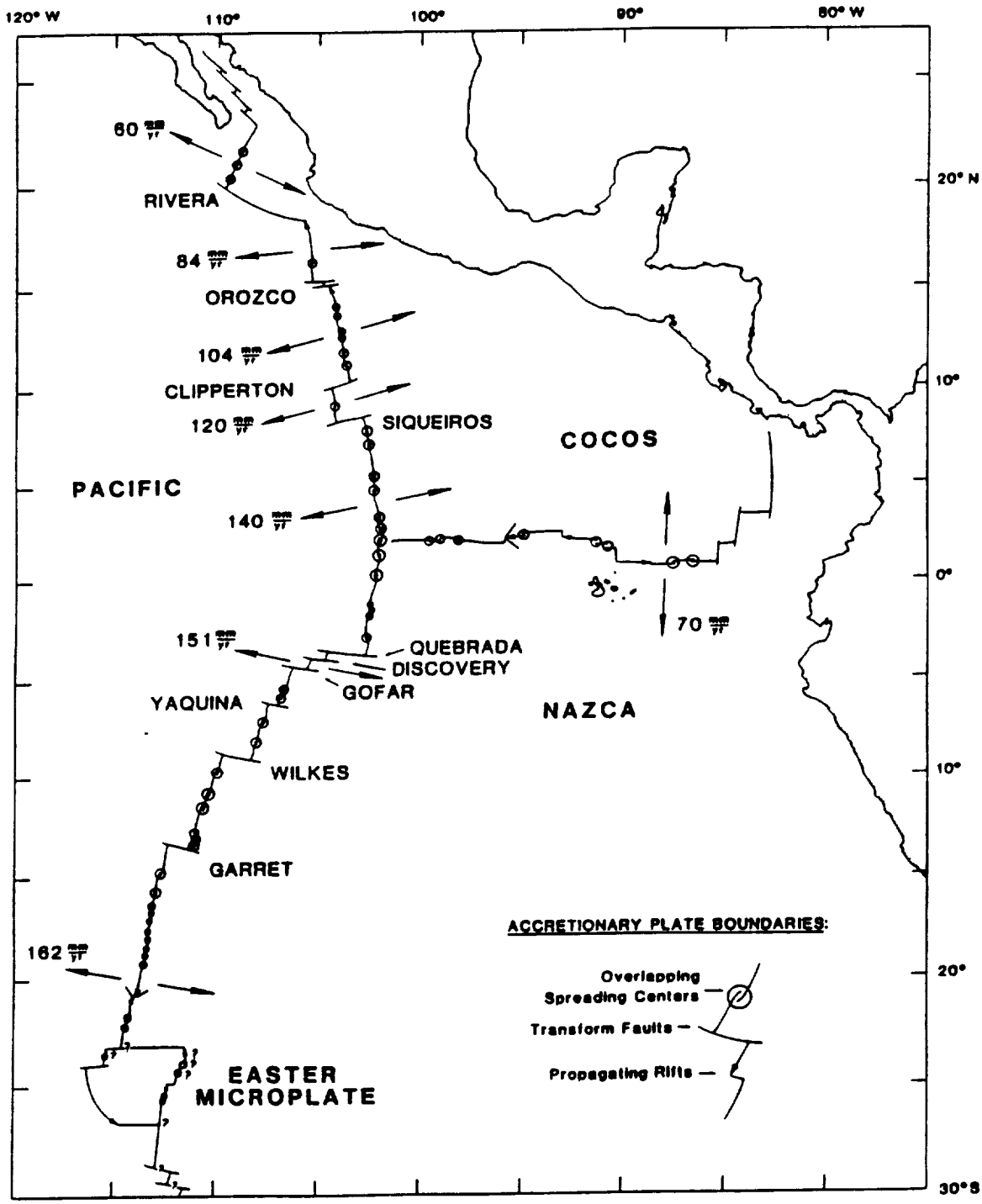
120° W
110°
100°
90°
80° W
20° N
10°
0°
10°
20°
30°S
60
RIVERA
84
OROZCO
104
CLIPPERTON
120
SIQUEIROS
COCOS
PACIFIC
140
70
151
QUEBRADA
DISCOVERY
GOFAR
YAQUINA
NAZCA
WILKES
GARRET
162
EASTER
MICROPLATE
ACCRETIONARY PLATE BOUNDARIES:
Overlapping
Spreading Centers
Transform Faults
Propagating Rifts

Figure 4.1

EPR Sources and Stations

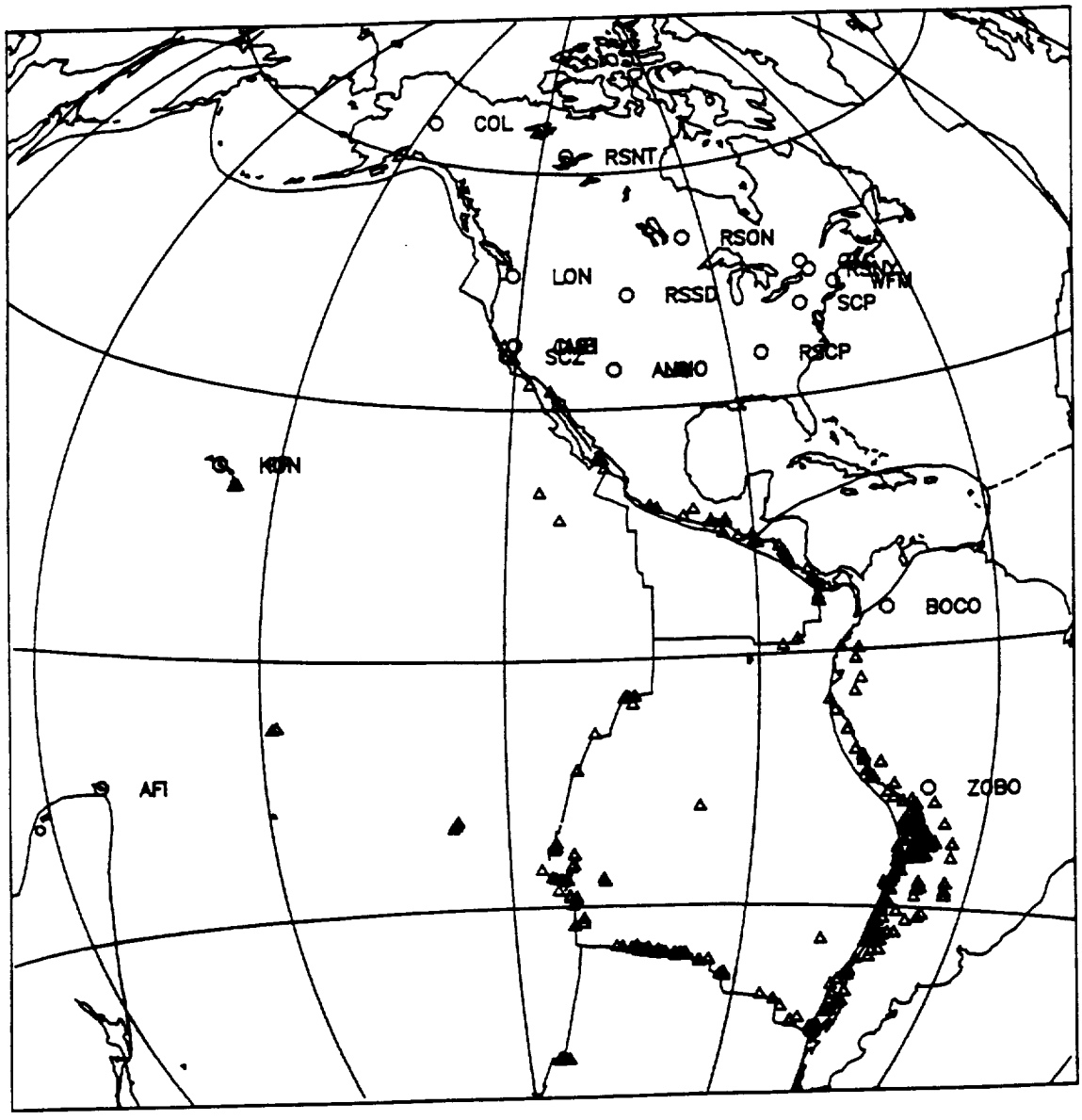

Figure 4.2

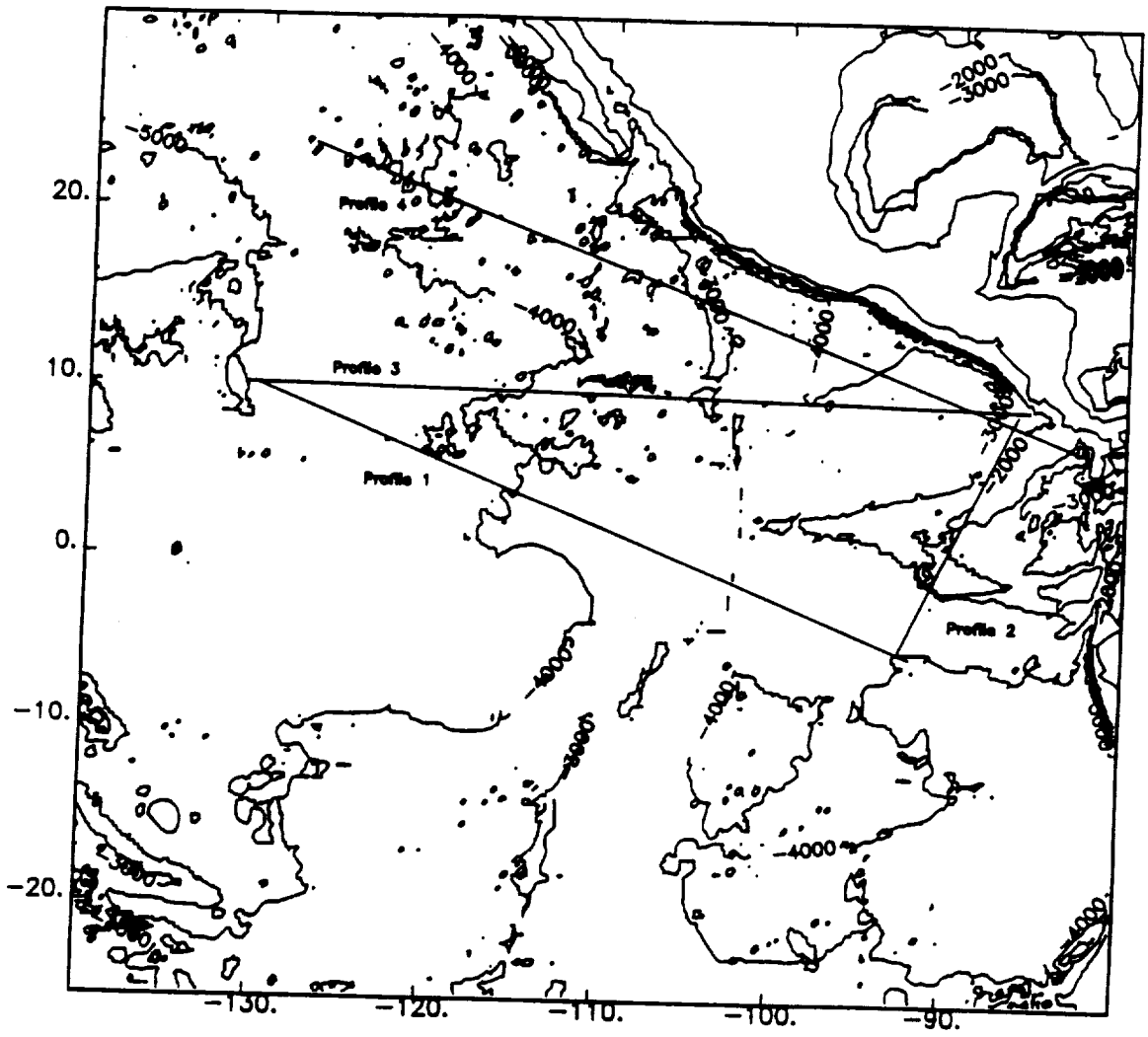
Profile 4
Profile 3
Profile 1
Profile 2
20.
10.
0.
-10.
-20.
-130.
-120.
-110.
-100.
-90.
-2000
-3000
-4000
-5000

Figure 4.3

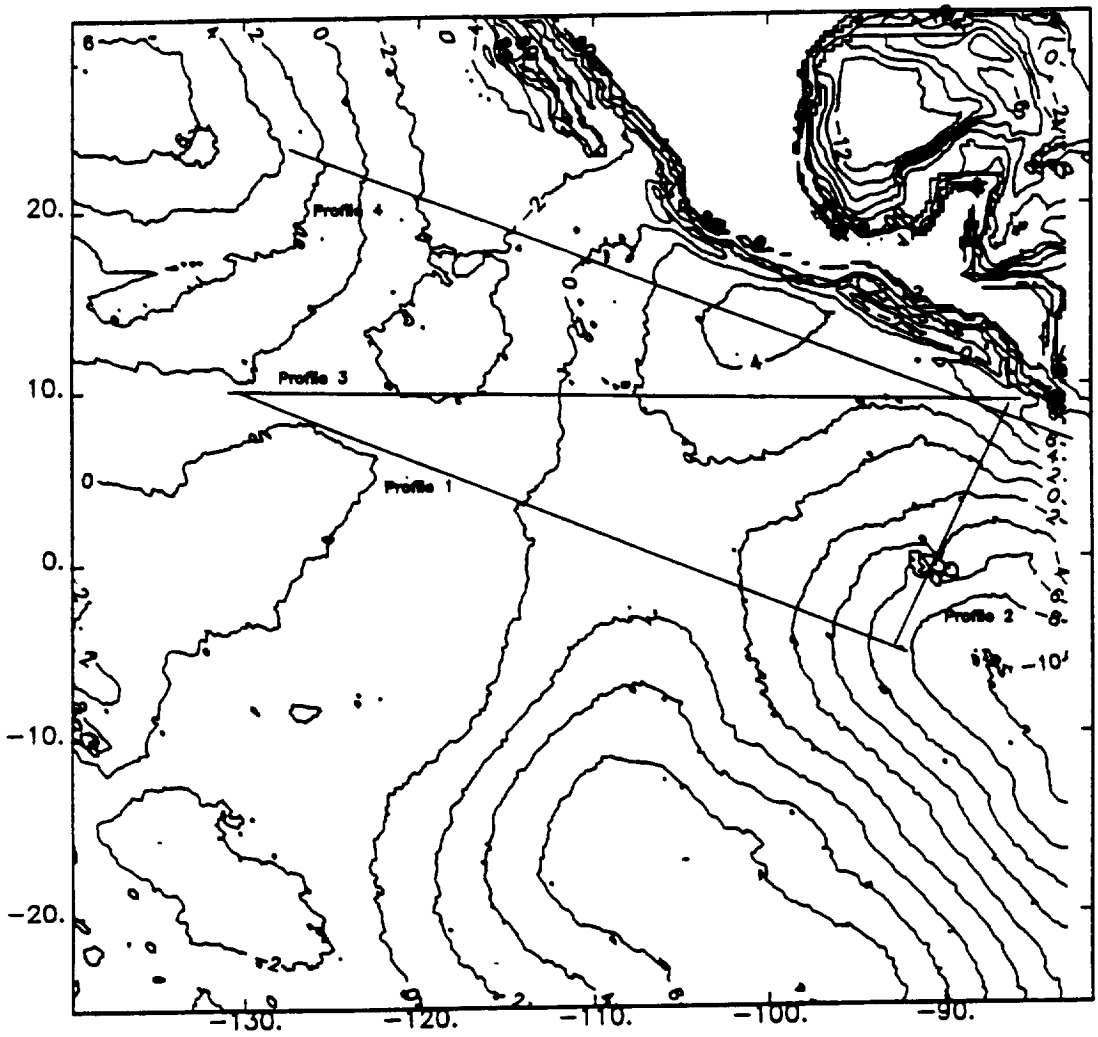
Profile 4
Profile 3
Profile 1
Profile 2
20.
10.
0.
-10.
-20.
-130.
-120.
-110.
-100.
-90.

Figure 4.4

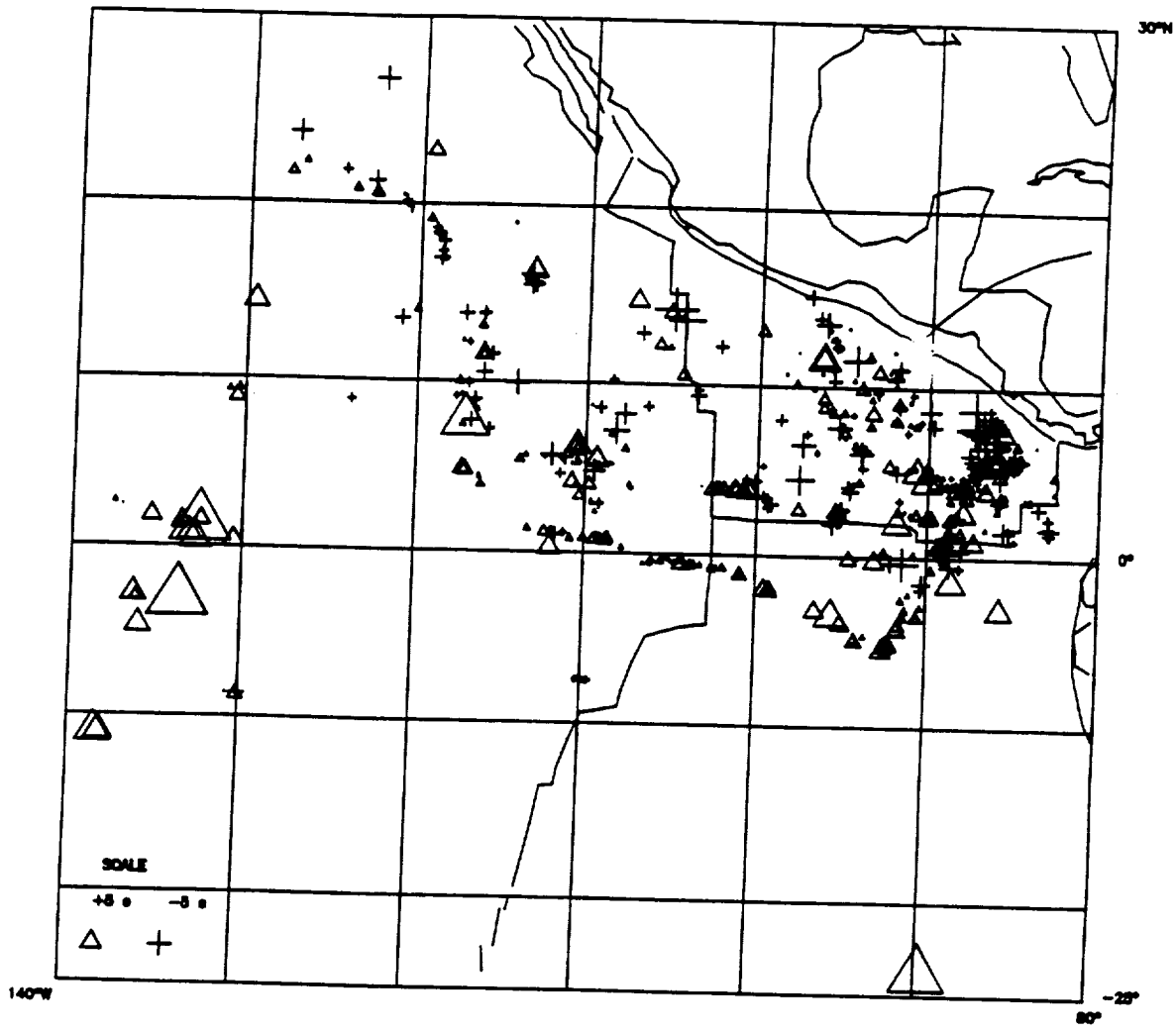

Figure 4.5

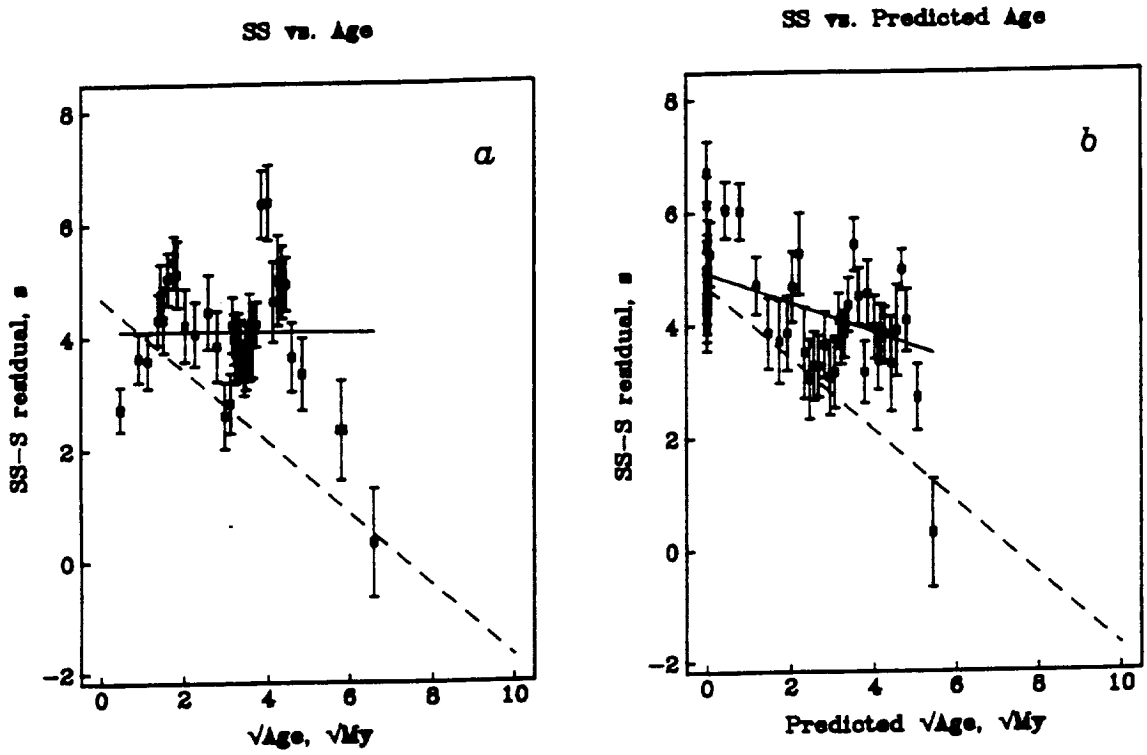
SS vs. Age
a
SS−S residual, s
√Age, √My
SS vs. Predicted Age
b
SS−S residual, s
Predicted √Age, √My

Figure 4.6

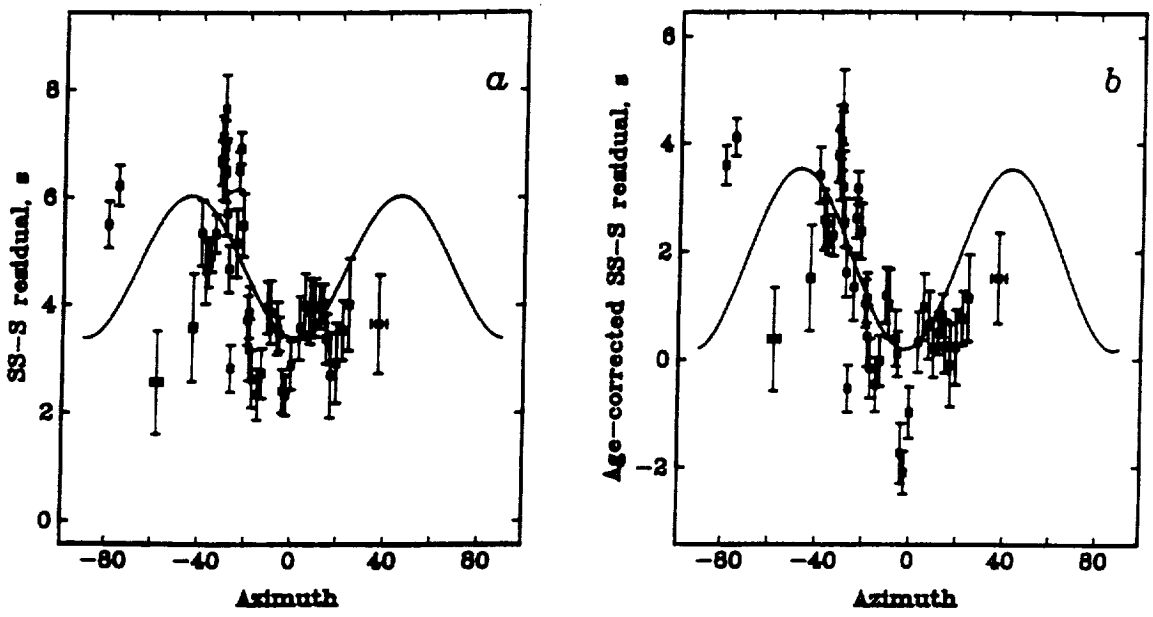
a
SS-S residual, s
8
6
4
2
0
-80
-40
0
40
80
Azimuth
b
Age-corrected SS-S residual, s
6
4
2
0
-2
-80
-40
0
40
80
Azimuth

Figure 4.7

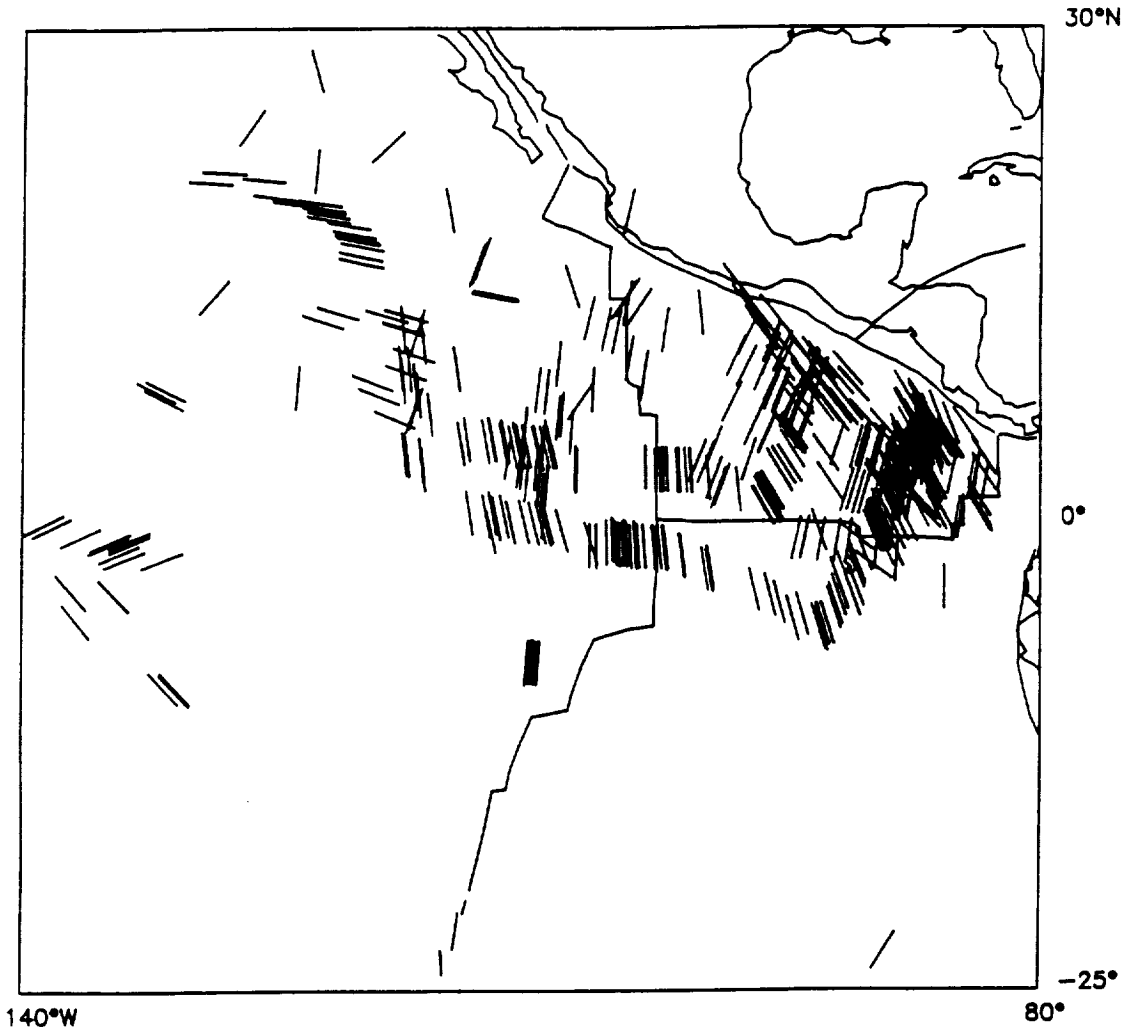

Figure 4.8

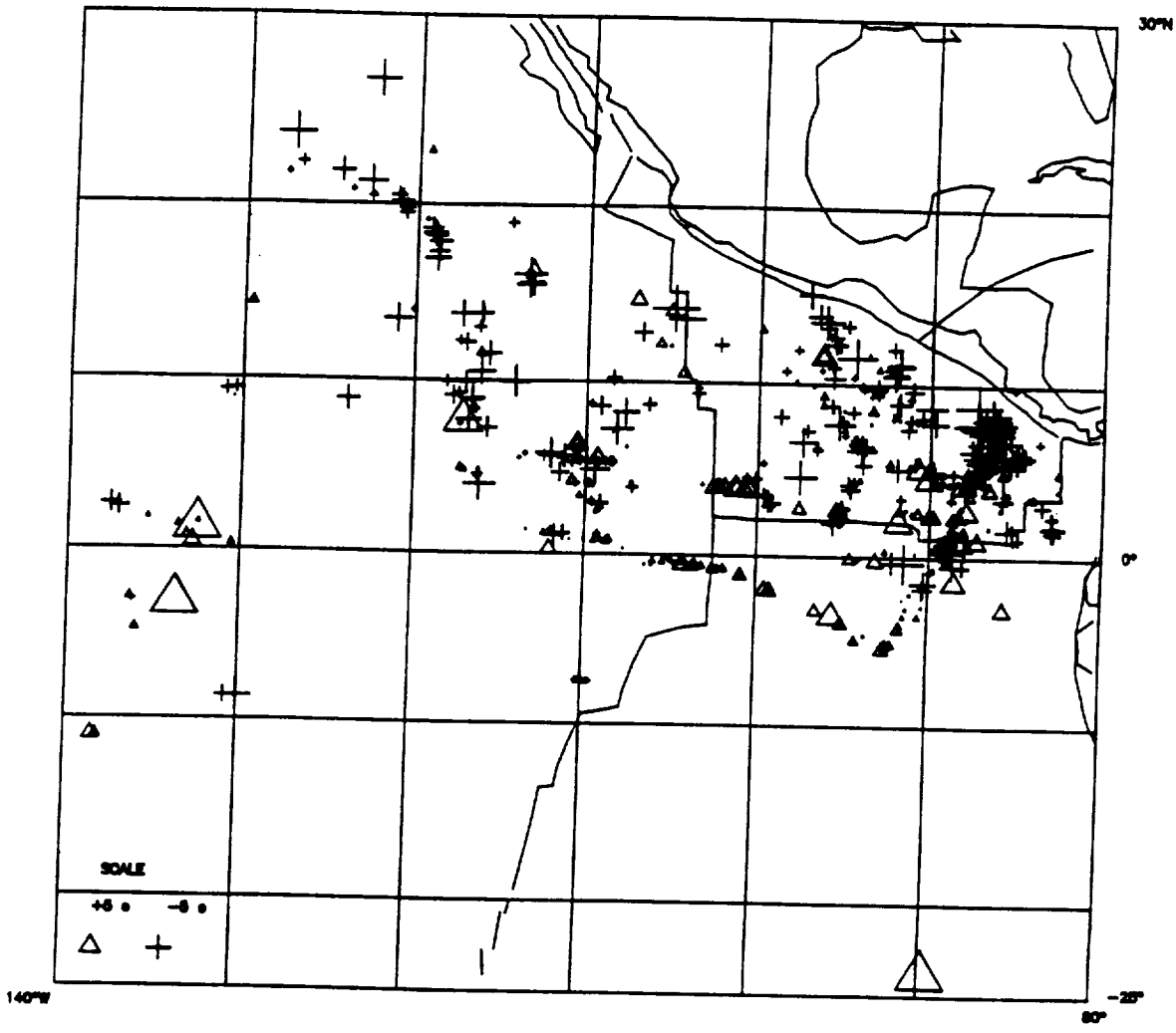

Figure 4.9

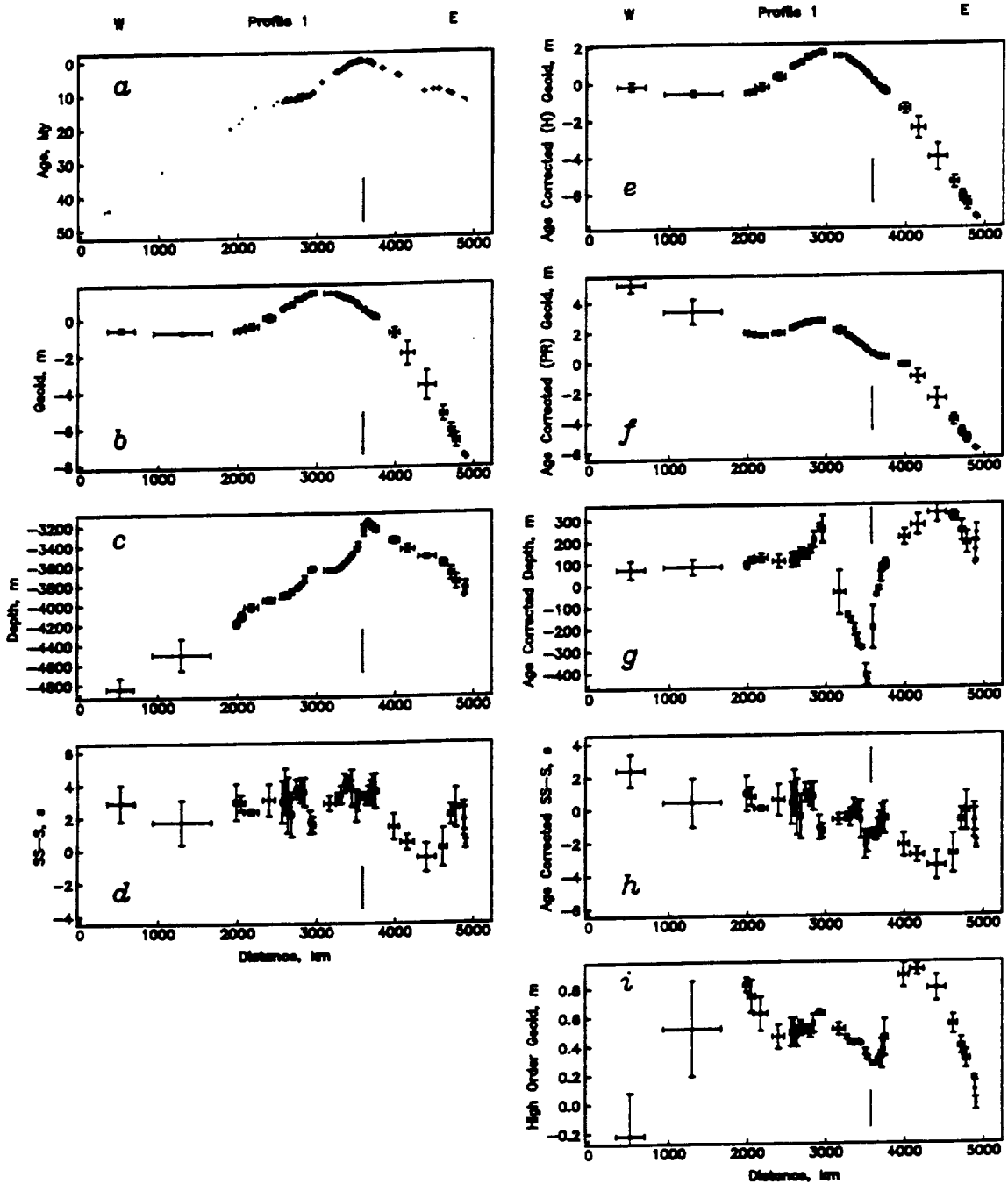
W
Profile 1
E
a
Age, My
b
Geoid, m
c
Depth, m
d
SS-S, m
Distance, km
e
Age Corrected (H) Geoid, m
f
Age Corrected (PR) Geoid, m
g
Age Corrected Depth, m
h
Age Corrected SS-S, m
i
High Order Geoid, m

Figure 4.10

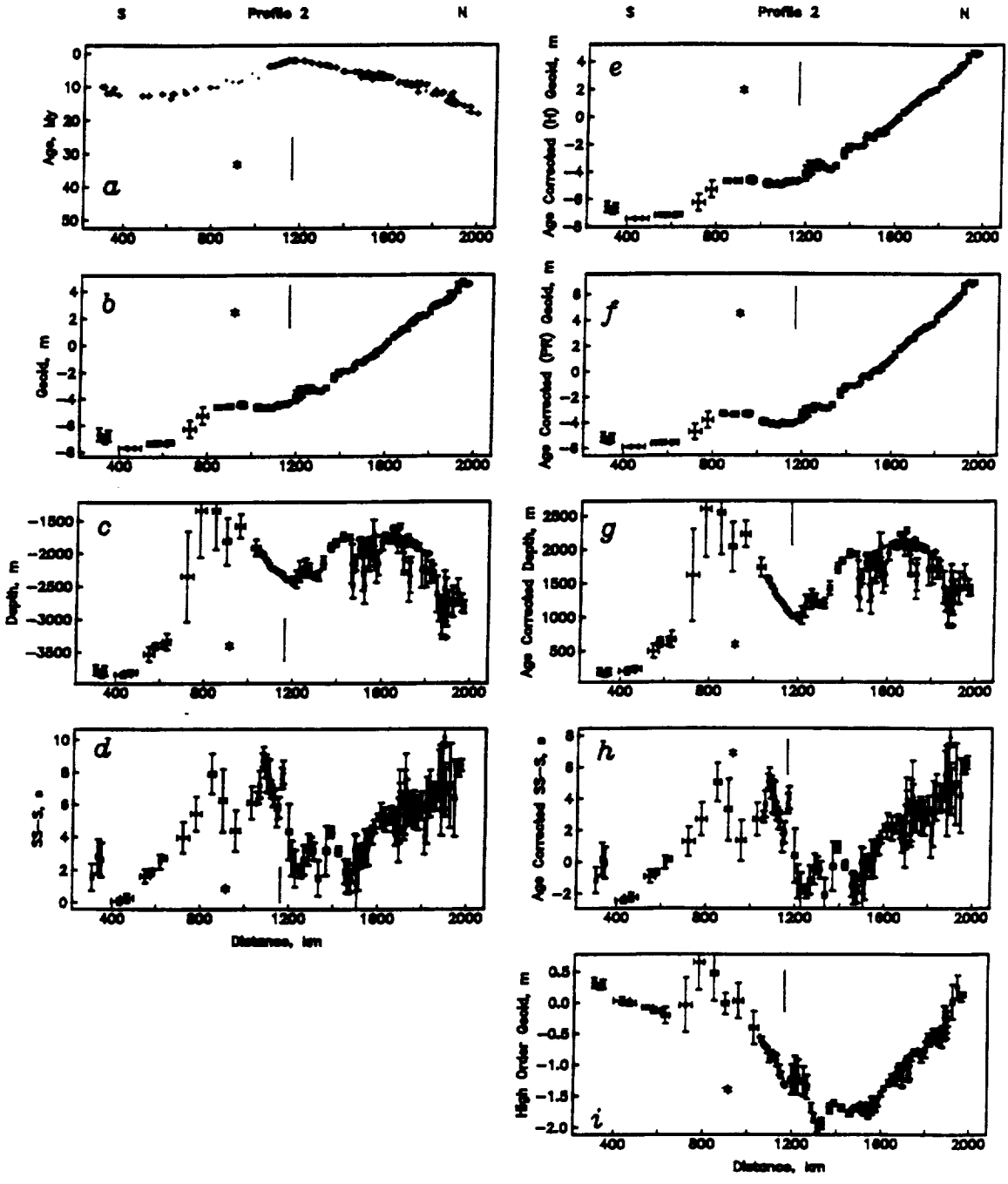
S
Profile 2
N
a
b
c
d
e
f
g
h
i
Age, My
Geoid, m
Depth, m
SS-S, m
Age Corrected (N) Geoid, m
Age Corrected (FK) Geoid, m
Age Corrected Depth, m
Age Corrected SS-S, m
High Order Geoid, m
Distance, km

Figure 4.11

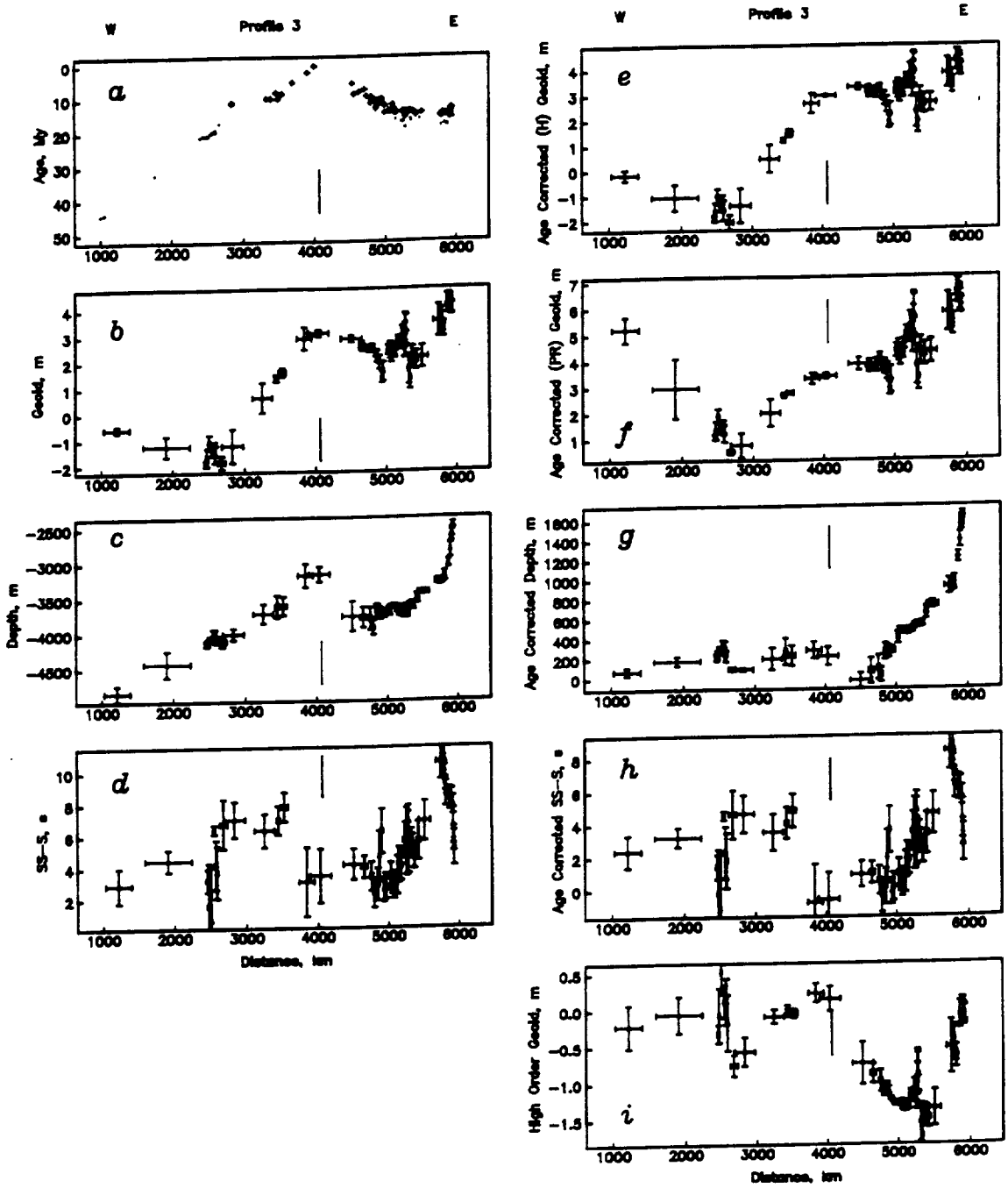
W
Profile 3
E
a
Age, My
b
Geoid, m
c
Depth, m
d
SS-S, s
Distance, km
e
Age Corrected (N) Geoid, m
f
Age Corrected (FR) Geoid, m
g
Age Corrected Depth, m
h
Age Corrected SS-S, s
i
High Order Geoid, m
Distance, km

Figure 4.12

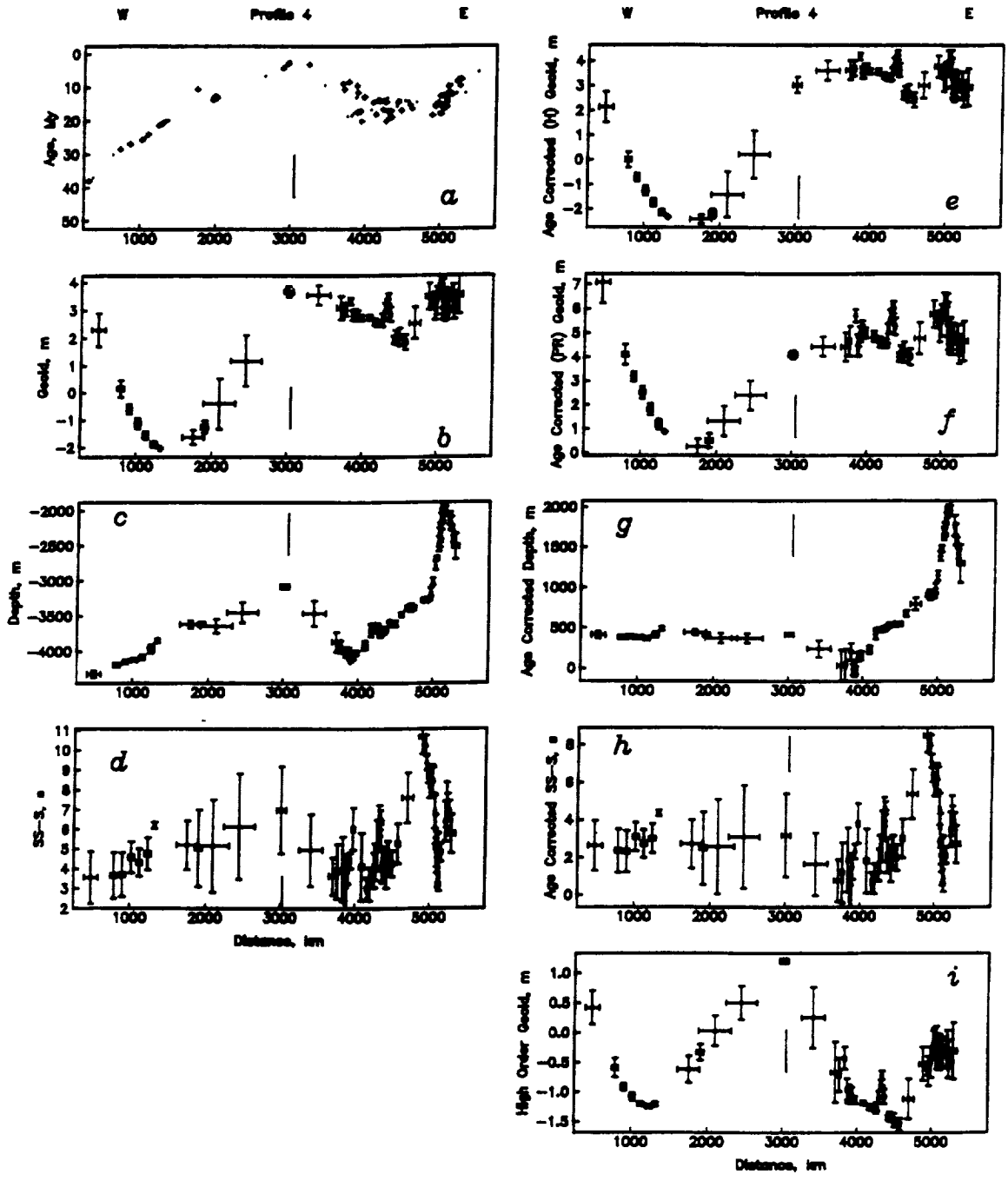

Figure 4.13

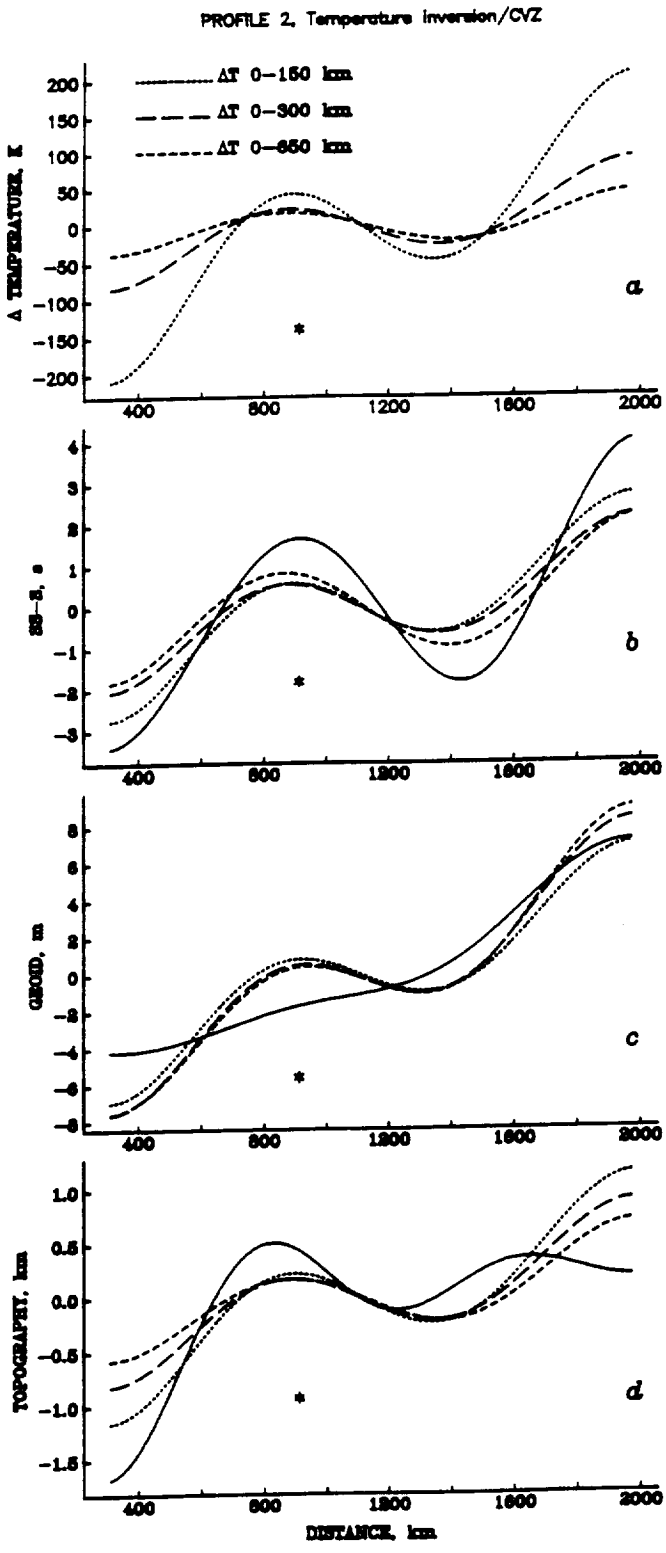
PROFILE 2, Temperature inversion/CVZ
ΔT 0–150 km
ΔT 0–300 km
ΔT 0–650 km
Δ TEMPERATURE, K
a
SS–S, e
b
GEOID, m
c
TOPOGRAPHY, km
d
DISTANCE, km

Figure 4.14

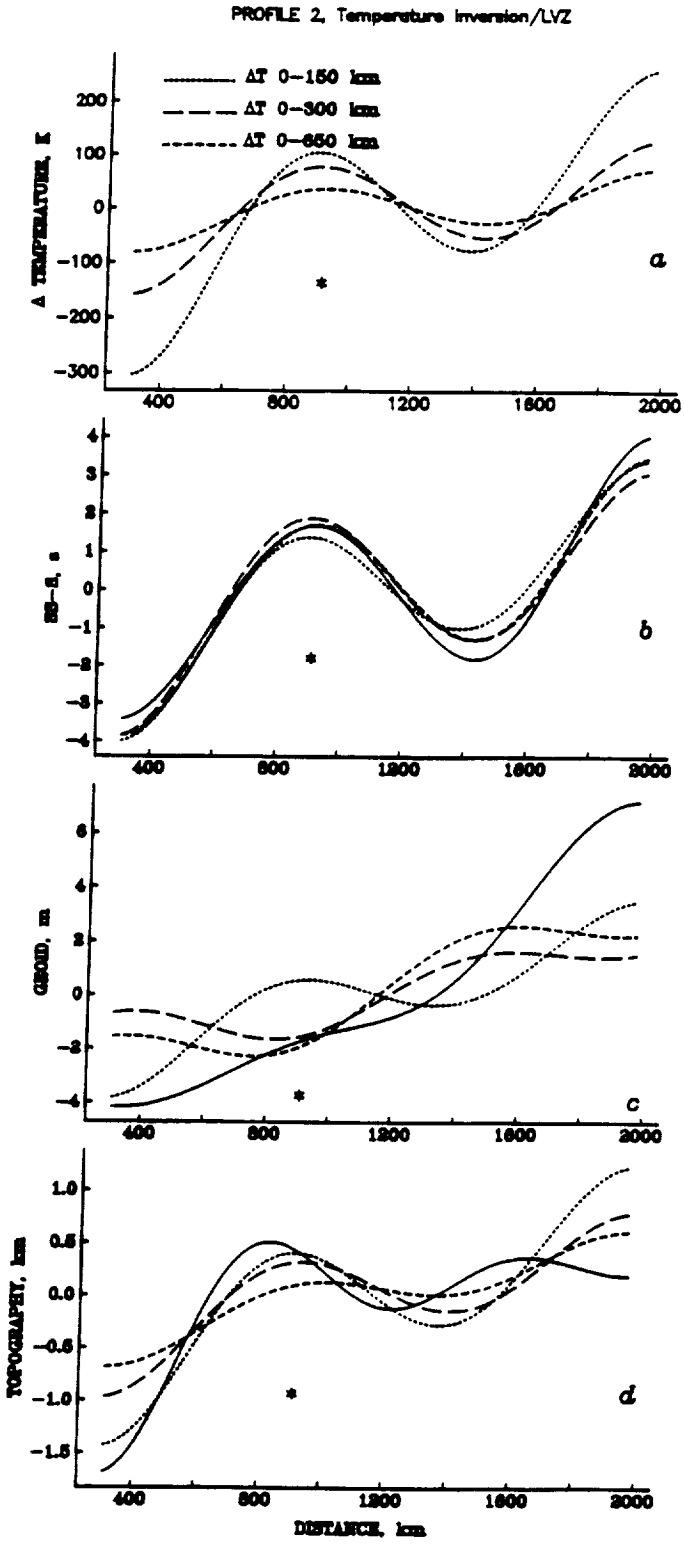
PROFILE 2, Temperature inversion/LVZ
ΔT 0–150 km
ΔT 0–300 km
ΔT 0–650 km
Δ TEMPERATURE, K
a
b
c
d
TOPOGRAPHY, km
DISTANCE, km

Figure 4.15

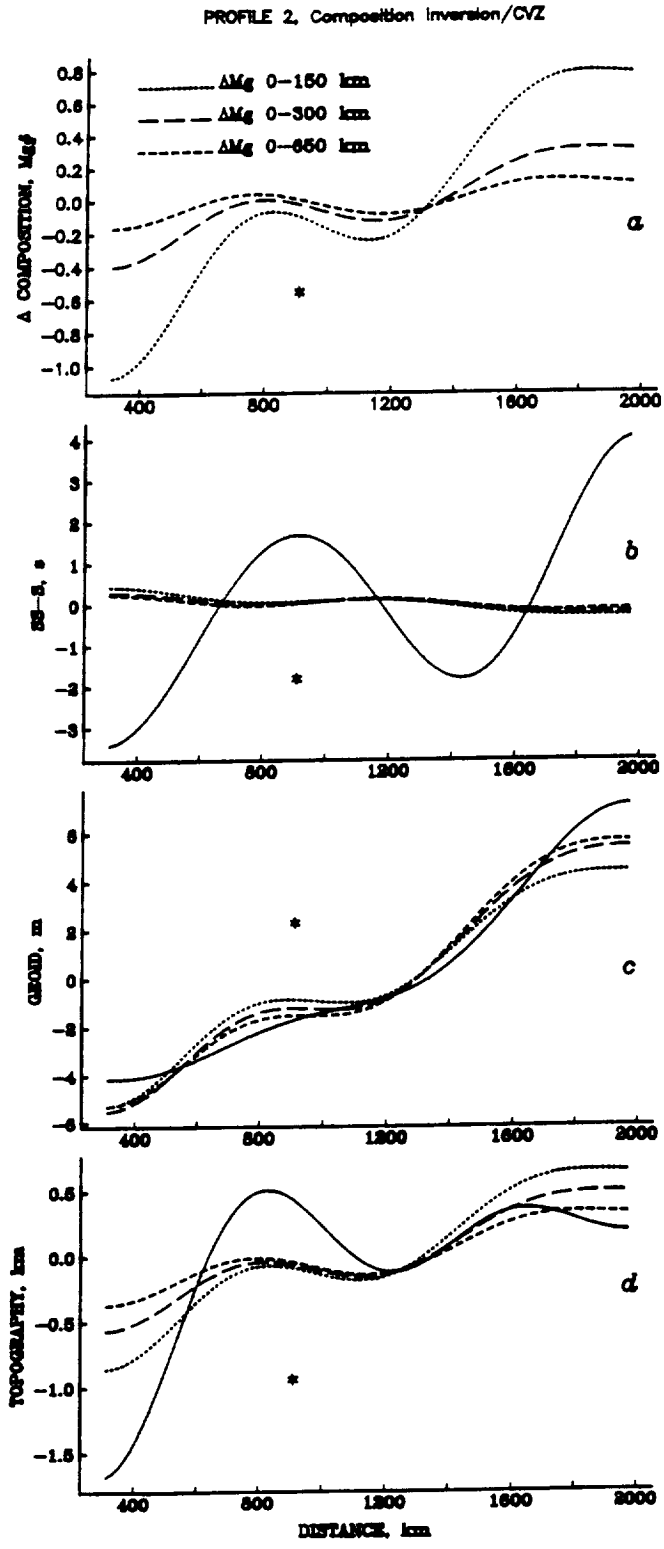
PROFILE 2, Composition inversion/CVZ
ΔMg 0–150 km
ΔMg 0–300 km
ΔMg 0–650 km
Δ COMPOSITION, Mg#
a
SS–S, s
b
GEOID, m
c
TOPOGRAPHY, km
d
DISTANCE, km

Figure 4.16

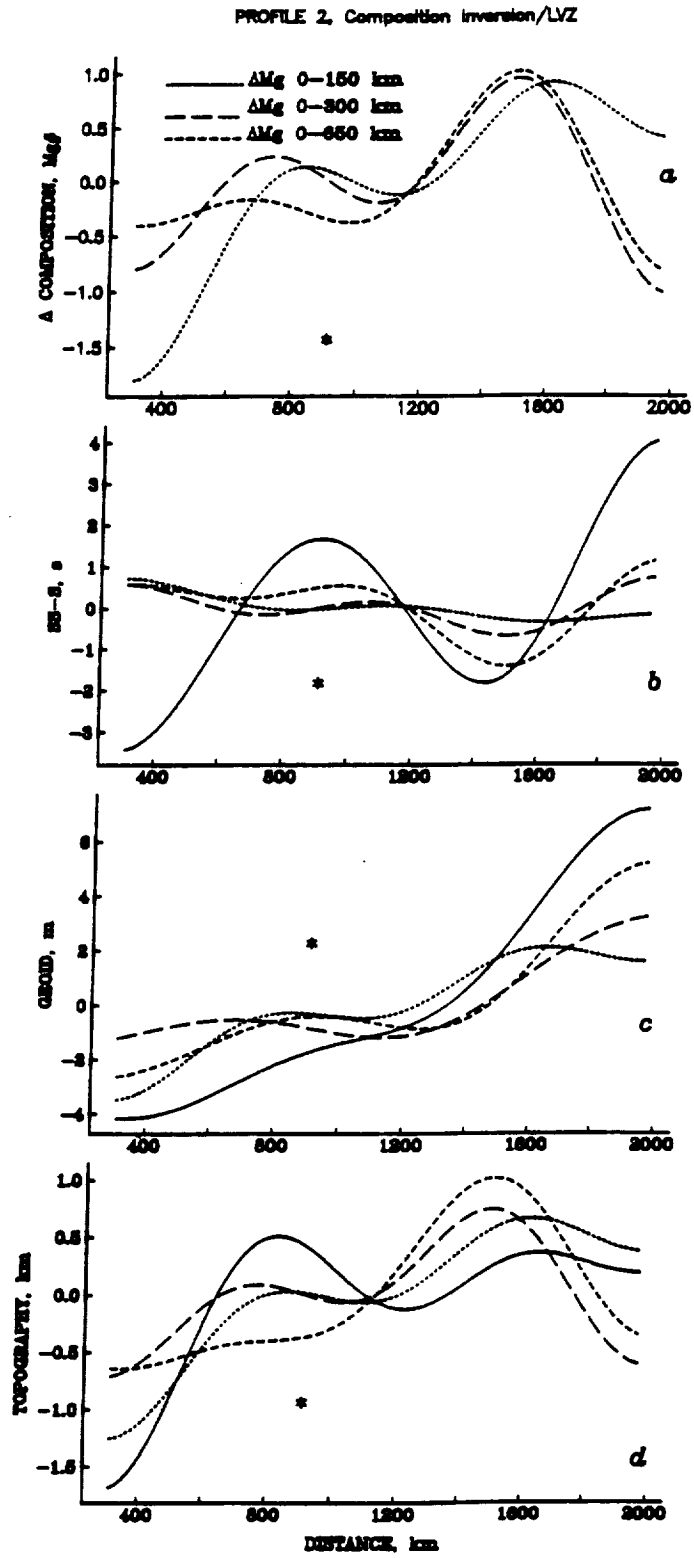
PROFILE 2, Composition inversion/LVZ
ΔMg 0–150 km
ΔMg 0–300 km
ΔMg 0–650 km
Δ COMPOSITION, Mg#
a
b
c
d
DISTANCE, km

Figure 4.17

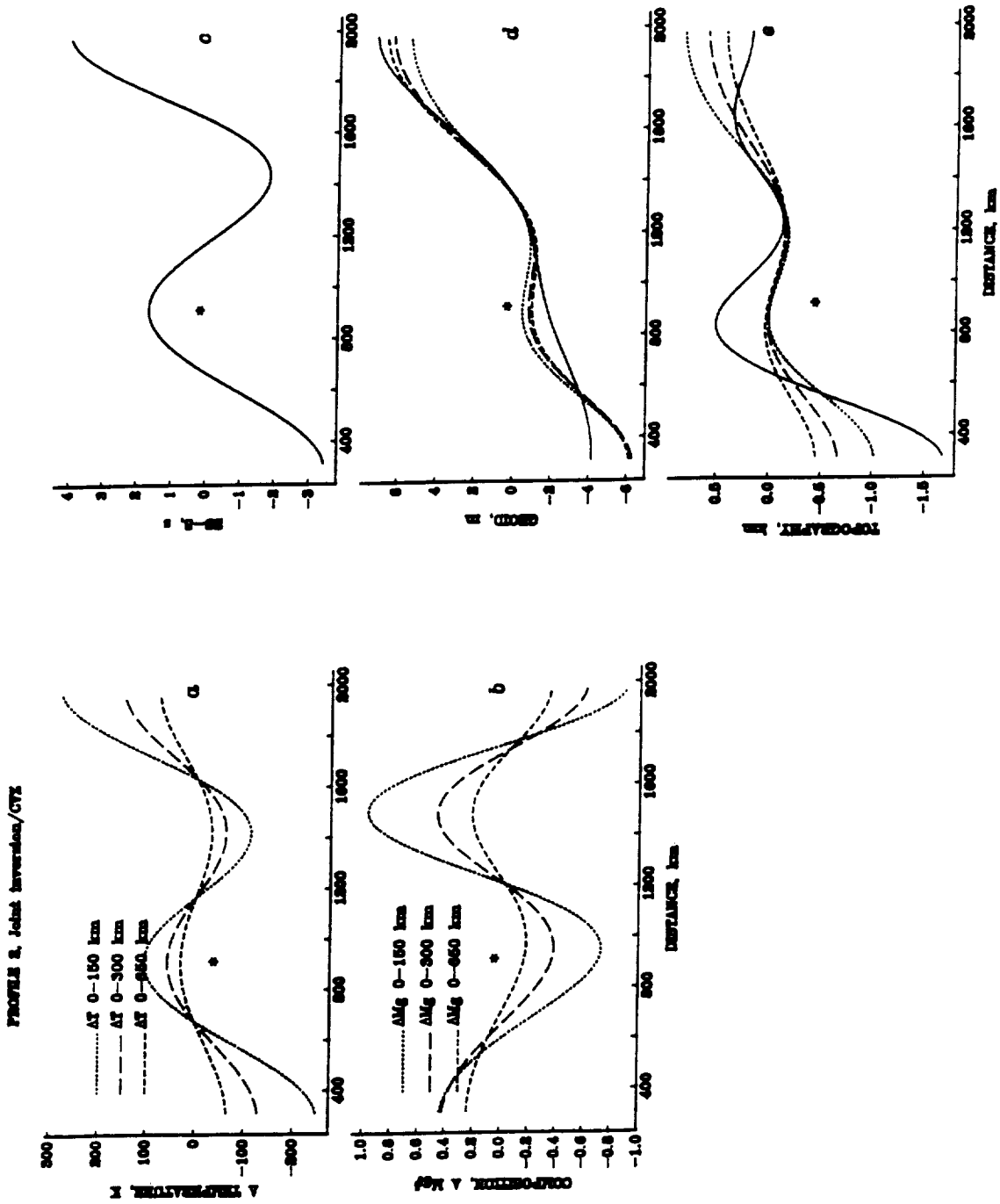
PROFILE 2, Joint inversion/GTS
a
b
c
d
e
ΔT 0–150 km
ΔT 0–300 km
ΔT 0–650 km
Δdg 0–150 km
Δdg 0–300 km
Δdg 0–650 km
DISTANCE, km

Figure 4.18

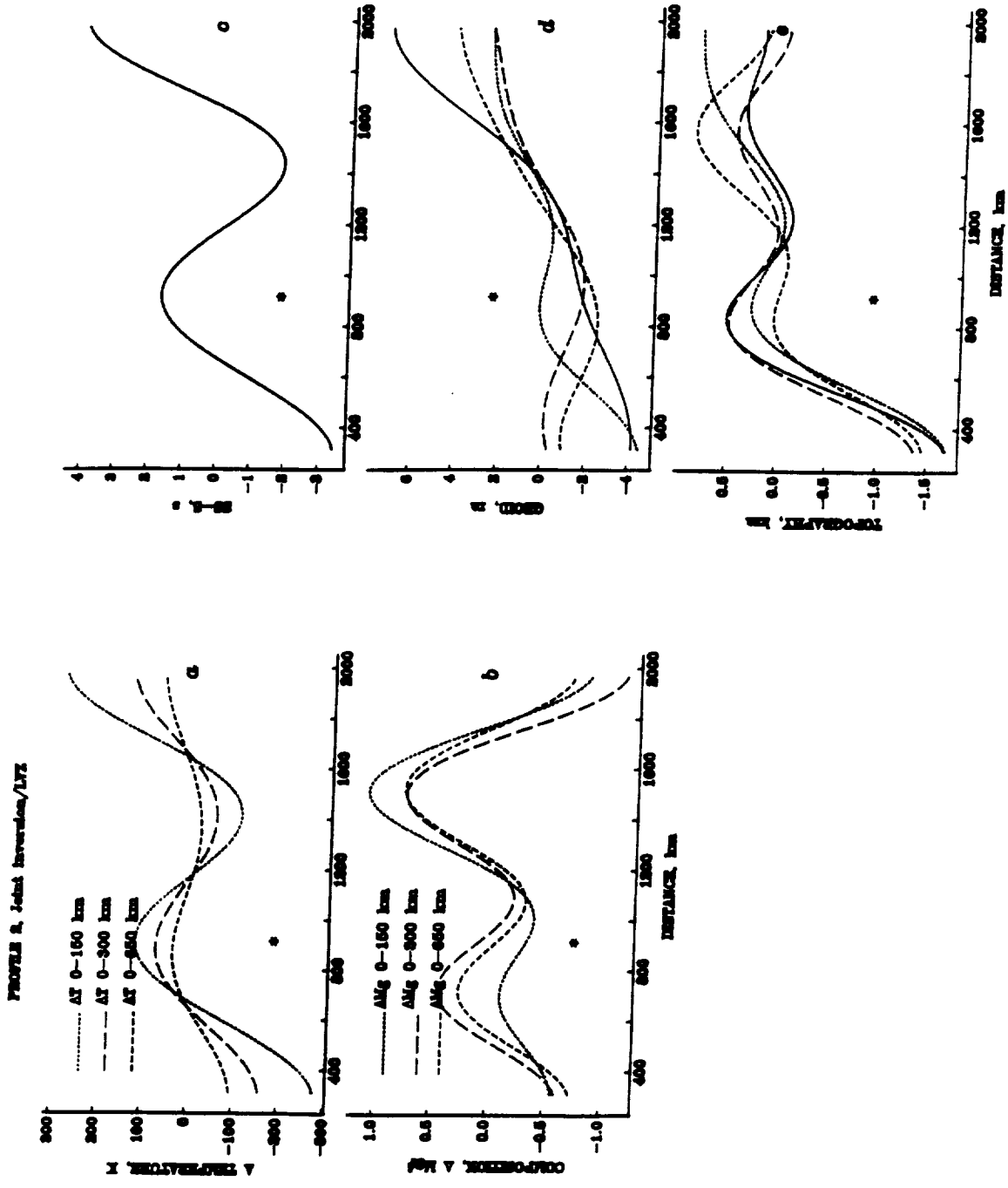
PROFILE 2. Joint Inversion/LTI
a
b
c
d
ΔT 0-150 km
ΔT 0-300 km
ΔT 0-950 km
ΔMg 0-150 km
ΔMg 0-300 km
ΔMg 0-950 km
DISTANCE, km

Figure 4.19

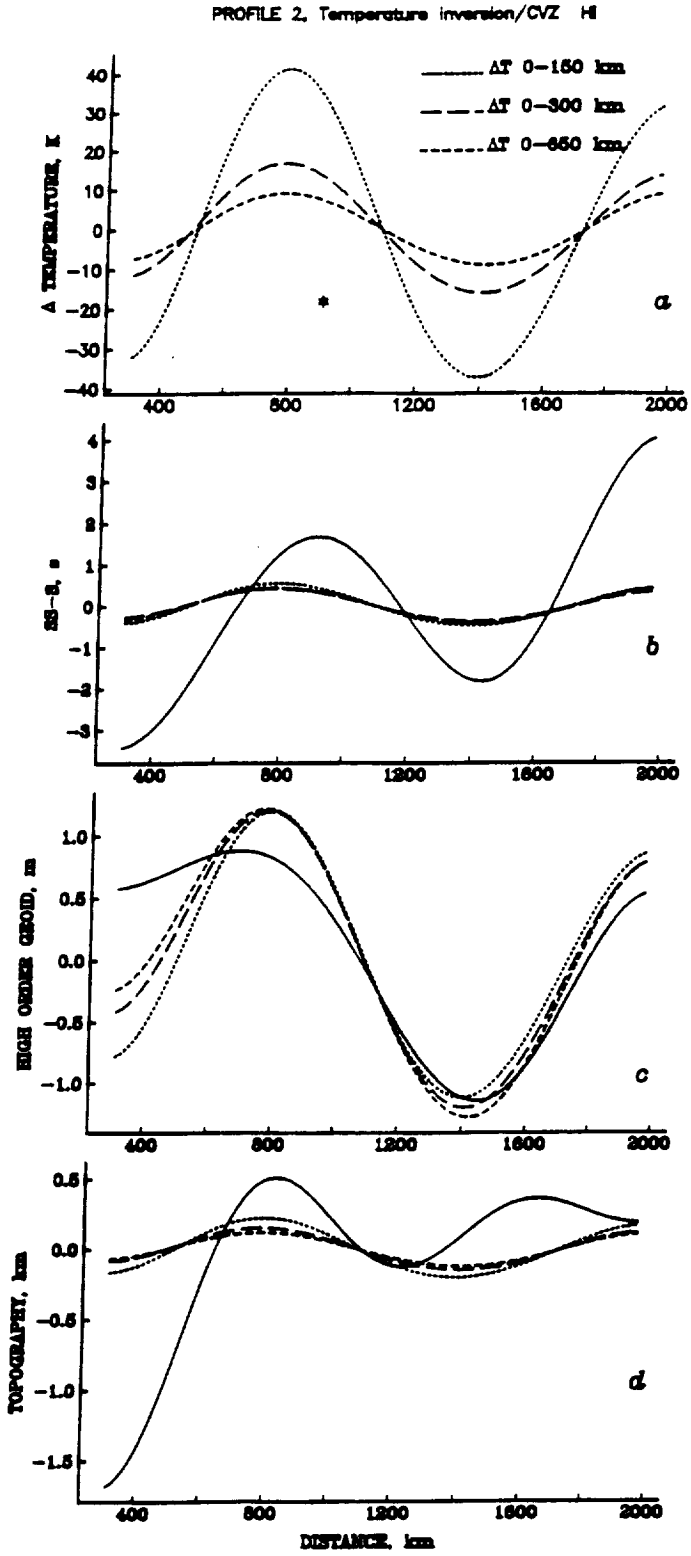
PROFILE 2, Temperature inversion/CVZ HI
ΔT 0–150 km
ΔT 0–300 km
ΔT 0–650 km
Δ TEMPERATURE, K
a
b
c
d
HIGH ORDER GEOID, m
TOPOGRAPHY, km
DISTANCE, km

Figure 4.20

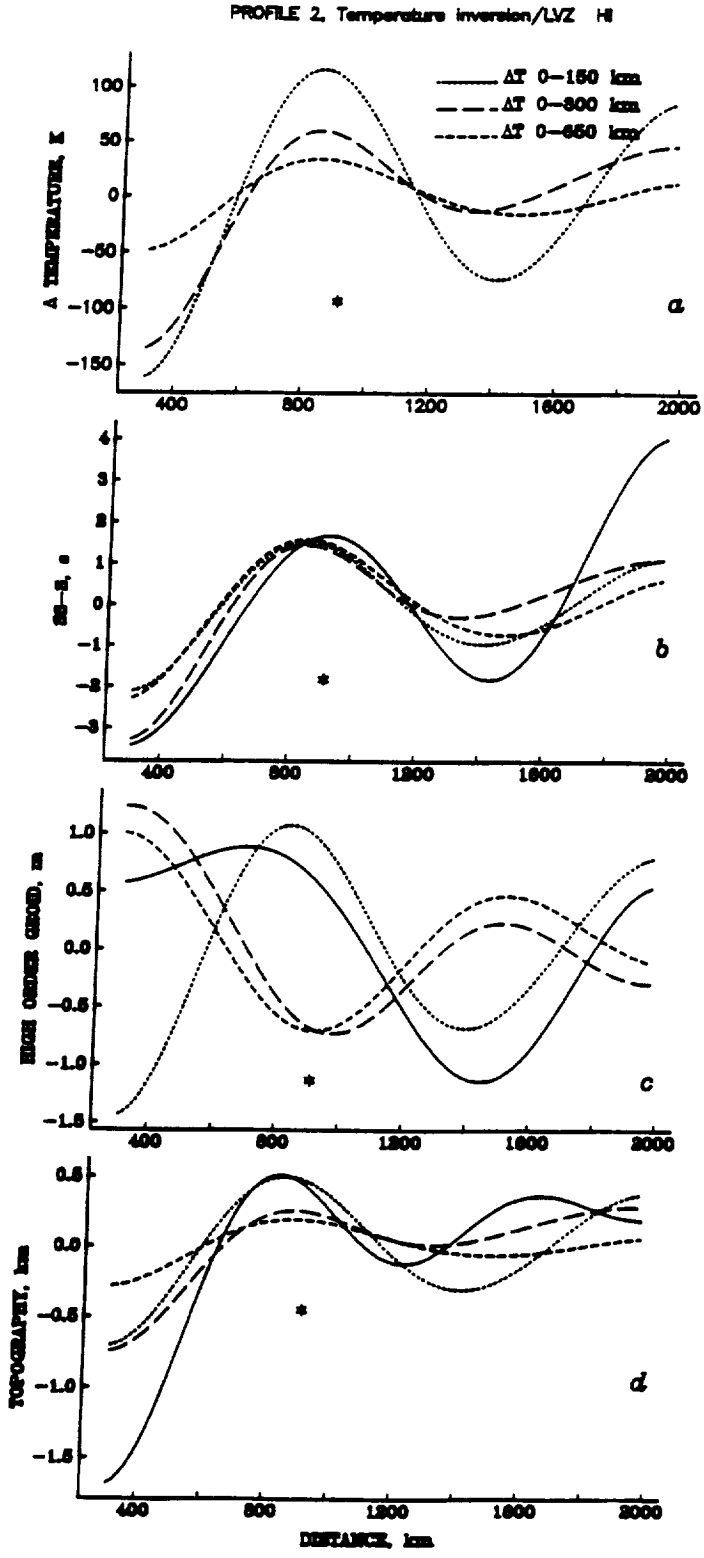
PROFILE 2. Temperature inversion/LVZ HI
ΔT 0–150 km
ΔT 0–300 km
ΔT 0–650 km
Δ TEMPERATURE, K
100
50
0
-50
-100
-150
400
800
1200
1600
2000
a
4
3
2
1
0
-1
-2
-3
b
1.0
0.5
0.0
-0.5
-1.0
-1.5
c
0.5
0.0
-0.5
-1.0
-1.5
d
DISTANCE, km

Figure 4.21

Chapter 5

Conclusions

In this thesis we have examined lateral heterogeneity in the lithosphere and asthenosphere beneath oceanic regions through a combined analysis of seismic body wave differential travel times and attenuation, geoid anomalies, and residual depth anomalies. Our focus has been to assess variations at the 1000 km scale, comparable to the thickness of the upper mantle. We have examined the data to determine whether convection on this scale can produce observable temperature and compositional anomalies. We have developed an inversion technique which allows shear wave travel time, geoid, and bathymetry data to be combined and jointly inverted for lateral variations in upper mantle temperature and composition structure, and we have applied it to data sets from both the north Atlantic and east Pacific.

Several general conclusions can be drawn from our study of SS-S differential travel times. In the Atlantic, the SS-S travel time residual decreases linearly with square root of age, in general agreement with the plate cooling model to an age of 80-100 My [*Parsons and Sclater*, 1977]. In the Pacific, SS-S travel time residuals are only weakly correlated with seafloor age, although this may be partially attributable to the fact that we do not sample a large range of plate ages in the Pacific. The travel time - age correlation in the Pacific is stronger if rather than using the actual plate age we use the age predicted by the

depth of the seafloor at the SS bounce point, in the same sense as that predicted by the lithospheric rejuvenation hypothesis [*Menard and McNutt*, 1982]. The Pacific travel time residuals are significantly larger than the Atlantic data, even at a fixed age.

Azimuthal anisotropy is not clearly resolved in the Atlantic but may be present in the east Pacific. Although not conclusive, our east Pacific data are consistent with the presence of anisotropy, with the fast axis of olivine oriented approximately parallel to the absolute plate motion vector for the Cocos plate. It has been suggested that anisotropy may be more pronounced at fast spreading rates than at slow spreading rates both in the lithosphere (due to rate-dependence of the mechanism for orienting olivine crystals) and in the asthenosphere (due to the flow regime), and our results are consistent with this suggestion. There is substantial ambiguity in our Pacific anisotropy measurements, however, due to a poor sampling of azimuths.

We have observed lateral variations in age-corrected SS-S residuals with a dominant wavelength of 1000 to 2000 km. Comparable variations are also observed in bathymetry and geoid height. We have formulated a joint inversion of geoid, travel time, and bathymetry for lateral variations in temperature and composition as a means to assess more quantitatively the observed correlations. In the north Atlantic, inversion for temperature favors the presence of an upper mantle low viscosity zone and temperature anomalies concentrated at depths less than 300 km. We are unable to match travel time residuals simultaneously with geoid and bathymetry solely with lateral variations in bulk composition (Mg#). Joint inversions for temperature and composition provide good fits to both travel time and and geoid regardless of viscosity structure or layer depth and thickness, but the best fits to bathymetry come from models with a low-viscosity zone and thermal or compositional variations confined to shallow depth. The variations in Mg# predicted in the joint inversion for temperature and composition are comparable to those found by *Michael and Bonatti* [1985] in a study of dredged peridotites along the

Mid-Atlantic Ridge and may be related to variations in melt production along the ridge. In the Pacific we applied the inversion techniques to a north-south profile orthogonal to the Galapagos spreading center. In this region we also find that compositional variations alone are inadequate to produce good fits to travel time and geoid and bathymetry simultaneously. Temperature variations alone, however, produce significant variance reduction. The models predict excess temperature in the vicinity of the Galapagos hotspot in the range 50 to 150 K.

As a complement to the travel time studies, we also measured SS-S differential attenuation in the north Atlantic region. As with the travel time residuals, we find that δt^* decreases with increasing seafloor age. We do not observe evidence for a narrow region of very low Q lying beneath the Mid-Atlantic Ridge as reported by *Solomon* [1973], although this may be due to the limited spatial resolution of the long-period shear waves utilized in our study. We derive empirical Q^{-1}-temperature relations by predicting δt^* as a function of lithospheric age by means of the plate cooling model [*Parsons and Sclater*, 1977]. We find that our δt^* variations versus age are well fit with a simple Q-temperature relation, but the relation generally predicts smaller variations in Q^{-1} for a given temperature change than the laboratory-derived Q-temperature relation of *Sato and Sacks* [1989]. Along-axis δt^* profiles are constructed by combining the temperature variations along the axis of the Mid-Atlantic Ridge derived in Chapter 2 and the empirical Q-temperature relation derived for the lithosphere.

The techniques developed in this thesis should be of general utility for both global and regional studies of the upper mantle. The Hawaiian hotspot would be an interesting new area in which to apply these inversion techniques. Mid-plate swells have been hypothesized to result from several effects, including elevated temperature in the convecting mantle [*Sandwell and Poehls*, 1980], thermal expansion within the conducting portion of the lithosphere [*Crough*, 1978; *Detrick and Crough*, 1978; *Menard and*

McNutt, 1982], and underplating of the lithosphere with depleted mantle material [*Jordan*, 1979]. Each of these processes involves a different source of the anomaly causing the swell, and each predicts a correspondingly different geophysical signature. The methods proposed here, which distinguish between thermal and compositional mechanisms, offer great promise for distinguishing between these competing models. *Woodward and Masters* [1991], for instance, have observed negative SS-S travel time residuals with SS bounce points in the vicinity of the Hawaiian swell, a result which would favor a lateral variation in composition in the upper mantle beneath the swell.

Application of these techniques and measurements to a global travel time data set will allow general constraints to be placed on upper mantle viscosity structure, the presence of partial melt, and the mechanism of lateral heterogeneity. The viscosity structure of the mantle is poorly known yet plays a key role in models of mantle convection. The viscosity structures we employ in this thesis are quite simple but have been chosen to represent two models widely invoked in other studies - a constant or nearly constant viscosity mantle [e.g., *Peltier*, 1989] and a mantle with a thin low viscosity layer [e.g., *Craig and McKenzie*, 1986; *Robinson et al.*, 1987]. The viscosity structure of the Earth may be temperature and pressure-dependent or vary laterally, but we have not considered viscosity structures of this type [e.g., *Revenaugh and Parsons*, 1987]. Much work remains to be done to determine ways to incorporate lateral variations in viscosity into quantitative treatments of these problems.

Several other improvements could be made in future studies of the type presented here. Our models thus far have been limited to simply parameterized one-dimensional variations in temperature and composition within a single layer. It is likely that these lateral variations are not constant within a given layer and that there are two-dimensional lateral variations independent of lithospheric aging. The techniques outlined in this thesis can be generalized to a multilayer system and to two-dimensional wavenumber, although

we feel that an areally denser distribution of seismic data would be necessary to justify these more complicated models. Kernels for seismic surface waves are strongly peaked in the upper mantle, and such data would provide a useful constraint independent of differential body wave travel times. The inclusion of surface wave data would help to distinguish between lithospheric and asthenospheric effects and may allow for two or more layers to be independently resolved. Extension of the modelling to three dimensions would permit an assessment of the degree to which mantle anomalies beneath the ridge extend off axis. Implicit in our age-correction is the assumption that the anomalous properties of the ridge mantle are steady state on a time scale of tens of millions of years. Examination of the cross-axis profiles in the east Pacific suggests that this assumption might not always hold.

We have not modelled the effects of partial melting which could accompany the temperature variations we predict. The effect of retained melt on the physical properties of the mantle depends critically on the melt fraction and geometry, characteristics presently poorly known. *Sato et al.* [1988, 1989] downplay the importance of partial melt and suggest that most mantle seismic velocity anomalies can be explained by temperature variations at subsolidus conditions. Our attenuation measurements can also be explained with a thermal mechanism. Combined analysis of compressional as well as shear wave differential travel times and attenuation may help to resolve whether significant partial melting is required to explain the travel time residuals in the oceanic upper mantle.

Further analysis of the East Pacific Rise data set is warranted to refine the conclusions from that study. We hope to improve our azimuthal distribution of data by obtaining seismograms from new stations which have begun operating only recently. Since we have gathered data only through 1987, there is currently considerable data to which we have not yet obtained access. Sampling at a more uniform distribution of

azimuths should make our conclusions regarding anisotropy in the region less ambiguous, and as more seismic stations are deployed at new locations our chances of resolving this issue improves. Additional data would also be of use in extending the analysis of age dependence to older lithosphere, and would be of use in attempts to assess further why the upper mantle in the east Pacific region is slower than in the north Atlantic.

The data from the Cocos plate show interesting small-scale (λ from 800 to 1200 km) patterns which might be best examined in two dimensions. We may find it necessary to refine the numerical techniques for obtaining kernels at the smaller wavelengths, however, as we employ a predictor-corrector algorithm which becomes unstable when the derivative of the kernels approaches zero (as is the case for geoid kernels at short wavelength for a mantle with a thin low viscosity zone).

Other complicating factors for the East Pacific Rise study include the effect of the subduction zone along the Middle America Trench and possible crustal thickness variations in the eastern Cocos plate. Crustal thickness variations can be removed from the bathymetry and the geoid by simple isostatic mass balance, and from the travel time residuals by calculating the additional delay due to excess crust relative to an equivalent thickness of mantle. The predicted slab effect can presumably be removed from the low-order geoid in the manner of *Hager* [1984]. The effect of the slab on the differential travel times is more difficult to assess.

An attenuation study in the east Pacific would be a natural extension of this work, as the relevant seismograms have already been collected for the travel time study in Chapter 4. From their study of Rayleigh wave phase propagation, *Canas and Mitchell* [1981] found that the east Pacific region has lower Q than the Atlantic. An analysis of body wave differential attenuation, with horizontal resolution superior to that achievable with surface waves, would constitute an interesting complement to our travel time analysis. In another study *Schlue* [1981] examined differential attenuation between the S

and SS phases with SS bounce points in a small area close to our Profile 1 of Chapter 4. The results of the *Schlue* [1981] suggested that Q^{-1} does not decrease with age, at least in the small range of plate ages (0-15 My) that were included in his study.

In conclusion, we feel that the procedures developed in this thesis represent an important first step towards the discrimination of the global extent and mechanism of lateral heterogeneity in the upper mantle on a regional (1000 to 4000 km) scale.

REFERENCES

Akimoto, S. I., The system MgO-FeO-SiO_2 at high pressures and temperatures - phase equilibria and elastic properties, *Tectonophysics, 13*, 161-187, 1972.

Allègre, C. J., B. Hamelin, and B. Dupré, Statistical analysis of isotopic ratios in MORB: The mantle blob cluster model and the convective regime of the mantle, *Earth Planet. Sci. Lett., 71*, 71-84, 1984.

Anderson, D. L., and J. . Given, Absorption band Q model for the Earth, *J. Geophys. Res., 87*, 3893-3904, 1982.

Anderson, D. L., and R. S. Hart, Q of the Earth, *J. Geophys. Res., 83*, 5869-5882, 1978.

Anderson, O. L., E. Schreiber, R. C. Lieberman, and N. Soga, Some elastic constant data on minerals relevant to geophysics, *Rev. Geophys., 6*, 491-524, 1968.

Anderson, R. N., D. McKenzie, and J. G. Sclater, Gravity, bathymetry, and convection in the Earth, *Earth Planet. Sci. Lett., 18*, 391-407, 1973.

Atwater, T. M., Plate tectonic history of the northeast Pacific and western North America, in *The Eastern Pacific Ocean and Hawaii, The Geology of North America, Vol. N*, edited by E. L. Winterer, D. M. Hussong, and R. W. Decker, Geological Society of America, Boulder, Colo., pp. 21-72, 1989.

Atwater, T. M., and J. Severinghaus, Tectonic maps of the northeast Pacific, in *The Eastern Pacific Ocean and Hawaii, The Geology of North America, Vol. N*, edited by E. L Winterer, D. M. Hussong, and R. W. Decker, Geological Society of America, Boulder, Colo., pp. 15-20, 1989.

Backus, G. E., Possible forms of seismic anisotropy of the upper mantle under oceans, *J. Geophys. Res., 70*, 3429-3439, 1965.

Berggren, W. A., D. V. Kent, J. J. Flynn, and J. A. van Couvering, Cenozoic

geochronology, *Geol. Soc. Am. Bull.*, *96*, 1407-1418, 1985.

Bergman, E. A., and S. C. Solomon, P wave travel times for Mid-Atlantic Ridge earthquakes and evidence for mantle heterogeneity (abstract), *Eos Trans. AGU*, *70*, 1227, 1989.

Bjornsson, S., Crust and upper mantle beneath Iceland, in *Structure and Development of the Greenland-Scotland Ridge*, edited by M.H.P. Bott, S. Saxov, and M. Talwani, NATO Conf. Ser., *4*, pp. 31-61, Plenum Press, New York, 1983.

Bonatti, E., Not so hot "hot spots" in the oceanic mantle, *Science*, *250*, 107-111, 1990.

Boyd, F. R., and R. H. McCallister, Densities of fertile and sterile garnet peridotites, *Geophys. Res. Lett.*, *3*, 509-512, 1976.

Brune, J. N., Q of shear waves estimated from S-SS spectral ratios, *Geophys. Res. Lett.*, *4*, 179-181, 1977.

Buck, W. R., and E. M. Parmentier, Convection beneath young oceanic lithosphere: Implications for thermal structure and gravity, *J. Geophys. Res.*, *91*, 1961-1974, 1986.

Butler, R., Shear-wave travel times from SS, *Bull. Seismol. Soc. Am.*, *69*, 1715-1732, 1979.

Canas, J. A., and B. J. Mitchell, Rayleigh-wave attenuation and its variation across the Atlantic Ocean, *Geophys. J. R. Astron. Soc.*, *67*, 159-176, 1981.

Cara, M., and J. J. Leveque, Anisotropy of the asthenosphere - The higher mode data of the Pacific revisited, *Geophys. Res. Lett.*, *15*, 205-208, 1988.

Cazenave, A., K. Dominh, C. J. Allegre, and J. G. Marsh, Global relationship between oceanic geoid and topography, *J. Geophys. Res.*, *91*, 11439-11450, 1986.

Cazenave, A., K. Dominh, M. Rabinowicz, and G. Ceuleneer, Geoid and depth anomalies over ocean swells and troughs: Evidence of an increasing trend of the geoid to depth ratio with age of plate, *J. Geophys. Res.*, *93*, 8064-8077, 1988.

Chapman, D. S., and H. N. Pollack, Global heat flow: A new look, *Earth Planet. Sci.*

Lett., *28*, 23-32, 1975.

Choy, G. L., and P. G. Richards, Pulse distortion and Hilbert transformation in multiply reflected and refracted body waves, *Bull. Seismol. Soc. Am.*, *65*, 55-70, 1975.

Circum-Pacific Map Project, Plate tectonic map of the circum-Pacific region, Amer. Assoc. Petrol. Geol., Tulsa, Okla., 1981.

Cooper, R. F., and D. L. Kohlstedt, Rheology and structure of olivine-basalt partial melts, *J. Geophys. Res.*, *91*, 9315-9323, 1986.

Craig, C. H., and D. P. McKenzie, The existence of a thin low viscosity layer beneath the lithosphere, *Earth Planet. Sci. Lett.*, 78, 420-426, 1986.

Crampin, S., A review of the effects of anisotropic layering on the propagation of seismic waves, *Geophys. J. R. Astron. Soc.*, *49*, 9-27, 1977.

Creager, K. C., and T. H. Jordan, Slab penetration into the lower mantle beneath the Mariana and other island arcs of the Northwest Pacific, *J. Geophys. Res.*, *91*, 3573-3589, 1986.

Crough, S. T., Thermal origin of mid-plate hot-spot swells, *Geophys. J. R. Astron. Soc.*, *55*, 451-469, 1978.

Davies, G. F., Geophysical and isotopic constraints on mantle convection: An interim synthesis, *J. Geophys. Res.*, *89*, 6017-6040, 1984.

DeMets, C., R. G. Gordon, D. F. Argus, and S. Stein, Current plate motions, *Geophys. J. Int.*, 101, 425-478, 1990.

Detrick, R. S., and S. T. Crough, Island subsidence, hot spots and lithospheric thinning, *J. Geophys. Res.*, *83*, 1236-1244, 1978.

Dick, H. J. B., Abyssal peridotites, very-slow spreading ridges and ocean ridge magmatism, in *Magmatism in the Ocean Basins*, edited by A. D. Saunders and M. J. Norry, *Spec. Pub. Geol. Soc. London*, *42*, pp. 71-105, 1989.

Dick, H. J. B., R. L. Fisher, and W. B. Bryan, Mineralogic variability of the uppermost mantle along mid-ocean ridges, *Earth Planet. Sci. Lett.*, *69*, 88-106, 1984.

Ding, X.-Y., and S. P. Grand, Q as a function of depth beneath a tectonically active area (abstract), *Eos Trans. AGU, 68*, 1376, 1987.

Duffy, T. S., and D. L. Anderson, Seismic velocities in mantle minerals and the mineralogy of the upper mantle, *J. Geophys. Res., 94*, 1895-1912, 1989.

Duschenes, J. D., and S. C. Solomon, Shear wave travel time residuals from oceanic earthquakes and the evolution of oceanic lithosphere, *J. Geophys. Res., 82*, 1985-2000, 1977.

Dziewonski, A. M., Mapping the lower mantle: Determination of lateral heterogeneity in P velocity up to degree and order 6, *J. Geophys. Res., 89*, 5929-5952, 1984.

Dziewonski, A. M., and D. L. Anderson, Preliminary reference Earth model, *Phys. Earth Planet. Inter., 25*, 297-356, 1981.

Dziewonski, A. M., and J. F. Gilbert, The effect of small, aspherical perturbations on travel times and a re-examination of the corrections for ellipticity, *Geophys. J. R. Astron. Soc., 44*, 7-17, 1976.

Dziewonski, A. M., and J. H. Woodhouse, An experiment in systematic study of global seismicity: Centroid-moment tensor solutions for 201 moderate and large earthquakes in 1981, *J. Geophys. Res., 88*, 3247-3271, 1983.

Dziewonski, A. M., and J. H. Woodhouse, Global images of the Earth's interior, *Science, 236*, 37-48, 1987.

Dziewonski, A. M., B. H. Hager, and R. J. O'Connell, Large-scale heterogeneities in the lower mantle, *J. Geophys. Res., 82*, 239-255, 1977.

Dziewonski, A. M., T. A. Chou, and J. H. Woodhouse, Determination of earthquake source patterns from wave-form data for studies of global and regional seismicity, *J. Geophys. Res., 86*, 2825-2852, 1981.

Ewing, M., G. Carpenter, C. C. Windisch, and J. I. Ewing, Sediment distribution in the oceans: The Atlantic, *Geol. Soc. Am. Bull., 84*, 71-88, 1973.

Fischer, K. M., T. H. Jordan, and K. C. Creager, Seismic constraints on the morphology

of deep slabs, *J. Geophys. Res.*, *93*, 4773-4783, 1988.

Flanagan, M. P., and D. A. Wiens, Attenuation structure beneath the Lau back arc spreading center from teleseismic S phases, *Geophys. Res. Lett.*, *17*, 2117-2120, 1990.

Forsyth, D. W., The early structural evolution and anisotropy of the oceanic upper mantle, *Geophys. J. R. Astron. Soc.*, *43*, 103-162, 1975.

Gee, L. S., and T. H. Jordan, Generalized seismological data functionals, I: Theory and observational procedures (abstract), *Eos Trans. AGU, 70*, 1201, 1989.

Girardin, N., and G. Poupinet, Teleseismic S travel-time delay for Mid-Atlantic Ridge earthquakes, *Phys. Earth Planet. Inter., 9*, 306-313, 1974.

Goetze, C., A brief summary of our present day understanding of the effect of volatiles and partial melt on the mechanical properties of the upper mantle, in *High-Pressure Research, Applications in Geophysics*, edited by M. H. Manghnani and S. I. Akimoto, pp. 3-24, Academic Press, New York, 1977.

Grand, S. P., Tomographic inversion for shear velocity beneath the North American plate, *J. Geophys. Res., 92*, 14,065-14,090, 1987.

Grand, S. P., Mantle shear structure from 30°S to 90°N and 120°W to 60°E (abstract), *Eos Trans. AGU, 70*, 389, 1989.

Grand, S. P., and D. V. Helmberger, Upper mantle shear structure beneath the northwest Atlantic Ocean, *J. Geophys. Res., 89*, 11465-11475, 1984.

Green, D. H., and R. C. Liebermann, Phase equilibria and elastic properties of a pyrolite model for the oceanic upper mantle, *Tectonophysics, 32*, 61-92, 1976.

Gripp, A. E., and R. G. Gordon, Current plate velocities relative to the hotspots incorporating the NUVEL-1 global plate motion model, *Geophys. Res. Lett., 17*, 1109-1112, 1990.

Gudmundsson, O., J. H. Davies, and R. W. Clayton, Stochastic analysis of global traveltime data: Mantle heterogeneity and random errors in the ISC data, *Geophys. J.*

Int., *102*, 25-44, 1990.

Gueguen, Y., J. Woirgard, and M. Darot, Attenuation mechanisms and anelasticity in the upper mantle, in *Anelasticity in the Earth*, edited by F. D. Stacey, M. S. Paterson, and A. Nicholas, *Geodynamics Ser.*, *4*, pp. 86-94, AGU, Washington, D. C., 1981.

Hager, B. H., Global isostatic geoid anomalies for plate and boundary layer models of the lithosphere, *Earth Planet. Sci. Lett.*, *63*, 97-109, 1983.

Hager, B. H., Subducted slabs and the geoid: Constraints on mantle rheology and flow, *J. Geophys. Res.*, *89*, 6003-6015, 1984.

Hager, B. H., and R. W. Clayton, Constraints on the structure of mantle convection using seismic observation, flow models, and the geoid, in *Mantle Convection*, edited by W.R. Peltier, Gordan and Breach, New York, pp. 657-763, 1989.

Hager, B. H., and R. J. O'Connell, Kinematic models of large-scale flow in the Earth's mantle, *J. Geophys. Res.*, *84*, 1031-1048, 1979.

Hager, B. H., and R. J. O'Connell, A simple global model of plate dynamics and mantle convection, *J. Geophys. Res.*, *86*, 1031-1048, 1981.

Hager, B. H., and M. A. Richards, Long-wavelength variations in Earth's geoid: Physical models and dynamical implications, *Phil. Trans. R. Soc. Lond. A*, *328*, 309-327, 1989.

Hager, B. H., R. W. Clayton, M. A. Richards, R. P. Comer, and A. M. Dziewonski, Lower mantle heterogeneity, dynamic topography and the geoid, *Nature*, *313*, 541-545, 1985.

Harris, F. J., On the use of windows for harmonic analysis with the discrete Fourier transform, *Trans. IEEE*, *66*, 51-83, 1978.

Hart, R. S., and R. Butler, Shear-wave travel times and amplitudes for two well-constrained earthquakes, *Bull. Seismol. Soc. Am.*, *68*, 973-985, 1978.

Haxby, W. F., and J. K. Weissel, Evidence for small-scale convection from SEASAT altimeter data, *J. Geophys. Res.*, *91*, 3507-3520, 1986.

Honda, S., and T. Tanimoto, Regional 3-D heterogeneities by waveform inversion - application to the Atlantic area, *Geophys. J. R. Astron. Soc., 91*, 737-753, 1987.

Hong, H. J., D. A. Yuen, and J. Wu, Dynamical effects of a hard garnet layer in the transition zone on geophysical signatures: Geoid anomalies and postglacial rebound, *Phys. Earth Planet. Inter., 64*, 37-51, 1990.

Jaques, A. L., and D. H. Green, Anhydrous melting of peridotite at 0-15 kb pressure and the genesis of tholeiitic basalts, *Contrib. Mineral. Petrol., 73*, 287-310, 1980.

Johnson, K. T. M., H. J. B. Dick, and N. Shimizu, Melting in the oceanic upper mantle: An ion microprobe study of diopsides in abyssal peridotites, *J. Geophys. Res., 95*, 2661-2678, 1990.

Jordan, T. H., Mineralogies, densities, and seismic velocities of garnet lherzolites and their geophysical implication, in *The Mantle Sample: Inclusions in Kimberlites and Other Volcanics*, edited by F. R. Boyd and H.O.A. Meyer, pp. 1-14, AGU, Washington, D.C., 1979.

Jordan, T. H., and W. S. Lynn, A velocity anomaly in the lower mantle, *J. Geophys. Res., 79*, 2679-2685, 1974.

Kampfmann, W., and H. Berckhemer, High temperature experiments on the elastic and anelastic behaviour of magmatic rocks, *Phys. Earth Planet. Inter., 40*, 233-247, 1985.

Kent, D. V., and F. Gradstein, A Jurassic to recent geochronology, in *The Western North Atlantic Region, The Geology of North America, Volume M*, edited by P. R. Vogt and B. E. Tucholke, Geological Society of America, Boulder, Colo., pp. 45-50, 1986.

Klein, E. M., and C. H. Langmuir, Global correlations of ocean ridge basalt chemistry with axial depth and crustal thickness, *J. Geophys. Res., 92*, 8089-8115, 1987.

Klitgord, K. D., and J. Mammerickx, Northern East Pacific Rise: Magnetic anomaly and bathymetric framework, *J. Geophys. Res., 87*, 6725-6750, 1982.

Klitgord, K. D., and H. Schouten, Plate kinematics of the central Atlantic, in *The Western North Atlantic Region, The Geology of North America, Volume M*, edited by P. R.

Vogt and B. E. Tucholke, Geological Society of America, Boulder, Colo., pp. 351-378, 1986.

Kumazawa, M., and O. L. Anderson, Elastic moduli, pressure derivatives, and temperature derivatives of single-crystal olivine and single-crystal forsterite, *J. Geophys. Res.*, *74*, 5961-5972, 1969.

Kuo, B.-Y., D. W. Forsyth, and M. E. Wysession, Lateral heterogeneity and azimuthal anisotropy in the north Atlantic determined from SS-S differential travel times, *J. Geophys. Res.*, *92*, 6421-6436, 1987.

Larson, R. L., W. C. Pitman III, X. Golovchenko, S. C. Cande, J. F. Dewey, W. F. Haxby, and J. L. LaBrecque, *The Bedrock Geology of the World (map)*, W.H. Freeman, New York, NY, 1985.

Leeds, A. R., Lithospheric thickness in the western Pacific, *Phys. Earth Planet. Inter.*, *11*, 61-64, 1975.

Lees, J. M., and J. C. VanDecar, Seismic tomography constrained by Bouguer gravity anomalies: Applications in western Washington, *Pure Appl. Geophys.*, *135*, 31-52, 1991.

Lerch, F. J., S. M. Klosko, R. E. Laubscher, and C. A. Wagner, Gravity model improvement using Geos 3 (GEM 9 and 10), *J. Geophys. Res.*, *84*, 3897-3916, 1979.

Liebermann, R. C., Velocity-density systematics for the olivine and spinel phases of Mg_2SiO_4-Fe_2SiO_4, *J. Geophys. Res.*, *75*, 4029-4034, 1970.

Lindsley, D. H., Pyroxene thermometry, *Am. Mineral.*, *68*, 477-493, 1983.

Lines, L. R., A. K. Schultz, and S. Treitel, Cooperative inversion of geophysical data, *Geophysics*, *53*, 8-20, 1988.

Ludwig, W. J., and R. E. Houtz, Isopach map of sediments in the Pacific Ocean Basin and marginal sea basins, Amer. Assoc. Petrol. Geol., Tulsa, Okla., 1979.

Macdonald, K. C., Tectonic and magmatic processes on the East Pacific Rise, in *The Eastern Pacific Ocean and Hawaii, The Geology of North America, Vol. N*, edited by

E. L. Witerer, D. M. Hussong, and R. W. Decker, Geological Society of America, Boulder, Colo., pp. 93-110, 1989.

Marsh, J. G., A. C. Brenner, B. D. Beckley, and T. V. Martin, Global mean sea surface based upon the Seasat altimeter data, *J. Geophys. Res.*, *91*, 3501-3506, 1986.

Marsh, J. G., F. J. Lerch, B. H. Putney, T. L. Felsentreger, B. V. Sanchez, S. M. Kolsko, G. B. Patel, J. W. Robbins, R. G. Williamson, T. L. Engelis, W. F. Eddy, N. L. Chandler, D. S. Chinn, S. Kapoor, K. E. Rachlin, L. E. Braatz, and E. C. Pavlis, The GEM-T2 gravitational model, *J. Geophys. Res.*, *95*, 22,043-22,073, 1990.

Mauk, F. J., A tectonic-based Rayleigh wave group velocity model for prediction of dispersion character through ocean basins, Ph.D. thesis, University of Michigan, Ann Arbor, 260 pp., 1977.

McKenzie, D. P., Surface deformation, gravity anomalies and convection, *Geophys. J. R. Astron. Soc.*, *48*, 211-238, 1977.

McKenzie, D. P., Finite deformation during fluid flow, *Geophys. J. R. Astron. Soc.*, *58*, 689-715, 1979.

McKenzie, D. P., and C. O. Bowin, The relationship between bathymetry and gravity in the Atlantic ocean, *J. Geophys. Res.*, *81*, 1903-1915, 1976.

McKenzie, D. P., A. B. Watts, B. E. Parsons, and M. Roufosse, Planform of mantle convection beneath the Pacific Ocean, *Nature, 288*, 442-466, 1980.

McNutt, M. K., and A. V. Judge, The superswell and mantle dynamics beneath the south Pacific, *Science, 248*, 969-975, 1990.

Menard, H. W., and L. M. Dorman, Dependence of depth anomalies upon latitude and plate motion, *J. Geophys. Res.*, *82*, 5329-5335, 1977.

Menard, H. W., and M. K. McNutt, Evidence for and consequences of thermal rejuvenation, *J. Geophys. Res.*, *87*, 8570-8580, 1982.

Michael, P. J., The concentration, behavior and storage of H_2O in the suboceanic upper

mantle: Implications for mantle metasomatism, *Geochim. Cosmochim. Acta*, *52*, 555-566, 1988.

Michael, P. J., and E. Bonatti, Periodotite composition from the north Atlantic: Regional and tectonic variations and implications for partial melting, *Earth Planet. Sci. Lett.*, *73*, 91-104, 1985.

Mocquet, A., and B. A. Romanowicz, Three-dimensional structure of the upper mantle beneath the Atlantic Ocean inferred from long-period Rayleigh waves, 2, Inversion, *J. Geophys. Res.*, *95*, 6787-6798, 1990.

Mocquet, A., B. A. Romanowicz, and J. P. Montagner, Three-dimensional structure of the upper mantle beneath the Atlantic Ocean inferred from long-period Rayleigh waves, 1, Group and phase velocity distributions, *J. Geophys. Res.*, *94*, 7449-7468, 1989.

Molnar, P., and J. Oliver, Lateral variations of attenuation in the upper mantle and discontinuities in the lithosphere, *J. Geophys. Res.*, *74*, 2649-2683, 1969.

Monnereau, M., and A. Cazenave, Variation of the apparent compensation depth of hotspot swells with age of plate, *Earth Planet. Sci. Lett.*, *91*, 179-197, 1988.

Montagner, J. P., and T. Tanimoto, Global anisotropy in the mantle inferred from the regionalization of phase velocities, *J. Geophys. Res.*, *95*, 4797-4819, 1990.

Moritz, H., Geodetic Reference System 1980, *Geodesique*, *54*, 395-408, 1980.

Nakanishi, I., and D. L. Anderson, Measurement of mantle wave velocities and inversion for lateral heterogeneity and anisotropy, Part II: Analysis by the single station method, *Geophys. J. R. Astron. Soc.*, *78*, 573 - 617, 1984.

Nishimura, C. E., and D. W. Forsyth, Anomalous Love-wave phase velocities in the Pacific: Sequential pure-path and spherical harmonic inversion, *Geophys. J. R. Astron. Soc.*, *81*, 389-407, 1985.

Nishimura, C. E., and D. W. Forsyth, Rayleigh wave phase velocities in the Pacific with implications for azimuthal anisotropy and lateral heterogeneities, *Geophys. J. Int.*, *94*, 479-501, 1988.

Nishimura, C. E., and D. W. Forsyth, The anisotropic structure of the upper mantle in the Pacific, *Geophys. J. Int..*, *96*, 203-229, 1989.

Nolet, G., and N. J. Vlaar, The NARS project: Probing the Earth's interior with a large seismic antenna, *Terra Cognita*, *2*, 17-25, 1982.

O'Hara, M. J., Is there an Icelandic mantle plume? *Nature*, *253*, 708-710, 1975.

Oxburgh, E. R., and E. M. Parmentier, Compositional and density stratification in oceanic lithosphere - causes and consequences, *J. Geol. Soc. London*, *133*, 343-355, 1977.

Parmentier, E. M., and J. E. Oliver, A study of shallow mantle flow due to the accretion and subduction of lithospheric plates, *Geophys. J. R. Astron. Soc.*, *57*, 1-22, 1979.

Parsons, B. E. and S. Daly, The relationship between surface topography, gravity anomalies, and temperature structure of convection, *J. Geophys. Res*, *88*, 1129-1144, 1983.

Parsons, B. E. and F. M. Richter, A relation between the driving force and geoid anomaly associated with mid-ocean ridges, *Earth. Planet. Sci. Lett.*, *51*, 445-450, 1980.

Parsons, B. E., and J. G. Sclater, An analysis of the variation of ocean floor bathymetry and heat flow with age, *J. Geophys. Res.*, *82*, 803-827, 1977.

Peltier, W. R., Mantle viscosity, in *Mantle Convection*, edited by W.R. Peltier, Gordon and Breach, New York, pp. 389-478, 1989.

Peterson, J., and C. R. Hutt, Test and calibration of the digital world-wide standardized seismograph, Open-File Report 82-1087, U.S. Geol. Survey, Albuquerque, N.M., 170 pp., 1982.

Peterson, J., H. M. Butler, L. G. Holcomb, and C. R. Hutt, The seismic research observatory, *Bull. Seismol. Soc. Am.*, *66*, 2049-2068, 1976.

Pockalny, R. A., R. S. Detrick, and P. J. Fox, Morphology and tectonics of the Kane transform from Sea Beam bathymetry data, *J. Geophys. Res.*, *93*, 3179-3193, 1988.

Purdy, G. M., and R. S. Detrick, Crustal structure of the Mid-Atlantic Ridge at 23°N from seismic refraction studies, *J. Geophys. Res.*, *91*, 3739-3762, 1986.

Rader, C. M., and B. Gold, Digital filter design techniques in the frequency domain, *Proc. IEEE, 55*, 149-171, 1967.

Randall, M. J., A revised travel-time table for S, *Geophys. J. R. Astron. Soc., 22*, 229-234, 1971.

Revenaugh, J. S., and T. H. Jordan, Observations of first-order mantle reverberations, *Bull. Seismol. Soc. Am., 77*, 1704-1717, 1987.

Revenaugh, J. S., and B. Parsons, Dynamic topography and gravity anomalies for fluid layers whose viscosity varies exponentially with depth, *Geophys. J. R. Astron. Soc., 90*, 349-368, 1987.

Ribe, N.M., Seismic anisotropy and mantle flow, *J. Geophys Res., 94*, 4213-4223, 1989.

Richards, M. A., and B. H. Hager, Geoid anomalies in a dynamic Earth, *J. Geophys. Res., 89*, 5987-6002, 1984.

Richter, F. M., and B. E. Parsons, On the interaction of two scales of convection in the mantle, *J. Geophys. Res., 80*, 2529-2541, 1975.

Ritzwoller, M. H., J. J. Durek, and J. H. Woodhouse, Inferences from measurements of aspherical Q (abstract), *Eos Trans. AGU, 70*, 1212, 1989.

Robinson, E. M., B. E. Parsons, and S. F. Daly, The effect of a shallow low viscosity zone on the apparent compensation of midplate swells, *Earth Planet. Sci. Lett., 82*, 335-348, 1987.

Romanowicz, B., M. Cara, F. F. Fels, and D. Rouland, GEOSCOPE: A French initiative in long period, three component, global seismic networks, *Eos Trans. AGU, 65*, 753-754, 1984.

Sandwell, D. T., and K. R. MacKenzie, Geoid height versus topography for oceanic plateaus and swells, *J. Geophys. Res., 94*, 7403-7418, 1989.

Sandwell, D. T., and K. A. Poehls, A compensation mechanism for the central Pacific, *J. Geophys. Res., 85*, 3751-3758, 1980.

Sandwell, D. T., and M. L. Renkin, Compensation of swells and plateaus in the North

Pacific: No direct evidence for mantle convection, *J. Geophys. Res., 93*, 2775-2783, 1988.

Sato, H., and I. S. Sacks, Anelasticity and thermal structure of the oceanic upper mantle: Temperature calibration with heat flow data, *J. Geophys. Res., 94*, 5705-5715, 1989.

Sato, H., I. S. Sacks, T. Murase, and C. M. Scarfe, Thermal structure of the low velocity zone derived from laboratory and seismic investigations, *Geophys. Res. Lett., 15*, 1227-1230, 1988.

Sato, H., I. S. Sacks, T. Murase, G. Muncill, and H. Fukuyama, Q_p-melting temperature relation in peridotite at high pressure and temperature: Attenuation mechanism and implications for the mechanical properties of the upper mantle, *J. Geophys. Res., 94*, 10,647-10,661, 1989.

Schilling, J. G., Geochemical and isotopic variation along the Mid-Atlantic Ridge axis from 79°N to 0°N, in *The Western North Atlantic Region, The Geology of North America, Volume M*, edited by P. R. Vogt and B. E. Tucholke, Geological Society of America, Boulder, Colo., pp. 137-156, 1986.

Schilling, J. G., M. B. Bergeron, and R. Evans, Halogens in the mantle beneath the North Atlantic, *Phil. Trans. Roy. Soc. London, Ser. A, 297*, 147-178, 1980.

Schilling, J. G., M. Zajac, R. Evans, T. H. Johnston, W. M. White, J. D. Devine, and R. H. Kingsley, Petrologic and geochemical variations along the Mid-Atlantic ridge from 29°N to 73°N, *Am. J. Sci., 283*, 510-586, 1983.

Schlue, J. W., Differential shear-wave attenuation (δt^*) across the East Pacific Rise, *Geophys. Res. Lett., 8*, 861-864, 1981.

Schlue, J. W., and L. Knopoff, Shear-wave polarization anisotropy in the Pacific Basin, *Geophys. J.R. Astron. Soc., 49*, 145-165, 1977.

Schouten, H., A fundamental analysis of magnetic anomalies and oceanic ridges, *Mar. Geophys. Res., 1*, 111-144, 1971.

Schroeder, W., The empirical age-depth relation and depth anomalies in the Pacific Ocean

basin, *J. Geophys. Res.*, *89*, 9873-9883, 1984.

Sclater, J. G., B. Parsons, and C. Jaupart, Oceans and continents: Similarities and differences in the mechanism of heat loss, *J. Geophys. Res.*, *86*, 11535-11552, 1981.

Scott, D. R., and D. J. Stevenson, A self-consistent model of melting, magma migration and buoyancy-driven circulation beneath mid-ocean ridges, *J. Geophys. Res.*, *94*, 2973-2988, 1989.

Searle, R. C., Lithospheric structure of the Azores Plateau from Rayleigh-wave dispersion, *Geophys. J. R. Astron. Sci.*, *44*, 537-546, 1976.

Sheehan, A. F., and M. K. McNutt, Constraints on thermal and mechanical structure of the oceanic lithosphere at the Bermuda Rise from geoid height and depth anomalies, *Earth Planet. Sci. Lett.*, *93*, 377-391, 1989.

Sheehan, A. F., and S. C. Solomon, Joint inversion of shear wave travel time residuals, geoid, and depth anomalies along the Mid-Atlantic Ridge for long-wavelength variations in upper mantle temperature and composition, *J. Geophys. Res.*, submitted, 1991.

Sipkin, S. A., and T. H. Jordan, Lateral heterogeneity of the upper mantle determined from the travel times of multiple ScS, *J. Geophys. Res.*, *81*, 6397-6320, 1976.

Sipkin, S. A., and T. H. Jordan, Multiple ScS travel times in the western Pacific: Implications for mantle heterogeneity, *J. Geophys. Res.*, *85*, 853-861, 1980a.

Sipkin, S. A., and T. H. Jordan, Regional variation of Q_{ScS}, *Bull. Seismol. Soc. Am.*, *70*, 1071-1102, 1980b.

Sleep, N. H., Segregation of magma from a mostly crystalline mush, *Geol. Soc. Am. Bull.*, *85*, 1225-1232, 1974.

Solomon, S. C., Seismic wave attenuation and partial melting in the upper mantle of North America, *J. Geophys. Res.*, *77*, 1483-1502, 1972.

Solomon, S. C., Shear wave attenuation and melting beneath the Mid-Atlantic Ridge, *J. Geophys. Res.*, *78*, 6044-6059, 1973.

Sotin, C., and E. M. Parmentier, Dynamical consequences of compositional and thermal density stratification beneath spreading centers, *Geophys. Res. Lett., 16*, 835-838, 1989.

Spudich, P. K., and J. A. Orcutt, A new look at the seismic velocity structure of the oceanic crust, *Rev. Geophys., 18*, 627-645, 1980.

Stacey, F. D., A thermal model of the Earth, *Phys. Earth. Planet. Inter., 15*, 341-348, 1977.

Stark, M., and D. Forsyth, The geoid, small-scale convection, and differential travel time anomalies of shear waves in the central Indian Ocean, *J. Geophys. Res., 88*, 2273-2288, 1983.

Stewart, I. C. F., and C. E. Keen, Anomalous upper mantle structure beneath the Cretaceous Fogo seamounts indicated by P-wave reflection delays, *Nature, 274*, 788-791, 1978.

Takahashi, E., Melting of a dry peridotite KLB-1 up to 14 GPa: Implications on the origin of peridotitic upper mantle, *J. Geophys. Res., 91*, 9367-9382, 1986.

Tanimoto, T., Long wavelength S-wave velocity structure throughout the mantle, *Geophys. J. Int., 100*, 327-336, 1990.

Tanimoto, T., and D. L. Anderson, Mapping convection in the mantle, *Geophys. Res. Lett.*, 11, 287-290, 1984.

Tanimoto, T., and D. L. Anderson, Lateral heterogeneity and azimuthal anisotropy of the upper mantle: Love and Rayleigh waves 100-250 sec, *J. Geophys. Res., 90*, 1842-1858, 1985.

Teng, T. L., Attenuation of body waves and the Q-structure of the mantle, *J. Geophys. Res., 73*, 2195-2208, 1968.

Tucholke, B. E., Structure of basement and distribution of sediments in the western North Atlantic, in *The Western North Atlantic Region, The Geology of North America, Volume M*, edited by P. R. Vogt and B. E. Tucholke, Geological Society of America,

Boulder, Colo., pp. 331-340, 1986.

Uhrhammer, R. A., S-wave travel times for a spherically averaged earth, *Geophys. J. R. Astron. Soc., 55*, 283-309, 1978.

Uhrhammer, R. A., Shear-wave velocity structure for a spherically averaged Earth, *Geophys. J. R. Astron. Soc., 58*, 749-767, 1979.

U.S. Naval Oceanographic Office, Digital bathymetric database 5 (DBDB5), Nat. Geophys. Data Center, Boulder, Colo., 1985.

Watts, A. B., D. P. McKenzie, B. E.Parsons, and M. Roufosse, The relation between gravity and bathymetry in the Pacific Ocean, *Geophys. J. R. Astron. Soc., 83*, 263-298, 1985.

Wells, P. R. A., Pyroxene thermometry in simple and complex systems, *Contrib. Mineral. Petrol., 62*, 129-139, 1977.

White, R. S., Atlantic ocean crust: Seismic structure of a slow spreading ridge, in *Ophiolites and Oceanic Lithosphere, Spec. Pub. Geol. Soc. London, 13*, edited by I. G. Glass, S. J. Lippard, and A. W. Shelton, pp. 101-112, Blackwell Scientific, St. Louis, Mo., 1984.

White, R. S., A hot-spot model for early Tertiary volcanism in the N Atlantic, in *Early Tertiary Volcanism and the Opening of the NE Atlantic*, edited by A. C. Morton and L. M. Parson, *Spec. Pub. Geol. Soc. London, 39*, pp. 3-13, 1988.

White, R. S., and D. McKenzie, Magmatism at rift zones: The generation of volcanic continental margins and flood basalts, *J. Geophys. Res., 94*, 7685-7729, 1989.

Whitmarsh, R. B., A. Ginzburg, and R. C. Searle, The structure and origin of the Azores-Biscay Rise, north-east Atlantic Ocean, *Geophys. J. R. Astron. Soc., 70*, 79-108, 1982.

Winterer, E. L., Sediment thickness map of the northeast Pacific, in *The Eastern Pacific Ocean and Hawaii, The Geology of North America, Vol. N*, edited by E. L. Winterer, D. M. Hussong, and R. W. Decker, Geological Society of America, Boulder, Colo.,

pp. 307-310, 1989.

Wood, D. A., A variably veined suboceanic upper mantle - Genetic significance for mid-ocean ridge basalts from geochemical evidence, *Geology*, *7*, 499-503, 1979.

Woodhouse, J. H., and A. M. Dziewonski, Mapping the upper mantle: Three dimensional modelling of Earth structure by inversion of seismic waveforms, *J. Geophys. Res.*, *89*, 5953-5986, 1984.

Woodward, R. L., and G. Masters, Global upper mantle structure from long-period differential travel times, *J. Geophys. Res.*, *96*, 6351-6378, 1991.

Wyllie, P. J., Role of water in magma generation and initiation of diapiric uprise in the mantle, *J. Geophys. Res.*, *76*, 1328-1338, 1971.

Yu, G.-K., and B. J. Mitchell, Regionalized shear velocity models of the Pacific upper mantle from observed Love and Rayleigh wave dispersion, *Geophys. J. R. Astron. Soc.*, *57*, 311-341, 1978.

Zehnder, C. M., and J. C. Mutter, Systematics of thickness variations in ocean crust (abstract), *Eos Trans. AGU, 71*, 1573, 1990.

Zhang, Y. S., and T. Tanimoto, Investigation of the SV-velocity variation of the upper mantle by using Rayleigh waves (abstract), *Eos Trans. AGU, 71*, 1449, 1990a.

Zhang, Y. S., and T. Tanimoto, Global Love wave phase velocity variation and its significance to plate tectonics, *Phys. Earth Planet. Inter.*, submitted, 1990b.

Appendix I. SS-S Travel Time Data for the North Atlantic Region

Stn	Origin time						Dep	m_b	Epicenter		Dist	Bouncepoint		Azim	Obs time	Pred time	Ellip corr.	Resid	r	Grade	Water depth	Depth cor	Dcor resid
	Yr	Mo	Da	Hr	Mn	Sec			Lat	Long		Lat	Long										
KON	77	10	22	1:	23:	27.0	169.3	5.3	7.17	-72.91	79.8	40.10	-48.13	41.4	311.1	315.77	0.17	-4.7	0.55	C	-4346.69	-2.72	-2.0
ANMO	78	3	20	15:	42:	46.7	15.0	5.7	0.81	-29.76	78.9	22.40	-63.38	298.2	299.8	305.85	0.26	-6.0	0.65	B	-5740.42	-3.59	-2.4
ANMO	78	3	20	18:	9:	43.6	15.0	5.7	0.77	-29.68	79.0	22.42	-63.30	298.1	300.9	306.23	0.26	-5.3	0.58	C	-5746.42	-3.59	-1.7
ANMO	78	11	5	6:	39:	35.7	15.0	5.2	8.11	-38.60	67.1	25.46	-68.95	295.4	256.8	262.01	0.15	-5.3	0.59	C	-5551.47	-3.47	-1.8
GRFO	79	1	22	4:	25:	45.7	21.7	5.1	19.10	-64.70	66.6	40.65	-35.04	58.5	255.6	260.39	0.23	-4.8	0.49	C	-4248.71	-2.66	-2.1
ANMO	79	1	28	19:	45:	21.5	15.0	5.8	11.92	-43.70	61.1	26.58	-72.07	294.3	241.9	242.71	0.11	-0.8	0.70	B	-5253.98	-3.28	2.5
ANMO	79	2	11	8:	0:	56.5	15.0	5.4	10.28	-40.84	64.3	26.42	-70.17	294.2	249.6	252.13	0.12	-2.5	0.89	A	-5480.62	-3.43	0.9
ANMO	79	2	13	1:	50:	59.6	15.0	5.2	12.08	-43.88	60.8	26.92	-72.11	293.7	239.6	241.88	0.10	-2.3	0.86	A	-5209.76	-3.26	1.0
GRFO	79	3	23	19:	32:	31.1	73.0	6.1	18.02	-69.04	70.3	40.68	-38.29	58.3	270.5	273.42	0.25	-2.9	0.46	C	-4564.67	-2.85	0.0
KONO	79	3	23	19:	32:	31.1	73.0	6.1	18.02	-69.04	69.0	45.00	-44.02	45.7	264.1	268.57	0.32	-4.5	0.65	C	-4683.59	-2.93	-1.5
BOCO	79	5	3	1:	14:	5.4	15.0	5.0	54.09	-35.29	58.5	30.77	-60.01	209.7	233.1	236.52	0.19	-3.4	0.46	C	-5337.63	-3.34	-0.1
ANMO	79	5	30	16:	8:	47.2	15.0	5.4	14.63	-44.99	58.4	28.11	-72.97	291.9	231.3	235.73	0.07	-4.4	0.86	A	-4757.13	-2.97	-1.5
ANMO	79	6	6	11:	36:	26.7	15.0	5.3	12.07	-43.80	60.3	26.64	-72.51	294.2	245.1	242.07	0.11	3.0	0.67	C	-5157.25	-3.22	6.3
ANMO	79	6	9	6:	31:	47.0	15.0	5.2	11.85	-43.73	61.0	26.71	-72.07	294.0	241.0	242.57	0.11	-1.6	0.90	A	-5224.54	-3.27	1.7
ANMO	79	8	25	8:	44:	4.0	10.0	6.1	10.72	-41.68	63.3	26.47	-70.79	294.2	245.1	249.28	0.12	-4.2	0.84	A	-5484.11	-3.43	-0.8
KONO	79	11	5	1:	51:	12.9	78.3	5.9	17.89	-68.61	68.7	44.93	-43.67	45.6	263.1	268.56	0.32	-5.5	0.57	B	-4744.83	-2.97	-2.5
ZOBO	80	1	1	16:	42:	40.0	10.0	6.0	38.75	-27.75	66.6	11.98	-50.11	212.8	259.1	259.97	0.62	-0.8	0.88	A	-4985.95	-3.12	2.3
KONO	80	5	2	1:	47:	6.9	15.0	5.1	7.22	-72.18	79.3	40.33	-47.13	41.6	300.5	310.74	0.17	-10.3	0.83	B	-3925.97	-2.45	-7.8
GRFO	80	6	25	12:	4:	56.9	151.1	5.7	4.50	-75.73	84.2	34.43	-43.80	51.8	333.6	336.68	0.04	-3.0	0.92	A	-4236.89	-2.65	-0.4
KONO	80	6	25	12:	4:	56.9	151.1	5.7	4.50	-75.73	83.4	38.93	-49.90	40.6	323.5	332.55	0.12	-9.0	0.76	C	-5403.57	-3.38	-5.7
ANMO	80	7	26	12:	53:	40.7	15.0	5.2	7.19	-34.04	71.5	25.65	-66.18	294.8	269.0	277.63	0.15	-8.7	0.74	C	-5330.27	-3.33	-5.3
GRFO	80	7	26	12:	53:	40.7	15.0	5.2	7.19	-34.04	56.4	30.43	-16.33	39.3	226.6	231.93	0.13	-5.3	0.70	C	-3732.76	-2.33	-3.0
KONO	80	7	26	12:	53:	40.7	15.0	5.2	7.19	-34.04	61.5	35.29	-19.54	28.8	239.4	245.42	0.06	-6.0	0.75	B	-5248.45	-3.28	-2.7
ANMO	80	8	13	20:	46:	22.0	15.0	5.1	8.87	-39.83	65.9	25.61	-69.62	295.3	254.8	257.27	0.14	-2.4	0.80	B	-5514.47	-3.45	1.0
ZOBO	80	10	10	12:	25:	23.5	10.1	6.5	36.16	1.40	83.8	12.07	-36.84	228.4	324.0	329.48	0.68	-5.5	0.91	B	-5468.70	-3.42	-2.1
ZOBO	80	10	10	15:	39:	9.8	10.0	6.2	36.25	1.61	83.5	11.76	-36.72	228.8	327.0	330.44	0.67	-3.5	0.79	A	-5338.41	-3.34	-0.1
ZOBO	80	10	13	6:	37:	39.2	15.0	5.2	36.31	1.59	84.4	12.30	-36.59	228.4	323.6	330.48	0.68	-6.9	0.82	B	-5563.84	-3.48	-3.4
ANMO	80	10	27	8:	46:	40.8	15.0	5.5	-0.14	-24.85	83.2	22.78	-60.57	297.4	321.9	326.32	0.26	-4.4	0.64	C	-5897.12	-3.69	-0.7
ANMO	80	11	1	10:	48:	3.3	15.0	5.2	0.44	-25.59	82.1	23.03	-61.07	297.2	317.8	321.96	0.25	-4.1	0.73	C	-5882.84	-3.68	-0.4
KONO	80	11	1	10:	48:	3.3	15.0	5.2	0.44	-25.59	64.5	31.36	-13.82	22.2	248.9	254.89	0.22	-6.0	0.68	C	-3166.82	-1.98	-4.0
BOCO	80	12	5	13:	32:	5.9	15.0	5.0	35.97	1.34	75.8	24.96	-40.75	243.1	295.7	292.60	0.18	3.1	0.62	C	-4629.10	-2.89	5.9
ZOBO	81	2	1	13:	19:	59.2	15.0	5.5	36.43	1.68	84.2	12.14	-36.59	228.6	328.8	331.01	0.68	-2.2	0.75	C	-5529.73	-3.46	1.3
BOCO	81	2	12	1:	50:	6.7	15.0	5.4	38.47	-26.75	55.0	23.28	-53.12	230.6	233.4	226.57	0.24	6.8	0.58	C	-5629.40	-3.52	10.4
ZOBO	81	2	12	1:	50:	6.7	15.0	5.4	38.47	-26.75	67.1	11.81	-49.34	214.1	264.1	261.07	0.62	3.1	0.46	C	-4860.54	-3.04	6.1
KONO	81	3	8	8:	43:	45.4	15.0	5.3	-0.15	-24.82	64.4	31.09	-12.86	21.3	251.0	256.51	0.23	-5.5	0.63	C	-2503.91	-1.56	-4.0

Stn	Origin time							Epicenter		Bouncepoint				Obs	Pred	Ellip	Resid	r	Grade	Water	Depth	Dcor
	Yr	Mo	Da	Hr	Mn	Sec	Dep	m_b	Lat	Long	Dist	Lat	Long	Azim	time	time	corr.				depth	cor	resid
KONO	81	3	23	13:	19:	25.2	15.0	5.3	13.39	-44.95	61.1	39.38	-27.01	36.5	239.2	242.95	0.09	-3.7	0.60	B	-1627.03	-1.02	-2.7
ANMO	81	4	22	23:	16:	54.1	15.0	5.1	7.49	-36.29	69.8	25.22	-67.41	295.4	265.4	269.85	0.16	-4.4	0.74	B	-5520.54	-3.45	-1.0
GRFO	81	4	22	23:	16:	54.1	15.0	5.1	7.49	-36.29	57.8	30.51	-17.70	40.4	227.2	234.07	0.13	-6.9	0.64	C	-4492.49	-2.81	-4.1
KONO	81	4	22	23:	16:	54.1	15.0	5.1	7.49	-36.29	62.6	35.36	-21.04	29.8	236.8	246.88	0.06	-10.0	0.77	A	-5182.67	-3.24	-6.8
GRFO	81	6	11	18:	34:	20.6	15.0	5.2	16.84	-86.07	81.8	44.40	-49.95	60.1	314.6	319.98	0.48	-5.4	0.89	A	-45.04	-0.03	-5.3
SCP	81	7	7	21:	10:	57.7	10.0	5.7	-0.04	-18.73	67.2	23.05	-43.72	309.8	265.4	261.75	0.30	3.6	0.74	C	-3962.89	-2.48	6.1
GRFO	81	7	12	1:	27:	56.3	15.0	5.2	67.70	-161.44	62.5	80.71	2.65	169.3	244.4	246.61	1.08	-2.2	0.87	A	-1302.31	-0.81	-1.4
ALQ	81	8	13	2:	58:	11.2	18.0	5.5	44.85	17.33	85.6	60.38	-52.28	258.6	335.4	336.89	1.18	-1.5	0.68	B	-3239.93	-2.02	0.6
ANMO	81	8	13	2:	58:	11.2	18.0	5.5	44.85	17.33	85.6	60.38	-52.28	258.6	334.7	336.87	1.18	-2.1	0.85	A	-3239.93	-2.02	-0.1
BER	81	8	25	16:	54:	38.8	15.0	5.2	6.95	-76.60	79.8	40.34	-51.86	40.4	300.0	311.51	0.17	-11.5	0.50	B	-4931.51	-3.08	-8.5
GRFO	81	8	25	16:	54:	38.8	15.0	5.2	6.95	-76.60	83.2	36.33	-44.15	53.4	320.9	326.76	0.12	-5.9	0.60	B	-4823.52	-3.01	-2.9
KONO	81	8	25	16:	54:	38.8	15.0	5.2	6.95	-76.60	82.0	40.80	-50.42	42.0	308.6	321.03	0.20	-12.4	0.64	C	-4001.93	-2.50	-9.9
BER	81	9	14	12:	44:	29.6	159.6	5.8	18.34	-68.86	66.1	44.81	-45.55	44.1	254.2	262.14	0.31	-7.9	0.79	B	-3942.53	-2.46	-5.4
GRFO	81	9	14	12:	44:	29.6	159.6	5.8	18.34	-68.86	69.6	40.95	-38.28	58.7	275.0	274.28	0.27	0.7	0.66	C	-4546.84	-2.84	3.6
KONO	81	10	18	4:	31:	2.7	26.0	5.4	8.17	-72.47	78.9	40.81	-47.46	42.0	301.4	307.64	0.19	-6.2	0.88	A	-3719.41	-2.32	-3.9
KEV	81	11	28	19:	24:	5.6	15.0	5.1	23.84	-45.42	61.3	51.56	-27.27	33.5	238.6	244.35	0.44	-5.7	0.84	A	-3598.48	-2.25	-3.5
ALQ	81	12	6	14:	54:	29.6	10.0	5.5	8.08	-38.43	67.5	25.50	-68.71	295.2	262.5	262.66	0.15	-0.1	0.45	C	-5565.11	-3.48	3.4
ANMO	81	12	6	14:	54:	29.6	10.0	5.5	8.08	-38.43	67.5	25.50	-68.70	295.3	260.0	262.66	0.15	-2.6	0.48	C	-5571.81	-3.48	0.9
GRFO	81	12	6	14:	54:	29.6	10.0	5.5	8.08	-38.43	58.3	31.24	-19.04	42.1	222.1	235.95	0.10	-13.9	0.64	C	-4664.76	-2.92	-11.0
KEV	81	12	6	14:	54:	29.6	10.0	5.5	8.08	-38.43	73.9	42.57	-22.77	26.2	280.7	286.80	0.15	-6.1	0.46	C	-3537.22	-2.21	-3.9
KONO	81	12	6	14:	54:	29.6	10.0	5.5	8.08	-38.43	62.6	36.09	-22.51	31.2	235.8	247.94	0.03	-12.2	0.56	C	-4641.60	-2.90	-9.3
SCP	81	12	19	14:	10:	52.9	10.0	6.3	39.22	25.25	74.2	53.27	-25.24	272.1	278.9	285.75	0.76	-6.8	0.75	A	-3539.89	-2.21	-4.6
BER	82	1	3	14:	9:	50.4	10.0	5.8	-0.92	-21.84	64.7	30.31	-12.93	16.9	243.1	253.78	0.27	-10.7	0.82	A	-1847.86	-1.15	-9.5
KONO	82	1	3	14:	9:	50.4	10.0	5.8	-0.92	-21.84	65.2	30.15	-11.41	19.7	250.2	255.48	0.27	-5.3	0.78	C	-2064.14	-1.29	-4.0
SCP	82	1	3	14:	9:	50.4	10.0	5.8	-0.92	-21.84	65.6	22.26	-45.64	311.7	255.8	256.66	0.32	-0.8	0.80	B	-3152.74	-1.97	1.1
KONO	82	1	5	13:	44:	43.5	15.0	5.2	-0.84	-21.82	64.7	30.39	-11.23	19.7	250.7	255.22	0.26	-4.5	0.73	B	-2156.73	-1.35	-3.2
GRFO	82	1	12	5:	48:	17.2	10.0	5.8	13.15	-87.56	85.8	42.14	-51.26	57.6	333.0	337.67	0.40	-4.7	0.84	B	-3046.45	-1.90	-2.8
SCP	82	1	18	19:	27:	24.4	10.0	5.8	39.96	24.39	73.3	53.40	-26.03	271.3	276.6	281.94	0.75	-5.3	0.64	C	-3622.35	-2.26	-3.1
BER	82	1	30	2:	35:	11.0	34.6	6.0	16.73	-61.44	64.2	43.00	-40.02	41.5	241.1	252.68	0.22	-11.6	0.61	B	-4779.72	-2.99	-8.6
GRFO	82	1	30	2:	35:	11.0	34.6	6.0	16.73	-61.44	66.3	38.78	-33.30	56.1	253.6	259.44	0.16	-5.8	0.44	B	-2488.23	-1.56	-4.3
TOL	82	4	6	19:	56:	53.7	42.6	5.9	14.28	-92.11	79.7	34.89	-54.55	67.5	309.8	310.70	0.16	-0.9	0.83	B	-5475.32	-3.42	2.5
ANMO	82	4	10	9:	47:	4.4	15.0	5.0	7.25	-35.77	69.8	25.46	-67.28	295.1	266.1	271.90	0.15	-5.8	0.68	B	-5459.33	-3.41	-2.4
KONO	82	4	10	9:	47:	4.4	15.0	5.0	7.25	-35.77	62.2	35.53	-20.85	29.8	237.3	246.94	0.05	-9.6	0.79	A	-5191.08	-3.24	-6.3
GRFO	82	4	10	16:	25:	34.1	10.0	5.8	17.45	-83.47	79.6	43.93	-47.80	60.2	311.9	310.66	0.44	1.2	0.58	C	-3677.03	-2.30	3.5
TOL	82	4	10	16:	25:	34.1	10.0	5.8	17.45	-83.47	70.8	35.43	-48.84	69.2	266.8	275.12	0.14	-8.3	0.92	A	-4567.93	-2.85	-5.4
BOCO	82	5	2	7:	12:	44.5	15.0	5.4	43.57	-28.94	55.7	26.01	-55.33	223.2	219.0	228.83	0.22	-9.8	0.72	B	-5837.68	-3.65	-6.2
GRFO	82	5	10	1:	25:	56.8	79.8	5.3	10.70	-62.51	71.6	35.43	-34.76	52.3	275.0	278.48	0.05	-3.5	0.68	C	-2275.78	-1.42	-2.1

Stn	Origin time							m_b	Epicenter			Bouncepoint			Obs	Pred	Ellip	Resid	r	Grade	Water	Depth	Dcor
	Yr	Mo	Da	Hr	Mn	Sec	Dep		Lat	Long	Dist	Lat	Long	Azim	time	time	corr.				depth	cor	resid
KONO	82	5	10	1:	25:	56.8	79.8	5.3	10.70	-62.51	72.0	40.00	-39.90	40.6	277.0	279.96	0.14	-3.0	0.56	C	-4738.09	-2.96	0.0
ZOBO	82	6	6	10:	20:	31.5	10.0	5.2	35.39	-35.95	59.7	9.89	-53.32	209.6	238.5	239.74	0.58	-1.2	0.97	A	-4726.46	-2.95	1.7
TOL	82	6	19	6:	21:	57.4	51.9	6.1	13.29	-89.39	78.1	33.69	-52.55	66.5	301.9	304.83	0.11	-2.9	0.68	C	-5356.98	-3.35	0.4
TOL	82	7	7	1:	52:	41.2	18.0	5.3	11.49	-86.44	77.2	32.15	-51.33	64.9	295.5	300.29	0.05	-4.8	0.51	C	-5443.37	-3.40	-1.4
KEV	82	7	11	10:	40:	12.4	15.0	5.1	23.78	-44.91	61.3	51.41	-26.82	33.3	238.2	244.01	0.44	-5.8	0.70	B	-3653.59	-2.28	-3.5
GAC	82	7	23	2:	53:	28.9	15.0	5.2	1.09	-27.90	60.8	25.36	-47.11	319.0	239.3	242.59	0.26	-3.3	0.80	B	-3719.18	-2.32	-0.9
SCP	82	7	23	2:	53:	28.9	15.0	5.2	1.09	-27.90	59.9	22.97	-49.10	313.1	237.0	240.00	0.27	-3.0	0.43	C	-4496.55	-2.81	-0.2
ANMO	82	8	12	8:	41:	50.5	10.1	5.2	-1.17	-24.62	84.2	21.88	-60.46	298.3	329.3	330.16	0.30	-0.9	0.93	A	-5742.04	-3.59	2.7
GAC	82	8	12	8:	41:	50.5	10.1	5.2	-1.17	-24.62	64.8	24.34	-45.04	318.6	246.0	253.83	0.31	-7.8	0.56	C	-3620.83	-2.26	-5.6
KEV	82	8	12	8:	41:	50.5	10.1	5.2	-1.17	-24.62	78.5	36.39	-11.82	20.1	297.1	305.87	0.13	-8.7	0.85	B	-3527.51	-2.20	-6.5
SCP	82	8	12	8:	41:	50.5	10.1	5.2	-1.17	-24.62	64.0	21.93	-47.10	313.0	255.3	251.25	0.32	4.0	0.48	B	-3857.05	-2.41	6.4
KONO	82	8	14	3:	10:	55.8	15.0	5.2	6.93	-77.70	82.9	41.04	-51.66	42.2	316.8	323.75	0.22	-7.0	0.67	C	-4797.89	-3.00	-4.0
KONO	82	8	19	15:	59:	5.5	25.3	6.3	6.75	-82.72	85.2	41.61	-54.86	42.4	331.5	336.45	0.26	-4.9	0.83	A	-4830.95	-3.02	-1.9
BOCO	82	8	30	8:	39:	25.2	15.0	5.0	0.06	-17.57	56.7	2.90	-45.66	274.3	227.1	231.42	0.33	-4.4	0.73	C	-3646.95	-2.28	-2.1
BOCO	82	10	1	5:	35:	47.3	16.0	5.0	-1.60	-15.62	58.9	2.04	-44.63	275.7	232.5	236.70	0.35	-4.2	0.68	C	-3951.33	-2.47	-1.7
GAC	82	10	1	5:	35:	47.3	16.0	5.0	-1.60	-15.62	70.4	25.27	-39.54	314.6	268.9	274.04	0.30	-5.1	0.59	C	-4875.65	-3.05	-2.1
ANMO	82	11	14	17:	29:	24.3	15.0	5.2	0.99	-29.07	79.5	22.61	-62.93	297.9	300.2	307.98	0.26	-7.8	0.66	C	-5797.79	-3.62	-4.2
COL	82	11	16	23:	41:	20.5	10.4	5.6	40.82	19.58	74.8	76.76	4.37	340.9	285.0	286.12	1.29	-1.1	0.53	C	-2795.26	-1.75	0.7
TOL	82	11	18	14:	57:	51.7	190.2	6.0	-1.73	-76.73	77.7	22.80	-46.21	54.4	295.4	307.12	0.32	-11.7	0.63	C	-3460.08	-2.16	-9.5
ANMO	82	12	4	12:	54:	3.9	15.0	5.1	8.76	-39.56	66.0	25.57	-69.56	295.3	253.2	258.31	0.14	-5.1	0.76	B	-5514.47	-3.45	-1.6
GRFO	82	12	4	12:	54:	3.9	15.0	5.1	8.76	-39.56	58.7	31.62	-19.94	43.1	222.5	236.21	0.09	-13.7	0.73	C	-4533.04	-2.83	-11.9
KONO	82	12	9	8:	25:	45.7	15.0	5.3	7.50	-81.83	84.3	42.02	-54.51	42.8	325.2	331.17	0.27	-6.0	0.64	B	-4785.10	-2.99	-3.0
ZOBO	82	12	22	15:	40:	13.3	15.0	5.3	46.02	-27.57	72.2	15.92	-51.27	208.3	276.2	279.62	0.66	-3.5	0.64	A	-4381.65	-2.74	-0.7
GAC	83	1	3	0:	12:	25.6	102.2	5.4	34.53	24.31	72.4	51.98	-19.39	283.0	275.7	280.57	0.70	-4.9	0.56	C	-4089.05	-2.56	-2.3
COL	83	1	17	12:	41:	29.3	10.1	6.0	38.07	20.25	76.9	75.88	7.28	343.2	297.0	297.26	1.32	-0.3	0.90	A	-2388.12	-1.49	1.2
GAC	83	1	17	12:	41:	29.3	10.1	6.0	38.07	20.25	67.5	53.20	-23.77	278.5	256.5	262.14	0.66	-5.7	0.79	B	-3657.67	-2.29	-3.4
RSCP	83	1	17	12:	41:	29.3	10.1	6.0	38.07	20.25	79.6	51.23	-33.84	267.5	305.6	309.22	0.78	-3.7	0.88	A	-3729.20	-2.33	-1.3
RSNY	83	1	17	12:	41:	29.3	10.1	6.0	38.07	20.25	67.6	52.41	-23.98	277.1	257.5	262.30	0.64	-4.8	0.64	C	-3606.95	-2.25	-2.5
RSON	83	1	17	12:	41:	29.3	10.1	6.0	38.07	20.25	74.2	60.68	-27.05	285.6	278.7	286.60	0.96	-7.9	0.81	A	-1478.54	-0.92	-7.0
SCP	83	1	17	12:	41:	29.3	10.1	6.0	38.07	20.25	71.7	51.51	-27.46	272.8	272.6	276.93	0.67	-4.4	0.88	A	-3556.55	-2.22	-2.2
GAC	83	1	19	0:	2:	13.6	15.0	5.1	38.11	20.25	68.0	53.22	-23.37	278.8	257.6	262.04	0.67	-4.5	0.71	B	-3823.04	-2.39	-2.1
RSCP	83	1	19	0:	2:	13.6	15.0	5.1	38.11	20.25	80.1	51.27	-33.45	267.8	305.6	309.09	0.79	-3.5	0.89	A	-3662.80	-2.29	-1.2
RSNY	83	1	19	0:	2:	13.6	15.0	5.1	38.11	20.25	68.0	52.42	-23.58	277.4	258.9	262.19	0.65	-3.3	0.60	C	-3644.85	-2.28	-1.0
RSON	83	1	19	0:	2:	13.6	15.0	5.1	38.11	20.25	74.7	60.73	-26.54	285.9	277.8	286.45	0.97	-8.6	0.77	B	-1647.02	-1.03	-7.6
RSCP	83	1	31	15:	27:	0.0	28.0	5.1	38.15	20.34	80.1	51.63	-33.48	267.3	305.7	309.79	0.80	-4.1	0.78	B	-3558.58	-2.22	-1.9
RSNY	83	1	31	15:	27:	0.0	28.0	5.1	38.15	20.34	68.0	52.76	-23.53	276.9	257.9	262.77	0.66	-4.9	0.69	B	-3748.13	-2.34	-2.6
RSON	83	1	31	15:	27:	0.0	28.0	5.1	38.15	20.34	74.5	61.06	-26.51	285.5	278.5	287.02	0.98	-8.5	0.52	C	-1440.09	-0.90	-7.6

Stn	Origin time							Epicenter			Bouncepoint			Obs	Pred	Ellip	Resid	r	Grade	Water	Depth	Dcor
	Yr	Mo	Da	Hr	Mn	Sec	Dep	m_b	Lat	Long	Dist	Lat	Long	Azim	time	time	corr.				depth	cor	resid
GAC	83	2	21	0:	13:	7.6	26.0	5.0	37.82	20.08	68.0	52.81	-23.42	279.3	264.9	262.45	0.66	2.4	0.40	C	-3785.07	-2.37	4.8
RSNY	83	3	4	19:	6:	13.1	15.0	5.2	-14.24	-14.32	79.9	17.45	-39.25	320.1	305.0	312.33	0.63	-7.4	0.67	A	-5207.59	-3.25	-4.1
KEV	83	3	8	17:	6:	36.2	85.0	5.9	11.03	-62.34	79.4	46.95	-42.98	30.5	300.9	310.84	0.39	-10.0	0.90	C	-3396.64	-2.12	-7.8
KONO	83	3	8	17:	6:	36.2	85.0	5.9	11.03	-62.34	71.3	40.20	-39.53	40.7	271.1	278.21	0.14	-7.1	0.84	B	-4791.62	-2.99	-4.1
GAC	83	3	19	21:	41:	44.3	65.0	5.6	35.02	25.32	72.5	52.70	-19.37	282.0	273.6	281.29	0.72	-7.7	0.53	C	-3173.86	-1.98	-5.7
RSCP	83	3	19	21:	41:	44.3	65.0	5.6	35.02	25.32	84.6	51.02	-29.53	271.1	330.5	333.57	0.85	-3.1	0.78	C	-2792.85	-1.75	-1.3
RSNY	83	3	19	21:	41:	44.3	65.0	5.6	35.02	25.32	72.5	51.90	-19.67	280.7	273.3	281.51	0.69	-8.2	0.80	A	-3902.20	-2.44	-5.8
RSON	83	3	19	21:	41:	44.3	65.0	5.6	35.02	25.32	79.1	60.47	-21.51	289.6	302.6	307.67	1.05	5.0	0.69	B	-2496.95	-1.56	-3.5
COL	83	3	23	23:	51:	6.3	32.7	5.7	38.23	20.29	77.1	75.79	7.55	343.5	293.6	296.66		3.0	0.52	C	-2538.69	-1.59	-1.4
RSCP	83	3	24	4:	17:	31.6	25.0	5.3	38.14	20.31	79.5	51.51	-33.97	267.0	305.7	309.34	0.79	-3.7	0.76	C	-3710.56	-2.32	-1.4
RSNY	83	3	24	4:	17:	31.6	25.0	5.3	38.14	20.31	67.4	52.68	-24.06	276.7	258.8	262.39	0.65	-3.6	0.54	C	-3579.56	-2.24	-1.4
GAC	83	3	25	11:	57:	49.4	33.0	5.2	36.13	52.36	85.6	63.18	-3.22	281.3	338.2	338.08	1.28	0.2	0.67	C	-2021.86	-1.26	1.4
BER	83	3	31	13:	12:	52.3	56.8	5.4	2.46	-76.68	84.0	37.69	-52.33	38.5	321.3	329.58	0.05	-8.3	0.81	C	-5416.86	-3.39	-4.9
TOL	83	3	31	13:	12:	52.3	56.8	5.4	2.46	-76.68	75.2	25.47	-46.13	57.2	292.4	291.33	0.21	1.0	0.75	C	-3326.88	-2.08	3.1
KONO	83	4	3	2:	50:	0.7	28.0	6.5	8.80	-83.11	83.9	43.06	-55.63	43.5	327.5	329.72	0.32	-2.2	0.56	C	-3985.82	-2.49	0.3
TOL	83	4	3	2:	50:	0.7	28.0	6.5	8.80	-83.11	76.1	30.29	-49.63	62.8	288.9	295.52	0.03	-6.6	0.46	C	-5113.66	-3.20	-3.5
GRFO	83	4	10	1:	16:	5.8	15.0	5.2	16.61	-46.59	56.8	36.47	-23.74	51.3	221.8	231.51	0.06	-9.8	0.67	C	-4025.62	-2.52	-7.2
KONO	83	4	10	1:	16:	5.8	15.0	5.2	16.61	-46.59	59.0	41.19	-27.80	38.7	238.5	236.89	0.14	1.6	0.80	B	-2498.03	-1.56	3.2
BCAO	83	4	11	8:	18:	10.3	19.2	6.0	10.43	-62.71	80.5	9.52	-21.74	94.4	307.2	315.37	0.37	-8.2	0.74	B	-4364.04	-2.73	-5.4
BER	83	4	11	8:	18:	10.3	19.2	6.0	10.43	-62.71	70.4	39.71	-41.25	38.6	263.2	272.64	0.11	-9.4	0.81	B	-4949.51	-3.09	-6.3
GRFO	83	4	11	8:	18:	10.3	19.2	6.0	10.43	-62.71	71.9	35.38	-34.55	52.3	280.1	278.35	0.05	1.7	0.70	B	-2261.35	-1.41	3.1
KEV	83	4	11	8:	18:	10.3	19.2	6.0	10.43	-62.71	80.5	46.78	-43.30	30.4	302.8	312.75	0.38	-10.0	0.89	A	-2917.38	-1.82	-8.1
KONO	83	4	11	8:	18:	10.3	19.2	6.0	10.43	-62.71	72.4	40.00	-39.73	40.6	270.3	279.83	0.13	-9.6	0.44	C	-4750.36	-2.97	-6.6
TOL	83	4	11	8:	18:	10.3	19.2	6.0	10.43	-62.71	59.6	28.04	-37.33	58.0	234.0	238.82	0.11	-4.8	0.72	B	-4822.02	-3.01	-1.8
TOL	83	5	9	15:	53:	2.7	11.0	5.5	8.26	-82.95	76.3	29.78	-49.42	62.3	287.0	296.29	0.05	-9.3	0.62	C	-5036.37	-3.15	-6.2
ANMO	83	5	12	10:	51:	49.6	10.1	5.6	17.61	-46.55	56.0	29.34	-73.94	289.9	225.5	228.91	0.04	-3.4	0.68	B	-4490.89	-2.81	-0.6
BER	83	5	12	10:	51:	49.6	10.1	5.6	17.61	-46.55	56.9	41.37	-29.40	36.3	223.8	230.49	0.14	-6.7	0.64	C	-1906.63	-1.19	-5.6
KEV	83	5	12	10:	51:	49.6	10.1	5.6	17.61	-46.55	68.4	48.08	-29.05	30.8	270.1	263.86	0.36	6.2	0.61	B	-3037.99	-1.90	8.1
KONO	83	5	12	10:	51:	49.6	10.1	5.6	17.61	-46.55	58.6	41.49	-27.80	39.0	236.8	234.59	0.15	2.2	0.85	A	-2509.51	-1.57	3.8
RSSD	83	5	12	10:	51:	49.6	10.1	5.6	17.61	-46.55	55.1	33.89	-70.79	301.6	226.3	226.72	0.02	-0.4	0.68	A	-5334.63	-3.33	2.9
RSCP	83	5	14	23:	13:	46.5	15.0	5.0	38.47	20.36	79.8	51.25	-33.72	267.6	304.9	308.56	0.78	-3.7	0.86	A	-3715.40	-2.32	-1.4
RSNY	83	5	14	23:	13:	46.5	15.0	5.0	38.47	20.36	67.7	52.42	-23.86	277.2	260.1	261.74	0.64	-1.7	0.71	B	-3617.02	-2.26	0.6
GRFO	83	5	20	17:	40:	14.4	15.0	5.2	18.05	-69.42	70.8	41.30	-38.75	59.0	273.4	273.40	0.27	0.0	0.74	B	-4554.13	-2.85	2.9
BER	83	7	3	17:	14:	23.2	11.7	5.7	9.77	-83.53	81.0	42.96	-56.93	42.5	310.4	315.97	0.29	-5.6	0.69	C	-4111.89	-2.57	-3.0
NE04	83	7	3	17:	14:	23.2	11.7	5.7	9.77	-83.53	82.4	39.80	-51.78	51.6	320.4	322.41	0.24	-2.1	0.53	C	-5076.95	-3.17	1.1
NE12	83	7	3	17:	14:	23.2	11.7	5.7	9.77	-83.53	75.5	31.18	-49.85	62.6	292.4	293.27	0.00	-0.9	0.62	C	-5154.70	-3.22	2.3
RSNT	83	7	5	12:	1:	27.4	15.0	5.5	40.33	27.21	72.9	72.22	-8.57	311.4	281.0	281.62	1.18	-0.6	0.38	C	-2352.69	-1.47	0.8

Stn	Origin time							Epicenter			Bouncepoint			Obs	Pred	Ellip	Resid	r	Grade	Water	Depth	Dcor
	Yr	Mo	Da	Hr	Mn	Sec	Dep	m_b	Lat	Long	Dist	Lat	Long	Azim	time	time	corr.				depth	cor	resid
RSNY	83	7	14	2:	54:	18.6	25.0	5.2	35.74	21.93	69.2	51.86	-22.72	278.8	272.2	271.18	0.65	1.0	0.60	C	-3373.05	-2.11	3.1
GRFO	83	7	18	12:	52:	43.1	46.7	5.5	12.69	-87.21	86.0	41.90	-51.36	57.4	337.3	340.30	0.40	-3.0	0.71	C	-3619.62	-2.26	-0.8
BER	83	7	26	2:	22:	59.1	15.0	5.3	5.45	-82.56	83.9	40.78	-56.60	40.8	326.2	331.02	0.20	-4.8	0.76	B	-5145.86	-3.22	-1.6
GAC	83	8	6	15:	43:	52.6	10.0	6.3	40.14	24:74	68.9	55.23	-22.18	276.6	262.9	266.16	0.73	-3.3	0.93	A	-2443.04	-1.53	-1.8
RSCP	83	8	6	15:	43:	52.6	10.0	6.3	40.14	24.74	81.2	53.52	-32.82	265.6	314.8	315.43	0.88	-0.6	0.88	A	-2758.91	-1.72	1.1
RSNY	83	8	6	15:	43:	52.6	10.0	6.3	40.14	24.74	69.0	54.43	-22.44	275.3	260.5	266.66	0.72	-6.2	0.89	A	-3444.92	-2.15	-4.0
RSON	83	8	6	15:	43:	52.6	10.0	6.3	40.14	24.74	74.8	62.87	-25.23	284.1	281.5	287.90	1.03	-6.4	0.34	C	-679.12	-0.42	-6.0
RSSD	83	8	6	15:	43:	52.6	10.0	6.3	40.14	24.74	84.4	64.27	-35.71	275.4	330.9	329.92	1.28	1.0	0.77	B	-1013.91	-0.63	1.6
SCP	83	8	6	15:	43:	52.6	10.0	6.3	40.14	24.74	73.2	53.62	-26.12	271.0	276.1	282.18	0.76	-6.1	0.63	C	-3585.12	-2.24	-3.9
RSNY	83	8	20	5:	46:	26.0	39.8	5.1	40.79	51.84	82.5	64.20	-7.48	274.8	319.8	321.72	1.24	-2.0	0.62	C	-1799.29	-1.12	-0.9
BOCO	83	9	8	20:	36:	12.8	15.0	5.0	0.22	-17.04	57.3	2.99	-45.37	274.1	228.8	232.66	0.33	-3.9	0.73	C	-3802.07	-2.38	-1.5
RSCP	83	9	8	20:	36:	12.8	15.0	5.0	0.22	-17.04	72.4	21.59	-47.16	301.1	281.2	281.15	0.29	0.0	0.21	C	-3871.76	-2.42	2.5
RSNY	83	9	8	20:	36:	12.8	15.0	5.0	0.22	-17.04	67.0	25.32	-40.39	313.5	254.4	262.17	0.27	-7.7	0.47	C	-4747.79	-2.97	-4.8
TOL	83	9	15	10:	39:	3.2	121.5	5.7	16.06	-93.24	79.5	36.35	-55.55	68.8	305.9	310.78	0.22	-4.9	0.61	C	-5318.40	-3.32	-1.6
RSNY	83	9	25	18:	41:	17.0	15.0	5.1	-1.15	-24.40	63.9	23.72	-44.64	317.8	246.7	250.59	0.31	-3.9	0.76	A	-3860.66	-2.41	-1.5
RSON	83	9	25	18:	41:	17.0	15.0	5.1	-1.15	-24.40	78.3	29.18	-49.80	316.0	302.3	303.08	0.23	-0.7	0.64	C	-5084.27	-3.18	2.4
RSNT	83	9	27	23:	59:	38.2	170.3	5.5	36.72	26.93	76.4	70.52	-4.50	315.7	293.7	298.56	1.24	-4.9	0.74	B	-2538.12	-1.59	-3.3
GAC	83	9	29	6:	34:	15.3	15.0	5.3	-12.76	-14.76	80.0	18.82	-39.34	320.1	307.6	311.17	0.59	-3.6	0.57	C	-5193.90	-3.25	-0.3
RSCP	83	9	29	6:	34:	15.3	15.0	5.3	-12.76	-14.76	82.6	13.88	-46.25	308.6	323.1	322.60	0.59	0.5	0.87	B	-3577.83	-2.24	2.7
RSNY	83	9	29	6:	34:	15.3	15.0	5.3	-12.76	-14.76	78.9	18.11	-39.30	319.6	300.8	306.13	0.59	-5.4	0.79	B	-5291.40	-3.31	-2.1
BER	83	10	13	13:	6:	38.2	10.0	5.6	-0.82	-21.79	64.4	30.46	-12.86	16.9	244.2	253.43	0.27	-9.2	0.67	C	-1945.02	-1.22	-8.0
GAC	83	10	13	13:	6:	38.2	10.0	5.6	-0.82	-21.79	66.0	24.84	-43.46	317.1	256.5	258.47	0.30	-2.0	0.57	C	-3905.09	-2.44	0.5
GDH	83	10	13	13:	6:	38.2	10.0	5.6	-0.82	-21.79	73.0	35.06	-29.88	346.1	283.0	283.52	0.19	-0.5	0.64	C	-3237.63	-2.02	1.5
KONO	83	10	13	13:	6:	38.2	10.0	5.6	-0.82	-21.79	64.9	30.30	-11.34	19.7	251.8	255.13	0.27	-3.3	0.71	C	-2143.13	-1.34	-2.0
RSCP	83	10	13	13:	6:	38.2	10.0	5.6	-0.82	-21.79	69.3	20.30	-49.97	303.6	272.4	269.72	0.32	2.7	0.59	C	-4567.14	-2.85	5.5
RSSD	83	10	13	13:	6:	38.2	10.0	5.6	-0.82	-21.79	84.9	27.65	-54.71	306.1	327.2	334.95	0.20	-7.7	0.75	C	-5652.86	-3.53	-4.2
SCP	83	10	13	13:	6:	38.2	10.0	5.6	-0.82	-21.79	65.4	22.43	-45.57	311.5	263.8	256.54	0.31	7.3	0.62	C	-3023.84	-1.89	9.2
ANMO	83	10	13	23:	27:	33.2	10.0	5.3	7.31	-34.63	71.2	25.46	-66.44	295.0	269.8	275.18	0.15	-5.3	0.73	B	-5396.64	-3.37	-2.0
GRFO	83	10	13	23:	27:	33.2	10.0	5.3	7.31	-34.63	56.9	30.35	-16.63	39.5	226.6	232.19	0.13	-5.6	0.62	C	-4038.06	-2.52	-3.1
RSSD	83	10	13	23:	27:	33.2	10.0	5.3	7.31	-34.63	70.4	30.21	-62.82	304.8	266.2	272.29	0.09	-6.1	0.68	A	-4875.86	-3.05	-3.0
ZOBO	83	10	17	19:	36:	21.4	10.0	5.9	37.59	-17.41	71.9	11.85	-45.32	219.4	274.1	278.42	0.64	-4.4	0.63	B	-3989.09	-2.49	-1.9
RSNT	83	10	21	20:	34:	49.1	15.0	5.1	40.14	29.35	73.5	73.08	-4.81	313.1	282.0	284.24	1.21	-2.2	0.63	B	-2795.65	-1.75	-0.5
RSNY	83	10	21	20:	34:	49.1	15.0	5.1	40.14	29.35	71.6	56.29	-19.83	274.6	273.6	276.24	0.81	-2.6	0.69	B	-1440.95	-0.90	-1.7
RSON	83	10	21	20:	34:	49.1	15.0	5.1	40.14	29.35	76.6	64.97	-22.00	283.9	303.0	296.05	1.12	6.9	0.67	C	177.45	0.11	6.8
SCP	83	10	21	20:	34:	49.1	15.0	5.1	40.14	29.35	75.9	55.59	-23.73	270.3	286.6	292.93	0.86	-6.4	0.63	C	-2432.02	-1.52	-4.9
TOL	83	10	28	14:	6:	6.3	13.7	6.2	44.10	-113.81	75.1	57.55	-56.16	95.1	279.9	290.49	0.90	-10.5	0.73	B	-2965.17	-1.85	-8.7
GAC	83	10	30	4:	12:	27.7	11.6	6.1	40.35	42.18	77.6	60.93	-12.67	276.3	295.6	301.17	1.04	-5.6	0.63	B	-1041.79	-0.65	-4.9

Stn	Origin time							Epicenter			Bouncepoint			Obs	Pred	Ellip	Resid	r	Grade	Water	Depth	Dcor
	Yr	Mo	Da	Hr	Mn	Sec	Dep	m_b	Lat	Long	Dist	Lat	Long	Azim	time	time	corr.				depth	cor	resid
RSNY	83	10	30	4:	12:	27.7	11.6	6.1	40.35	42.18	78.0	60.13	-13.20	274.8	299.2	302.74	1.03	-3.5	0.83	A	-931.41	-0.58	-3.0
SCP	83	10	30	4:	12:	27.7	11.6	6.1	40.35	42.18	82.4	59.74	-17.66	270.4	324.2	322.33	1.10	1.9	0.83	C	-2200.99	-1.38	3.3
GAC	83	10	30	12:	40:	23.3	33.1	5.2	40.45	42.17	78.0	60.67	-12.29	276.9	298.2	301.13	1.05	-2.9	0.71	B	-838.34	-0.52	-2.4
RSNY	83	10	30	12:	40:	23.3	33.1	5.2	40.45	42.17	78.3	59.87	-12.83	275.5	300.1	302.71	1.03	-2.6	0.77	A	-1014.95	-0.63	-2.0
GDH	83	11	3	7:	41:	11.5	97.9	5.9	-4.00	-79.40	75.5	32.64	-72.82	11.0	290.9	293.51	0.31	-2.6	0.81	B	-5262.24	-3.29	0.6
RSNY	83	11	17	14:	53:	17.3	15.0	5.1	-7.22	-13.52	75.3	21.39	-38.28	316.3	286.6	291.74	0.44	-5.2	0.66	B	-5515.57	-3.45	-1.7
GDH	83	11	22	14:	20:	58.8	35.2	6.3	0.48	-79.79	71.1	35.28	-73.17	11.8	275.4	275.50	0.18	-0.1	0.92	A	-3983.98	-2.49	2.4
TOL	83	11	22	14:	20:	58.8	35.2	6.3	0.48	-79.79	79.0	24.75	-47.94	56.8	305.6	307.14	0.25	-1.5	0.90	A	-4010.75	-2.51	1.0
KONO	83	11	26	20:	18:	23.5	41.9	5.6	7.34	-82.32	85.0	41.61	-54.72	42.5	331.1	333.04	0.26	-1.9	0.84	B	-4843.28	-3.03	1.1
NE09	83	12	2	3:	9:	5.6	31.0	5.9	14.07	-91.95	82.6	38.90	-55.02	63.1	315.3	322.98	0.29	-7.7	0.58	B	-5310.18	-3.32	-4.4
NE14	83	12	2	3:	9:	5.6	31.0	5.9	14.07	-91.95	80.7	33.58	-53.44	70.3	309.0	314.41	0.14	-5.4	0.73	C	-5356.69	-3.35	-2.1
ANMO	83	12	22	4:	11:	29.3	10.0	6.4	11.85	-13.51	85.5	32.10	-54.74	288.4	334.7	338.09	0.10	-3.4	0.60	C	-5406.33	-3.38	0.0
GDH	83	12	22	4:	11:	29.3	10.0	6.4	11.85	-13.51	62.6	41.96	-23.93	340.3	234.4	247.57	0.11	-13.1	0.82	B	-3711.92	-2.32	-10.8
RSNT	83	12	22	4:	11:	29.3	10.0	6.4	11.85	-13.51	84.4	47.61	-40.62	318.5	325.1	332.60	0.52	-7.5	0.89	A	-4514.47	-2.82	-4.7
RSON	83	12	22	4:	11:	29.3	10.0	6.4	11.85	-13.51	74.5	38.15	-43.40	306.5	284.5	289.33	0.16	-4.8	0.60	C	-5043.73	-3.15	-1.7
RSSD	83	12	22	4:	11:	29.3	10.0	6.4	11.85	-13.51	82.0	36.79	-50.04	297.6	310.6	321.59	0.20	-10.9	0.83	A	-5280.54	-3.30	-7.7
GDH	84	1	13	2:	29:	8.2	115.6	5.6	-3.88	-78.47	74.8	32.82	-72.06	10.6	285.9	292.98	0.29	-7.1	0.52	C	-5333.18	-3.33	-3.8
KEV	84	1	15	7:	14:	10.7	10.0	5.3	28.80	-43.51	56.5	53.68	-25.32	35.5	229.5	230.68	0.46	-1.1	0.39	C	-3470.21	-2.17	1.0
GDH	84	1	17	16:	19:	5.4	13.4	5.9	-3.92	-81.41	75.4	33.36	-74.49	12.0	287.8	293.07	0.28	-5.3	0.37	C	-4272.87	-2.67	-2.7
RSON	84	2	11	8:	2:	50.0	15.0	5.3	38.38	22.08	74.9	61.14	-26.02	285.7	278.8	289.08	0.99	-10.3	0.57	C	-1501.99	-0.94	-9.3
RSSD	84	2	11	8:	2:	50.0	15.0	5.3	38.38	22.08	84.6	62.38	-35.94	277.3	328.7	331.47	1.23	-2.8	0.61	C	-2621.57	-1.64	-1.1
RSNY	84	2	22	5:	44:	41.3	40.6	5.1	39.52	54.11	84.3	64.23	-5.38	276.5	329.3	330.42	1.28	-1.1	0.72	B	-3103.20	-1.94	0.8
RSON	84	2	22	5:	44:	41.3	40.6	5.1	39.52	54.11	85.6	73.71	-0.52	291.7	334.0	336.36	1.55	-2.3	0.60	B	-2776.31	-1.74	-0.6
TOL	84	2	26	8:	18:	16.6	115.6	5.9	-17.32	-70.53	84.1	13.14	-41.69	44.1	332.4	332.65	0.72	-0.2	0.52	C	-4662.43	-2.91	2.7
BER	84	3	20	17:	19:	6.4	10.0	5.1	10.77	-42.24	60.5	37.67	-26.57	31.3	234.9	241.60	0.02	-6.7	0.80	C	-2142.77	-1.34	-5.3
KEV	84	3	20	17:	19:	6.4	10.0	5.1	10.77	-42.24	72.8	44.28	-25.70	27.7	280.9	281.91	0.22	-1.0	0.61	C	-2854.56	-1.78	0.7
BER	84	3	30	7:	59:	53.6	10.0	5.8	17.38	-59.63	62.6	43.30	-38.72	41.5	242.8	247.40	0.23	-4.6	0.72	C	-4215.36	-2.63	-1.9
GRFO	84	3	30	7:	59:	53.6	10.0	5.8	17.38	-59.63	64.5	39.04	-32.09	56.4	246.0	253.17	0.17	-7.2	0.45	C	-1686.23	-1.05	-6.1
KEV	84	3	30	7:	59:	53.6	10.0	5.8	17.38	-59.63	72.5	50.27	-40.28	32.8	275.0	281.08	0.47	-6.1	0.90	A	-4340.54	-2.71	-3.4
KONO	84	3	30	7:	59:	53.6	10.0	5.8	17.38	-59.63	64.6	43.58	-37.14	43.7	248.7	253.38	0.25	-4.7	0.73	B	-3931.72	-2.46	-2.2
BER	84	4	22	6:	14:	21.7	10.0	5.8	-0.51	-19.85	63.4	30.65	-11.41	15.8	242.0	251.04	0.25	-9.1	0.75	B	-2241.54	-1.40	-7.7
GAC	84	4	22	6:	14:	21.7	10.0	5.8	-0.51	-19.85	67.0	25.32	-42.14	315.9	258.0	261.67	0.28	-3.6	0.68	C	-4126.54	-2.58	-1.0
GDH	84	4	22	6:	14:	21.7	10.0	5.8	-0.51	-19.85	72.9	35.44	-28.27	345.2	283.6	283.85	0.17	-0.3	0.82	B	-3436.05	-2.15	1.9
RSNY	84	4	22	6:	14:	21.7	10.0	5.8	-0.51	-19.85	65.9	24.62	-42.07	315.2	258.7	258.00	0.29	0.7	0.74	A	-4453.33	-2.78	3.5
GDH	84	4	28	20:	12:	6.4	15.5	5.5	-1.86	-78.10	73.1	34.07	-71.81	10.8	282.1	283.30	0.24	-1.2	0.79	A	-4919.84	-3.07	1.9
RSNY	84	4	29	5:	2:	59.9	10.0	5.2	43.25	12.52	59.9	52.81	-30.25	272.0	237.3	238.48	0.55	-1.2	0.26	C	-3276.14	-2.05	0.9
GAC	84	5	6	9:	12:	1.7	10.0	5.0	38.80	25.61	70.2	54.88	-21.07	277.9	270.6	271.28	0.74	-0.7	0.84	A	-2875.34	-1.80	1.1

Stn	Origin time							m_b	Epicenter			Bouncepoint			Obs	Pred	Ellip	Resid	r	Grade	Water	Depth	Dcor
	Yr	Mo	Da	Hr	Mn	Sec	Dep		Lat	Long	Dist	Lat	Long	Azim	time	time	corr.				depth	cor	resid
RSNT	84	5	6	9:	12:	1.7	10.0	5.0	38.80	25.61	74.2	71.05	-9.18	312.2	283.3	285.90	1.18	-2.6	0.39	C	-889.41	-0.56	-2.0
RSNY	84	5	6	9:	12:	1.7	10.0	5.0	38.80	25.61	70.3	54.09	-21.35	276.5	268.3	271.74	0.72	-3.4	0.79	A	-3097.78	-1.94	-1.5
ANMO	84	5	7	17:	49:	41.6	10.0	5.5	41.76	13.90	86.1	57.54	-50.95	262.9	334.7	339.22	1.10	-4.6	0.67	B	-3587.12	-2.24	-2.3
GAC	84	5	13	12:	45:	53.4	10.0	5.2	43.00	17.77	62.8	54.84	-27.52	273.3	238.3	247.81	0.64	-9.5	0.51	C	-3076.67	-1.92	-7.5
RSCP	84	5	13	12:	45:	53.4	10.0	5.2	43.00	17.77	75.1	52.71	-37.79	262.3	288.7	291.00	0.75	-2.3	0.68	C	-3455.03	-2.16	-0.1
RSNY	84	5	13	12:	45:	53.4	10.0	5.2	43.00	17.77	62.9	54.07	-27.69	271.9	237.8	248.15	0.62	-10.3	0.79	A	-3266.92	-2.04	-8.3
RSNY	84	5	22	13:	57:	5.5	73.0	5.3	35.83	22.57	70.3	52.01	-21.39	279.4	266.7	272.96	0.67	-6.2	0.78	A	-3681.33	-2.30	-3.9
GDH	84	6	5	4:	15:	24.8	26.5	5.9	-7.83	-76.71	79.0	30.87	-70.81	9.5	302.4	306.14	0.41	-3.7	0.92	B	-5397.08	-3.37	-0.3
GAC	84	6	17	7:	48:	2.6	15.0	5.0	38.87	25.68	70.2	55.02	-21.08	277.7	271.1	271.12	0.75	0.0	0.77	B	-2751.59	-1.72	1.7
RSNY	84	6	17	7:	48:	2.6	15.0	5.0	38.87	25.68	70.3	54.23	-21.35	276.3	269.6	271.59	0.73	-2.0	0.50	C	-3073.65	-1.92	-0.1
GAC	84	6	21	10:	43:	40.5	34.3	5.7	35.31	23.28	71.2	52.93	-20.70	280.9	267.6	275.26	0.70	-7.6	0.80	B	-3120.03	-1.95	-5.7
RSCP	84	6	21	10:	43:	40.5	34.3	5.7	35.31	23.28	83.3	51.15	-30.87	269.9	323.1	325.79	0.83	-2.7	0.84	C	-2878.82	-1.80	-0.9
RSNT	84	6	21	10:	43:	40.5	34.3	5.7	35.31	23.28	76.6	69.18	-9.44	313.8	297.9	297.18	1.19	0.7	0.48	C	-1862.35	-1.16	1.9
GRFO	84	6	24	11:	17:	12.0	16.4	6.0	18.02	-69.30	70.3	40.97	-38.15	58.7	272.8	272.85	0.26	0.0	0.83	A	-4539.56	-2.84	2.8
KONO	84	6	24	11:	17:	12.0	16.4	6.0	18.02	-69.30	68.9	45.33	-43.94	46.0	261.5	267.89	0.33	-6.4	0.56	C	-4679.35	-2.92	-3.5
NE10	84	6	24	11:	17:	12.0	16.4	6.0	18.02	-69.30	62.3	35.46	-40.08	63.8	240.8	246.60	0.09	-5.9	0.51	C	-3794.13	-2.37	-3.5
NE13	84	6	24	11:	17:	12.0	16.4	6.0	18.02	-69.30	59.7	32.61	-40.27	68.0	239.9	239.26	0.03	0.6	0.73	B	-2561.01	-1.60	2.2
NE14	84	6	24	11:	17:	12.0	16.4	6.0	18.02	-69.30	60.1	31.88	-39.68	69.8	241.3	240.33	0.02	1.0	0.42	C	-2984.83	-1.87	2.8
TOL	84	6	24	11:	17:	12.0	16.4	6.0	18.02	-69.30	59.7	33.26	-40.56	66.7	239.2	239.39	0.04	-0.2	0.94	A	-3074.51	-1.92	1.7
GRFO	84	6	25	18:	45:	10.3	42.0	5.1	18.00	-69.22	70.3	40.98	-38.31	58.7	271.2	272.82	0.26	-1.6	0.82	B	-4560.43	-2.85	1.3
TOL	84	6	25	18:	45:	10.3	42.0	5.1	18.00	-69.22	59.8	33.27	-40.71	66.7	238.5	239.33	0.04	-0.8	0.93	B	-3207.32	-2.00	1.2
GAC	84	7	19	5:	22:	15.7	10.0	5.4	-6.94	-12.80	76.5	22.44	-37.87	316.4	292.8	297.05	0.42	-4.3	0.78	A	-5659.54	-3.54	-0.7
GDH	84	7	19	5:	22:	15.7	10.0	5.4	-6.94	-12.80	80.9	32.53	-22.93	343.8	306.8	316.61	0.33	-9.8	0.68	B	-5332.69	-3.33	-6.5
RSNY	84	7	19	5:	22:	15.7	10.0	5.4	-6.94	-12.80	75.4	21.72	-37.85	315.8	286.4	292.59	0.43	-6.2	0.79	A	-5559.50	-3.47	-2.8
GRFO	84	8	16	3:	9:	49.5	10.0	5.0	17.94	-81.74	78.1	43.78	-46.48	60.4	298.8	304.35	0.42	-5.5	0.83	B	-4092.57	-2.56	-3.0
GRFO	84	8	20	23:	55:	13.0	21.8	5.1	10.45	-62.45	71.5	35.66	-34.47	52.5	282.8	277.13	0.06	5.6	0.41	C	-2069.63	-1.29	6.9
KONO	84	8	20	23:	55:	13.0	21.8	5.1	10.45	-62.45	71.9	40.27	-39.64	40.8	272.1	278.73	0.14	-6.7	0.64	B	-4762.88	-2.98	-3.7
ANMO	84	8	30	20:	12:	59.7	10.0	5.0	7.05	-33.84	71.8	25.51	-66.08	294.9	271.0	278.13	0.15	-7.2	0.50	B	-5398.23	-3.37	-3.8
KONO	84	8	30	20:	12:	59.7	10.0	5.0	7.05	-33.84	61.7	35.15	-19.42	28.6	238.7	245.23	0.07	-6.5	0.61	C	-5206.89	-3.25	-3.2
RSNT	84	8	30	20:	12:	59.7	10.0	5.0	7.05	-33.84	79.4	41.11	-56.89	322.2	307.0	309.36	0.18	-2.4	0.86	A	-5088.54	-3.18	0.8
RSON	84	8	30	20:	12:	59.7	10.0	5.0	7.05	-33.84	65.7	32.42	-56.39	315.1	252.6	257.18	0.08	-4.6	0.89	A	-5457.66	-3.41	-1.2
KONO	84	9	1	23:	39:	5.8	38.2	5.2	18.30	-69.38	68.8	45.40	-43.99	46.1	260.6	268.32	0.33	-7.7	0.34	C	-4646.75	-2.90	-4.8
RSNT	84	9	7	0:	44:	41.0	10.0	5.1	43.32	20.97	68.4	72.22	-18.20	304.8	264.3	265.73	1.09	-1.5	0.72	B	-635.80	-0.40	-1.1
RSNY	84	9	7	0:	44:	41.0	10.0	5.1	43.32	20.97	64.6	55.37	-26.18	271.0	246.6	252.78	0.68	-6.2	0.40	C	-3335.48	-2.08	-4.1
RSON	84	9	7	0:	44:	41.0	10.0	5.1	43.32	20.97	70.2	63.50	-30.18	279.5	273.7	271.89	0.97	1.8	0.49	C	-2176.21	-1.36	3.2
RSNT	84	9	9	13:	6:	31.5	11.6	5.3	36.96	-24.55	58.0	58.17	-54.61	304.1	230.8	233.89	0.63	-3.1	0.51	C	-3345.13	-2.09	-1.0
RSNY	84	9	18	13:	26:	1.9	10.0	5.3	40.90	42.24	78.1	60.32	-13.11	274.7	300.6	300.99	1.04	-0.4	0.73	B	-954.49	-0.60	0.2

Stn	Origin time							Epicenter			Bouncepoint			Obs	Pred	Ellip	Resid	r	Grade	Water	Depth	Dcor
	Yr	Mo	Da	Hr Mn Sec	Dep	m_b	Lat	Long	Dist	Lat	Long	Azim	time	time	corr.				depth	cor	resid
RSNY	84	9	19	8:32:19.8	10.0	5.1	1.05	-28.14	59.9	24.60	-46.90	318.4	236.0	239.05	0.27	-3.1	0.58	C	-3417.27	-2.14	-0.9
KEV	84	10	5	10:30:47.5	41.2	5.7	11.71	-60.16	78.3	47.02	-40.88	30.6	293.2	304.30	0.38	-11.1	0.76	C	-4529.35	-2.83	-8.3
KONO	84	10	5	10:30:47.5	41.2	5.7	11.71	-60.16	69.9	40.27	-37.72	40.5	266.5	271.62	0.14	-5.1	0.76	C	-4528.83	-2.83	-2.3
RSNY	84	10	9	11:23:12.4	10.0	5.3	-0.52	-19.80	65.7	24.72	-42.04	315.1	260.2	258.13	0.29	2.1	0.62	C	-4396.28	-2.75	4.8
GRFO	84	10	18	15:30:23.1	21.9	5.3	42.36	-105.60	72.7	62.95	-53.12	80.5	277.8	281.70	1.00	-3.9	0.63	B	-2056.15	-1.29	-2.6
GAC	84	10	21	3:51:47.0	10.0	5.1	-6.97	-12.55	76.6	22.44	-37.81	316.4	294.9	297.80	0.42	-2.9	0.82	A	-5659.54	-3.54	0.6
GDH	84	11	1	4:48:49.9	10.0	6.5	8.16	-38.77	61.6	38.98	-42.68	352.5	241.4	244.81	0.00	-3.4	0.90	A	-5015.17	-3.13	-0.2
KONO	84	11	1	4:48:49.9	10.0	6.5	8.16	-38.77	62.7	36.20	-22.90	31.5	234.9	248.15	0.03	-13.2	0.58	C	-4454.62	-2.78	-10.4
LON	84	11	1	4:48:49.9	10.0	6.5	8.16	-38.77	79.2	34.52	-71.18	303.6	309.3	308.75	0.07	0.5	0.61	C	-4875.50	-3.05	3.5
RSNT	84	11	1	4:48:49.9	10.0	6.5	8.16	-38.77	76.1	40.92	-60.92	322.7	296.8	295.56	0.16	1.2	0.90	A	-4795.04	-3.00	4.2
RSON	84	11	1	4:48:49.9	10.0	6.5	8.16	-38.77	61.8	32.45	-59.70	316.5	239.8	245.51	0.08	-5.7	0.83	B	-5001.08	-3.13	-2.5
RSSD	84	11	1	4:48:49.9	10.0	6.5	8.16	-38.77	66.5	30.20	-65.61	305.4	262.4	260.06	0.09	2.4	0.57	B	-4833.41	-3.02	5.4
RSNY	84	11	2	3:38:41.3	10.0	5.3	-10.38	-13.17	77.8	19.53	-38.43	318.0	299.7	302.51	0.53	-2.8	0.75	C	-5579.22	-3.49	0.7
GAC	84	11	5	4:17:32.9	10.0	5.1	-11.97	-13.84	79.4	19.60	-38.91	319.3	308.6	310.92	0.56	-2.4	0.78	A	-5561.55	-3.48	1.1
RSNY	84	11	5	4:17:32.9	10.0	5.1	-11.97	-13.84	78.3	18.86	-38.86	318.8	296.4	305.95	0.56	-9.5	0.74	A	-5353.89	-3.35	-6.2
SCP	84	11	5	4:17:32.9	10.0	5.1	-11.97	-13.84	78.7	17.05	-41.23	314.5	303.1	307.76	0.56	-4.6	0.62	B	-5006.99	-3.13	-1.5
GDH	84	11	23	18:40:11.7	140.3	5.9	-8.16	-76.12	78.7	30.56	-70.24	9.2	303.5	309.35	0.43	-5.9	0.60	C	-5381.02	-3.36	-2.5
GAC	84	12	5	13:39:23.6	10.0	5.1	-1.12	-13.93	71.2	25.81	-38.31	313.5	270.5	276.71	0.28	-6.2	0.56	B	-5002.88	-3.13	-3.0
RSNY	84	12	5	13:39:23.6	10.0	5.1	-1.12	-13.93	70.2	25.08	-38.28	312.8	266.6	272.86	0.29	-6.2	0.87	A	-5161.50	-3.23	-3.0
RSNY	84	12	7	10:19:10.8	10.0	5.9	-1.39	-15.02	69.6	24.67	-39.12	313.6	265.8	271.01	0.30	-5.2	0.92	A	-4930.30	-3.08	-2.1
RSON	84	12	7	10:19:10.8	10.0	5.9	-1.39	-15.02	83.8	30.66	-43.66	313.4	332.7	329.86	0.17	2.8	0.58	B	-3536.14	-2.21	5.0
KEV	84	12	8	12:24:41.9	10.0	5.7	-1.04	-23.42	77.9	36.41	-10.73	19.8	297.3	303.91	0.13	-6.6	0.85	B	-3883.83	-2.43	-4.2
RSON	84	12	8	12:24:41.9	10.0	5.7	-1.04	-23.42	78.6	29.44	-49.20	315.6	306.8	305.24	0.22	1.6	0.63	C	-4971.87	-3.11	4.7
RSSD	84	12	8	12:24:41.9	10.0	5.7	-1.04	-23.42	84.2	27.32	-55.49	306.5	326.4	330.12	0.21	-3.7	0.86	A	-5806.22	-3.63	-0.1
SCP	84	12	8	12:24:41.9	10.0	5.7	-1.04	-23.42	64.7	22.21	-46.29	312.2	253.7	253.48	0.31	0.2	0.35	C	-3521.57	-2.20	2.4
TOL	84	12	20	16:26:11.6	43.1	5.4	11.39	-86.35	77.5	32.51	-51.87	65.2	296.6	299.76	0.06	-3.1	0.75	B	-5334.31	-3.33	0.2
ANMO	84	12	20	23:31:18.0	10.0	5.2	7.06	-33.86	72.2	25.42	-65.83	295.0	271.5	278.05	0.15	-6.6	0.80	C	-5490.31	-3.43	-3.2
GRFO	84	12	20	23:31:18.0	10.0	5.2	7.06	-33.86	56.6	30.10	-16.00	38.7	226.1	231.67	0.14	-5.6	0.60	B	-3334.40	-2.08	-3.5
RSON	84	12	20	23:31:18.0	10.0	5.2	7.06	-33.86	66.2	32.35	-56.13	315.1	255.5	257.12	0.09	-1.6	0.58	C	-5455.02	-3.41	1.8
GRFO	85	1	5	11:11:31.1	45.2	6.2	10.21	-80.03	82.8	38.82	-46.23	55.5	318.9	325.88	0.23	-7.0	0.80	C	-4880.31	-3.05	-4.0
KONO	85	1	5	11:11:31.1	45.2	6.2	10.21	-80.03	80.8	43.10	-52.79	43.7	307.3	316.51	0.31	-9.2	0.82	C	-2989.46	-1.87	-7.3
ANMO	85	1	10	17:47:56.1	10.0	5.8	10.80	-43.46	61.8	26.30	-71.77	294.6	242.1	244.94	0.12	-2.8	0.81	A	-5397.96	-3.37	0.6
GDH	85	1	10	17:47:56.1	10.0	5.8	10.80	-43.46	58.7	40.05	-46.10	354.6	229.0	236.44	0.03	-7.5	0.94	A	-4222.20	-2.64	-4.8
JAS1	85	1	10	17:47:56.1	10.0	5.8	10.80	-43.46	73.2	29.97	-76.96	294.3	277.8	283.47	0.02	-5.7	0.73	B	-1709.57	-1.07	-4.6
KEV	85	1	10	17:47:56.1	10.0	5.8	10.80	-43.46	73.2	44.50	-26.91	28.1	280.5	283.25	0.24	-2.8	0.86	B	-2646.26	-1.65	-1.1
KONO	85	1	10	17:47:56.1	10.0	5.8	10.80	-43.46	62.6	37.93	-26.02	34.6	244.3	247.13	0.04	-2.8	0.83	B	-1765.05	-1.10	-1.7
RSNT	85	1	10	17:47:56.1	10.0	5.8	10.80	-43.46	71.8	41.53	-64.56	322.7	275.1	277.92	0.16	-2.9	0.61	B	-3068.05	-1.92	-0.9

Stn	Origin time					Epicenter			Bouncepoint			Obs	Pred	Ellip	Resid	r	Grade	Water	Depth	Dcor
	Yr	Mo	Da	Hr Mn Sec	Dep	m_b	Lat	Long	Dist	Lat	Long	Azim	time	time	corr.				depth	cor	resid
RSON	85	1	10	17:47:56.1	10.0	5.8	10.80	-43.46	57.1	33.26	-62.73	317.1	226.2	232.50	0.05	-6.3	0.51	B	-4513.28	-2.82	-3.5
RSSD	85	1	10	17:47:56.1	10.0	5.8	10.80	-43.46	61.5	30.95	-68.54	305.3	241.1	244.11	0.06	-3.0	0.86	B	-5211.95	-3.26	0.3
ANTO	85	3	16	14:54: 1.1	14.0	6.2	16.98	-62.46	83.1	38.60	-21.61	70.5	319.4	326.24	0.32	-6.9	0.77	C	-4553.82	-2.85	-4.0
GRFO	85	3	16	14:54: 1.1	14.0	6.2	16.98	-62,46	66.5	39.16	-33.77	56.6	262.7	260.12	0.18	2.6	0.86	B	-3056.83	-1.91	4.5
KEV	85	3	16	14:54: 1.1	14.0	6.2	16.98	-62.46	73.9	50.37	-42.52	32.8	280.0	286.39	0.49	-6.4	0.85	B	-4332.50	-2.71	-3.7
NE06	85	3	16	14:54: 1.1	14.0	6.2	16.98	-62.46	62.3	38.29	-36.30	54.4	252.6	246.82	0.13	5.8	0.54	C	-3849.62	-2.41	8.2
NE14	85	3	16	14:54: 1.1	14.0	6.2	16.98	-62.46	55.1	30.43	-35.90	67.2	225.8	228.12	0.03	-2.3	0.55	C	-4138.15	-2.59	0.3
NE16	85	3	16	14:54: 1.1	14.0	6.2	16.98	-62.46	60.9	35.86	-35.35	59.1	239.4	242.72	0.08	-3.3	0.42	C	-2388.85	-1.49	-1.8
TOL	85	4	19	17:43:10.3	50.0	5.3	11.69	-86.81	77.7	32.56	-52.05	65.3	297.8	300.73	0.06	-2.9	0.50	C	-5325.27	-3.33	0.4
GRFO	85	4	20	18:23:48.2	12.3	5.6	9.00	-77.40	82.3	37.59	-44.56	54.5	314.7	321.83	0.17	-7.1	0.90	A	-5097.99	-3.19	-3.9
NE16	85	4	20	18:23:48.2	12.3	5.6	9.00	-77.40	77.0	33.88	-45.41	57.3	289.3	298.55	0.05	-9.3	0.54	B	-4472.38	-2.80	-6.5
TOL	85	4	20	18:23:48.2	12.3	5.6	9.00	-77.40	71.5	29.43	-46.04	61.7	275.4	277.02	0.07	-1.7	0.46	B	-3774.24	-2.36	0.7
TOL	85	5	18	16:59:13.3	126.0	5.4	-19.24	-69.13	84.6	12.03	-40.89	42.9	325.9	335.25	0.77	-9.3	0.72	B	-4598.75	-2.87	-6.4
NE16	85	6	3	2:45:32.1	19.9	5.1	13.14	-90.19	83.8	39.33	-52.68	62.2	322.1	325.88	0.29	-3.8	0.28	C	-5287.79	-3.30	-0.5
TOL	85	6	3	2:45:32.1	19.9	5.1	13.14	-90.19	79.6	34.32	-52.76	67.2	303.7	307.09	0.12	-3.4	0.84	B	-5262.54	-3.29	-0.1
RSNY	85	6	4	12: 6: 3.6	10.0	5.1	-0.35	-19.49	66.0	24.79	-41.76	314.8	258.5	258.34	0.28	0.2	0.81	A	-4466.18	-2.79	3.0
SCP	85	6	4	12: 6: 3.6	10.0	5.1	-0.35	-19.49	66.8	23.09	-44.00	309.9	262.1	260.68	0.29	1.5	0.56	C	-3719.57	-2.32	3.8
ZOBO	85	6	5	1:41:42.3	14.5	5.1	56.99	-33.77	77.9	20.99	-56.09	198.6	301.4	305.61	0.70	-4.2	0.48	B	-5415.44	-3.38	-0.8
NE06	85	6	6	2:40:12.8	10.0	6.3	0.97	-28.44	56.3	26.41	-15.42	27.8	231.5	231.03	0.27	0.5	0.54	B	-1971.69	-1.23	1.7
NE17	85	6	6	2:40:12.8	10.0	6.3	0.97	-28.44	44.5	20.84	-17.68	28.6	205.5	207.46	0.27	-2.0	0.43	B	-617.99	-0.39	-1.6
RSNY	85	6	6	2:40:12.8	10.0	6.3	0.97	-28.44	59.7	24.49	-47.18	318.8	235.9	238.74	0.27	-2.8	0.57	B	-3656.47	-2.29	-0.6
RSON	85	6	6	2:40:12.8	10.0	6.3	0.97	-28.44	74.0	29.79	-52.60	316.3	288.2	286.21	0.19	2.0	0.62	C	-5419.60	-3.39	5.4
RSSD	85	6	6	2:40:12.8	10.0	6.3	0.97	-28.44	79.2	27.59	-58.74	306.8	303.3	307.50	0.19	-4.2	0.74	B	-6246.33	-3.90	-0.3
SCP	85	6	6	2:40:12.8	10.0	6.3	0.97	-28.44	59.9	22.77	-49.29	313.5	236.0	239.26	0.28	-3.3	0.50	C	-4526.62	-2.83	-0.4
TOL	85	6	10	3:23:31.8	26.0	5.6	3.05	-78.52	76.4	26.34	-47.28	58.3	291.7	295.56	0.18	-3.9	0.58	B	-4175.09	-2.61	-1.3
BCAO	85	6	26	17:10: 1.9	26.6	5.6	18.89	-64.60	82.2	15.67	-21.74	101.4	322.5	322.27	0.31	0.3	0.63	C	-3543.54	-2.21	2.5
TOL	85	6	26	17:10: 1.9	26.6	5.6	18.89	-64.60	55.6	33.25	-37.89	66.5	231.0	229.46	0.03	1.6	0.90	B	-2860.42	-1.79	3.4
KONO	85	7	1	9:53:36.1	10.0	5.0	0.88	-26.80	64.7	31.50	-14.56	22.8	251.2	254.95	0.22	-3.8	0.78	B	-4087.38	-2.55	-1.2
RSNY	85	7	1	9:53:36.1	10.0	5.0	0.88	-26.80	60.6	24.68	-46.22	317.8	236.6	241.63	0.27	-5.0	0.62	C	-3196.17	-2.00	-3.0
GAC	85	7	4	5: 8:32.1	15.0	5.2	42.15	45.80	78.3	63.32	-11.51	274.3	300.8	302.77	1.12	-2.0	0.44	B	-435.72	-0.27	-1.7
RSNY	85	7	4	5: 8:32.1	15.0	5.2	42.15	45.80	78.7	62.53	-12.12	272.8	301.8	304.67	1.11	-2.8	0.71	A	-842.93	-0.53	-2.3
KEV	85	7	5	6:17:16.9	35.0	5.1	18.44	-63.06	72.8	51.20	-43.06	33.3	277.6	282.79	0.51	-5.2	0.73	C	-4230.64	-2.64	-2.6
KEV	85	7	21	13:10:33.3	23.0	5.7	19.11	-67.93	74.0	52.33	-47.47	33.8	280.5	285.99	0.57	-5.5	0.82	B	-3856.84	-2.41	-3.1
KONO	85	7	21	13:10:33.3	23.0	5.7	19.11	-67.93	67.5	45.67	-43.00	46.4	254.9	262.35	0.34	-7.5	0.77	C	-4667.16	-2.92	-4.6
RSNY	85	7	22	21:32:27.9	15.0	5.4	34.37	28.27	75.0	52.65	-17.70	280.9	282.1	289.48	0.75	-7.4	0.89	A	-3885.66	-2.43	-4.9
RSON	85	7	22	21:32:27.9	15.0	5.4	34.37	28.27	81.2	61.48	-18.97	290.2	306.2	315.24	1.11	-9.0	0.47	C	-2197.07	-1.37	-7.7
ANMO	85	9	22	18:23:12.2	10.0	5.7	12.52	-44.31	60.1	27.08	-72.45	293.5	237.5	240.38	0.10	-2.9	0.87	A	-5106.69	-3.19	0.3

Stn	Origin time							Epicenter			Bouncepoint			Obs	Pred	Ellip	Resid	r	Grade	Water	Depth	Dcor
	Yr	Mo	Da	Hr Mn Sec	Dep	m_b	Lat	Long	Dist	Lat	Long	Azim	time	time	corr.				depth	cor	resid
KEV	85	9	22	18:23:12.2	10.0	5.7	12.52	-44.31	72.0	45.47	-27.67	28.8	279.0	278.26	0.27	0.7	0.88	B	-2312.25	-1.45	2.2
RSON	85	9	22	18:23:12.2	10.0	5.7	12.52	-44.31	55.2	34.01	-63.46	316.6	221.5	228.11	0.03	-6.6	0.79	B	-4911.14	-3.07	-3.5
RSSD	85	9	22	18:23:12.2	10.0	5.7	12.52	-44.31	59.7	31.70	-69.24	304.5	234.7	239.17	0.04	-4.5	0.85	B	-5311.59	-3.32	-1.1
RSNY	85	9	23	17:28:41.8	10.0	5.2	-17.75	-13.75	83.3	15.24	-39.34	321.7	325.3	326.32	0.74	-1.0	0.46	C	-5032.57	-3.15	2.1
GAC	85	9	27	16:39:48.6	43.8	5.5	34.40	26.55	74.2	52.96	-18.06	282.5	279.0	284.59	0.75	-5.6	0.76	B	-3614.26	-2.26	-3.3
RSNY	85	9	27	16:39:48.6	43.8	5.5	34.40	26.55	74.2	52.15	-18.39	281.1	277.4	284.84	0.72	-7.4	0.78	B	-4399.01	-2.75	-4.7
ANTO	85	10	5	15:24: 2.2	10.0	6.5	62.22	-124.26	76.2	75.73	4.81	144.2	292.9	295.73	1.31	-2.9	0.72	A	-2751.57	-1.72	-1.1
ANMO	85	10	12	22:20:37.6	10.0	5.3	0.87	-29.90	79.0	22.49	-63.27	298.0	300.9	305.21	0.26	-4.3	0.74	B	-5759.59	-3.60	-0.7
GAC	85	10	12	22:20:37.6	10.0	5.3	0.87	-29.90	60.3	25.08	-47.97	319.9	235.9	239.75	0.27	-3.8	0.79	C	-4237.21	-2.65	-1.2
NE06	85	10	12	22:20:37.6	10.0	5.3	0.87	-29.90	56.7	26.47	-16.08	28.5	235.2	232.66	0.27	2.5	0.46	C	-3256.79	-2.04	4.5
NE13	85	10	12	22:20:37.6	10.0	5.3	0.87	-29.90	44.0	20.25	-18.20	30.5	196.8	207.00	0.27	-10.2	0.56	C	-1692.59	-1.06	-9.2
NE14	85	10	12	22:20:37.6	10.0	5.3	0.87	-29.90	43.1	19.51	-17.86	32.3	201.0	205.25	0.26	-4.3	0.37	C	-1909.93	-1.19	-3.1
NE16	85	10	12	22:20:37.6	10.0	5.3	0.87	-29.90	52.8	24.18	-15.98	30.9	217.3	223.93	0.28	-6.6	0.71	B	-44.70	-0.03	-6.6
RSNY	85	10	12	22:20:37.6	10.0	5.3	0.87	-29.90	59.1	24.40	-47.82	319.4	236.4	236.57	0.27	-0.2	0.89	A	-4150.05	-2.59	2.4
RSON	85	10	12	22:20:37.6	10.0	5.3	0.87	-29.90	73.4	29.64	-53.29	316.7	283.0	283.00	0.20	0.0	0.59	C	-5433.34	-3.40	3.4
SCP	85	10	12	22:20:37.6	10.0	5.3	0.87	-29.90	59.2	22.69	-49.92	314.0	240.1	236.79	0.28	3.3	0.64	C	-4696.43	-2.94	6.2
ANMO	85	10	27	19:34:57.0	10.0	5.5	36.43	6.78	85.7	52.59	-50.60	268.5	332.5	337.04	0.92	-4.6	0.95	A	-2406.05	-1.50	-3.1
GAC	85	10	27	19:34:57.0	10.0	5.5	36.43	6.78	60.2	49.14	-30.76	280.7	237.8	239.73	0.46	-1.9	0.64	A	-3426.81	-2.14	0.2
RSCP	85	10	27	19:34:57.0	10.0	5.5	36.43	6.78	71.6	46.43	-39.67	269.1	276.1	276.87	0.52	-0.8	0.59	C	-4564.31	-2.85	2.0
GAC	85	10	29	13:13:42.7	14.6	6.0	36.75	54.81	86.2	64.13	-2.23	281.1	339.0	340.84	1.32	-1.9	0.79	A	-2855.66	-1.78	-0.1
RSNY	85	11	7	8:26:18.1	10.0	5.1	40.37	42.29	78.4	59.68	-12.92	275.6	298.1	303.22	1.02	-5.1	0.77	B	-1158.17	-0.72	-4.4
ANMO	85	11	10	12:39:50.8	10.0	5.2	4.19	-32.47	74.7	24.23	-64.96	296.3	283.0	288.75	0.19	-5.7	0.73	C	-5770.11	-3.61	-2.1
GAC	85	11	10	12:39:50.8	10.0	5.2	4.19	-32.47	55.7	26.73	-49.69	319.4	226.3	229.30	0.21	-3.0	0.69	B	-4853.84	-3.03	0.1
KEV	85	11	10	12:39:50.8	10.0	5.2	4.19	-32.47	75.3	40.02	-17.80	23.6	282.4	294.02	0.04	-11.7	0.68	C	-4822.06	-3.01	-8.7
RSCP	85	11	10	12:39:50.8	10.0	5.2	4.19	-32.47	58.1	22.25	-55.82	303.8	229.2	234.78	0.23	-5.6	0.61	B	-5639.63	-3.52	-2.1
RSNT	85	11	10	12:39:50.8	10.0	5.2	4.19	-32.47	82.6	40.01	-55.41	322.9	320.3	323.60	0.13	-3.4	0.67	C	-5202.67	-3.25	-0.1
RSON	85	11	10	12:39:50.8	10.0	5.2	4.19	-32.47	68.9	31.23	-55.18	315.9	261.9	267.68	0.13	-5.8	0.62	C	-5431.74	-3.39	-2.4
RSSD	85	11	10	12:39:50.8	10.0	5.2	4.19	-32.47	74.0	29.06	-61.25	305.7	279.2	286.32	0.13	-7.1	0.84	A	-5557.55	-3.47	-3.6
GAC	85	11	21	21:57:14.9	10.1	5.4	41.73	19.41	65.0	54.67	-25.68	274.9	244.6	252.95	0.67	-8.4	0.72	A	-3012.90	-1.88	-6.5
RSSD	85	11	21	21:57:14.9	10.1	5.4	41.73	19.41	80.9	63.00	-39.88	273.3	309.5	313.54	1.17	-4.0	0.85	B	-1132.58	-0.71	-3.3
ANTO	85	11	28	0:13:59.7	49.0	5.3	11.76	-61.37	85.2	35.22	-21.54	67.0	333.5	339.67	0.19	-6.1	0.68	B	-5110.01	-3.19	-2.9
GDH	85	11	28	0:13:59.7	49.0	5.3	11.76	-61.37	57.3	40.57	-58.99	4.0	226.5	234.68	0.05	-8.2	0.75	C	-5081.94	-3.18	-5.0
GRFO	85	11	28	0:13:59.7	49.0	5.3	11.76	-61.37	69.3	36.15	-33.43	53.0	273.6	272.29	0.07	1.3	0.80	B	-2052.02	-1.28	2.6
KEV	85	11	28	0:13:59.7	49.0	5.3	11.76	-61.37	78.0	47.48	-41.79	30.9	297.7	306.19	0.40	-8.5	0.81	C	-4258.78	-2.66	-5.8
KONO	85	11	28	0:13:59.7	49.0	5.3	11.76	-61.37	69.8	40.74	-38.48	41.0	267.1	273.90	0.16	-6.8	0.83	A	-4595.82	-2.87	-3.9
GRFO	85	12	16	2:44:35.6	10.0	5.9	11.71	-85.86	85.6	41.03	-50.16	56.9	336.5	338.29	0.35	-1.7	0.91	A	-3780.69	-2.36	0.6
TOL	85	12	16	2:44:35.6	10.0	5.9	11.71	-85.86	76.2	32.37	-50.79	65.2	292.2	296.40	0.05	-4.2	0.82	B	-5302.21	-3.31	-0.9

Stn	Origin time						Dep	m_b	Epicenter		Dist	Bouncepoint		Azim	Obs time	Pred time	Ellip corr.	Resid	r	Grade	Water depth	Depth cor	Dcor resid
	Yr	Mo	Da	Hr	Mn	Sec			Lat	Long		Lat	Long										
ANTO	85	12	23	5:	16:	3.9	14.7	6.4	62.19	-124.27	76.4	75.76	4.33	143.6	292.8	295.80	1.32	-3.0	0.79	A	-2861.60	-1.79	-1.2
NE14	85	12	23	5:	16:	3.9	14.7	6.4	62.19	-124.27	69.8	65.11	-39.09	125.8	270.5	270.82	0.97	-0.3	0.54	C	-244.83	-0.15	-0.2
GDH	85	12	24	4:	13:	21.2	10.0	5.0	7.04	-34.75	63.0	38.65	-39.01	350.2	243.0	249.46	0.02	-6.5	0.89	A	-4472.47	-2.80	-3.7
GDH	85	12	24	4:	13:	21.2	10.0	5.0	7.04	-34.75	63.0	38.71	-39.02	350.2	243.0	249.46	0.01	-6.5	0.89	A	-4516.70	-2.82	-3.7
KEV	85	12	24	4:	13:	21.2	10.0	5.0	7.04	-34.75	73.1	41.73	-19.28	24.9	275.9	286.04	0.11	-10.1	0.65	C	-4451.71	-2.78	-7.4
RSNT	85	12	24	4:	13:	21.2	10.0	5.0	7.04	-34.75	79.1	41.27	-57.03	322.1	305.8	307.56	0.18	-1.8	0.73	A	-5042.00	-3.15	1.3
RSON	85	12	24	4:	13:	21.2	10.0	5.0	7.04	-34.75	65.4	32.59	-56.51	314.9	251.7	255.47	0.08	-3.8	0.83	A	-5453.37	-3.41	-0.3
KONO	86	1	29	13:	34:	9.6	15.0	5.6	6.86	-76.73	82.0	40.78	-50.42	42.0	309.6	321.72	0.20	-12.1	0.57	C	-4065.25	-2.54	-9.6
GRFO	86	2	12	23:	41:	38.5	15.0	5.2	17.01	-62.33	66.4	39.28	-33.80	56.8	268.6	259.84	0.18	8.8	0.71	C	-3187.57	-1.99	10.8
KEV	86	2	12	23:	41:	38.5	15.0	5.2	17.01	-62.33	73.7	50.49	-42.56	32.8	279.8	286.19	0.49	-6.4	0.73	A	-4308.57	-2.69	-3.7
KONO	86	2	12	23:	41:	38.5	15.0	5.2	17.01	-62.33	66.1	43.78	-39.03	44.2	251.8	258.90	0.26	-7.1	0.77	A	-4175.38	-2.61	-4.5
GAC	86	3	6	0:	5:	38.3	35.0	6.2	40.37	51.60	82.1	64.38	-6.78	277.1	321.2	320.26	1.24	1.0	0.61	B	-2529.61	-1.58	2.6
RSNY	86	3	6	0:	5:	38.3	35.0	6.2	40.37	51.60	82.6	63.59	-7.54	275.4	322.3	322.54	1.23	-0.3	0.82	B	-1229.93	-0.77	0.5
RSON	86	3	6	0:	5:	38.3	35.0	6.2	40.37	51.60	84.2	73.02	-4.11	289.4	323.4	329.86	1.49	-6.5	0.73	C	-2716.90	-1.70	-4.8
ANTO	86	3	21	23:	56:	17.4	15.0	5.4	54.24	-121.85	84.3	76.65	-14.93	122.0	322.9	327.43	1.55	-4.5	0.70	B	-204.17	-0.13	-4.4
RSNY	86	3	25	1:	41:	34.5	15.0	5.1	38.36	25.14	70.1	53.91	-21.52	276.7	265.1	271.69	0.72	-6.6	0.74	C	-3301.12	-2.06	-4.5
NE16	86	5	7	20:	43:	32.6	23.1	6.1	51.42	-174.84	83.0	87.01	-15.01	160.9	323.8	324.43	1.64	-0.7	0.70	A	-4060.89	-2.54	1.9
SSB	86	5	7	20:	43:	32.6	23.1	6.1	51.42	-174.84	83.5	87.22	-2.44	172.6	324.8	326.75	1.66	-2.0	0.66	A	-4352.56	-2.72	0.7
NE10	86	5	7	22:	47:	10.2	31.3	6.5	51.54	-174.84	85.9	85.29	-29.17	149.2	336.0	336.22	1.71	-0.3	0.69	C	-2236.33	-1.40	1.1
NE16	86	5	7	22:	47:	10.2	31.3	6.5	51.54	-174.84	83.3	87.69	-12.41	163.8	322.8	324.12	1.66	-1.3	0.81	A	-4012.49	-2.51	1.2
NE16	86	5	8	5:	37:	22.2	24.0	6.0	51.35	-175.41	83.1	87.18	-12.63	163.4	322.0	325.02	1.64	-3.1	0.59	C	-4068.75	-2.54	-0.5
NE17	86	5	9	16:	23:	51.2	15.0	5.5	-17.17	-65.62	80.2	13.35	-38.52	42.5	306.5	315.23	0.69	-8.7	0.29	C	-5264.94	-3.29	-5.4
GAC	86	5	13	8:	44:	2.0	15.0	5.6	41.44	43.72	78.1	61.84	-11.98	275.8	298.9	300.55	1.08	-1.6	0.81	B	-1203.23	-0.75	-0.9
RSNY	86	5	13	8:	44:	2.0	15.0	5.6	41.44	43.72	78.5	61.04	-12.55	274.2	301.5	302.27	1.07	-0.7	0.90	A	-1177.11	-0.74	0.0
RSON	86	5	13	8:	44:	2.0	15.0	5.6	41.44	43.72	81.3	70.26	-11.96	285.8	316.0	314.06	1.36	1.9	0.59	C	-1469.53	-0.92	2.9
SSB	86	5	17	16:	20:	22.8	15.0	5.7	52.26	-174.29	82.6	87.00	-1.39	173.7	321.6	323.22	1.63	-1.6	0.79	A	-4307.44	-2.69	1.1
ANMO	86	5	21	1:	45:	24.8	15.0	5.2	14.36	-20.13	78.8	32.44	-58.82	287.1	303.2	307.03	0.11	-3.8	0.71	B	-5036.88	-3.15	-0.6
GAC	86	5	21	1:	45:	24.8	15.0	5.2	14.36	-20.13	55.5	33.33	-42.89	306.0	222.9	229.25	0.00	-6.3	0.23	C	-3886.91	-2.43	-3.9
RSCP	86	5	21	1:	45:	24.8	15.0	5.2	14.36	-20.13	61.7	29.25	-49.60	291.2	241.5	245.19	0.04	-3.7	0.48	B	-5074.61	-3.17	-0.5
RSNT	86	5	21	1:	45:	24.8	15.0	5.2	14.36	-20.13	79.0	47.79	-46.37	317.5	303.4	308.76	0.48	-5.3	0.55	C	-903.24	-0.56	-4.8
RSON	86	5	21	1:	45:	24.8	15.0	5.2	14.36	-20.13	68.3	38.58	-47.92	306.1	262.7	266.54	0.15	-3.9	0.94	A	-5349.89	-3.34	-0.5
RSSD	86	5	21	1:	45:	24.8	15.0	5.2	14.36	-20.13	75.5	37.05	-54.45	296.6	288.6	293.71	0.19	-5.2	0.80	B	-5368.10	-3.36	-1.8
GAC	86	5	22	19:	52:	19.5	33.2	5.1	34.64	26.52	74.0	52.94	-18.29	282.4	273.4	284.79	0.74	-11.4	0.54	C	-3582.93	-2.24	-9.1
RSNY	86	5	22	19:	52:	19.5	33.2	5.1	34.64	26.52	74.1	52.13	-18.61	281.0	275.1	285.05	0.72	-9.9	0.88	A	-4369.89	-2.73	-7.2
GAC	86	6	6	10:	39:	46.7	15.0	5.6	38.01	37.91	78.0	58.10	-13.10	279.5	289.8	299.61	0.97	-9.8	0.64	C	-947.34	-0.59	-9.2
RSNT	86	6	6	10:	39:	46.7	15.0	5.6	38.01	37.91	78.1	73.58	9.09	322.2	288.9	299.31	1.32	-10.4	0.16	C	-2411.25	-1.51	-8.9
GRFO	86	6	9	2:	17:	38.3	49.5	5.0	54.13	-168.22	76.1	88.50	1.47	169.9	295.6	295.90	1.47	-0.3	0.68	B	-4330.33	-2.71	2.4

Stn	Origin time							m_b	Epicenter			Bouncepoint			Obs	Pred	Ellip	Resid	r	Grade	Water	Depth	Dcor
	Yr	Mo	Da	Hr	Mn	Sec	Dep		Lat	Long	Dist	Lat	Long	Azim	time	time	corr.				depth	cor	resid
BCAO	86	6	11	13:	48:	3.3	20.0	6.0	10.60	-62.93	80.8	9.94	-21.85	94.8	309.2	316.18	0.36	-7.0	0.61	C	-4648.09	-2.91	-4.1
GRFO	86	6	11	13:	48:	3.3	20.0	6.0	10.60	-62.93	71.7	35.77	-34.72	52.7	281.6	278.29	0.06	3.4	0.63	C	-2105.73	-1.32	4.7
KONO	86	6	11	13:	48:	3.3	20.0	6.0	10.60	-62.93	72.0	40.38	-39.92	40.9	274.2	279.57	0.15	-5.4	0.42	B	-4739.24	-2.96	-2.5
NE04	86	6	11	13:	48:	3.3	20.0	6.0	10.60	-62.93	69.2	36.62	-37.55	48.0	268.1	269.43	0.06	-1.3	0.50	C	-3382.53	-2.11	0.8
NE06	86	6	11	13:	48:	3.3	20.0	6.0	10.60	-62.93	67.5	34.94	-37.18	50.4	264.8	263.35	0.02	1.4	0.67	A	-2402.07	-1.50	2.9
NE11	86	6	11	13:	48:	3.3	20.0	6.0	10.60	-62.93	61.7	29.75	-36.91	57.4	238.4	244.57	0.08	-6.1	0.60	C	-4040.58	-2.53	-3.6
NE13	86	6	11	13:	48:	3.3	20.0	6.0	10.60	-62.93	59.1	27.77	-37.23	59.9	233.2	238.14	0.11	-4.9	0.64	B	-4864.43	-3.04	-1.9
NE15	86	6	11	13:	48:	3.3	20.0	6.0	10.60	-62.93	68.4	35.51	-37.06	49.9	268.0	266.33	0.03	1.6	0.55	C	-2920.73	-1.83	3.5
TOL	86	6	11	13:	48:	3.3	20.0	6.0	10.60	-62.93	59.4	28.41	-37.48	58.6	232.9	238.88	0.10	-6.0	0.72	A	-4630.02	-2.89	-3.1
RSON	86	6	11	20:	15:	42.7	50.3	5.1	40.28	51.71	84.5	73.01	-3.27	290.1	327.4	330.72	1.50	-3.3	0.41	C	-2757.85	-1.72	-1.6
GAC	86	6	15	23:	58:	44.1	15.0	5.0	0.85	-26.81	61.7	25.39	-46.34	318.4	237.9	244.99	0.26	-7.1	0.35	C	-3387.22	-2.12	-4.9
KONO	86	6	15	23:	58:	44.1	15.0	5.0	0.85	-26.81	64.7	31.52	-14.54	22.8	249.6	255.05	0.22	-5.5	0.70	C	-4041.56	-2.53	-2.9
RSON	86	6	15	23:	58:	44.1	15.0	5.0	0.85	-26.81	74.9	30.09	-51.54	315.7	291.8	290.47	0.18	1.4	0.64	C	-5375.12	-3.36	4.7
GAC	86	6	17	8:	48:	18.6	15.0	5.4	4.41	-32.64	55.4	26.68	-50.04	319.8	230.9	228.66	0.21	2.3	0.66	C	-4906.57	-3.07	5.3
RSCP	86	6	17	8:	48:	18.6	15.0	5.4	4.41	-32.64	57.7	22.19	-56.16	304.1	230.6	234.09	0.23	-3.5	0.76	C	-5608.76	-3.51	0.0
GAC	86	6	24	6:	56:	53.0	15.0	5.7	-0.09	-17.79	67.8	25.91	-40.81	314.5	258.8	265.18	0.27	-6.4	0.75	B	-4306.36	-2.69	-3.7
RSCP	86	6	24	6:	56:	53.0	15.0	5.7	-0.09	-17.79	72.0	21.45	-47.50	301.4	283.0	279.81	0.29	3.1	0.43	C	-3987.83	-2.49	5.7
RSNY	86	6	24	6:	56:	53.0	15.0	5.7	-0.09	-17.79	66.8	25.19	-40.74	313.8	258.4	261.51	0.27	-3.1	0.62	C	-4597.76	-2.87	-0.2
WFM	86	6	24	6:	56:	53.0	15.0	5.7	-0.09	-17.79	63.9	23.86	-40.00	313.4	256.1	252.38	0.28	3.7	0.48	C	-4956.75	-3.10	6.8
GDH	86	6	29	20:	11:	50.3	160.1	5.1	6.76	-73.00	63.3	38.02	-68.12	9.7	252.4	253.55	0.04	-1.2	0.37	C	-4414.66	-2.76	1.6
TOL	86	6	30	22:	52:	12.0	44.7	5.2	11.18	-86.11	77.6	32.23	-51.77	64.9	295.6	299.47	0.05	-3.9	0.78	B	-5430.50	-3.39	-0.5
GAC	86	7	10	6:	53:	4.3	15.0	5.4	4.30	-32.60	55.6	26.56	-50.00	319.9	227.4	228.92	0.21	-1.5	0.53	C	-4882.45	-3.05	1.6
RSCP	86	7	10	6:	53:	4.3	15.0	5.4	4.30	-32.60	57.9	22.06	-56.11	304.2	229.4	234.35	0.24	-5.0	0.65	B	-5560.11	-3.48	-1.5
RSON	86	7	10	6:	53:	4.3	15.0	5.4	4.30	-32.60	68.8	31.03	-55.52	316.2	262.4	267.10	0.14	-4.7	0.74	C	-5442.69	-3.40	-1.3
RSSD	86	7	10	6:	53:	4.3	15.0	5.4	4.30	-32.60	73.8	28.83	-61.57	306.0	278.8	285.65	0.14	-6.8	0.78	B	-5533.91	-3.46	-3.4
GRFO	86	7	18	17:	22:	41.6	15.0	5.8	10.78	-69.43	75.7	36.97	-38.91	54.2	294.4	293.71	0.13	0.6	0.67	B	-3631.80	-2.27	2.9
NE06	86	7	18	17:	22:	41.6	15.0	5.8	10.78	-69.43	71.4	36.01	-41.29	52.3	272.6	277.13	0.07	-4.5	0.31	C	-4021.59	-2.51	-2.0
GRFO	86	8	7	22:	32:	50.9	15.0	5.4	7.45	-81.24	85.8	37.55	-47.27	54.3	334.9	339.26	0.19	-4.4	0.48	C	-5257.11	-3.29	-1.1
TOL	86	8	7	22:	32:	50.9	15.0	5.4	7.45	-81.24	75.2	29.17	-48.35	61.5	292.2	292.38	0.07	-0.2	0.56	C	-4684.99	-2.93	2.7
KONO	86	8	13	4:	11:	41.1	15.0	5.4	5.83	-82.43	86.0	41.31	-55.15	42.2	334.8	339.60	0.25	-4.8	0.80	C	-4887.72	-3.05	-1.8
RSNT	86	8	30	21:	28:	35.9	132.7	6.3	45.54	26.31	67.7	74.18	-12.60	306.5	254.3	265.52	1.13	-11.2	0.84	C	-2649.86	-1.66	-9.6
RSNY	86	8	30	21:	28:	35.9	132.7	6.3	45.54	26.31	66.2	57.70	-23.78	269.3	248.2	260.35	0.78	-12.1	0.63	C	-2935.77	-1.83	-10.3
WFM	86	8	30	21:	28:	35.9	132.7	6.3	45.54	26.31	65.8	56.00	-23.32	267.0	255.0	259.02	0.72	-4.0	0.12	C	-2267.89	-1.42	-2.6
GAC	86	9	13	17:	24:	33.7	15.0	5.8	37.08	22.15	69.8	53.15	-21.91	279.8	263.9	268.56	0.69	-4.7	0.88	A	-3879.65	-2.42	-2.2
RSNT	86	9	13	17:	24:	33.7	15.0	5.8	37.08	22.15	75.3	69.40	-11.53	312.3	284.5	289.22	1.17	-4.7	0.49	B	-1823.50	-1.14	-3.5
ANMO	86	9	20	1:	31:	14.0	15.0	5.4	0.88	-29.25	79.3	22.34	-63.18	298.2	299.2	307.62	0.27	-8.5	0.71	C	-5753.58	-3.60	-4.9
RSON	86	9	20	1:	31:	14.0	15.0	5.4	0.88	-29.25	73.7	29.51	-53.20	316.8	283.2	284.61	0.21	-1.4	0.68	C	-5427.76	-3.39	2.0

Stn	Origin time							Epicenter		Bouncepoint				Obs	Pred	Ellip	Resid	r	Grade	Water	Depth	Dcor
	Yr	Mo	Da	Hr	Mn	Sec	Dep	m_b	Lat	Long	Dist	Lat	Long	Azim	time	time	corr.				depth	cor	resid
RSSD	86	9	20	1:	31:	14.0	15.0	5.4	0.88	-29.25	78.8	27.29	-59.32	307.1	303.1	305.30	0.21	-2.2	0.67	B	-6163.45	-3.85	1.7
RSNY	86	10	2	10:	12:	39.8	15.0	5.3	34.82	28.31	75.2	53.13	-17.46	280.5	288.1	288.63	0.77	-0.5	0.51	C	-3155.34	-1.97	1.5
GAC	86	10	11	9:	0:	13.1	15.0	5.4	37.94	28.56	72.9	55.13	-18.59	279.3	276.6	279.55	0.79	-3.0	0.52	B	-1264.79	-0.79	-2.2
RSNY	86	10	11	9:	0:	13.1	15.0	5.4	37.94	28.56	73.1	54.33	-18.92	277.9	275.7	280.12	0.77	-4.4	0.47	B	-1617.24	-1.01	-3.4
ZOBO	86	10	27	0:	9:	31.9	15.0	5.3	46.03	-27.63	72.2	15.83	-51.12	208.5	274.0	279.63	0.66	-5.7	0.86	B	-4320.84	-2.70	-3.0
ANMO	86	10	27	14:	11:	58.0	15.0	5.2	7.50	-36.66	69.7	25.21	-67.50	295.5	264.4	268.80	0.16	-4.4	0.62	C	-5535.04	-3.46	-0.9
GRFO	86	10	27	14:	11:	58.0	15.0	5.2	7.50	-36.66	57.9	30.53	-17.78	40.5	228.0	234.60	0.13	-6.6	0.62	C	-4511.15	-2.82	-3.8
KONO	86	10	27	14:	11:	58.0	15.0	5.2	7.50	-36.66	62.7	35.38	-21.13	29.8	236.8	247.33	0.06	-10.5	0.80	A	-5169.57	-3.23	-7.3
GRFO	86	10	31	7:	5:	52.0	153.2	5.2	6.79	-73.01	80.9	35.43	-42.18	52.7	320.3	320.60	0.08	-0.3	0.56	C	-4088.24	-2.56	2.3
ANMO	86	11	25	13:	59:	42.1	15.0	5.3	44.13	16.36	86.2	59.51	-51.35	260.5	333.8	337.23	1.16	-3.5	0.82	B	-3414.91	-2.13	-1.3
GAC	86	11	25	13:	59:	42.1	15.0	5.3	44.13	16.36	61.9	54.82	-28.34	272.7	233.0	243.23	0.63	-10.2	0.57	C	-2935.57	-1.83	-8.4
GRFO	86	11	30	5:	19:	48.1	15.0	5.0	-5.49	-35.75	68.4	23.84	-17.63	33.8	264.0	266.06	0.41	-2.1	0.67	C	-2029.69	-1.27	-0.8
KONO	86	11	30	5:	19:	48.1	15.0	5.0	-5.49	-35.75	74.1	28.81	-20.96	25.3	280.3	287.43	0.37	-7.1	0.62	C	-4755.76	-2.97	-4.1
GAC	86	12	7	14:	17:	10.5	15.0	5.1	43.29	25.94	67.5	57.08	-23.10	273.2	257.4	261.26	0.77	-3.9	0.70	B	-3003.33	-1.88	-2.0
ZOBO	86	12	8	3:	3:	26.1	15.0	5.1	46.94	-27.42	73.2	16.68	-51.61	207.3	277.2	282.64	0.67	-5.4	0.76	B	-4632.86	-2.90	-2.5
GRFO	87	1	13	13:	23:	59.7	15.0	5.5	5.77	-78.99	85.8	35.99	-45.85	53.0	332.0	338.46	0.11	-6.4	0.75	C	-4849.39	-3.03	-3.4
KONO	87	1	13	13:	23:	59.7	15.0	5.5	5.77	-78.99	84.4	40.45	-52.31	41.7	322.6	331.46	0.20	-8.9	0.87	B	-5084.63	-3.18	-5.7
GRFO	87	1	13	19:	30:	10.9	15.0	5.3	5.66	-78.74	85.6	36.10	-45.81	53.1	332.1	338.25	0.11	-6.1	0.83	B	-4928.83	-3.08	-3.0
KONO	87	1	13	19:	30:	10.9	15.0	5.3	5.66	-78.74	84.2	40.55	-52.27	41.8	322.1	331.48	0.20	-9.4	0.88	A	-5053.31	-3.16	-6.2
GAC	87	2	1	6:	56:	1.2	15.0	5.6	-0.07	-17.81	67.8	25.92	-40.85	314.5	257.7	264.76	0.27	-7.1	0.70	C	-4306.36	-2.69	-4.4
GDH	87	2	1	6:	56:	1.2	15.0	5.6	-0.07	-17.81	72.7	35.92	-26.67	344.3	283.3	283.71	0.15	-0.4	0.83	A	-3764.33	-2.35	1.9
NE04	87	2	18	0:	0:	52.6	33.9	6.2	51.29	-179.28	76.0	87.61	111.18	287.5	295.0	294.04	1.45	0.9	0.31	C	-4241.80	-2.65	3.6
NE16	87	2	18	0:	0:	52.6	33.9	6.2	51.29	-179.28	83.1	87.09	22.34	200.3	325.3	325.32	1.64	-0.1	0.53	C	-4110.00	-2.57	2.5
GAC	87	2	27	23:	34:	53.1	15.0	5.4	38.46	20.33	67.7	53.56	-23.57	278.1	258.4	261.31	0.67	-3.0	0.67	C	-3680.34	-2.30	-0.7
SCP	87	2	27	23:	34:	53.1	15.0	5.4	38.46	20.33	71.8	51.88	-27.30	272.4	269.1	276.09	0.69	-6.9	0.65	A	-3592.70	-2.25	-4.7
NE04	87	3	6	1:	54:	50.7	15.0	6.1	0.07	-77.64	86.5	33.25	-48.17	46.2	339.4	342.06	0.07	-2.7	0.64	A	-4988.80	-3.12	0.4
NE10	87	3	6	1:	54:	50.7	15.0	6.1	0.07	-77.64	80.5	26.65	-46.32	54.0	312.0	313.70	0.22	-1.7	0.34	C	-3844.56	-2.40	0.7
NE10	87	3	6	4:	10:	41.9	15.0	6.5	0.12	-77.80	80.7	26.57	-46.36	53.9	313.2	314.14	0.22	-0.9	0.48	C	-3835.63	-2.40	1.5
NE14	87	3	6	4:	10:	41.9	15.0	6.5	0.12	-77.80	77.5	22.76	-45.63	58.5	300.5	300.60	0.28	-0.1	0.65	C	-2987.24	-1.87	1.8
NE16	87	3	12	12:	18:	11.9	17.0	5.7	15.68	-94.55	84.1	41.51	-56.00	63.5	327.4	330.91	0.40	-3.5	0.56	C	-4839.86	-3.02	-0.5
GRFO	87	3	16	17:	20:	48.1	15.0	5.0	53.35	-167.23	77.3	88.42	-11.30	156.7	293.1	299.63	1.49	-6.5	0.64	B	-4060.44	-2.54	-4.0
GRFO	87	3	19	1:	28:	55.0	15.0	5.7	6.78	-76.47	83.0	36.28	-43.95	53.4	321.8	327.01	0.12	-5.2	0.64	B	-4791.63	-2.99	-2.3
KONO	87	3	19	1:	28:	55.0	15.0	5.7	6.78	-76.47	81.8	40.75	-50.20	41.9	310.7	321.43	0.20	-10.7	0.57	C	-3947.77	-2.47	-8.2
NE04	87	3	21	10:	41:	36.2	84.5	6.0	52.04	-177.56	75.5	88.29	119.35	294.7	289.1	292.90	1.45	-3.8	0.56	B	-4143.71	-2.59	-1.3
TOL	87	4	8	17:	42:	36.0	20.0	5.1	11.62	-86.46	77.2	32.45	-51.50	65.2	295.7	299.34	0.06	-3.6	0.88	B	-5399.28	-3.37	-0.3
GAC	87	4	14	0:	13:	13.1	15.0	5.3	-15.62	-14.98	81.5	17.59	-39.72	321.2	316.6	320.67	0.65	-4.0	0.69	C	-5187.05	-3.24	-0.8
ZOBO	87	5	4	23:	48:	34.2	15.0	5.1	37.61	-31.90	63.4	11.20	-51.85	210.8	248.9	250.71	0.61	-1.8	0.61	C	-4962.54	-3.10	1.3

Stn	Origin time							m_b	Epicenter		Bouncepoint				Obs	Pred	Ellip	Resid	r	Grade	Water	Depth	Dcor
	Yr	Mo	Da	Hr	Mn	Sec	Dep		Lat	Long	Dist	Lat	Long	Azim	time	time	corr.				depth	cor	resid
GAC	87	5	5	10:	50:	55.3	15.0	5.0	0.03	-19.13	67.5	25.42	-41.65	315.5	257.4	261.78	0.28	-4.4	0.68	C	-4091.46	-2.56	-1.9
GDH	87	5	5	10:	50:	55.3	15.0	5.0	0.03	-19.13	73.1	35.50	-27.66	344.9	283.9	282.39	0.17	1.5	0.76	B	-3430.36	-2.14	3.6
SCP	87	5	5	10:	50:	55.3	15.0	5.0	0.03	-19.13	67.1	23.01	-43.84	309.9	263.1	260.64	0.30	2.5	0.72	A	-3844.53	-2.40	4.9
NE16	87	5	6	4:	6:	15.5	20.1	6.3	51.26	-179.88	83.3	87.09	24.76	202.9	328.2	325.49	1.65	2.7	0.53	C	-3990.60	-2.49	5.2
GAC	87	6	7	14:	48:	50.7	15.0	5.0	-0.36	-19.06	67.5	25.46	-41.55	315.4	257.5	262.95	0.28	-5.5	0.74	C	-4089.43	-2.56	-2.9
KBS	87	6	9	18:	39:	17.3	15.0	5.0	12.75	-44.53	71.5	47.64	-36.12	14.2	269.5	276.24	0.30	-6.8	0.88	B	-4340.33	-2.71	-4.1
KONO	87	6	9	18:	39:	17.3	15.0	5.0	12.75	-44.53	61.4	38.99	-26.70	35.9	240.5	243.55	0.07	-3.0	0.70	C	-1634.09	-1.02	-2.0
KONO	87	6	22	19:	23:	32.0	15.0	5.2	7.13	-82.28	84.7	42.13	-55.04	42.8	331.1	333.80	0.28	-2.7	0.84	B	-4575.73	-2.86	0.2
GAC	87	7	28	1:	44:	9.7	15.0	5.0	0.67	-25.99	62.3	25.39	-45.83	318.0	238.9	246.84	0.26	-7.9	0.66	C	-3218.57	-2.01	-5.9
KEV	87	7	28	1:	44:	9.7	15.0	5.0	0.67	-25.99	76.8	37.62	-12.82	21.0	290.2	299.99	0.07	-9.8	0.71	C	-4792.05	-3.00	-6.8
KONO	87	7	28	1:	44:	9.7	15.0	5.0	0.67	-25.99	64.5	31.41	-13.96	22.3	249.7	254.74	0.22	-5.1	0.75	B	-3428.52	-2.14	-2.9
KBS	87	8	6	23:	11:	24.3	15.0	5.2	0.95	-28.56	80.4	40.89	-21.92	9.6	308.9	314.33	0.02	-5.4	0.63	C	-3948.88	-2.47	-3.0
ANTO	87	8	12	3:	9:	59.8	15.0	5.7	14.10	-59.21	82.5	36.02	-20.02	68.2	317.9	323.91	0.21	-6.1	0.73	C	-5259.35	-3.29	-2.8
GRFO	87	8	12	3:	9:	59.8	15.0	5.7	14.10	-59.21	66.6	37.01	-31.95	53.8	257.8	260.56	0.10	-2.7	0.71	B	-1974.96	-1.23	-1.5
KONO	87	8	12	3:	9:	59.8	15.0	5.7	14.10	-59.21	67.2	41.61	-36.90	41.6	255.4	262.25	0.18	-6.9	0.80	B	-4257.41	-2.66	-4.2
GAC	87	9	7	11:	32:	27.4	29.0	5.5	39.37	54.76	84.5	65.17	-3.74	278.7	328.9	330.63	1.31	-1.7	0.67	B	-3243.35	-2.03	0.3
NE15	87	9	22	13:	43:	39.7	15.0	6.1	-0.99	-78.05	86.9	31.57	-47.75	47.7	343.0	343.91	0.12	-0.9	0.61	A	-4907.73	-3.07	2.2
GRFO	87	11	11	15:	4:	52.5	29.9	5.3	6.80	-76.34	83.1	36.09	-43.89	53.2	323.7	326.95	0.11	-3.3	0.78	A	-4733.59	-2.96	-0.3
KONO	87	11	11	15:	4:	52.5	29.9	5.3	6.80	-76.34	81.9	40.56	-50.12	41.8	312.7	321.46	0.19	-8.7	0.86	B	-4161.88	-2.60	-6.1
NE13	87	11	17	3:	40:	8.9	56.0	5.8	12.53	-87.03	77.3	32.25	-51.60	66.8	295.4	299.41	0.06	-4.0	0.64	C	-5456.47	-3.41	-0.6

Explanation of abbreviations:
Stn = Station
Origin time = earthquake origin time (year, month, day, hour, minutes, seconds)
Dep = Event depth in km
mb = body wave magnitude
Dist = epicentral distance in degrees
Azim = azimuth from source to receiver measured at the SS bouncepoint, in clockwise degrees from north
Obs time = observed differential travel time between the phases S and SS
Pred time = predicted time between S and SS, from PREM
Ellip corr. = ellipticity correction (see text)
Resid = Obs. time - Pred time
r = correlation coefficient of crosscorrelation of S and SS
Grade = quality rating assigned to cross-correlogram
Water depth = bathymetry at the SS bouncepoint
Depth cor = correction for the water depth
Dcor resid = depth corrected SS-S differential travel time residual

Appendix II. SS-S Relative Attenuation (δt*) Values for the North Atlantic Region

	Origin time							Epicenter			Bouncepoint				
Stn	Yr	Mo	Da	Hr	Mn	Sec	Dep	mb	Lat	Long	Dist	Lat	Long	Azim	δt* grade
GRFO	80	6	25	12:	4:	56.9	151.1	5.7	4.70	-75.35	84.2	34.43	-43.80	51.8	0.8 A
GRFO	80	7	26	12:	53:	40.7	15.0	5.2	7.47	-33.89	56.4	30.43	-16.33	39.3	1.8 A
ZOBO	80	10	10	12:	25:	23.5	10.1	6.5	36.25	1.36	83.8	12.07	-36.84	228.4	11.1 B
ZOBO	80	10	10	15:	39:	9.8	10.0	6.2	35.72	1.31	83.5	11.76	-36.72	228.8	8.7 A
ZOBO	80	10	13	6:	37:	39.2	15.0	5.2	36.53	2.07	84.4	12.30	-36.59	228.4	1.1 A
GRFO	80	11	26	17:	35:	39.1	40.0	5.0	7.96	-72.64	80.0	35.97	-41.46	53.2	3.1 C
BOCO	80	12	5	13:	32:	5.9	15.0	5.0	35.87	1.68	75.8	24.96	-40.75	243.1	0.8 C
KONO	81	4	22	23:	16:	54.1	15.0	5.1	7.25	-36.06	62.6	35.36	-21.04	29.8	1.3 A
SCP	81	7	7	21:	10:	57.7	10.0	5.7	-0.07	-18.59	67.2	23.05	-43.72	309.8	3.7 B
SCP	81	8	13	2:	58:	11.2	18.0	5.5	44.86	17.33	65.9	53.95	-32.31	265.4	0.9 C
GRFO	81	10	18	4:	31:	2.7	26.0	5.4	8.45	-72.81	79.8	36.31	-41.50	53.5	0.5 A
KEV	81	11	28	19:	24:	5.6	15.0	5.1	24.22	-45.19	61.3	51.56	-27.27	33.5	2.1 A
KONO	81	12	6	14:	54:	29.6	10.0	5.5	8.25	-38.25	62.6	36.09	-22.51	31.2	2.1 C
SCP	82	1	3	14:	9:	50.4	10.0	5.8	-0.96	-21.83	65.6	22.26	-45.63	311.7	0.0 C
BER	82	1	30	2:	35:	11.0	34.6	6.0	16.71	-61.47	64.2	43.00	-40.02	41.5	4.5 C
TOL	82	4	6	19:	56:	53.7	42.6	5.9	13.79	-91.95	79.7	34.89	-54.55	67.5	3.9 C
ANMO	82	4	10	9:	47:	4.4	15.0	5.0	7.61	-35.81	69.8	25.46	-67.28	295.1	3.8 B
BOCO	82	5	2	7:	12:	44.5	15.0	5.4	44.01	-28.97	55.7	26.01	-55.33	223.2	3.3 B
KONO	82	5	10	1:	25:	56.8	79.8	5.3	10.50	-62.56	72.0	40.00	-39.90	40.6	3.9 C
SCP	82	8	12	8:	41:	50.5	10.1	5.2	-1.13	-24.34	64.0	21.94	-47.10	313.0	1.9 C
ANMO	82	8	12	8:	41:	50.5	10.1	5.2	-1.13	-24.34	84.2	21.88	-60.46	298.3	4.6 A
GAC	82	10	1	5:	35:	47.3	16.0	5.0	-1.03	-15.35	70.4	25.27	-39.54	314.6	8.5 C
ZOBO	82	12	22	15:	40:	13.3	15.0	5.3	46.25	-27.54	72.2	15.92	-51.27	208.3	1.1 B
GAC	83	1	17	12:	41:	29.3	10.1	6.0	38.13	20.38	67.5	53.20	-23.77	278.5	3.9 A
RSNT	83	1	17	12:	41:	29.3	10.1	6.0	38.13	20.38	73.4	69.42	-14.97	310.1	2.3 B
RSON	83	1	17	12:	41:	29.3	10.1	6.0	38.13	20.38	74.2	60.68	-27.05	285.6	4.3 A
COL	83	1	17	12:	41:	29.3	10.1	6.0	38.13	20.38	76.9	75.88	7.28	343.2	9.5 A
RSCP	83	1	17	12:	41:	29.3	10.1	6.0	38.13	20.38	79.6	51.23	-33.84	267.5	3.5 A
GAC	83	1	19	0:	2:	13.6	15.0	5.1	37.88	20.90	68.0	53.22	-23.37	278.8	4.7 A
RSCP	83	1	19	0:	2:	13.6	15.0	5.1	37.88	20.90	80.1	51.27	-33.45	267.8	3.1 A
RSNY	83	3	19	21:	41:	44.3	65.0	5.6	34.75	24.89	72.5	51.90	-19.67	280.7	2.3 C
GAC	83	3	19	21:	41:	44.3	65.0	5.6	34.75	24.89	72.5	52.70	-19.37	282.0	3.8 C
RSCP	83	3	19	21:	41:	44.3	65.0	5.6	34.75	24.89	84.6	51.02	-29.53	271.1	5.6 C
RSCP	83	3	24	4:	17:	31.6	25.0	5.3	38.58	20.54	79.5	51.51	-33.97	267.0	1.0 C
BER	83	3	31	13:	12:	52.3	56.8	5.4	2.45	-76.81	84.0	37.69	-52.33	38.5	3.5 C
KONO	83	4	10	1:	16:	5.8	15.0	5.2	16.48	-46.45	59.0	41.19	-27.80	38.7	3.8 B
GRFO	83	4	11	8:	18:	10.3	19.2	6.0	10.08	-62.61	71.9	35.38	-34.55	52.3	1.4 B
BCAO	83	4	11	8:	18:	10.3	19.2	6.0	10.08	-62.61	80.5	9.52	-21.74	94.4	2.0 A
TOL	83	5	9	15:	53:	2.7	11.0	5.5	8.06	-82.87	76.3	29.78	-49.42	62.3	5.5 B
KONO	83	5	12	10:	51:	49.6	10.1	5.6	17.04	-46.52	58.6	41.49	-27.80	39.0	7.5 A
KEV	83	5	12	10:	51:	49.6	10.1	5.6	17.04	-46.52	68.4	48.08	-29.05	30.8	3.2 B
RSCP	83	5	14	23:	13:	46.5	15.0	5.0	38.06	20.55	79.8	51.25	-33.72	267.6	6.1 A
GRFO	83	5	20	17:	40:	14.4	15.0	5.2	18.32	-70.20	70.8	41.30	-38.75	59.0	3.8 C
GAC	83	7	14	2:	54:	18.6	25.0	5.2	36.51	21.37	69.2	52.65	-22.49	280.1	2.7 C
RSNY	83	8	6	15:	43:	52.6	10.0	6.3	39.89	24.66	69.0	54.43	-22.44	275.3	1.1 A
RSCP	83	8	6	15:	43:	52.6	10.0	6.3	39.89	24.66	81.2	53.52	-32.82	265.6	3.8 B
SCP	83	10	13	13:	6:	38.2	10.0	5.6	-0.66	-21.73	65.4	22.43	-45.58	311.5	2.3 B
RSSD	83	10	13	13:	6:	38.2	10.0	5.6	-0.66	-21.73	84.9	27.65	-54.71	306.1	3.2 C
GRFO	83	10	13	23:	27:	33.2	10.0	5.3	7.25	-34.35	56.9	30.35	-16.63	39.5	0.0 B
RSON	83	10	13	23:	27:	33.2	10.0	5.3	7.25	-34.35	65.3	32.38	-56.80	315.3	1.3 C
SCP	83	10	21	20:	34:	49.1	15.0	5.1	40.54	30.05	75.9	55.59	-23.73	270.3	2.0 C
SCP	83	10	30	4:	12:	27.7	11.6	6.1	40.47	42.05	82.4	59.74	-17.66	270.4	2.8 A
TOL	83	11	22	14:	20:	58.8	35.2	6.3	0.31	-79.99	79.0	24.75	-47.94	56.8	5.4 A

	Origin time						Epicenter			Bouncepoint				
Stn	Yr	Mo	Da	Hr Mn Sec	Dep	mb	Lat	Long	Dist	Lat	Long	Azim	δt*	
RSSD	83	12	22	4:11:29.3	10.0	6.4	12.02	-13.64	82.0	36.79	-50.04	297.6	3.3	B
ANMO	83	12	22	4:11:29.3	10.0	6.4	12.02	-13.64	85.5	32.10	-54.74	288.4	5.3	C
SCP	84	2	11	8: 2:50.0	15.0	5.3	38.11	21.86	72.6	51.92	-26.67	272.9	4.0	C
TOL	84	2	26	8:18:16.6	115.6	5.9	-17.31	-70.65	84.1	13.14	-41.69	44.1	2.8	C
KEV	84	3	20	17:19: 6.4	10.0	5.1	10.75	-41.96	72.8	44.28	-25.70	27.7	4.2	B
BER	84	3	30	7:59:53.6	10.0	5.8	17.65	-59.84	62.6	43.30	-38.72	41.5	1.3	B
GAC	84	4	22	6:14:21.7	10.0	5.8	-0.14	-19.59	67.0	25.32	-42.14	315.8	1.0	B
GAC	84	5	6	9:12: 1.7	10.0	5.0	38.66	25.57	70.2	54.88	-21.07	277.9	-0.3	C
GAC	84	6	21	10:43:40.5	34.3	5.7	35.74	23.80	71.2	52.93	-20.70	280.9	6.2	C
RSCP	84	6	21	10:43:40.5	34.3	5.7	35.74	23.80	83.3	51.15	-30.87	269.9	8.6	C
NE13	84	6	24	11:17:12.0	16.4	6.0	18.09	-69.23	59.7	32.61	-40.27	68.0	1.5	B
TOL	84	6	24	11:17:12.0	16.4	6.0	18.09	-69.23	59.7	33.26	-40.56	66.7	2.5	A
GRFO	84	6	25	18:45:10.3	42.0	5.1	18.13	-69.35	70.3	40.98	-38.31	58.7	1.5	B
GAC	84	7	19	5:22:15.7	10.0	5.4	-6.68	-12.48	76.5	22.44	-37.87	316.4	7.7	A
GDH	84	7	19	5:22:15.7	10.0	5.4	-6.68	-12.48	80.9	32.53	-22.93	343.8	7.5	B
RSON	84	8	30	20:12:59.7	10.0	5.0	7.19	-33.72	65.7	32.42	-56.39	315.1	3.4	A
ANMO	84	8	30	20:12:59.7	10.0	5.0	7.19	-33.72	71.8	25.51	-66.08	294.9	2.4	B
GAC	84	10	21	3:51:47.0	10.0	5.1	-6.71	-12.38	76.6	22.44	-37.81	316.4	1.3	B
KONO	84	11	1	4:48:49.9	10.0	6.5	8.36	-38.82	62.7	36.20	-22.90	31.5	1.7	A
ANMO	84	11	1	4:48:49.9	10.0	6.5	8.36	-38.82	66.9	25.49	-69.04	295.3	0.9	C
GAC	84	11	5	4:17:32.9	10.0	5.1	-11.54	-13.79	79.4	19.60	-38.91	319.3	3.5	A
GAC	84	12	5	13:39:23.6	10.0	5.1	-0.46	-13.36	71.2	25.81	-38.31	313.5	2.6	C
SCP	84	12	8	12:24:41.9	10.0	5.7	-0.86	-22.95	64.7	22.21	-46.29	312.2	3.5	C
RSON	84	12	8	12:24:41.9	10.0	5.7	-0.86	-22.95	78.6	29.44	-49.20	315.6	5.7	B
RSSD	84	12	8	12:24:41.9	10.0	5.7	-0.86	-22.95	84.2	27.32	-55.49	306.5	6.7	B
ANMO	84	12	20	23:31:18.0	10.0	5.2	6.94	-33.32	72.2	25.42	-65.83	295.0	2.0	B
KONO	85	1	10	17:47:56.1	10.0	5.8	10.83	-43.44	62.6	37.93	-26.02	34.6	2.6	A
KEV	85	1	10	17:47:56.1	10.0	5.8	10.83	-43.44	73.2	44.50	-26.91	28.1	3.7	A
NE16	85	3	16	14:54: 1.1	14.0	6.2	17.10	-62.34	60.9	35.86	-35.35	59.1	8.5	C
NE06	85	3	16	14:54: 1.1	14.0	6.2	17.10	-62.34	62.3	38.29	-36.30	54.4	2.9	C
GRFO	85	3	16	14:54: 1.1	14.0	6.2	17.10	-62.34	66.5	39.16	-33.77	56.6	5.8	B
ANTO	85	3	16	14:54: 1.1	14.0	6.2	17.10	-62.34	83.1	38.60	-21.61	70.5	7.3	C
GRFO	85	4	20	18:23:48.2	12.3	5.6	01	-77.35	82.3	37.59	-44.56	54.5	3.5	A
RSNY	85	6	4	12: 6: 3.6	10.0	5.1	08	-19.07	66.0	24.79	-41.76	314.8	2.4	A
ZOBO	85	6	5	1:41:42.3	14.5	5.1	56.72	-34.72	77.9	20.99	-56.09	198.6	4.8	C
RSNY	85	6	6	2:40:12.8	10.0	6.3	1.00	-28.08	59.7	24.49	-47.18	318.8	4.0	C
TOL	85	6	10	3:23:31.8	26.0	5.6	3.24	-78.99	76.4	26.34	-47.28	58.3	1.4	C
BCAO	85	6	26	17:10: 1.9	26.6	5.6	19.25	-64.73	82.2	15.67	-21.74	101.4	2.0	C
ANTO	85	6	26	17:10: 1.9	26.6	5.6	19.25	-64.73	83.5	40.50	-22.72	72.1	6.1	C
GAC	85	7	1	9:53:36.1	10.0	5.0	1.13	-26.48	61.7	25.37	-46.34	318.4	5.0	C
RSON	85	7	1	9:53:36.1	10.0	5.0	1.13	-26.48	74.9	30.07	-51.55	315.7	1.7	C
RSNY	85	7	22	21:32:27.9	15.0	5.4	34.16	28.40	75.0	52.65	-17.70	280.9	4.3	B
RSON	85	9	22	18:23:12.2	10.0	5.7	12.46	-44.47	55.2	34.01	-63.46	316.6	0.7	B
RSNY	85	9	23	17:28:41.8	10.0	5.2	-18.00	-13.75	83.3	15.24	-39.34	321.7	5.0	C
RSNY	85	9	27	16:39:48.6	43.8	5.5	34.05	26.94	74.2	52.15	-18.39	281.1	0.7	B
ANTO	85	10	5	15:24: 2.2	10.0	6.5	62.53	-123.93	76.2	75.73	4.81	144.2	2.8	C
SCP	85	10	12	22:20:37.6	10.0	5.3	0.99	-29.15	59.2	22.69	-49.92	314.0	1.1	C
ANMO	85	10	12	22:20:37.6	10.0	5.3	0.99	-29.15	79.0	22.49	-63.27	298.0	7.5	C
RSON	85	10	27	19:34:57.0	10.0	5.5	36.46	6.87	68.7	55.92	-35.15	286.7	7.1	A
GAC	85	11	10	12:39:50.8	10.0	5.2	4.57	-31.96	55.7	26.73	-49.69	319.4	2.2	B
RSON	85	11	10	12:39:50.8	10.0	5.2	4.57	-31.96	68.9	31.23	-55.18	315.9	6.8	C
RSSD	85	11	10	12:39:50.8	10.0	5.2	4.57	-31.96	74.0	29.06	-61.25	305.7	3.6	A
KEV	85	11	10	12:39:50.8	10.0	5.2	4.57	-31.96	75.3	40.02	-17.80	23.6	1.2	C
GAC	85	11	21	21:57:14.9	10.1	5.4	41.49	19.69	65.0	54.67	-25.68	274.9	2.6	B
RSNT	85	11	21	21:57:14.9	10.1	5.4	41.49	19.69	70.1	70.79	-18.08	306.6	7.7	C

	Origin time							Epicenter			Bouncepoint				
Stn	Yr	Mo	Da	Hr	Mn	Sec	Dep	mb	Lat	Long	Dist	Lat	Long	Azim	δt*	
ANTO	85	12	23	19:	37:	54.8	10.0	5.5	62.24	-123.95	76.5	75.81	4.32	143.6	9.4	B
GDH	85	12	24	4:	13:	21.2	10.0	5.0	7.53	-33.88	63.0	38.65	-39.01	350.2	2.3	A
KONO	86	2	12	23:	41:	38.5	15.0	5.2	17.30	-62.41	66.1	43.78	-39.03	44.2	1.6	A
GAC	86	3	6	0:	5:	38.3	35.0	6.2	40.33	51.60	82.1	64.38	-6.78	277.1	5.3	B
RSON	86	3	6	0:	5:	38.3	35.0	6.2	40.33	51.60	84.2	73.02	-4.11	289.4	6.6	B
RSNT	86	5	5	3:	35:	38.8	15.0	5.8	37.72	37.70	77.7	73.68	8.39	321.7	2.4	C
NE16	86	5	7	20:	43:	32.6	23.1	6.1	51.60	-174.65	83.0	87.01	-15.01	160.9	2.5	A
NE16	86	5	7	22:	47:	10.2	31.3	6.5	51.33	-175.43	83.3	87.69	-12.41	163.8	3.4	B
NE10	86	5	7	22:	47:	10.2	31.3	6.5	51.33	-175.43	85.9	85.29	-29.17	149.2	6.2	C
RSON	86	5	13	8:	44:	2.0	15.0	5.6	41.03	43.92	81.3	70.26	-11.96	285.8	4.3	A
RSSD	86	5	21	1:	45:	24.8	15.0	5.2	14.90	-20.02	75.5	37.05	-54.45	296.6	6.3	B
GAC	86	5	22	19:	52:	19.5	33.2	5.1	34.12	26.72	74.0	52.94	-18.29	282.4	0.9	B
RSNY	86	5	22	19:	52:	19.5	33.2	5.1	34.12	26.72	74.1	52.13	-18.61	281.0	0.5	A
GRFO	86	6	9	2:	17:	38.3	49.5	5.0	54.59	-168.10	76.1	88.50	1.47	169.9	1.4	B
NE13	86	6	11	13:	48:	3.3	20.0	6.0	10.70	-62.93	59.1	27.77	-37.23	59.9	6.2	B
TOL	86	6	11	13:	48:	3.3	20.0	6.0	10.70	-62.93	59.4	28.41	-37.48	58.6	0.6	B
NE11	86	6	11	13:	48:	3.3	20.0	6.0	10.70	-62.93	61.7	29.75	-36.91	57.4	3.2	C
BCAO	86	6	11	13:	48:	3.3	20.0	6.0	10.70	-62.93	80.8	9.94	-21.85	94.8	2.8	B
RSCP	86	6	15	23:	58:	44.1	15.0	5.0	1.16	-26.46	64.5	20.87	-52.67	304.1	4.4	C
RSON	86	6	17	8:	48:	18.6	15.0	5.4	4.55	-32.55	68.5	31.15	-55.56	316.1	1.4	C
WFM	86	6	24	6:	56:	53.0	15.0	5.7	0.53	-17.41	63.9	23.86	-40.00	313.4	3.4	C
RSNY	86	6	24	6:	56:	53.0	15.0	5.7	0.53	-17.41	66.8	25.19	-40.74	313.8	4.4	B
GAC	86	6	24	6:	56:	53.0	15.0	5.7	0.53	-17.41	67.8	25.91	-40.81	314.5	6.9	B
RSCP	86	6	24	6:	56:	53.0	15.0	5.7	0.53	-17.41	72.0	21.44	-47.49	301.4	10.2	A
GAC	86	7	10	6:	53:	4.3	15.0	5.4	4.31	-32.49	55.6	26.56	-50.00	319.9	6.3	A
RSON	86	7	10	6:	53:	4.3	15.0	5.4	4.31	-32.49	68.8	31.03	-55.52	316.2	7.1	A
RSSD	86	7	10	6:	53:	4.3	15.0	5.4	4.31	-32.49	73.8	28.83	-61.57	306.0	5.9	B
GRFO	86	7	18	17:	22:	41.6	15.0	5.8	10.84	-69.24	75.7	36.97	-38.90	54.2	1.2	B
GRFO	86	8	7	22:	32:	50.9	15.0	5.4	7.53	-81.06	85.8	37.55	-47.27	54.3	1.0	C
GAC	86	9	13	17:	24:	33.7	15.0	5.8	36.80	22.64	69.8	53.15	-21.91	279.8	3.9	C
RSNT	86	9	13	17:	24:	33.7	15.0	5.8	36.80	22.64	75.3	69.40	-11.53	312.3	3.9	B
ANMO	86	9	20	1:	31:	14.0	15.0	5.4	0.72	-29.00	79.3	22.34	-63.18	298.2	1.6	B
RSNY	86	10	2	10:	12:	39.8	15.0	5.3	34.65	29.16	75.2	53.13	-17.46	280.5	7.1	B
ZOBO	86	10	27	0:	9:	31.9	15.0	5.3	46.06	-27.27	72.2	15.83	-51.12	208.5	3.2	C
KONO	86	10	27	14:	11:	58.0	15.0	5.2	7.26	-36.20	62.7	35.38	-21.13	29.8	1.5	B
GAC	86	12	7	14:	17:	10.5	15.0	5.1	43.01	26.01	67.5	57.08	-23.10	273.2	3.9	A
ZOBO	86	12	8	3:	3:	26.1	15.0	5.1	47.72	-27.70	73.2	16.68	-51.61	207.3	1.4	C
GRFO	87	1	13	13:	23:	59.7	15.0	5.5	5.68	-78.90	85.8	35.99	-45.85	53.0	5.0	B
GRFO	87	1	13	19:	30:	10.9	15.0	5.3	5.87	-78.86	85.6	36.10	-45.81	53.1	1.0	B
GDH	87	2	1	6:	56:	1.2	15.0	5.6	0.55	-17.47	72.7	35.92	-26.67	344.3	1.3	B
NE14	87	3	6	4:	10:	41.9	15.0	6.5	-0.06	-77.84	77.5	22.76	-45.63	58.5	2.2	B
GAC	87	3	12	23:	10:	31.4	15.0	5.4	0.36	-17.81	67.7	25.77	-41.04	314.8	6.4	C
GAC	87	4	14	0:	13:	13.1	15.0	5.3	-14.96	-14.74	81.5	17.59	-39.72	321.2	3.6	C
SCP	87	5	5	10:	50:	55.3	15.0	5.0	-0.11	-18.78	67.1	23.01	-43.84	309.9	3.6	A
GAC	87	5	5	10:	50:	55.3	15.0	5.0	-0.11	-18.78	67.5	25.42	-41.65	315.5	4.3	A
GDH	87	5	5	10:	50:	55.3	15.0	5.0	-0.11	-18.78	73.1	35.50	-27.66	344.9	5.0	A
GAC	87	7	28	1:	44:	9.7	15.0	5.0	1.02	-25.62	62.3	25.39	-45.83	318.0	0.6	A

δt* = Differential attenuation between the S and SS phases
Other abbreviations as in Appendix I

Appendix III. SS-S Travel Time Data for the East Pacific Region

Stn	Origin time							Epicenter			Bouncepoint			Obs	Pred	Ellip	Resid	r	Grade	Water	Depth	Dcor
	Yr	Mo	Da	Hr	Mn	Sec	Dep	m_b	Lat	Long	Dist	Lat	Long	Azim	time	time	corr.				depth	cor	resid
ANMO	80	1	14	21	51	1.8	14.0	5.6	-33.19	-69.46	76.1	0.91	-87.75	334.7	299.3	296.24	0.93	3.1	0.67	C	-2507.98	-1.57	4.6
ANMO	80	1	20	1	3	33.2	33.0	5.0	-22.73	-114.20	57.8	6.07	-110.56	7.0	233.3	235.11	0.66	-1.8	0.71	C	-3895.99	-2.43	0.6
ZOBO	80	1	24	19	0	9.5	11.0	5.3	37.85	-121.82	73.7	12.05	-92.16	139.3	288.5	286.24	0.64	2.3	0.94	A	-3827.72	-2.39	4.7
ANMO	80	1	27	16	38	1.1	10.0	5.7	-35.38	-105.87	70.0	-0.61	-106.16	359.6	273.5	272.33	0.92	1.2	0.95	A	-3652.54	-2.28	3.5
ANMO	80	1	28	16	59	22.9	33.0	5.3	-44.96	-76.11	84.2	-5.24	-92.41	342.7	329.9	332.39	1.14	-2.5	0.70	C	-3933.57	-2.46	0.0
ANMO	80	2	14	14	7	1.6	45.0	5.3	-31.77	-71.42	74.1	1.57	-88.57	335.3	292.4	288.58	0.90	3.8	0.70	C	-2538.14	-1.59	5.4
ANMO	80	3	29	6	41	50.5	33.0	5.6	-43.08	-75.20	82.7	-4.27	-91.74	341.6	323.7	325.67	1.11	-2.0	0.69	B	-3795.94	-2.37	0.4
ANMO	80	3	29	17	49	10.9	33.0	5.2	-37.93	-73.50	78.7	-1.60	-90.29	338.9	312.2	307.47	1.02	4.7	0.68	C	-365.76	-0.23	5.0
ANMO	80	4	9	8	17	55.1	10.0	5.5	-31.65	-67.48	75.7	1.74	-86.58	332.9	296.0	294.35	0.91	1.6	0.68	C	-2805.21	-1.75	3.4
ANMO	80	4	9	19	56	26.0	10.0	5.5	-44.61	-80.10	82.7	-4.97	-94.22	344.7	323.4	325.13	1.12	-1.7	0.96	A	-3653.02	-2.28	0.6
ANMO	80	4	14	23	57	27.6	100.0	5.4	-21.29	-68.73	66.4	6.84	-86.12	329.0	264.9	261.61	0.70	3.3	0.80	C	-2446.43	-1.53	4.8
ANMO	80	5	2	19	9	7.8	163.0	5.4	-24.13	-66.94	69.7	5.35	-85.36	329.2	280.1	274.42	0.77	5.7	0.48	C	-2340.67	-1.46	7.1
ANMO	80	5	26	18	41	36.8	62.0	6.0	-19.36	-69.29	64.5	8.04	-86.41	328.4	262.1	254.66	0.65	7.4	0.91	B	-2949.76	-1.84	9.3
ANMO	80	5	30	16	56	22.2	33.0	5.3	-23.11	-70.93	66.9	6.16	-87.61	331.3	267.7	261.74	0.72	6.0	0.85	A	-2744.67	-1.72	7.7
ZOBO	80	6	9	3	28	18.9	5.0	5.6	32.22	-114.99	65.9	8.68	-89.99	138.8	264.3	257.88	0.59	6.4	0.71	B	-3443.62	-2.15	8.6
ANMO	80	6	11	14	21	18.9	35.0	5.5	-32.72	-71.65	74.8	1.11	-88.80	335.8	297.1	291.28	0.92	5.8	0.55	B	-2364.30	-1.48	7.3
ANMO	80	6	16	5	45	6.9	87.0	5.5	-22.03	-68.47	67.2	6.53	-86.07	329.2	267.0	263.88	0.71	3.1	0.76	B	-2199.25	-1.37	4.5
ANMO	80	7	13	6	20	30.3	103.0	5.6	-33.47	-70.15	76.1	0.43	-87.98	335.2	303.8	298.08	0.95	5.7	0.60	B	-2438.18	-1.52	7.2
ANMO	80	8	3	3	0	49.7	151.0	5.3	-35.25	-69.99	77.7	-0.56	-88.08	335.9	310.4	306.01	0.99	4.4	0.79	B	-2354.32	-1.47	5.9
ANMO	80	8	3	13	42	35.4	10.0	5.1	-35.58	-104.63	70.2	-0.42	-105.54	358.7	273.6	273.12	0.92	0.5	0.92	A	-3613.14	-2.26	2.7
ANMO	80	9	2	22	18	41.6	10.0	5.0	-26.79	-112.92	61.7	4.06	-109.83	5.4	243.8	245.34	0.74	-1.5	0.81	B	-3923.27	-2.45	0.9
ANMO	80	9	26	20	26	34.8	10.0	4.9	-35.90	-102.94	70.6	-0.52	-104.71	357.5	275.6	274.49	0.92	1.1	0.95	A	-3545.63	-2.22	3.3
ANMO	80	11	8	21	35	43.1	103.0	5.4	-24.34	-67.65	69.5	5.25	-85.77	329.8	282.9	272.42	0.77	10.5	0.48	C	-1949.12	-1.22	11.7
ANMO	80	12	11	18	15	3.5	80.0	6.1	-21.27	-68.15	66.7	6.97	-85.87	328.6	263.9	262.14	0.70	1.8	0.70	C	-2353.37	-1.47	3.2
ANMO	80	12	20	20	26	47.2	571.0	5.2	-24.37	-63.42	71.7	3.93	-82.63	327.3	295.8	294.05	0.85	1.8	0.83	C	-3002.56	-1.88	3.6
ANMO	81	1	7	16	26	42.5	37.0	5.5	-23.75	-70.62	67.6	5.82	-87.49	331.4	269.9	264.17	0.74	5.7	0.84	A	-2327.73	-1.45	7.2
JAS	81	1	7	16	26	42.5	37.0	5.5	-23.75	-70.62	77.2	7.76	-93.51	325.0	300.8	300.84	0.81	0.0	0.41	C	-3621.82	-2.26	2.2
ANMO	81	1	7	20	31	12.1	10.0	5.1	-49.91	-114.14	84.8	-7.53	-109.84	4.1	337.6	334.81	1.19	2.8	0.90	B	-3401.91	-2.13	4.9
ANMO	81	3	2	21	19	56.0	246.0	5.1	-22.64	-65.99	69.0	5.86	-84.54	328.0	277.1	273.67	0.75	3.4	0.83	A	-2540.51	-1.59	5.0
ALQ	81	3	23	19	28	10.7	46.0	5.8	-33.66	-71.89	75.5	0.58	-89.00	336.3	299.6	294.47	0.94	5.1	0.53	B	-2222.75	-1.39	6.5
ANMO	81	3	23	19	28	10.7	46.0	5.8	-33.66	-71.89	75.5	0.58	-89.00	336.3	300.2	294.48	0.94	5.7	0.65	B	-2222.75	-1.39	7.1
ANMO	81	3	26	18	4	44.7	138.0	5.8	-19.37	-68.96	64.7	7.77	-86.07	328.2	264.4	256.76	0.66	7.6	0.83	C	-2583.31	-1.61	9.3
ALQ	81	4	1	18	3	36.5	554.0	5.9	-27.31	-63.32	74.1	2.38	-82.93	328.7	306.9	303.17	0.92	3.7	0.85	B	-3110.09	-1.94	5.7
ANMO	81	4	6	14	34	1.3	88.0	5.3	-35.37	-71.05	77.4	-0.51	-88.67	336.5	309.8	303.10	0.98	6.7	0.59	C	-2105.08	-1.32	8.0
ANMO	81	4	16	22	5	53.0	33.0	5.1	-20.16	-70.70	64.5	7.71	-87.30	329.7	262.3	253.95	0.66	8.4	0.87	B	-3313.75	-2.07	10.4
ANMO	81	5	17	17	4	58.0	33.0	5.4	-27.22	-71.83	70.0	4.00	-88.39	333.7	271.2	272.64	0.80	-1.4	0.75	B	-1998.41	-1.25	-0.2
ALQ	81	5	24	11	44	3.5	10.0	5.2	-22.16	-114.20	57.3	6.39	-110.57	7.1	228.9	233.37	0.65	-4.5	0.67	C	-3830.30	-2.39	-2.1
ANMO	81	5	24	11	44	3.5	10.0	5.2	-22.16	-114.20	57.3	6.39	-110.57	7.1	230.9	233.38	0.65	-2.5	0.81	C	-3830.30	-2.39	-0.1

Stn	Origin time							Epicenter			Bouncepoint			Obs	Pred	Ellip	Resid	r	Grade	Water	Depth	Dcor
	Yr	Mo	Da	Hr Mn Sec	Dep	m_b	Lat	Long	Dist	Lat	Long	Azim	time	time	corr.				depth	cor	resid
ANMO	81	5	24	11:44: 3.5	10.0	5.2	-22.16	-114.20	57.3	6.39	-110.57	7.1	230.9	233.38	0.65	-2.5	0.81	C	-3830.30	-2.39	-0.1
LON	81	5	24	11:44: 3.5	10.0	5.2	-22.16	-114.20	68.9	12.32	-117.44	354.7	269.5	268.51	0.79	1.0	0.78	C	-4130.04	-2.58	3.6
LON	81	5	24	11:44: 3.5	10.0	5.2	-22.16	-114.20	68.9	12.32	-117.44	354.7	269.5	268.51	0.79	1.0	0.78	C	-4130.04	-2.58	3.6
ANMO	81	6	1	19:50:13.3	330.0	5.0	-20.49	-65.19	67.6	6.69	-83.70	326.4	273.8	271.07	0.72	2.7	0.38	C	-2021.52	-1.26	4.0
ANMO	81	6	4	7:39:40.4	33.0	5.1	-34.20	-78.83	73.5	0.33	-92.56	340.8	286.3	285.98	0.93	0.3	0.60	B	-2913.46	-1.82	2.1
ANMO	81	6	10	4: 6:10.2	10.0	4.8	-35.80	-102.17	70.5	-0.45	-104.32	357.0	275.9	274.26	0.92	1.6	0.90	A	-3503.32	-2.19	3.8
JAS	81	6	16	5:41:49.1	76.0	5.4	-21.49	-68.34	76.7	8.92	-91.91	322.8	302.9	299.97	0.77	2.9	0.56	C	-3607.67	-2.25	5.2
ALQ	81	6	21	10:30: 1.1	36.0	5.2	-20.26	-70.45	64.7	7.66	-87.17	329.6	261.8	254.66	0.66	7.1	0.69	B	-3282.78	-2.05	9.2
ANMO	81	6	21	10:30: 1.1	36.0	5.2	-20.26	-70.45	64.7	7.66	-87.17	329.6	262.5	254.67	0.66	7.8	0.92	B	-3282.78	-2.05	9.9
JAS	81	6	21	10:30: 1.1	36.0	5.2	-20.26	-70.45	74.5	9.68	-93.09	323.3	292.6	290.03	0.73	2.6	0.85	A	-3631.79	-2.27	4.8
JAS	81	6	22	17:53:21.3	24.0	5.1	-13.17	-74.52	66.6	13.38	-94.91	321.7	262.4	260.57	0.57	1.8	0.90	B	-4014.69	-2.51	4.3
ANMO	81	7	10	18: 2: 4.9	10.0	5.2	-37.22	-95.37	72.5	-1.15	-100.99	352.4	280.6	281.90	0.96	-1.3	0.66	C	-3307.67	-2.07	0.8
JAS	81	7	10	18: 2: 4.9	10.0	5.2	-37.22	-95.37	78.3	0.36	-107.84	344.1	306.1	305.32	1.05	0.8	0.41	C	-3693.83	-2.31	3.1
ANMO	81	7	18	11:15:18.1	246.0	5.0	-22.68	-66.24	68.9	5.83	-84.68	328.1	279.0	273.31	0.75	5.7	0.84	A	-2463.50	-1.54	7.2
ALQ	81	7	28	3: 3:21.6	43.0	5.5	-41.57	-73.20	82.0	-3.54	-90.58	340.0	321.8	322.66	1.09	-0.9	0.38	C	-3293.09	-2.06	1.2
ANMO	81	7	28	3: 3:21.6	43.0	5.5	-41.57	-73.20	82.0	-3.54	-90.58	340.0	322.4	322.67	1.09	-0.3	0.89	B	-3293.09	-2.06	1.8
AFI	81	8	17	2:18:59.9	37.0	5.5	14.52	-93.77	82.2	0.42	-132.78	248.2	316.3	322.67	0.53	-6.4	0.69	C	-4455.81	-2.78	-3.6
ANMO	81	8	21	22:52:40.6	10.0	5.1	-26.51	-114.76	61.6	4.20	-110.79	7.0	242.7	245.10	0.73	-2.4	0.65	C	-3940.62	-2.46	0.1
ANMO	81	8	22	23:47:41.4	10.0	5.2	-35.83	-103.30	70.5	-0.45	-104.89	357.8	275.9	274.18	0.92	1.7	0.95	A	-3562.40	-2.23	4.0
JAS	81	8	22	23:47:41.4	10.0	5.2	-35.83	-103.30	75.1	1.06	-111.75	348.7	296.4	292.02	1.00	4.4	0.28	C	-3875.51	-2.42	6.8
SCP	81	8	22	23:47:41.4	10.0	5.2	-35.83	-103.30	79.8	2.54	-91.03	15.6	313.7	311.68	1.07	2.0	0.72	C	-2280.88	-1.43	3.5
LON	81	9	6	16:43:19.9	10.0	5.4	-36.17	-100.70	84.7	5.37	-110.38	348.3	336.3	334.51	1.18	1.8	0.90	A	-3973.10	-2.48	4.3
SCP	81	9	6	16:43:19.9	10.0	5.4	-36.17	-100.70	79.4	2.35	-89.66	14.1	311.2	310.18	1.08	1.0	0.70	B	-2011.65	-1.26	2.3
ANMO	81	9	19	11:40:56.9	30.0	5.6	-39.08	-74.81	79.3	-2.19	-91.06	340.0	311.0	309.88	1.04	1.1	0.85	B	-3247.33	-2.03	3.2
ANMO	81	9	20	10:48:20.3	234.0	5.1	-23.08	-66.63	69.0	5.72	-84.99	328.6	280.7	273.47	0.76	7.2	0.64	C	-2378.76	-1.49	8.7
BOCO	82	1	21	21:52:41.0	10.0	5.5	19.22	-155.60	80.5	15.55	-113.49	101.5	320.0	314.40	0.30	5.6	0.82	A	-3707.94	-2.32	7.9
BOCO	82	1	21	22:29:13.0	13.0	5.5	19.20	-155.57	80.5	15.54	-113.48	101.5	319.7	314.33	0.30	5.4	0.66	B	-3720.70	-2.33	7.7
ALQ	82	2	10	20:38: 3.5	226.0	5.9	-22.79	-66.66	68.7	5.91	-85.00	328.4	278.6	272.35	0.75	6.3	0.95	A	-2218.47	-1.39	7.6
ANMO	82	2	10	20:38: 3.5	226.0	5.9	-22.79	-66.66	68.7	5.91	-85.00	328.4	278.7	272.36	0.75	6.3	0.95	A	-2218.47	-1.39	7.7
ANMO	82	3	22	21:44: 9.3	126.0	5.1	-19.88	-68.74	65.2	7.52	-85.99	328.3	264.6	258.26	0.67	6.3	0.75	B	-2515.72	-1.57	7.9
ALQ	82	4	18	11:30:55.3	10.0	5.9	-28.16	-114.07	63.2	3.38	-110.40	6.2	248.6	249.69	0.77	-1.1	0.80	C	-3885.43	-2.43	1.3
LON	82	4	18	11:30:55.3	10.0	5.9	-28.16	-114.07	74.9	9.28	-117.45	355.1	292.2	291.09	0.96	1.1	0.78	A	-4091.18	-2.56	3.7
SCP	82	4	18	11:30:55.3	10.0	5.9	-28.16	-114.07	76.4	6.63	-97.40	24.2	304.2	297.15	0.91	7.1	0.86	C	-3344.89	-2.09	9.1
ANMO	82	4	19	11:54:27.5	250.0	5.3	-22.60	-66.02	68.9	5.86	-84.54	328.0	278.9	273.59	0.75	5.3	0.55	C	-2540.51	-1.59	6.9
ANMO	82	5	3	7:26: 2.5	107.0	5.5	-23.47	-68.81	68.2	5.67	-86.31	330.1	270.8	267.87	0.74	2.9	0.79	B	-1797.63	-1.12	4.1
ANMO	82	5	17	2:39:26.1	10.0	5.0	-35.35	-103.84	70.0	-0.22	-105.15	358.1	275.2	272.36	0.91	2.8	0.93	A	-3586.13	-2.24	5.1
GAC	82	5	17	2:39:26.1	10.0	5.0	-35.35	-103.84	84.7	5.33	-90.78	15.9	335.6	334.27	1.15	1.3	0.62	C	-3478.85	-2.17	3.5

Stn	Origin time							Epicenter			Bouncepoint			Obs	Pred	Ellip	Resid	r	Grade	Water	Depth	Dcor
	Yr	Mo	Da	Hr	Mn	Sec	Dep	m_b	Lat	Long	Dist	Lat	Long	Azim	time	time	corr.				depth	cor	resid
LON	82	5	17	2:39:26.1			10.0	5.0	-35.35	-103.84	83.3	5.76	-112.04	349.9	333.5	327.91	1.16	5.6	0.68	B	-4101.69	-2.56	8.1
SCP	82	5	17	2:39:26.1			10.0	5.0	-35.35	-103.84	79.5	2.79	-91.35	16.1	313.1	310.34	1.06	2.8	0.60	C	-2351.47	-1.47	4.2
COL	82	5	27	1:39:19.5			10.0	5.3	-13.38	-111.62	82.7	26.72	-122.39	344.0	330.8	324.48	0.58	6.3	0.67	C	-4024.84	-2.52	8.8
ALQ	82	5	29	3:26:58.7			116.0	5.2	-22.35	-68.37	67.5	6.25	-85.98	329.3	265.1	265.57	0.72	-0.5	0.65	C	-1996.53	-1.25	0.8
ANMO	82	5	29	3:26:58.7			116.0	5.2	-22.35	-68.37	67.5	6.25	-85.98	329.3	268.9	265.58	0.72	3.3	0.80	C	-1996.53	-1.25	4.6
ANMO	82	5	29	17:22:24.4			47.0	5.1	-24.99	-70.25	68.8	5.14	-87.36	331.7	273.9	268.66	0.76	5.2	0.78	B	-1879.81	-1.17	6.4
ALQ	82	6	1	4:14:15.3			32.0	6.1	-41.63	-74.99	81.5	-3.52	-91.45	341.0	319.5	319.90	1.08	-0.4	0.76	A	-3444.81	-2.15	1.8
ANMO	82	6	1	4:14:15.3			32.0	6.1	-41.63	-74.99	81.5	-3.52	-91.45	341.0	319.9	319.92	1.08	0.0	0.92	A	-3444.81	-2.15	2.1
ANMO	82	6	5	0:17: 0.3			33.0	5.4	-43.10	-75.21	82.7	-4.28	-91.74	341.6	323.2	325.73	1.11	-2.5	0.83	A	-3795.94	-2.37	-0.2
ALQ	82	6	15	1:20:35.2			10.0	5.2	-36.52	-98.65	71.5	-0.81	-102.59	354.6	278.1	277.85	0.94	0.2	0.65	B	-3163.56	-1.98	2.2
ANMO	82	6	15	1:20:35.2			10.0	5.2	-36.52	-98.65	71.5	-0.81	-102.59	354.6	278.3	277.87	0.94	0.4	0.90	A	-3163.56	-1.98	2.4
GAC	82	6	15	1:20:35.2			10.0	5.2	-36.52	-98.65	84.5	4.68	-87.89	12.9	335.8	333.44	1.18	2.4	0.82	B	-2259.91	-1.41	3.8
LON	82	6	15	1:20:35.2			10.0	5.2	-36.52	-98.65	85.5	5.21	-109.29	347.3	338.6	338.23	1.19	0.4	0.90	B	-3966.93	-2.48	2.8
SCP	82	6	15	1:20:35.2			10.0	5.2	-36.52	-98.65	79.3	2.16	-88.57	12.8	310.4	309.57	1.08	0.8	0.69	B	-2380.33	-1.49	2.3
JAS	82	7	11	2:13:37.7			39.0	5.3	-16.65	-73.21	70.1	11.53	-94.35	322.9	280.8	273.11	0.65	7.7	0.53	C	-4048.50	-2.53	10.2
ANMO	82	8	5	9:16:41.3			40.0	5.4	-26.68	-70.66	70.0	4.27	-87.72	332.7	273.9	273.01	0.80	0.9	0.76	B	-1914.61	-1.20	2.1
JAS	82	8	5	9:16:41.3			40.0	5.4	-26.68	-70.66	79.4	6.14	-93.85	326.5	312.5	310.74	0.88	1.8	0.27	C	-3592.21	-2.25	4.0
ANMO	82	8	23	21:35: 5.9			10.0	5.1	-29.04	-111.78	63.8	2.94	-109.21	4.3	255.2	251.74	0.78	3.5	0.45	C	-3818.91	-2.39	5.8
GAC	82	8	23	21:35: 5.9			10.0	5.1	-29.04	-111.78	81.4	8.75	-95.73	21.8	321.8	318.82	1.00	3.0	0.90	B	-3689.50	-2.31	5.3
ANMO	82	8	27	3:56:49.0			10.0	5.5	-35.52	-104.61	70.1	-0.34	-105.54	358.7	273.8	272.90	0.92	0.9	0.93	A	-3613.14	-2.26	3.2
GAC	82	8	27	3:56:49.0			10.0	5.5	-35.52	-104.61	85.0	5.25	-91.18	16.3	336.9	336.06	1.16	0.8	0.76	A	-3523.39	-2.20	3.0
JAS	82	8	27	3:56:49.0			10.0	5.5	-35.52	-104.61	74.6	1.21	-112.40	349.5	288.8	289.81	0.99	-1.0	0.62	C	-3897.01	-2.44	1.4
LON	82	8	27	3:56:49.0			10.0	5.5	-35.52	-104.61	83.3	5.67	-112.46	350.3	330.2	328.08	1.16	2.1	0.71	B	-4065.29	-2.54	4.7
SCP	82	8	27	3:56:49.0			10.0	5.5	-35.52	-104.61	79.8	2.70	-91.73	16.5	312.7	311.99	1.07	0.7	0.70	B	-2388.95	-1.49	2.2
ANMO	82	9	9	6:40:21.4			10.0	5.0	-35.55	-102.42	70.2	-0.33	-104.44	357.1	275.7	273.30	0.92	2.4	0.96	A	-3511.99	-2.19	4.6
GAC	82	9	9	6:40:21.4			10.0	5.0	-35.55	-102.42	84.5	5.22	-90.00	15.1	336.2	333.36	1.16	2.8	0.58	B	-3357.89	-2.10	4.9
JAS	82	9	9	6:40:21.4			10.0	5.0	-35.55	-102.42	75.0	1.21	-111.29	348.1	294.6	291.64	1.00	3.0	0.78	C	-3844.89	-2.40	5.4
LON	82	9	9	6:40:21.4			10.0	5.0	-35.55	-102.42	83.8	5.67	-111.27	349.1	334.6	330.04	1.16	4.6	0.70	B	-4079.44	-2.55	7.1
ANMO	82	9	26	4: 2: 6.6			10.0	5.2	-42.70	-82.26	80.4	-3.97	-95.03	345.4	311.9	314.46	1.08	-2.6	0.97	A	-3534.36	-2.21	-0.3
ANMO	82	10	24	10:43:41.1			35.0	5.4	-22.27	-70.08	66.6	6.61	-87.10	330.3	266.8	260.77	0.71	6.0	0.84	B	-2903.27	-1.81	7.8
ZOBO	82	10	25	22:26: 4.4			11.0	5.4	36.32	-120.51	72.0	11.14	-91.86	138.8	283.9	279.50	0.63	4.4	0.87	A	-3757.89	-2.35	6.8
ANMO	82	10	26	3:24:30.6			69.0	5.6	-29.67	-71.26	72.3	2.55	-88.22	334.4	284.0	282.28	0.86	1.7	0.71	B	-1982.76	-1.24	3.0
JAS	82	10	26	3:24:30.6			69.0	5.6	-29.67	-71.26	81.5	4.34	-94.45	328.1	323.4	320.62	0.96	2.8	0.76	C	-3420.65	-2.14	4.9
AFI	82	10	31	6: 3: 4.5			97.0	5.3	14.15	-90.19	85.4	0.33	-130.55	249.2	335.7	339.52	0.56	-3.8	0.53	B	-4511.18	-2.82	-1.0
ANMO	82	11	18	20:39:51.2			160.0	5.5	-31.25	-65.86	76.1	1.58	-85.51	331.9	306.3	299.53	0.92	6.8	0.78	C	-2846.50	-1.78	8.6
JAS	82	11	18	20:39:51.2			160.0	5.5	-31.25	-65.86	85.6	3.40	-91.71	326.3	346.5	342.60	1.02	3.9	0.69	B	-2630.08	-1.64	5.5
ANMO	82	12	9	1:41:37.6			10.0	5.6	-29.01	-112.66	63.9	2.94	-109.66	5.0	253.2	251.86	0.78	1.3	0.91	A	-3831.37	-2.39	3.7

Stn	Origin time						Epicenter			Bouncepoint			Obs	Pred	Ellip	Resid	r	Grade	Water	Depth	Dcor
	Yr	Mo	Da	Hr Mn Sec	Dep	m_b	Lat	Long	Dist	Lat	Long	Azim	time	time	corr.				depth	cor	resid
GAC	82	12	9	1:41:37.6	10.0	5.6	-29.01	-112.66	81.7	8.78	-96.23	22.3	319.2	320.18	1.00	-1.0	0.84	B	-3727.78	-2.33	1.4
JAS	82	12	9	1:41:37.6	10.0	5.6	-29.01	-112.66	67.0	4.44	-116.34	354.1	262.8	261.95	0.84	0.9	0.86	A	-4168.98	-2.61	3.5
LON	82	12	9	1:41:37.6	10.0	5.6	-29.01	-112.66	75.9	8.88	-116.68	354.3	298.4	295.05	0.98	3.3	0.87	B	-3939.47	-2.46	5.8
SCP	82	12	9	1:41:37.6	10.0	5.6	-29.01	-112.66	76.6	6.16	-96.56	23.1	300.6	297.97	0.93	2.6	0.72	B	-3650.69	-2.28	4.9
ANMO	82	12	31	1:35:35.2	130.0	5.3	-21.39	-68.05	66.8	6.74	-85.72	328.6	267.3	263.70	0.71	3.6	0.60	C	-2219.76	-1.39	5.0
ANMO	82	12	31	3:47:22.4	67.0	5.8	-21.05	-68.46	66.4	7.14	-86.06	328.7	264.2	260.73	0.69	3.5	0.82	B	-2535.72	-1.58	5.1
ANMO	83	1	10	9:17:32.8	98.0	5.6	-21.85	-68.32	67.1	6.56	-85.94	329.0	269.1	263.86	0.71	5.2	0.72	B	-2169.05	-1.36	6.6
ANMO	83	1	10	12:32:21.9	559.0	5.8	-27.30	-63.39	74.1	2.38	-82.96	328.7	307.3	303.19	0.92	4.1	0.52	C	-3179.66	-1.99	6.1
ANMO	83	1	13	9:23:47.9	10.0	5.6	-35.81	-102.63	70.5	-0.47	-104.55	357.3	276.0	274.21	0.92	1.8	0.96	A	-3528.81	-2.21	4.0
GAC	83	1	13	9:23:47.9	10.0	5.6	-35.81	-102.63	84.8	5.08	-90.09	15.2	332.5	334.80	1.16	-2.3	0.73	B	-3330.96	-2.08	-0.2
LON	83	1	13	9:23:47.9	10.0	5.6	-35.81	-102.63	84.0	5.53	-111.40	349.3	333.3	331.06	1.17	2.2	0.97	A	-4070.90	-2.54	4.8
RSCP	83	1	13	9:23:47.9	10.0	5.6	-35.81	-102.63	72.8	-0.11	-94.09	11.7	284.8	282.91	0.95	1.9	0.80	C	-3296.12	-2.06	4.0
RSNY	83	1	13	9:23:47.9	10.0	5.6	-35.81	-102.63	83.9	4.49	-89.51	16.0	329.1	330.90	1.15	-1.8	0.66	B	-2899.17	-1.81	0.0
RSSD	83	1	13	9:23:47.9	10.0	5.6	-35.81	-102.63	79.6	4.11	-103.29	359.2	313.0	310.89	1.11	2.1	0.98	A	-3328.51	-2.08	4.2
SCP	83	1	13	9:23:47.9	10.0	5.6	-35.81	-102.63	79.6	2.54	-90.68	15.3	310.8	310.81	1.07	0.0	0.85	B	-2221.89	-1.39	1.4
ANMO	83	1	18	2:22:54.7	10.0	5.0	-49.74	-114.83	84.6	-7.43	-110.15	4.5	337.3	334.25	1.18	3.0	0.84	B	-3447.53	-2.15	5.2
LON	83	1	23	6: 0:52.9	10.0	4.2	-17.90	-96.78	68.2	14.74	-107.22	342.0	262.9	265.86	0.70	-3.0	0.58	C	-3628.11	-2.27	-0.7
RSSD	83	1	23	6: 0:52.9	10.0	4.2	-17.90	-96.78	62.1	13.13	-99.90	354.2	245.6	246.32	0.65	-0.7	0.19	C	-3361.78	-2.10	1.4
ANMO	83	1	23	16:36:38.7	10.0	5.6	-37.28	-95.24	72.6	-1.18	-100.93	352.3	281.4	282.20	0.96	-0.8	0.29	C	-3308.11	-2.07	1.3
RSNY	83	1	23	16:36:38.7	10.0	5.6	-37.28	-95.24	83.6	3.69	-85.46	11.7	330.3	329.19	1.17	1.1	0.65	C	-3047.76	-1.90	3.0
RSSD	83	1	23	16:36:38.7	10.0	5.6	-37.28	-95.24	81.4	3.41	-99.41	354.9	322.8	319.17	1.15	3.6	0.39	C	-3385.33	-2.12	5.8
AFI	83	1	24	8:17:38.6	45.0	6.3	16.18	-95.15	81.4	1.49	-133.61	246.7	316.3	319.23	0.54	-2.9	0.57	B	-4355.47	-2.72	-0.2
ANMO	83	1	26	4:43:18.7	10.0	5.7	-49.75	-115.12	84.7	-7.44	-110.28	4.7	337.4	334.41	1.18	3.0	0.93	B	-3459.07	-2.16	5.2
ANMO	83	1	28	23:11: 5.8	10.0	5.2	-36.23	-100.97	71.0	-0.66	-103.73	356.1	276.3	276.10	0.93	0.2	0.94	A	-3427.60	-2.14	2.3
GAC	83	1	28	23:11: 5.8	10.0	5.2	-36.23	-100.97	84.7	4.85	-89.16	14.2	336.4	334.71	1.17	1.7	0.72	A	-2982.21	-1.86	3.5
LON	83	1	28	23:11: 5.8	10.0	5.2	-36.23	-100.97	84.7	5.33	-110.53	348.5	335.5	334.53	1.18	1.0	0.74	B	-3980.37	-2.49	3.5
RSNY	83	1	28	23:11: 5.8	10.0	5.2	-36.23	-100.97	83.9	4.26	-88.58	15.1	331.7	330.69	1.15	1.0	0.77	B	-2230.08	-1.39	2.4
RSSD	83	1	28	23:11: 5.8	10.0	5.2	-36.23	-100.97	80.0	3.91	-102.41	358.2	311.7	312.91	1.12	-1.2	0.91	A	-3170.96	-1.98	0.8
SCP	83	1	28	23:11: 5.8	10.0	5.2	-36.23	-100.97	79.5	2.33	-89.79	14.2	310.1	310.72	1.08	-0.6	0.69	C	-2000.30	-1.25	0.6
ANMO	83	2	1	4:22:51.1	102.0	5.2	-23.03	-68.80	67.8	5.92	-86.28	329.9	271.3	266.50	0.73	4.8	0.62	B	-1883.63	-1.18	6.0
ANMO	83	2	15	23:21: 6.9	202.0	5.0	-22.97	-66.50	69.0	5.91	-84.99	328.4	279.0	272.64	0.75	6.4	0.82	B	-2218.47	-1.39	7.8
JAS	83	2	25	22:49:54.7	146.0	5.9	-18.27	-69.44	73.6	10.50	-92.12	321.8	294.2	288.87	0.70	5.3	0.81	A	-3734.44	-2.33	7.7
ANMO	83	2	28	22:44:19.5	10.0	5.3	-43.98	-79.06	82.4	-4.65	-93.67	344.0	324.7	323.72	1.11	1.0	0.95	A	-3697.68	-2.31	3.3
JAS	83	3	2	7: 7:41.4	64.0	5.5	-11.60	-77.83	63.4	13.92	-96.59	322.8	255.7	251.09	0.53	4.6	0.60	C	-3578.12	-2.24	6.8
HON	83	4	3	2:50: 0.7	33.0	6.5	8.73	-83.12	72.9	18.67	-119.21	280.8	286.2	282.82	0.23	3.4	0.79	B	-3931.28	-2.46	5.8
HON	83	4	7	19:29:14.9	34.0	5.4	8.00	-82.69	73.5	18.27	-118.94	281.4	288.9	285.35	0.24	3.5	0.48	C	-3817.84	-2.39	5.9
HON	83	4	12	12: 7:54.6	107.0	6.5	-4.89	-78.18	82.3	10.54	-116.15	290.2	329.8	324.98	0.45	4.8	0.84	B	-4192.18	-2.62	7.4

Stn	Origin time							Epicenter			Bouncepoint			Obs	Pred	Ellip	Resid	r	Grade	Water	Depth	Dcor
	Yr	Mo	Da	Hr	Mn	Sec	Dep	m_b	Lat	Long	Dist	Lat	Long	Azim	time	time	corr.				depth	cor	resid
ZOBO	83	5	2	23:	42:	37.9	12.0	6.2	36.24	-120.30	71.8	11.09	-91.78	138.9	282.7	278.83	0.63	3.9	0.77	B	-3748.44	-2.34	6.2
ANMO	83	5	7	1:	7:	22.7	51.0	5.4	-28.01	-70.79	71.1	3.50	-87.87	333.4	278.5	277.24	0.82	1.3	0.44	C	-1711.96	-1.07	2.3
ANMO	83	5	9	10:	58:	26.7	33.0	5.8	-40.87	-74.84	80.9	-3.12	-91.29	340.6	317.4	317.07	1.07	0.3	0.93	A	-3413.77	-2.13	2.5
HON	83	5	9	15:	53:	2.7	36.0	5.5	8.28	-82.93	73.2	18.41	-119.07	281.1	288.3	284.16	0.23	4.1	0.64	C	-3857.06	-2.41	6.6
ANMO	83	5	23	0:	54:	11.6	110.0	5.5	-19.14	-69.15	64.4	7.92	-86.18	328.2	261.4	255.27	0.65	6.1	0.94	B	-2705.57	-1.69	7.8
JAS	83	5	23	0:	54:	11.6	110.0	5.5	-19.14	-69.15	74.5	10.08	-92.06	322.1	292.6	291.39	0.72	1.2	0.68	C	-3712.59	-2.32	3.5
ZOBO	83	6	11	3:	9:	54.0	2.0	5.4	36.26	-120.47	71.9	11.10	-91.85	138.8	284.5	279.14	0.63	5.4	0.88	A	-3754.17	-2.35	7.7
ANMO	83	6	17	11:	33:	16.4	10.0	5.5	-36.45	-97.44	71.5	-0.76	-101.99	353.7	278.5	278.07	0.94	0.4	0.91	A	-3201.34	-2.00	2.4
GAC	83	6	17	11:	33:	16.4	10.0	5.5	-36.45	-97.44	84.1	4.70	-87.25	12.3	335.4	331.86	1.17	3.5	0.87	B	-1723.13	-1.08	4.6
HON	83	6	17	11:	33:	16.4	10.0	5.5	-36.45	-97.44	81.0	-8.74	-130.17	317.9	314.8	317.14	0.77	-2.3	0.21	C	-4621.04	-2.89	0.6
JAS	83	6	17	11:	33:	16.4	10.0	5.5	-36.45	-97.44	77.0	0.75	-108.82	345.2	298.8	299.92	1.03	-1.1	0.78	A	-3633.01	-2.27	1.1
RSNY	83	6	17	11:	33:	16.4	10.0	5.5	-36.45	-97.44	83.3	4.13	-86.69	13.1	331.2	327.64	1.15	3.6	0.90	A	-1539.71	-0.96	4.5
RSSD	83	6	17	11:	33:	16.4	10.0	5.5	-36.45	-97.44	80.4	3.82	-100.55	356.1	311.2	314.66	1.13	-3.5	0.95	A	-3398.76	-2.12	-1.3
SCP	83	6	17	11:	33:	16.4	10.0	5.5	-36.45	-97.44	78.9	2.19	-87.95	12.1	310.8	308.14	1.08	2.7	0.54	B	-2436.95	-1.52	4.2
HON	83	7	3	17:	14:	23.2	33.0	5.7	9.66	-83.64	72.1	19.17	-119.54	280.1	279.6	279.79	0.22	-0.2	0.67	B	-3964.98	-2.48	2.3
ZOBO	83	7	9	7:	40:	50.9	10.0	5.3	36.24	-120.41	71.9	11.09	-91.83	138.8	283.2	279.06	0.63	4.1	0.89	A	-3754.17	-2.35	6.5
ZOBO	83	7	12	3:	39:	27.2	10.0	5.2	23.89	-108.37	56.0	4.06	-87.74	136.6	229.0	230.24	0.50	-1.2	0.68	A	-1806.27	-1.13	-0.1
ANMO	83	7	21	7:	11:	33.1	127.0	5.5	-22.30	-68.53	67.4	6.25	-86.05	329.4	269.7	265.39	0.72	4.3	0.73	B	-2039.90	-1.27	5.6
JAS	83	7	21	7:	11:	33.1	127.0	5.5	-22.30	-68.53	77.3	8.34	-92.01	323.3	305.0	303.35	0.80	1.6	0.60	B	-3551.47	-2.22	3.9
ZOBO	83	7	22	2:	39:	55.3	7.0	6.0	36.22	-120.40	71.9	11.08	-91.83	138.8	282.1	278.95	0.63	3.2	0.83	A	-3754.17	-2.35	5.5
ANMO	83	7	31	10:	26:	0.2	10.0	6.0	-20.14	-126.87	58.1	7.50	-117.37	18.6	235.7	235.48	0.62	0.2	0.76	B	-4035.05	-2.52	2.7
GAC	83	7	31	10:	26:	0.2	10.0	6.0	-20.14	-126.87	80.4	14.09	-105.22	32.5	312.5	314.26	0.79	-1.8	0.38	C	-3200.98	-2.00	0.2
JAS	83	7	31	10:	26:	0.2	10.0	6.0	-20.14	-126.87	58.1	8.88	-123.94	5.7	238.4	235.45	0.64	3.0	0.25	C	-4516.66	-2.82	5.8
RSCP	83	7	31	10:	26:	0.2	10.0	6.0	-20.14	-126.87	67.9	8.25	-107.77	33.5	270.7	264.69	0.68	6.0	0.48	C	-3723.87	-2.33	8.3
RSNT	83	7	31	10:	26:	0.2	10.0	6.0	-20.14	-126.87	82.9	21.23	-122.83	5.8	330.8	325.73	0.83	5.1	0.66	C	-4082.51	-2.55	7.6
RSON	83	7	31	10:	26:	0.2	10.0	6.0	-20.14	-126.87	76.5	15.96	-113.63	20.4	296.9	297.43	0.80	-0.5	0.64	B	-3651.05	-2.28	1.8
RSSD	83	7	31	10:	26:	0.2	10.0	6.0	-20.14	-126.87	67.3	12.21	-117.00	16.9	265.4	262.77	0.73	2.6	0.60	A	-4099.17	-2.56	5.2
ANMO	83	8	20	8:	30:	34.1	10.0	5.3	-36.25	-101.54	71.0	-0.66	-104.02	356.5	276.7	276.04	0.93	0.7	0.93	B	-3474.83	-2.17	2.8
JAS	83	8	20	8:	30:	34.1	10.0	5.3	-36.25	-101.54	75.9	0.85	-110.88	347.7	295.3	295.14	1.01	0.2	0.50	B	-3836.74	-2.40	2.6
LON	83	8	20	8:	30:	34.1	10.0	5.3	-36.25	-101.54	84.6	5.32	-110.84	348.8	335.9	334.09	1.18	1.8	0.84	A	-4000.70	-2.50	4.3
RSNY	83	8	20	8:	30:	34.1	10.0	5.3	-36.25	-101.54	84.1	4.26	-88.89	15.3	332.4	331.48	1.16	0.9	0.73	B	-2375.96	-1.48	2.4
RSSD	83	8	20	8:	30:	34.1	10.0	5.3	-36.25	-101.54	80.0	3.88	-102.71	358.5	311.8	312.93	1.13	-1.1	0.87	A	-3225.83	-2.02	0.9
SCP	83	8	20	8:	30:	34.1	10.0	5.3	-36.25	-101.54	79.7	2.31	-90.08	14.5	310.7	311.42	1.08	-0.7	0.61	C	-2011.62	-1.26	0.5
ANMO	83	8	21	18:	58:	19.2	10.0	5.4	-28.78	-112.65	63.7	3.07	-109.66	5.0	252.5	251.16	0.78	1.3	0.85	A	-3843.03	-2.40	3.7
JAS	83	8	21	18:	58:	19.2	10.0	5.4	-28.78	-112.65	66.8	4.57	-116.34	354.1	262.6	261.19	0.83	1.4	0.79	B	-4187.73	-2.62	4.0
LON	83	8	21	18:	58:	19.2	10.0	5.4	-28.78	-112.65	75.6	8.97	-116.66	354.2	298.5	294.12	0.97	4.4	0.71	B	-3939.47	-2.46	6.8
RSCP	83	8	21	18:	58:	19.2	10.0	5.4	-28.78	-112.65	68.9	3.50	-99.63	20.5	272.7	268.57	0.82	4.1	0.91	B	-3396.27	-2.12	6.3

Stn	Origin time					Epicenter			Bouncepoint			Obs	Pred	Ellip	Resid	r	Grade	Water	Depth	Dcor
	Yr	Mo	Da	Hr Mn Sec	Dep	m_b	Lat	Long	Dist	Lat	Long	Azim	time	time	corr.				depth	cor	resid
SCP	83	8	21	18:58:19.2	10.0	5.4	-28.78	-112.65	76.4	6.28	-96.57	23.2	299.2	297.10	0.93	2.1	0.85	A	-3654.84	-2.28	4.4
ANMO	83	8	31	8:50:37.2	10.0	5.3	-29.57	-111.84	64.4	2.66	-109.23	4.3	255.2	253.39	0.80	1.8	0.56	C	-3806.17	-2.38	4.2
GAC	83	8	31	8:50:37.2	10.0	5.3	-29.57	-111.84	81.9	8.48	-95.71	21.7	321.0	321.12	1.02	-0.1	0.92	A	-3641.18	-2.28	2.2
RSCP	83	8	31	8:50:37.2	10.0	5.3	-29.57	-111.84	69.4	3.08	-99.16	19.6	274.8	270.17	0.84	4.6	0.80	B	-3318.26	-2.07	6.7
RSNY	83	8	31	8:50:37.2	10.0	5.3	-29.57	-111.84	81.2	7.88	-95.11	22.7	320.6	318.26	1.01	2.3	0.84	B	-3655.30	-2.28	4.6
RSSD	83	8	31	8:50:37.2	10.0	5.3	-29.57	-111.84	73.7	7.27	-108.31	5.1	293.4	286.31	0.95	7.1	0.73	B	-3848.93	-2.41	9.5
JAS	83	9	1	20: 1:46.7	110.0	5.9	-17.58	-69.98	72.8	10.89	-92.39	321.7	286.6	284.68	0.68	1.9	0.87	A	-3776.67	-2.36	4.3
BOCO	83	9	9	16:30:55.4	9.0	5.4	19.33	-155.12	80.1	15.57	-113.25	101.6	317.1	312.35	0.30	4.8	0.78	A	-3714.20	-2.32	7.1
ANMO	83	9	14	0:47: 4.7	37.0	5.4	-36.42	-73.08	77.5	-0.83	-89.90	338.1	305.8	302.48	0.99	3.3	0.58	C	-1271.57	-0.79	4.1
RSSD	83	9	14	0:47: 4.7	37.0	5.4	-36.42	-73.08	84.9	3.93	-87.63	342.5	339.2	336.28	1.16	2.9	0.96	A	-1742.04	-1.09	4.0
JAS	83	9	21	10:27:56.7	112.0	5.3	-18.98	-69.12	74.4	10.16	-92.03	322.0	291.8	291.01	0.72	0.8	0.50	C	-3717.34	-2.32	3.1
ANMO	83	9	24	15:51:57.7	10.0	5.5	-41.85	-83.61	79.2	-3.53	-95.59	345.9	303.7	309.44	1.07	-5.7	0.27	C	-3528.81	-2.21	-3.5
ANMO	83	10	4	18:52:12.9	18.0	6.4	-26.62	-70.77	69.9	4.36	-87.81	332.7	274.1	272.19	0.79	1.9	0.89	A	-2016.00	-1.26	3.2
JAS	83	10	4	18:52:12.9	18.0	6.4	-26.62	-70.77	79.3	6.22	-93.94	326.5	314.7	309.76	0.88	4.9	0.93	B	-3599.77	-2.25	7.2
ANMO	83	10	6	15: 1:48.4	20.0	5.5	-26.72	-70.91	70.0	4.30	-87.89	332.9	274.2	272.31	0.79	1.9	0.55	B	-2045.81	-1.28	3.2
JAS	83	10	6	15: 1:48.4	20.0	5.5	-26.72	-70.91	79.3	6.16	-94.02	326.6	316.5	309.81	0.88	6.7	0.24	C	-3595.31	-2.25	8.9
ANMO	83	10	9	11:25:42.2	33.0	5.9	-26.26	-70.59	69.7	4.52	-87.67	332.5	274.0	271.67	0.79	2.3	0.91	B	-2019.74	-1.26	3.6
JAS	83	10	9	11:25:42.2	33.0	5.9	-26.26	-70.59	79.1	6.39	-93.78	326.2	312.9	309.29	0.87	3.6	0.97	A	-3613.54	-2.26	5.9
HON	83	10	12	3:39:39.0	22.0	5.7	8.06	-82.72	73.5	18.31	-119.00	281.3	289.0	284.91	0.23	4.1	0.39	C	-3839.21	-2.40	6.5
ANMO	83	10	16	9:59:45.8	66.0	5.7	-23.84	-70.21	67.8	5.64	-87.20	331.1	270.2	265.72	0.74	4.5	0.76	B	-1994.54	-1.25	5.7
RSSD	83	10	21	8:14:18.2	117.0	5.5	-30.64	-69.11	81.0	6.71	-84.81	338.8	320.8	319.56	1.04	1.2	0.67	C	-1745.80	-1.09	2.3
JAS	83	10	24	0:36: 6.7	55.0	5.6	-12.96	-76.75	65.1	13.28	-96.07	322.9	258.8	256.31	0.56	2.5	0.76	C	-4018.38	-2.51	5.0
ANMO	83	11	9	1:57:50.3	10.0	5.4	-36.13	-100.04	71.0	-0.61	-103.27	355.5	277.3	275.98	0.93	1.3	0.92	B	-3322.00	-2.08	3.4
GAC	83	11	9	1:57:50.3	10.0	5.4	-36.13	-100.04	84.4	4.89	-88.67	13.8	336.2	333.17	1.17	3.0	0.58	C	-2835.70	-1.77	4.8
JAS	83	11	9	1:57:50.3	10.0	5.4	-36.13	-100.04	76.1	0.91	-110.11	346.7	296.0	296.02	1.01	0.0	0.59	B	-3781.50	-2.36	2.3
LON	83	11	9	1:57:50.3	10.0	5.4	-36.13	-100.04	84.8	5.40	-110.02	348.0	337.2	334.97	1.18	2.2	0.82	A	-3947.40	-2.47	4.7
RSNY	83	11	9	1:57:50.3	10.0	5.4	-36.13	-100.04	83.6	4.31	-88.10	14.6	333.8	329.12	1.15	4.7	0.67	B	-2110.52	-1.32	6.0
RSSD	83	11	9	1:57:50.3	10.0	5.4	-36.13	-100.04	80.0	3.97	-101.92	357.6	312.0	312.62	1.12	-0.6	0.91	A	-3172.08	-1.98	1.4
BOCO	83	11	16	16:13: 0.0	11.0	6.3	19.43	-155.45	80.4	15.67	-113.39	101.7	318.8	313.76	0.30	5.0	0.76	A	-3695.22	-2.31	7.3
ANMO	83	11	17	10:39:30.9	575.0	5.4	-28.20	-63.22	74.9	1.85	-82.95	329.0	311.8	307.23	0.94	4.6	0.77	B	-3252.95	-2.03	6.6
HON	83	11	22	14:20:58.8	23.0	6.3	0.42	-79.94	78.7	13.87	-117.31	286.7	311.3	306.74	0.35	4.6	0.88	B	-4172.83	-2.61	7.2
JAS	83	11	23	8:12:15.0	54.0	5.1	-15.09	-75.55	67.5	12.19	-95.50	323.4	265.0	264.24	0.61	0.8	0.72	B	-4136.30	-2.59	3.3
ZOBO	83	11	25	9:23:27.8	33.0	5.3	24.25	-108.80	56.6	4.30	-87.96	136.6	231.3	231.81	0.50	-0.5	0.74	B	-2079.22	-1.30	0.8
HON	83	11	26	20:18:23.5	10.0	5.6	7.38	-82.26	74.1	17.95	-118.74	281.8	291.5	287.29	0.24	4.2	0.63	C	-3764.62	-2.35	6.6
ANMO	83	11	26	23:29: 8.9	10.0	5.3	-44.37	-80.15	82.5	-4.84	-94.22	344.7	323.6	324.04	1.12	-0.4	0.95	B	-3653.02	-2.28	1.8
ANMO	83	11	28	19:10: 7.0	19.0	5.6	-44.95	-76.01	84.2	-5.20	-92.37	342.6	330.0	332.16	1.14	-2.2	0.60	C	-3935.46	-2.46	0.3
ANMO	83	11	29	2:55:15.7	10.0	4.8	-49.75	-114.54	84.6	-7.43	-110.02	4.3	337.6	334.19	1.18	3.4	0.82		-3436.09	-2.15	5.6

Stn	Origin time						Epicenter			Bouncepoint			Obs	Pred	Ellip	Resid	r	Grade	Water	Depth	Dcor
	Yr	Mo	Da	Hr Mn Sec	Dep	m_b	Lat	Long	Dist	Lat	Long	Azim	time	time	corr.				depth	cor	resid
BOCO	83	11	29	2:55:15.7	10.0	4.8	-49.75	-114.54	64.5	-23.85	-89.79	30.5	241.3	253.24	0.39	-11.9	0.54	C	-4075.39	-2.55	-9.4
HON	83	12	2	3: 9: 5.6	69.0	5.9	14.05	-91.94	63.0	20.79	-123.96	277.2	249.1	249.57	0.17	-0.5	0.87	B	-4236.35	-2.65	2.2
ANMO	83	12	21	12: 5: 6.0	604.0	6.3	-28.23	-63.20	75.0	1.76	-82.90	329.0	315.0	308.57	0.95	6.4	0.60	C	-3277.37	-2.05	8.5
JAS	83	12	21	12: 5: 6.0	604.0	6.3	-28.23	-63.20	84.9	3.65	-88.72	323.8	356.2	353.76	1.04	2.4	0.67	C	-1953.27	-1.22	3.7
ANMO	83	12	23	22:56: 6.9	33.0	5.3	-27.54	-71.46	70.4	3.84	-88.23	333.6	277.1	274.25	0.81	2.8	0.67	C	-1834.18	-1.15	4.0
ANMO	84	1	1	22: 8:10.2	228.0	5.4	-22.61	-66.02	68.9	6.01	-84.64	328.0	277.4	273.08	0.75	4.3	0.77	B	-2270.43	-1.42	5.7
JAS	84	1	1	22: 8:10.2	228.0	5.4	-22.61	-66.02	79.0	8.08	-90.51	322.3	316.2	313.38	0.83	2.8	0.90	A	-3463.65	-2.16	5.0
ANMO	84	1	6	15: 1:34.6	103.0	5.4	-23.92	-68.65	68.7	5.45	-86.27	330.2	272.4	269.39	0.75	3.0	0.71	C	-1694.82	-1.06	4.1
ANMO	84	1	16	12:27:13.8	10.0	5.9	-30.00	-112.29	64.8	2.44	-109.46	4.6	255.9	254.85	0.80	1.0	0.84	B	-3806.08	-2.38	3.4
HON	84	1	16	12:27:13.8	10.0	5.9	-30.00	-112.29	67.4	-4.72	-136.02	321.0	258.2	262.98	0.66	-4.8	0.49	C	-4520.52	-2.83	-2.0
JAS	84	1	16	12:27:13.8	10.0	5.9	-30.00	-112.29	68.0	3.97	-116.17	354.0	265.0	265.43	0.86	-0.4	0.93	A	-4080.04	-2.55	2.1
LON	84	1	16	12:27:13.8	10.0	5.9	-30.00	-112.29	76.9	8.37	-116.49	354.1	300.2	299.27	1.01	0.9	0.95	A	-4020.49	-2.51	3.4
RSCP	84	1	16	12:27:13.8	10.0	5.9	-30.00	-112.29	69.9	2.87	-99.36	19.8	276.0	272.13	0.85	3.9	0.76	C	-3227.83	-2.02	5.9
RSNY	84	1	16	12:27:13.8	10.0	5.9	-30.00	-112.29	81.8	7.67	-95.32	22.8	327.6	320.80	1.02	6.8	0.89	B	-3654.26	-2.28	9.1
RSON	84	1	16	12:27:13.8	10.0	5.9	-30.00	-112.29	82.2	10.55	-104.47	10.4	321.5	322.51	1.07	-1.0	0.72	A	-3074.59	-1.92	0.9
RSSD	84	1	16	12:27:13.8	10.0	5.9	-30.00	-112.29	74.1	7.05	-108.55	5.4	288.4	288.16	0.96	0.2	0.86	B	-3863.60	-2.41	2.7
JAS	84	1	26	19:30:57.3	58.0	5.3	-12.35	-76.93	64.5	13.58	-96.13	322.7	261.1	254.48	0.54	6.6	0.54	C	-3860.86	-2.41	9.0
ANMO	84	2	3	8:29:47.7	33.0	5.7	-29.46	-71.13	72.2	2.83	-88.22	334.2	284.5	280.99	0.85	3.5	0.65	C	-1747.44	-1.09	4.6
JAS	84	2	9	4:31:18.5	41.0	5.4	-14.16	-76.23	66.4	12.73	-95.89	323.3	261.0	260.14	0.58	0.9	0.57	C	-4160.27	-2.60	3.5
AFI	84	3	1	19:21:24.6	10.0	5.5	-4.65	-106.05	65.3	-11.01	-138.42	261.4	249.5	256.01	0.32	-6.5	0.82	B	-3498.55	-2.19	-4.3
ANMO	84	3	4	22:34:24.0	33.0	5.4	-26.55	-70.70	69.9	4.36	-87.75	332.7	275.1	272.39	0.79	2.7	0.89	B	-1984.91	-1.24	4.0
ANMO	84	3	11	13:42:56.5	10.0	5.7	-26.64	-108.41	61.3	4.09	-107.48	1.6	245.0	244.12	0.73	0.9	0.54	C	-3844.12	-2.40	3.3
GAC	84	3	11	13:42:56.5	10.0	5.7	-26.64	-108.41	78.0	9.92	-94.02	20.7	302.3	303.84	0.93	-1.5	0.65	B	-3704.60	-2.32	0.8
RSCP	84	3	11	13:42:56.5	10.0	5.7	-26.64	-108.41	65.6	4.57	-97.54	18.2	265.2	257.13	0.77	8.1	0.67	C	-3426.52	-2.14	10.2
RSNY	84	3	11	13:42:56.5	10.0	5.7	-26.64	-108.41	77.3	9.34	-93.44	21.8	301.7	301.05	0.92	0.6	0.78	B	-3626.11	-2.27	2.9
RSON	84	3	11	13:42:56.5	10.0	5.7	-26.64	-108.41	78.2	12.19	-102.33	8.6	309.6	305.02	0.97	4.6	0.77	B	-3134.10	-1.96	6.5
RSSD	84	3	11	13:42:56.5	10.0	5.7	-26.64	-108.41	70.5	8.71	-106.46	3.0	278.2	274.32	0.88	3.9	0.39	C	-3368.66	-2.11	6.0
RSNY	84	4	13	5:54:52.1	10.0	4.8	-24.90	-112.11	77.2	10.35	-95.66	24.4	304.7	300.43	0.88	4.3	0.49	B	-3956.86	-2.47	6.7
ANMO	84	4	19	8:28:53.0	31.0	5.5	-31.80	-71.90	73.9	1.61	-88.84	335.6	289.1	287.58	0.90	1.5	0.77	A	-2501.85	-1.56	3.1
ANMO	84	5	7	14: 9:13.3	137.0	5.6	-27.82	-66.64	72.9	3.38	-85.54	330.8	288.9	285.95	0.85	3.0	0.63	B	-3062.78	-1.91	4.9
RSSD	84	5	9	23:56: 9.5	119.0	5.6	-34.14	-70.27	83.7	4.87	-85.80	340.4	332.1	332.57	1.13	-0.5	0.33	C	-2011.94	-1.26	0.8
ANMO	84	5	10	9:51: 2.3	10.0	5.1	-36.25	-98.75	71.2	-0.66	-102.63	354.6	278.4	276.83	0.93	1.6	0.88	A	-3171.85	-1.98	3.5
GAC	84	5	10	9:51: 2.3	10.0	5.1	-36.25	-98.75	84.2	4.82	-87.96	13.1	335.9	332.30	1.17	3.6	0.84	A	-2435.45	-1.52	5.1
LON	84	5	10	9:51: 2.3	10.0	5.1	-36.25	-98.75	85.2	5.35	-109.33	347.3	338.4	336.85	1.18	1.5	0.85	B	-3963.92	-2.48	4.0
RSCP	84	5	10	9:51: 2.3	10.0	5.1	-36.25	-98.75	72.5	-0.33	-92.13	9.1	287.6	281.87	0.95	5.7	0.50	C	-2863.36	-1.79	7.5
RSNY	84	5	10	9:51: 2.3	10.0	5.1	-36.25	-98.75	83.4	4.24	-87.40	13.9	330.9	328.17	1.15	2.7	0.83	B	-1732.34	-1.08	3.8
RSSD	84	5	10	9:51: 2.3	10.0	5.1	-36.25	-98.75	80.1	3.92	-101.24	356.9	312.0	313.42	1.13	-1.4	0.92	A	-3338.79	-2.09	0.7

Stn	Origin time					Epicenter			Bouncepoint			Obs	Pred	Ellip	Resid	r	Grade	Water	Depth	Dcor
	Yr Mo Da Hr Mn Sec	Dep	m_b	Lat	Long	Dist	Lat	Long	Azim	time	time	corr.					depth	cor	resid
ANMO	84 5 16 3:44:56.4	139.0	5.4	-27.17	-67.04	72.2	3.72	-85.68	330.7	283.8	283.15	0.83	0.6	0.47	C	-2932.82	-1.83	2.5
ANMO	84 5 25 13:20:23.9	31.0	5.5	-42.62	-75.13	82.3	-4.03	-91.65	341.4	322.4	323.79	1.10	-1.4	0.83	B	-3798.64	-2.37	1.0
ANMO	84 6 11 2: 5:33.8	45.0	6.2	-30.72	-71.21	73.3	2.13	-88.36	334.8	287.8	285.34	0.88	2.5	0.67	B	-2383.02	-1.49	4.0
JAS	84 6 11 2: 5:33.8	45.0	6.2	-30.72	-71.21	82.3	3.89	-94.64	328.6	329.4	323.99	0.98	5.4	0.84	A	-3283.91	-2.05	7.5
RSSD	84 6 11 2: 5:33.8	45.0	6.2	-30.72	-71.21	80.3	6.89	-86.07	339.9	318.4	314.79	1.03	3.6	0.62	C	-2499.81	-1.56	5.2
JAS	84 6 18 11:20:18.2	121.0	5.8	-15.73	-72.48	69.8	11.75	-93.63	322.0	273.6	273.87	0.64	-0.3	0.80	B	-4044.14	-2.53	2.3
ANMO	84 6 20 19:56:42.8	160.0	5.4	-23.98	-66.97	69.5	5.42	-85.36	329.2	279.0	273.84	0.77	5.2	0.67	B	-2300.49	-1.44	6.6
JAS	84 6 20 19:56:42.8	160.0	5.4	-23.98	-66.97	79.5	7.45	-91.32	323.4	316.9	313.73	0.85	3.2	0.67	A	-3590.28	-2.24	5.4
AFI	84 7 2 4:50:42.6	35.0	5.8	16.76	-98.51	78.5	1.80	-135.38	245.4	302.9	306.18	0.53	-3.3	0.56	B	-4344.99	-2.72	-0.6
HON	84 7 2 4:50:42.6	35.0	5.8	16.76	-98.51	56.2	21.67	-127.74	274.9	229.4	230.54	0.15	-1.1	0.76	B	-4484.37	-2.80	1.7
ANMO	84 7 24 4:49:45.3	34.0	5.6	-25.79	-70.52	69.3	4.76	-87.59	332.2	272.7	270.36	0.78	2.3	0.92	A	-2062.10	-1.29	3.6
HON	84 7 30 21:32:59.7	79.0	5.0	13.34	-90.07	64.9	20.57	-122.80	277.7	254.8	255.81	0.18	-1.0	0.30	C	-4198.62	-2.62	1.6
ANMO	84 8 12 11:51:40.9	101.0	5.6	-24.36	-69.25	68.7	5.21	-86.63	330.8	271.8	269.62	0.76	2.2	0.79	B	-1538.19	-0.96	3.1
AFI	84 8 26 5: 2: 7.9	16.0	5.4	15.91	-95.30	81.2	1.28	-133.74	246.9	315.6	317.58	0.54	-2.0	0.52	C	-4382.67	-2.74	0.8
HON	84 8 28 10: 4:24.6	10.0	5.3	-4.53	-105.87	57.2	9.32	-130.97	297.8	232.6	232.87	0.37	-0.3	0.41	C	-5003.73	-3.13	2.9
AFI	84 8 31 19:46: 3.9	119.0	5.3	16.10	-93.34	83.0	1.56	-132.46	247.2	325.6	328.67	0.55	-3.1	0.56	C	-4409.14	-2.76	-0.3
HON	84 8 31 19:46: 3.9	119.0	5.3	16.10	-93.34	61.1	21.79	-124.54	275.4	248.2	244.98	0.15	3.2	0.58	C	-4245.08	-2.65	5.9
ANMO	84 9 5 22:27:54.3	10.0	5.5	-25.51	-116.06	60.8	4.71	-111.49	8.2	246.3	242.77	0.71	3.5	0.62	C	-4001.60	-2.50	6.0
GAC	84 9 5 22:27:54.3	10.0	5.5	-25.51	-116.06	79.9	10.73	-98.47	25.2	314.3	312.16	0.92	2.1	0.92	A	-3832.23	-2.40	4.5
RSNY	84 9 5 22:27:54.3	10.0	5.5	-25.51	-116.06	79.4	10.15	-97.85	26.3	309.7	309.88	0.91	-0.2	0.91	A	-4015.16	-2.51	2.3
RSON	84 9 5 22:27:54.3	10.0	5.5	-25.51	-116.06	78.6	12.89	-106.89	13.2	311.0	306.34	0.94	4.7	0.77	B	-3561.66	-2.23	6.9
SCP	84 9 5 22:27:54.3	10.0	5.5	-25.51	-116.06	74.9	8.07	-98.71	26.3	295.2	291.06	0.85	4.1	0.53	B	-3527.35	-2.20	6.3
ZOBO	84 9 6 20:34:25.8	10.0	5.0	30.65	-113.93	64.2	7.80	-89.71	138.3	257.6	252.53	0.58	5.1	0.66	C	-3396.70	-2.12	7.2
ZOBO	84 9 12 21:56:28.2	10.0	5.0	19.88	-116.02	59.2	1.98	-91.82	128.6	233.9	238.18	0.49	-4.3	0.34	C	-2084.53	-1.30	-3.0
GAC	84 9 28 10:40:24.1	10.0	6.0	-31.63	-110.89	83.4	7.37	-94.99	20.6	327.5	328.26	1.07	-0.8	0.93	A	-3702.44	-2.31	1.5
RSNY	84 9 28 10:40:24.1	10.0	6.0	-31.63	-110.89	82.7	6.79	-94.38	21.5	327.3	325.16	1.06	2.1	0.83	B	-3677.98	-2.30	4.4
RSON	84 9 28 10:40:24.1	10.0	6.0	-31.63	-110.89	83.5	9.71	-103.58	9.4	332.9	328.86	1.11	4.0	0.83	B	-3123.84	-1.95	6.0
RSSD	84 9 28 10:40:24.1	10.0	6.0	-31.63	-110.89	75.6	6.21	-107.76	4.4	294.3	294.21	1.01	0.1	0.85	C	-3955.12	-2.47	2.6
AFI	84 10 10 5:43:51.0	10.0	5.1	-4.59	-105.51	65.9	-11.00	-138.13	261.4	252.9	257.74	0.32	-4.8	0.67	C	-3560.07	-2.23	-2.6
AFI	84 10 13 17:18:14.2	31.0	6.1	15.06	-94.24	81.9	0.75	-133.09	247.7	316.6	321.23	0.53	-4.6	0.61	B	-4413.54	-2.76	-1.9
ANMO	84 11 8 6:32:55.9	42.0	5.3	-30.67	-71.36	73.2	2.16	-88.44	334.8	288.7	284.85	0.88	3.8	0.35	C	-2375.99	-1.48	5.3
JAS1	84 12 10 10:22: 4.8	56.0	5.4	-14.86	-75.33	67.4	12.30	-95.36	323.1	266.3	264.01	0.60	2.3	0.46	C	-4133.20	-2.58	4.9
ANMO	84 12 11 23:22:20.6	122.0	5.6	-22.84	-68.80	67.7	5.97	-86.24	329.8	268.7	266.37	0.73	2.3	0.74	C	-1883.63	-1.18	3.5
JAS1	84 12 11 23:22:20.6	122.0	5.6	-22.84	-68.80	77.5	8.03	-92.21	323.7	305.0	304.22	0.81	0.8	0.58	C	-3549.98	-2.22	3.0
ANMO	84 12 31 13: 0:31.8	174.0	5.5	-23.06	-66.91	68.8	5.93	-85.26	328.7	276.5	271.52	0.75	5.0	0.83	C	-2033.80	-1.27	6.3
JAS1	84 12 31 13: 0:31.8	174.0	5.5	-23.06	-66.91	78.8	7.95	-91.18	322.9	313.6	311.04	0.83	2.6	0.68	C	-3534.23	-2.21	4.8
ANMO	85 1 18 15: 0: 8.3	82.0	5.8	-29.41	-70.71	72.4	2.63	-87.89	333.9	279.7	282.63	0.86	-2.9	0.76	B	-2033.50	-1.27	-1.7

Stn	Origin time							Epicenter			Bouncepoint			Obs	Pred	Ellip	Resid	r	Grade	Water	Depth	Dcor
	Yr	Mo	Da	Hr	Mn	Sec	Dep	m_b	Lat	Long	Dist	Lat	Long	Azim	time	time	corr.				depth	cor	resid
JAS1	85	1	18	15:	0:	8.3	82.0	5.8	-29.41	-70.71	81.5	4.45	-94.10	327.7	321.5	321.22	0.95	0.3	0.91	B	-3418.54	-2.14	2.4
RSSD	85	1	18	15:	0:	8.3	82.0	5.8	-29.41	-70.71	79.3	7.40	-85.62	339.3	308.8	311.15	1.00	-2.3	0.69	C	-2210.12	-1.38	-1.0
ANMO	85	1	26	3:	7:	2.5	38.0	6.1	-33.15	-68,54	76.5	0.89	-87.26	334.2	296.0	298.24	0.94	-2.2	0.57	C	-2614.38	-1.63	-0.6
ANMO	85	2	14	8:	30:	55.6	123.0	5.6	-23.85	-67.75	69.0	5.46	-85.76	329.6	278.3	271.21	0.76	7.1	0.55	C	-1884.61	-1.18	8.3
JAS1	85	2	21	18:	53:	8.5	33.0	4.7	-33.28	-71.72	84.1	2.51	-95.29	330.0	337.5	331.96	1.03	5.5	0.67	C	-2689.02	-1.68	7.2
RSSD	85	2	21	18:	53:	8.5	33.0	4.7	-33.28	-71.72	82.5	5.59	-86.60	340.9	329.2	324.44	1.09	4.8	0.68	C	-1743.69	-1.09	5.8
ANMO	85	2	21	21:	52:	56.5	33.0	5.3	-20.72	-70.37	65.1	7.43	-87.16	329.8	263.3	255.98	0.67	7.3	0.92	A	-3251.57	-2.03	9.4
JAS1	85	2	21	21:	52:	56.5	33.0	5.3	-20.72	-70.37	74.9	9.43	-93.09	323.4	293.4	291.49	0.74	1.9	0.75	C	-3617.90	-2.26	4.2
GAC	85	2	24	2:	7:	31.2	10.0	5.1	-32.25	-110.95	84.0	7.05	-94.96	20.4	332.5	331.03	1.09	1.5	0.61	C	-3722.79	-2.33	3.8
LON	85	2	24	2:	7:	31.2	10.0	5.1	-32.25	-110.95	79.2	7.26	-115.81	353.5	313.1	309.43	1.07	3.7	0.35	C	-4041.43	-2.53	6.2
RSNY	85	2	24	2:	7:	31.2	10.0	5.1	-32.25	-110.95	83.3	6.46	-94.35	21.4	330.5	327.89	1.07	2.6	0.72	C	-3638.76	-2.27	4.9
RSON	85	2	24	2:	7:	31.2	10.0	5.1	-32.25	-110.95	84.1	9.40	-103.59	9.3	337.0	331.80	1.13	5.2	0.54	C	-3100.60	-1.94	7.1
RSSD	85	3	3	22:	47:	6.9	33.0	6.9	-33.15	-71.98	82.3	5.66	-86.73	341.0	325.0	323.49	1.08	1.5	0.76	C	-1818.69	-1.14	2.7
JAS1	85	3	4	0:	32:	21.4	33.0	6.0	-33.23	-71.76	84.0	2.53	-95.30	329.9	330.3	331.68	1.03	-1.4	0.40	C	-2698.38	-1.69	0.3
RSSD	85	3	4	6:	6:	57.8	33.0	5.4	-33.58	-71.86	82.7	5.43	-86.70	341.1	322.7	325.51	1.10	-2.8	0.57	C	-1652.37	-1.03	-1.8
ANMO	85	3	4	13:	49:	29.6	33.0	4.9	-33.95	-71.96	75.8	0.47	-89.08	336.5	302.6	295.10	0.94	7.5	0.52	C	-2159.11	-1.35	8.9
RSSD	85	3	4	13:	49:	29.6	33.0	4.9	-33.95	-71.96	83.0	5.24	-86.79	341.2	331.3	326.96	1.10	4.3	0.50	C	-1570.69	-0.98	5.3
ANMO	85	3	4	15:	1:	6.2	33.0	6.1	-33.84	-71.32	75.9	0.53	-88.75	336.1	305.4	295.76	0.94	9.6	0.77	C	-2263.82	-1.41	11.1
JAS1	85	3	4	15:	1:	6.2	33.0	6.1	-33.84	-71.32	84.7	2.20	-95.17	330.0	340.4	335.07	1.04	5.3	0.87	C	-2701.35	-1.69	7.0
RSSD	85	3	4	15:	1:	6.2	33.0	6.1	-33.84	-71.32	83.1	5.31	-86.44	340.9	331.7	327.45	1.10	4.3	0.62	C	-1615.71	-1.01	5.3
ANMO	85	3	4	19:	3:	7.2	33.0	5.3	-32.75	-71.60	74.9	1.10	-88.78	335.8	297.0	291.42	0.92	5.6	0.58	A	-2382.31	-1.49	7.1
JAS1	85	3	4	19:	3:	7.2	33.0	5.3	-32.75	-71.60	83.7	2.80	-95.15	329.7	336.0	330.23	1.02	5.8	0.81	B	-2785.49	-1.74	7.5
RSSD	85	3	4	19:	3:	7.2	33.0	5.3	-32.75	-71.60	82.0	5.87	-86.49	340.7	327.1	322.36	1.08	4.7	0.71	C	-1883.38	-1.18	5.9
ANMO	85	3	5	9:	8:	54.6	33.0	5.4	-34.24	-71.72	76.1	0.32	-88.99	336.5	305.1	296.54	0.95	8.6	0.46	C	-2103.76	-1.31	9.9
ANMO	85	3	7	0:	54:	56.9	33.0	5.5	-33.01	-72.14	74.9	0.96	-89.08	336.2	296.9	291.46	0.92	5.4	0.35	C	-2268.53	-1.42	6.9
JAS1	85	3	7	0:	54:	56.9	33.0	5.5	-33.01	-72.14	83.7	2.65	-95.47	330.0	328.5	329.94	1.02	-1.4	0.47	C	-2776.37	-1.74	0.3
RSSD	85	3	7	0:	54:	56.9	33.0	5.5	-33.01	-72.14	82.1	5.73	-86.80	341.1	327.6	322.66	1.08	4.9	0.52	C	-1905.37	-1.19	6.1
ANMO	85	3	12	8:	23:	15.3	33.0	5.3	-33.10	-72.16	74.9	0.92	-89.10	336.3	295.8	291.74	0.92	4.1	0.68	B	-2268.53	-1.42	5.5
RSSD	85	3	12	8:	23:	15.3	33.0	5.3	-33.10	-72.16	82.2	5.68	-86.82	341.1	328.2	323.01	1.08	5.2	0.75	B	-1852.89	-1.16	6.3
ANMO	85	3	17	10:	41:	37.9	33.0	5.9	-32.66	-71.56	74.8	1.15	-88.75	335.7	297.3	291.17	0.92	6.1	0.65	A	-2405.07	-1.50	7.6
JAS1	85	3	17	10:	41:	37.9	33.0	5.9	-32.66	-71.56	83.7	2.85	-95.12	329.6	334.9	329.99	1.02	4.9	0.86	B	-2767.57	-1.73	6.6
RSSD	85	3	17	10:	41:	37.9	33.0	5.9	-32.66	-71.56	82.0	5.92	-86.45	340.7	327.2	322.04	1.07	5.2	0.72	C	-1938.66	-1.21	6.4
ANMO	85	3	19	4:	1:	6.5	33.0	5.9	-33.28	-71.76	75.3	0.83	-88.91	336.1	299.1	293.03	0.93	6.1	0.64	B	-2298.47	-1.44	7.5
JAS1	85	3	19	4:	1:	6.5	33.0	5.9	-33.28	-71.76	84.1	2.50	-95.31	330.0	336.3	331.87	1.03	4.4	0.92	B	-2698.38	-1.69	6.1
RSSD	85	3	19	4:	1:	6.5	33.0	5.9	-33.28	-71.76	82.5	5.59	-86.62	340.9	329.1	324.38	1.09	4.7	0.66	C	-1743.69	-1.09	5.8
ANMO	85	3	23	13:	45:	19.3	33.0	5.4	-34.28	-72.11	76.0	0.30	-89.19	336.7	302.0	296.05	0.95	5.9	0.53	B	-2051.49	-1.28	7.2
JAS1	85	3	23	13:	45:	19.3	33.0	5.4	-34.28	-72.11	84.7	1.95	-95.64	330.6	341.3	334.89	1.05	6.4	0.35	C	-2809.27	-1.76	8.2

Stn	Origin time							Epicenter			Bouncepoint			Obs	Pred	Ellip	Resid	r	Grade	Water	Depth	Dcor
	Yr	Mo	Da	Hr	Mn	Sec	Dep	m_b	Lat	Long	Dist	Lat	Long	Azim	time	time	corr.				depth	cor	resid
ANMO	85	3	23	14	36	57.0	33.0	5.6	-33.30	-72.22	75.1	0.81	-89.15	336.4	298.6	292.35	0.93	6.3	0.47	C	-2239.67	-1.40	7.7
JAS1	85	3	23	14	36	57.0	33.0	5.6	-33.30	-72.22	83.9	2.49	-95.55	330.2	333.2	330.86	1.03	2.3	0.69	C	-2730.04	-1.71	4.1
ANMO	85	3	24	16	16	33.0	33.0	5.4	-34.35	-72.13	76.1	0.26	-89.21	336.7	300.6	296.27	0.95	4.3	0.53	B	-1978.45	-1.24	5.6
RSSD	85	3	24	16	16	33.0	33.0	5.4	-34.35	-72.13	83.3	5.03	-86.92	341.4	332.2	328.44	1.11	3.8	0.58	C	-1568.06	-0.98	4.7
ANMO	85	3	25	5	14	33.2	33.0	6.1	-34.34	-72.28	76.0	0.27	-89.28	336.8	301.0	295.99	0.95	5.0	0.66	B	-1978.45	-1.24	6.3
JAS1	85	3	25	5	14	33.2	33.0	6.1	-34.34	-72.28	84.7	1.92	-95.74	330.7	337.9	334.72	1.05	3.2	0.89	B	-2816.43	-1.76	4.9
RSSD	85	3	25	5	14	33.2	33.0	6.1	-34.34	-72.28	83.3	5.03	-87.00	341.5	331.9	328.17	1.11	3.7	0.70	C	-1612.80	-1.01	4.7
ANMO	85	3	30	13	47	28.7	33.0	5.0	-45.46	-76.40	84.5	-5.49	-92.61	343.0	330.9	334.16	1.15	-3.3	0.54	C	-3930.29	-2.46	-0.8
ANMO	85	4	3	13	6	19.8	33.0	5.7	-32.62	-71.61	74.8	1.17	-88.77	335.8	295.9	290.95	0.92	4.9	0.53	B	-2405.07	-1.50	6.4
RSSD	85	4	3	13	6	19.8	33.0	5.7	-32.62	-71.61	81.9	5.94	-86.48	340.7	325.7	321.80	1.07	3.9	0.69	C	-1946.29	-1.22	5.1
ANMO	85	4	9	1	56	58.6	33.0	6.3	-34.17	-71.54	76.1	0.36	-88.89	336.3	305.2	296.59	0.95	8.6	0.78	B	-2131.35	-1.33	9.9
JAS1	85	4	9	1	56	58.6	33.0	6.3	-34.17	-71.54	84.9	2.02	-95.33	330.3	340.1	335.82	1.05	4.3	0.92	A	-2759.87	-1.72	6.0
RSSD	85	4	9	1	56	58.6	33.0	6.3	-34.17	-71.54	83.4	5.13	-86.59	341.1	332.8	328.54	1.11	4.3	0.59	C	-1493.38	-0.93	5.2
ANMO	85	4	15	4	41	50.5	33.0	5.0	-33.53	-72.02	75.4	0.69	-89.07	336.4	300.1	293.50	0.93	6.6	0.67	B	-2228.21	-1.39	8.0
RSSD	85	4	15	4	41	50.5	33.0	5.0	-33.53	-72.02	82.6	5.46	-86.79	341.1	330.8	325.06	1.09	5.7	0.59	C	-1728.65	-1.08	6.8
HON	85	4	19	17	43	10.3	66.0	5.3	11.93	-86.56	68.6	20.16	-121.03	278.6	271.4	267.93	0.19	3.5	0.41	C	-4119.83	-2.57	6.0
ANMO	85	4	28	2	53	44.1	60.0	5.0	-33.07	-71.49	75.2	0.79	-88.69	335.9	297.6	293.36	0.93	4.2	0.53	C	-2351.63	-1.47	5.7
RSSD	85	4	28	2	53	44.1	60.0	5.0	-33.07	-71.49	82.4	5.55	-86.40	340.7	328.1	324.57	1.09	3.5	0.39	C	-1760.94	-1.10	4.6
ANMO	85	4	28	8	30	32.6	33.0	6.0	-39.70	-75.61	79.6	-2.52	-91.52	340.7	311.8	311.23	1.05	0.6	0.37	C	-3274.05	-2.05	2.6
ZOBO	85	5	4	12	47	10.5	10.0	4.7	16.66	-113.53	55.5	0.22	-90.81	127.3	231.1	228.88	0.45	2.2	0.61	C	-1552.05	-0.97	3.2
ANMO	85	5	6	7	33	58.7	10.0	5.1	-36.37	-98.86	71.3	-0.73	-102.69	354.7	278.7	277.24	0.94	1.5	0.88	A	-3171.85	-1.98	3.4
GAC	85	5	6	7	33	58.7	10.0	5.1	-36.37	-98.86	84.4	4.76	-88.01	13.1	335.7	332.97	1.17	2.7	0.79	A	-2433.09	-1.52	4.3
HON	85	5	6	7	33	58.7	10.0	5.1	-36.37	-98.86	80.1	-8.63	-130.80	318.5	313.7	312.75	0.77	0.9	0.72	C	-4625.20	-2.89	3.8
JAS1	85	5	6	7	33	58.7	10.0	5.1	-36.37	-98.86	76.6	0.78	-109.53	346.0	297.4	298.03	1.02	-0.6	0.58	B	-3704.66	-2.32	1.7
LON	85	5	6	7	33	58.7	10.0	5.1	-36.37	-98.86	85.3	5.28	-109.40	347.4	338.6	337.30	1.19	1.3	0.87	A	-3970.35	-2.48	3.8
RSNY	85	5	6	7	33	58.7	10.0	5.1	-36.37	-98.86	83.5	4.17	-87.45	13.9	330.5	328.83	1.15	1.7	0.79	B	-1688.25	-1.06	2.7
RSSD	85	5	6	7	33	58.7	10.0	5.1	-36.37	-98.86	80.3	3.85	-101.30	356.9	311.3	313.93	1.13	-2.6	0.82	A	-3310.23	-2.07	-0.6
SCP	85	5	6	7	33	58.7	10.0	5.1	-36.37	-98.86	79.2	2.24	-88.69	12.9	308.8	309.14	1.08	-0.3	0.61	C	-2327.79	-1.45	1.1
ANMO	85	5	17	2	44	7.8	33.0	5.1	-34.28	-72.46	75.9	0.30	-89.37	336.9	301.1	295.48	0.95	5.6	0.49	C	-1979.08	-1.24	6.9
RSSD	85	5	17	2	44	7.8	33.0	5.1	-34.28	-72.46	83.2	5.06	-87.09	341.6	331.5	327.64	1.11	3.9	0.48	C	-1675.56	-1.05	4.9
ANMO	85	5	18	16	59	13.3	111.0	5.4	-19.20	-69.12	64.5	7.89	-86.16	328.2	261.7	255.50	0.66	6.2	0.91	B	-2705.57	-1.69	7.9
ANMO	85	5	19	7	7	46.2	33.0	5.2	-33.88	-72.30	75.6	0.51	-89.25	336.7	301.0	294.30	0.94	6.7	0.62	B	-2108.07	-1.32	8.0
RSSD	85	5	19	7	7	46.2	33.0	5.2	-33.88	-72.30	82.8	5.27	-86.97	341.4	330.6	326.15	1.10	4.4	0.47	C	-1690.40	-1.06	5.5
ANMO	85	5	19	18	9	15.4	39.0	5.9	-30.24	-71.28	72.8	2.40	-88.36	334.6	283.8	283.47	0.87	0.3	0.41	C	-2153.21	-1.35	1.7
RSSD	85	5	19	18	9	15.4	39.0	5.9	-30.24	-71.28	79.8	7.16	-86.08	339.8	315.4	312.58	1.01	2.8	0.72	B	-2535.72	-1.58	4.4
ANMO	85	6	2	16	26	58.0	33.0	5.4	-37.80	-73.59	78.5	-1.54	-90.31	338.9	314.6	306.83	1.02	7.8	0.42	C	-399.09	-0.25	8.0
HON	85	6	3	2	45	32.1	70.0	5.1	13.13	-90.18	64.9	20.42	-122.78	277.9	255.9	255.51	0.18	0.4	0.64	B	-4207.73	-2.63	3.0

Stn	Origin time						Epicenter			Bouncepoint			Obs	Pred	Ellip	Resid	r	Grade	Water	Depth	Dcor
	Yr	Mo	Da	Hr Mn Sec	Dep	m_b	Lat	Long	Dist	Lat	Long	Azim	time	time	corr.				depth	cor	resid
ANMO	85	6	9	18:46:30.1	33.0	5.0	-33.25	-71.97	75.2	0.84	-89.01	336.2	296.9	292.58	0.93	4.3	0.59	B	-2257.59	-1.41	5.7
ANMO	85	6	10	15:37: 3.3	180.0	5.8	-28.11	-67.19	72.9	3.23	-85.86	331.2	287.9	286.87	0.86	1.0	0.58	C	-2958.46	-1.85	2.9
JAS1	85	6	10	15:37: 3.3	180.0	5.8	-28.11	-67.19	82.5	5.09	-91.93	325.5	333.0	327.93	0.95	5.1	0.73	C	-3530.05	-2.21	7.3
ANMO	85	6	11	11:12:28.8	33.0	5.1	-32.48	-71.68	74.6	1.24	-88.79	335.7	297.7	290.35	0.91	7.3	0.54	B	-2437.31	-1.52	8.9
RSSD	85	6	11	11:12:28.8	33.0	5.1	-32.48	-71.68	81.8	6.01	-86.50	340.7	327.7	321.10	1.07	6.6	0.50	C	-2029.43	-1.27	7.9
ANMO	85	6	14	13:14:14.9	33.0	5.5	-40.74	-74.92	80.7	-3.06	-91.31	340.6	317.3	316.42	1.07	0.9	0.88	A	-3429.15	-2.14	3.0
ANMO	85	6	23	6:55:23.7	178.0	5.5	-24.06	-67.10	69.5	5.39	-85.44	329.3	279.2	274.24	0.77	5.0	0.79	B	-2206.89	-1.38	6.3
ANMO	85	7	5	15:22:38.1	33.0	5.0	-33.38	-72.17	75.2	0.77	-89.13	336.4	298.6	292.72	0.93	5.9	0.68	B	-2228.70	-1.39	7.3
RSSD	85	7	5	15:22:38.1	33.0	5.0	-33.38	-72.17	82.4	5.53	-86.85	341.2	330.0	324.19	1.09	5.8	0.65	C	-1758.02	-1.10	6.9
ANMO	85	7	6	8:33: 7.1	43.0	5.1	-33.36	-72.12	75.2	0.75	-89.09	336.4	298.0	292.96	0.93	5.0	0.54	B	-2246.38	-1.40	6.4
JAS1	85	7	6	8:33: 7.1	43.0	5.1	-33.36	-72.12	84.0	2.42	-95.49	330.2	336.9	331.57	1.03	5.3	0.65	C	-2703.29	-1.69	7.0
RSSD	85	7	6	8:33: 7.1	43.0	5.1	-33.36	-72.12	82.4	5.51	-86.81	341.2	330.0	324.43	1.09	5.6	0.73	B	-1758.02	-1.10	6.7
ANMO	85	7	7	11:25:12.0	32.0	5.4	-32.88	-72.00	74.8	1.04	-88.99	336.1	294.8	291.20	0.92	3.6	0.64	A	-2306.28	-1.44	5.0
JAS1	85	7	7	11:25:12.0	32.0	5.4	-32.88	-72.00	83.6	2.72	-95.38	329.9	334.6	329.75	1.02	4.8	0.91	A	-2797.27	-1.75	6.6
RSSD	85	7	7	11:25:12.0	32.0	5.4	-32.88	-72.00	82.0	5.80	-86.71	341.0	327.4	322.29	1.08	5.1	0.73	B	-1933.95	-1.21	6.3
ANMO	85	7	10	5: 6:33.1	10.0	5.3	-38.63	-91.65	74.5	-1.87	-99.23	350.2	289.0	289.51	0.99	-0.5	0.90	A	-3351.49	-2.09	1.6
GAC	85	7	10	5: 6:33.1	10.0	5.3	-38.63	-91.65	85.2	3.57	-84.02	8.8	339.8	336.98	1.22	2.8	0.81	A	-2997.69	-1.87	4.7
JAS1	85	7	10	5: 6:33.1	10.0	5.3	-38.63	-91.65	80.7	-0.37	-106.10	342.4	315.9	315.68	1.08	0.2	0.77	B	-3648.33	-2.28	2.5
RSCP	85	7	10	5: 6:33.1	10.0	5.3	-38.63	-91.65	74.1	-1.52	-88.55	4.0	284.2	287.90	1.00	-3.7	0.80	B	-1255.96	-0.78	-2.9
RSNY	85	7	10	5: 6:33.1	10.0	5.3	-38.63	-91.65	84.2	2.99	-83.49	9.6	337.4	332.29	1.20	5.1	0.88	A	-3082.14	-1.93	7.0
RSSD	85	7	10	5: 6:33.1	10.0	5.3	-38.63	-91.65	83.1	2.75	-97.58	353.0	326.0	327.09	1.19	-1.1	0.86	B	-3027.44	-1.89	0.8
SCP	85	7	10	5: 6:33.1	10.0	5.3	-38.63	-91.65	80.0	1.08	-84.87	8.3	316.2	313.00	1.12	3.2	0.80	B	-3063.78	-1.91	5.1
ANMO	85	7	11	20:31:13.9	33.0	5.2	-32.93	-72.00	74.9	1.01	-89.00	336.1	294.8	291.40	0.92	3.4	0.71	A	-2306.28	-1.44	4.8
RSSD	85	7	11	20:31:13.9	33.0	5.2	-32.93	-72.00	82.1	5.77	-86.72	341.0	327.2	322.53	1.08	4.7	0.72	B	-1869.30	-1.17	5.8
ANMO	85	7	17	13:53: 2.2	50.0	5.4	-32.65	-71.42	74.9	1.09	-88.64	335.6	300.0	291.76	0.92	8.2	0.61	B	-2396.95	-1.50	9.7
RSSD	85	7	17	13:53: 2.2	50.0	5.4	-32.65	-71.42	82.0	5.86	-86.35	340.6	327.2	322.64	1.08	4.6	0.73	C	-1872.48	-1.17	5.7
GAC	85	7	27	16:26:45.5	10.0	5.4	-26.94	-113.41	80.1	9.89	-96.84	23.3	314.0	313.07	0.95	0.9	0.94	A	-3942.85	-2.46	3.4
HON	85	7	27	16:26:45.5	10.0	5.4	-26.94	-113.41	64.5	-3.04	-136.22	319.6	252.3	253.76	0.62	-1.5	0.75	C	-4506.72	-2.82	1.4
LON	85	7	27	16:26:45.5	10.0	5.4	-26.94	-113.41	73.7	9.90	-117.06	354.6	289.9	286.50	0.92	3.4	0.73	C	-4210.76	-2.63	6.0
RSCP	85	7	27	16:26:45.5	10.0	5.4	-26.94	-113.41	67.5	4.45	-100.15	21.6	268.1	263.69	0.79	4.4	0.90	B	-3426.20	-2.14	6.6
RSNY	85	7	27	16:26:45.5	10.0	5.4	-26.94	-113.41	79.5	9.31	-96.23	24.4	309.2	310.53	0.94	-1.3	0.92	A	-3794.60	-2.37	1.0
RSON	85	7	27	16:26:45.5	10.0	5.4	-26.94	-113.41	79.4	12.11	-105.26	11.4	311.2	310.00	0.98	1.2	0.81	B	-3267.09	-2.04	3.2
RSSD	85	7	27	16:26:45.5	10.0	5.4	-26.94	-113.41	71.2	8.59	-109.23	6.4	280.9	276.92	0.89	4.0	0.89	B	-3874.46	-2.42	6.4
SCP	85	7	27	16:26:45.5	10.0	5.4	-26.94	-113.41	75.0	7.27	-97.14	24.3	295.1	291.63	0.88	3.5	0.84	A	-3363.22	-2.10	5.6
ANMO	85	8	4	4:54: 1.9	23.0	5.5	-44.89	-75.45	84.3	-5.18	-92.10	342.3	331.0	332.79	1.14	-1.8	0.73	B	-3944.73	-2.47	0.7
ANMO	85	8	6	2:29:44.0	10.0	4.8	-41.25	-85.78	78.2	-3.21	-96.57	347.1	302.2	304.79	1.05	-2.6	0.95	A	-3556.54	-2.22	-0.4
RSCP	85	8	6	2:29:44.0	10.0	4.8	-41.25	-85.78	76.5	-3.13	-85.67	0.1	293.4	297.67	1.06	-4.3	0.85	A	-3314.34	-2.07	-2.2

Stn	Origin time							Epicenter			Bouncepoint			Obs	Pred	Ellip	Resid	r	Grade	Water	Depth	Dcor
	Yr	Mo	Da	Hr	Mn	Sec	Dep	m_b	Lat	Long	Dist	Lat	Long	Azim	time	time	corr.				depth	cor	resid
ANMO	85	8	12	0:	4:	50.9	33.0	5.5	-38.42	-73.49	79.1	-1.86	-90.34	339.0	315.8	309.39	1.03	6.4	0.79	B	-399.09	-0.25	6.7
JAS1	85	8	19	7:	53:	48.0	33.0	5.3	-15.04	-75.60	67.4	12.30	-95.60	323.4	266.6	263.49	0.60	3.1	0.41	C	-4159.58	-2.60	5.7
ANMO	85	8	20	12:	21:	5.9	33.0	4.7	-33.75	-72.19	75.5	0.58	-89.18	336.5	301.1	294.01	0.94	7.1	0.39	C	-2181.08	-1.36	8.4
RSSD	85	8	20	12:	21:	5.9	33.0	4.7	-33.75	-72.19	82.8	5.34	-86.90	341.3	330.4	325.75	1.10	4.7	0.65	C	-1688.65	-1.06	5.7
HON	85	8	21	11:	26:	28.8	61.0	6.1	-9.21	-78.91	83.3	7.74	-116.88	293.3	332.8	328.43	0.52	4.4	0.85	C	-4082.43	-2.55	6.9
JAS1	85	8	21	11:	26:	28.8	61.0	6.1	-9.21	-78.91	60.8	15.14	-97.12	322.1	248.4	243.45	0.47	4.9	0.90	C	-3487.98	-2.18	7.1
ANMO	85	8	27	10:	44:	34.6	197.0	5.2	-21.46	-67.45	67.2	6.71	-85.39	328.3	270.1	266.40	0.72	3.7	0.80	B	-2022.38	-1.26	5.0
ANMO	85	9	1	8:	28:	21.3	10.0	4.9	-39.02	-91.61	74.9	-2.07	-99.23	350.2	288.8	291.06	1.00	-2.3	0.76	B	-3455.17	-2.16	-0.1
GAC	85	9	1	8:	28:	21.3	10.0	4.9	-39.02	-91.61	85.6	3.37	-83.98	8.8	340.2	338.81	1.23	1.4	0.64	A	-3017.85	-1.89	3.3
AFI	85	9	19	13:	17:	47.8	33.0	7.0	18.18	-102.57	75.3	2.62	-137.55	243.3	293.1	292.79	0.52	0.3	0.91	B	-4356.00	-2.72	3.0
AFI	85	9	21	1:	37:	13.8	33.0	6.3	17.82	-101.67	76.0	2.41	-137.07	243.8	297.0	295.58	0.52	1.4	0.89	A	-4359.56	-2.72	4.1
ANMO	85	10	8	9:	47:	21.9	222.0	5.5	-23.05	-66.43	69.1	5.80	-84.91	328.4	278.4	273.46	0.76	4.9	0.82	B	-2347.47	-1.47	6.4
JAS1	85	10	8	9:	47:	21.9	222.0	5.5	-23.05	-66.43	79.0	7.82	-90.80	322.7	314.0	313.49	0.84	0.5	0.43	C	-3518.09	-2.20	2.7
HON	85	10	12	20:	29:	24.5	75.0	5.2	13.19	-89.63	65.4	20.54	-122.66	277.8	256.2	257.19	0.18	-1.0	0.74	C	-4167.82	-2.60	1.6
AFI	85	10	29	15:	2:	27.1	33.0	5.6	18.17	-102.55	75.3	2.61	-137.54	243.3	294.2	292.85	0.52	1.4	0.73	C	-4361.99	-2.73	4.1
ANMO	85	10	31	21:	49:	20.0	595.0	5.8	-28.75	-63.19	75.4	1.50	-82.97	329.3	314.0	309.99	0.96	4.0	0.92	B	-3352.29	-2.10	6.1
JAS1	85	10	31	21:	49:	20.0	595.0	5.8	-28.75	-63.19	85.2	3.38	-88.82	324.1	358.7	355.19	1.05	3.5	0.83	A	-1879.75	-1.17	4.7
ANMO	85	11	12	3:	34:	19.8	10.0	5.4	-36.25	-98.02	71.3	-0.66	-102.27	354.1	279.2	277.10	0.93	2.1	0.91	A	-3166.94	-1.98	4.1
GAC	85	11	12	3:	34:	19.8	10.0	5.4	-36.25	-98.02	84.1	4.81	-87.57	12.7	335.3	331.53	1.17	3.8	0.83	A	-2088.54	-1.31	5.1
JAS1	85	11	12	3:	34:	19.8	10.0	5.4	-36.25	-98.02	76.7	0.85	-109.09	345.5	298.3	298.41	1.02	-0.1	0.82	C	-3647.18	-2.28	2.2
LON	85	11	12	3:	34:	19.8	10.0	5.4	-36.25	-98.02	85.3	5.35	-108.93	346.9	339.2	337.64	1.19	1.6	0.95	A	-3958.95	-2.47	4.0
RSNY	85	11	12	3:	34:	19.8	10.0	5.4	-36.25	-98.02	83.2	4.23	-87.01	13.4	330.1	327.36	1.15	2.7	0.82	A	-1542.21	-0.96	3.7
RSSD	85	11	12	3:	34:	19.8	10.0	5.4	-36.25	-98.02	80.2	3.92	-100.85	356.4	312.1	313.61	1.13	-1.5	0.93	A	-3396.71	-2.12	0.6
SCP	85	11	12	3:	34:	19.8	10.0	5.4	-36.25	-98.02	78.9	2.30	-88.27	12.5	309.1	307.83	1.08	1.3	0.78	C	-2251.52	-1.41	2.7
ANMO	85	11	17	20:	50:	50.9	10.0	5.1	-25.16	-112.33	60.0	4.89	-109.54	5.1	246.8	240.63	0.70	6.2	0.57	C	-3973.69	-2.48	8.6
GAC	85	11	17	20:	50:	50.9	10.0	5.1	-25.16	-112.33	78.1	10.80	-96.37	23.3	305.1	304.25	0.90	0.9	0.93	A	-4132.34	-2.58	3.4
RSCP	85	11	17	20:	50:	50.9	10.0	5.1	-25.16	-112.33	65.5	5.36	-99.68	21.5	259.7	256.98	0.75	2.7	0.40	C	-3409.81	-2.13	4.8
RSON	85	11	24	9:	28:	23.6	10.0	4.7	-7.69	-148.00	74.7	23.83	-127.34	35.3	295.6	289.87	0.45	5.7	0.27	C	-4256.75	-2.66	8.4
ANMO	85	11	27	15:	59:	2.6	10.0	9.9	-7.90	-148.60	58.3	14.44	-129.62	41.5	231.1	235.76	0.44	-4.7	0.61	C	-4884.70	-3.05	-1.6
GAC	85	11	27	15:	59:	2.6	10.0	9.9	-7.90	-148.60	84.0	22.92	-119.35	46.4	328.3	330.54	0.44	-2.2	0.31	C	-3959.77	-2.47	0.2
ANMO	85	11	29	4:	2:	11.3	521.0	5.3	-22.76	-63.62	70.3	4.91	-82.64	326.7	287.0	286.73	0.81	0.3	0.62	C	-3175.47	-1.98	2.3
RSON	86	1	7	16:	37:	47.8	10.0	4.9	-13.34	-111.59	65.8	18.96	-104.57	12.7	261.6	257.78	0.60	3.8	0.55	C	-1191.22	-0.74	4.6
ANMO	86	1	12	14:	0:	55.4	10.0	5.0	-35.97	-102.20	70.7	-0.54	-104.34	357.0	272.7	274.87	0.93	-2.2	0.70	C	-3503.32	-2.19	0.0
GAC	86	1	12	14:	0:	55.4	10.0	5.0	-35.97	-102.20	84.8	4.99	-89.84	14.9	340.3	335.00	1.17	5.3	0.39	C	-3236.16	-2.02	7.3
RSNY	86	1	12	14:	0:	55.4	10.0	5.0	-35.97	-102.20	84.0	4.41	-89.26	15.8	333.1	331.06	1.15	2.0	0.66	B	-2700.73	-1.69	3.7
ANMO	86	1	26	7:	48:	22.9	30.0	5.7	-27.12	-70.87	70.3	4.07	-87.89	333.0	271.7	273.82	0.80	-2.1	0.56	B	-1850.08	-1.16	-1.0
RSSD	86	2	9	23:	32:	11.7	86.0	5.0	-36.13	-71.27	85.2	3.89	-86.57	341.5	337.6	338.94	1.17	-1.3	0.53	C	-1816.67	-1.14	-0.2

Stn	Origin time							m_b	Epicenter			Bouncepoint			Obs	Pred	Ellip	Resid	r	Grade	Water	Depth	Dcor
	Yr	Mo	Da	Hr	Mn	Sec	Dep		Lat	Long	Dist	Lat	Long	Azim	time	time	corr.				depth	cor	resid
ANMO	86	2	20	9:	16:	2.4	33.0	5.7	-21.15	-70.11	65.6	7.21	-87.04	329.8	263.5	257.57	0.68	5.9	0.84	B	-3194.32	-2.00	7.9
HON	86	3	22	16:	56:	50.9	10.0	5.3	-4.45	-104.82	58.1	9.41	-130.43	297.3	234.6	235.07	0.37	-0.5	0.50	C	-4927.91	-3.08	2.6
ANMO	86	3	26	7:	4:	49.8	33.0	5.1	-34.10	-72.10	75.8	0.40	-89.17	336.6	302.5	295.41	0.95	7.1	0.68	C	-2093.81	-1.31	8.4
RSSD	86	3	26	7:	4:	49.8	33.0	5.1	-34.10	-72.10	83.1	5.16	-86.88	341.4	332.3	327.40	1.11	4.9	0.71	C	-1620.45	-1.01	5.9
ANMO	86	4	9	18:	10:	52.9	199.0	5.2	-22.96	-66.67	68.9	5.92	-85.09	328.5	276.6	272.23	0.75	4.4	0.61	C	-2164.05	-1.35	5.7
ANMO	86	4	30	14:	9:	39.7	116.0	5.5	-18.35	-69.70	63.5	8.30	-86.42	328.2	259.4	252.43	0.64	7.0	0.88	C	-3075.00	-1.92	8.9
RSCP	86	5	10	12:	2:	1.7	10.0	5.6	-37.04	-94.03	72.7	-0.73	-89.76	5.8	283.9	282.53	0.97	1.4	0.78	C	-1393.47	-0.87	2.2
ANMO	86	6	5	9:	1:	15.6	10.0	5.2	-36.30	-97.37	71.4	-0.69	-101.95	353.6	280.0	277.54	0.94	2.5	0.90	A	-3216.59	-2.01	4.5
HON	86	6	5	9:	1:	15.6	10.0	5.2	-36.30	-97.37	81.0	-8.65	-130.11	317.8	321.3	316.97	0.77	4.3	0.73	C	-4620.59	-2.89	7.2
LON	86	6	5	9:	1:	15.6	10.0	5.2	-36.30	-97.37	85.5	5.34	-108.58	346.6	340.5	338.59	1.19	1.9	0.81	A	-3939.80	-2.46	4.4
RSCP	86	6	5	9:	1:	15.6	10.0	5.2	-36.30	-97.37	72.4	-0.36	-91.44	8.1	291.3	281.27	0.95	10.0	0.46	C	-1738.93	-1.09	11.1
RSNY	86	6	5	9:	1:	15.6	10.0	5.2	-36.30	-97.37	83.1	4.20	-86.66	13.1	328.4	326.89	1.15	1.5	0.79	B	-1539.71	-0.96	2.5
RSSD	86	6	5	9:	1:	15.6	10.0	5.2	-36.30	-97.37	80.3	3.90	-100.51	356.1	312.1	314.02	1.13	-1.9	0.91	A	-3405.11	-2.13	0.2
ANMO	86	6	19	17:	18:	58.1	10.0	4.9	-36.12	-100.69	70.9	-0.61	-103.59	355.9	276.3	275.76	0.93	0.5	0.91	A	-3397.30	-2.12	2.7
LON	86	6	19	17:	18:	58.1	10.0	4.9	-36.12	-100.69	84.7	5.40	-110.37	348.3	336.1	334.29	1.18	1.8	0.75	C	-3958.56	-2.47	4.3
RSCP	86	6	19	17:	18:	58.1	10.0	4.9	-36.12	-100.69	72.7	-0.27	-93.11	10.4	279.9	282.64	0.95	-2.7	0.53	C	-3105.17	-1.94	-0.8
RSNY	86	6	19	17:	18:	58.1	10.0	4.9	-36.12	-100.69	83.7	4.32	-88.44	14.9	331.9	329.85	1.15	2.0	0.66	B	-2240.92	-1.40	3.5
RSSD	86	6	19	17:	18:	58.1	10.0	4.9	-36.12	-100.69	79.9	3.97	-102.26	358.0	311.8	312.46	1.12	-0.7	0.62	B	-3152.05	-1.97	1.3
RSNY	86	6	24	23:	53:	32.6	10.0	4.7	-36.10	-100.47	83.6	4.33	-88.33	14.8	331.6	329.49	1.15	2.1	0.68	C	-2205.19	-1.38	3.5
RSSD	86	6	24	23:	53:	32.6	10.0	4.7	-36.10	-100.47	79.9	3.98	-102.15	357.9	313.5	312.41	1.12	1.1	0.31	C	-3150.48	-1.97	3.1
RSON	86	6	27	1:	22:	53.0	10.0	4.7	-19.30	-126.20	75.5	16.37	-113.26	20.3	289.6	293.29	0.77	-3.7	0.42	B	-3565.41	-2.23	-1.5
HON	86	6	30	22:	52:	12.0	62.0	5.2	11.22	-86.09	69.3	19.79	-120.76	279.1	272.5	270.18	0.20	2.3	0.71	C	-4127.62	-2.58	4.9
ANMO	86	7	2	20:	45:	50.5	10.0	5.6	-26.72	-114.35	61.8	4.10	-110.58	6.6	247.0	245.57	0.74	1.4	0.66	C	-3932.50	-2.46	3.9
LON	86	7	2	20:	45:	50.5	10.0	5.6	-26.72	-114.35	73.4	10.01	-117.59	355.1	284.8	285.32	0.92	-0.5	0.73	A	-4218.29	-2.64	2.1
RSCP	86	7	2	20:	45:	50.5	10.0	5.6	-26.72	-114.35	67.7	4.58	-100.65	22.4	267.7	264.20	0.78	3.5	0.85	C	-3421.51	-2.14	5.6
RSON	86	7	2	20:	45:	50.5	10.0	5.6	-26.72	-114.35	79.4	12.24	-105.82	12.0	308.9	309.88	0.98	-1.0	0.77	C	-3368.98	-2.11	1.1
RSSD	86	7	2	20:	45:	50.5	10.0	5.6	-26.72	-114.35	71.1	8.73	-109.76	7.1	278.2	276.52	0.88	1.7	0.92	B	-3859.74	-2.41	4.1
WFM	86	7	2	20:	45:	50.5	10.0	5.6	-26.72	-114.35	79.5	8.52	-95.09	27.5	310.7	310.38	0.92	0.3	0.45	C	-3671.91	-2.29	2.6
ZOBO	86	7	13	13:	47:	8.0	5.0	5.6	33.02	-117.79	68.2	9.21	-91.17	137.9	267.0	265.74	0.60	1.3	0.62	C	-3621.51	-2.26	3.5
ANMO	86	7	18	0:	21:	38.7	10.0	4.9	-19.80	-126.50	57.7	7.67	-117.18	18.5	224.4	234.38	0.62	-10.0	0.65	B	-4059.15	-2.54	-7.4
GAC	86	7	18	0:	21:	38.7	10.0	4.9	-19.80	-126.50	79.9	14.26	-105.03	32.5	323.4	312.15	0.78	11.3	0.80	B	-3150.11	-1.97	13.2
RSNY	86	7	18	0:	21:	38.7	10.0	4.9	-19.80	-126.50	79.7	13.68	-104.37	33.7	320.9	310.99	0.77	9.9	0.54	C	-3005.35	-1.88	11.8
RSON	86	7	18	0:	21:	38.7	10.0	4.9	-19.80	-126.50	76.0	16.12	-113.42	20.3	302.6	295.61	0.79	7.0	0.72	B	-3618.73	-2.26	9.3
ANMO	86	7	28	20:	29:	1.5	32.0	5.1	-33.38	-72.13	75.2	0.78	-89.11	336.4	298.4	292.76	0.93	5.6	0.67	B	-2246.38	-1.40	7.0
RSSD	86	7	28	20:	29:	1.5	32.0	5.1	-33.38	-72.13	82.4	5.54	-86.83	341.2	329.9	324.23	1.09	5.7	0.71	C	-1758.02	-1.10	6.8
GAC	86	8	1	14:	9:	24.9	10.0	5.5	-35.89	-103.75	85.1	5.05	-90.69	15.8	331.5	336.60	1.17	-5.1	0.65	B	-3390.33	-2.12	-3.0
RSCP	86	8	1	14:	9:	24.9	10.0	5.5	-35.89	-103.75	73.1	-0.15	-94.64	12.5	282.2	284.11	0.95	-1.9	0.80	B	-3455.25	-2.16	0.2

Stn	Origin time						Epicenter			Bouncepoint			Obs	Pred	Ellip	Resid	r	Grade	Water	Depth	Dcor
	Yr	Mo	Da	Hr	Mn	Sec	Dep	m_b	Lat	Long	Dist	Lat	Long	Azim	time	time	corr.				depth	cor	resid
RSNY	86	8	1	14:	9:	24.9	10.0	5.5	-35.89	-103.75	84.3	4.47	-90.10	16.6	327.5	332.75	1.15	-5.3	0.62	B	-3052.30	-1.91	-3.3
HON	86	8	13	4:	11:	41.1	10.0	5.4	5.84	-82.40	74.5	16.99	-118.74	283.0	289.0	288.89	0.27	0.1	0.74	B	-3791.48	-2.37	2.5
LON	86	8	21	17:	1:	28.5	10.0	5.0	-8.90	-109.47	56.5	19.02	-114.52	349.4	233.7	231.31	0.47	2.4	0.89	A	-3558.33	-2.22	4.6
ZOBO	86	9	25	6:	15:	53.7	10.0	5.3	22.90	-108.07	55.2	3.54	-87.68	136.0	228.2	228.26	0.49	-0.1	0.83	A	-1779.15	-1.11	1.0
ANMO	86	10	5	7:	21:	37.5	10.0	5.3	-23.72	-112.03	58.6	5.57	-109.40	4.9	232.9	236.74	0.68	-3.8	0.64	C	-3942.95	-2.46	-1.4
GAC	86	10	5	7:	21:	37.5	10.0	5.3	-23.72	-112.03	76.7	11.54	-96.30	23.6	292.3	298.26	0.86	-6.0	0.27	C	-4191.48	-2.62	-3.3
LON	86	10	5	7:	21:	37.5	10.0	5.3	-23.72	-112.03	70.7	11.52	-116.21	353.4	273.9	274.89	0.84	-1.0	0.26	C	-4196.28	-2.62	1.6
RSNY	86	10	5	7:	21:	37.5	10.0	5.3	-23.72	-112.03	76.1	10.97	-95.70	24.7	298.2	295.90	0.85	2.3	0.63	C	-4080.70	-2.55	4.8
RSON	86	10	5	7:	21:	37.5	10.0	5.3	-23.72	-112.03	76.0	13.72	-104.57	11.2	296.4	295.51	0.89	0.9	0.73	B	-3051.44	-1.91	2.8
RSSD	86	10	5	7:	21:	37.5	10.0	5.3	-23.72	-112.03	67.9	10.21	-108.52	5.8	268.7	264.97	0.80	3.7	0.79	C	-3308.50	-2.07	5.8
ANMO	86	10	5	13:	15:	45.6	10.0	5.4	-23.62	-112.02	58.5	5.62	-109.40	4.9	233.2	236.48	0.67	-3.3	0.70	C	-3942.95	-2.46	-0.8
GAC	86	10	5	13:	15:	45.6	10.0	5.4	-23.62	-112.02	76.6	11.59	-96.31	23.7	294.0	297.87	0.86	-3.9	0.27	C	-4189.13	-2.62	-1.3
LON	86	10	5	13:	15:	45.6	10.0	5.4	-23.62	-112.02	70.6	11.59	-116.21	353.3	271.7	274.53	0.83	-2.8	0.60	C	-4187.49	-2.62	-0.2
RSON	86	10	5	13:	15:	45.6	10.0	5.4	-23.62	-112.02	75.9	13.75	-104.57	11.2	296.0	295.11	0.88	0.9	0.66	B	-3051.44	-1.91	2.8
RSSD	86	10	5	13:	15:	45.6	10.0	5.4	-23.62	-112.02	67.8	10.23	-108.52	5.8	268.1	264.62	0.80	3.5	0.82	B	-3308.50	-2.07	5.6
ANMO	86	10	24	2:	42:	50.9	50.0	5.4	-25.41	-70.15	69.2	4.91	-87.33	331.8	272.0	270.17	0.77	1.8	0.76	C	-1851.02	-1.16	3.0
HON	86	11	23	1:	39:	25.9	126.0	6.4	-3.36	-77.47	82.4	11.57	-115.69	289.1	330.0	325.84	0.43	4.2	0.93	A	-4164.50	-2.60	6.8
ANMO	86	11	28	20:	34:	52.5	33.0	4.6	-45.12	-76.67	84.1	-5.31	-92.69	343.0	333.0	332.31	1.14	0.7	0.77	B	-3928.37	-2.46	3.2
ANMO	86	12	5	1:	45:	37.4	10.0	5.2	-36.27	-97.53	71.3	-0.68	-102.03	353.8	279.4	277.37	0.93	2.0	0.92	A	-3187.79	-1.99	4.0
LON	86	12	5	1:	45:	37.4	10.0	5.2	-36.27	-97.53	85.5	5.35	-108.67	346.7	339.9	338.27	1.19	1.6	0.84	A	-3944.57	-2.47	4.1
HON	87	1	4	17:	52:	36.6	10.0	5.5	5.92	-82.67	74.2	17.01	-118.88	283.0	292.5	287.78	0.27	4.7	0.41	C	-3809.58	-2.38	7.1
ANMO	87	1	14	9:	38:	56.7	10.0	5.1	-49.92	-113.59	84.7	-7.51	-109.59	3.8	338.0	334.68	1.19	3.3	0.90	A	-3364.39	-2.10	5.4
ANMO	87	2	14	15:	44:	15.9	10.0	5.4	-45.71	-75.99	84.9	-5.58	-92.47	342.9	335.7	335.33	1.15	0.4	0.92	A	-3931.91	-2.46	2.8
ANMO	87	2	25	10:	42:	45.5	171.0	5.1	-27.94	-67.06	72.8	3.34	-85.78	331.1	292.1	286.34	0.85	5.8	0.27	C	-2989.20	-1.87	7.6
ANMO	87	3	5	9:	17:	0.0	27.0	6.5	-24.49	-70.17	68.4	5.47	-87.32	331.4	271.0	266.89	0.75	4.1	0.86	A	-1932.33	-1.21	5.3
HON	87	3	6	1:	54:	50.7	14.0	6.1	0.13	-77.67	80.9	13.91	-116.12	286.6	318.8	316.35	0.36	2.5	0.79	B	-4142.74	-2.59	5.0
HON	87	3	6	4:	10:	41.9	12.0	6.5	0.15	-77.83	80.8	13.91	-116.21	286.6	319.6	315.61	0.36	4.0	0.79	B	-4158.37	-2.60	6.6
ANMO	87	3	14	20:	18:	37.6	10.0	5.4	-38.89	-92.19	74.6	-2.00	-99.51	350.6	287.7	290.17	0.99	-2.5	0.79	B	-3446.28	-2.15	-0.3
GAC	87	3	14	20:	18:	37.6	10.0	5.4	-38.89	-92.19	85.5	3.43	-84.29	9.1	339.7	338.63	1.23	1.1	0.67	A	-2983.95	-1.86	2.9
SCP	87	3	14	20:	18:	37.6	10.0	5.4	-38.89	-92.19	80.4	0.95	-85.13	8.6	317.1	314.49	1.13	2.6	0.65	C	-2902.93	-1.81	4.4
ANMO	87	3	15	6:	3:	3.1	33.0	5.1	-24.30	-70.55	68.1	5.54	-87.49	331.6	270.7	265.82	0.75	4.9	0.57	C	-2068.53	-1.29	6.2
ANMO	87	3	22	3:	23:	57.7	42.0	5.9	-24.08	-70.08	68.1	5.64	-87.21	331.2	270.0	266.13	0.75	3.9	0.63	B	-2033.54	-1.27	5.1
ANMO	87	3	23	20:	47:	57.2	33.0	4.9	-34.07	-72.23	75.8	0.41	-89.23	336.7	303.2	295.09	0.94	8.1	0.60	C	-2060.52	-1.29	9.4
HON	87	4	8	17:	42:	36.0	49.0	5.1	11.66	-86.36	68.9	20.04	-121.02	278.7	271.8	268.52	0.19	3.3	0.63	C	-4146.15	-2.59	5.9
ANMO	87	5	10	15:	16:	20.2	160.0	5.6	-30.91	-65.42	76.0	1.77	-85.24	331.5	302.7	299.22	0.92	3.5	0.52	C	-2889.25	-1.81	5.3
ANMO	87	5	12	16:	12:	42.1	121.0	5.4	-21.79	-68.32	67.0	6.53	-85.90	329.0	266.7	264.17	0.71	2.5	0.24	C	-2113.14	-1.32	3.8
HON	87	5	14	16:	4:	26.5	29.0	5.6	-5.62	-81.39	79.7	9.95	-118.17	291.3	312.4	310.98	0.45	1.4	0.55	C	-4216.87	-2.64	4.1

Stn	Origin time						Epicenter			Bouncepoint			Obs	Pred	Ellip	Resid	r	Grade	Water	Depth	Dcor
	Yr	Mo	Da	Hr Mn Sec	Dep	m_b	Lat	Long	Dist	Lat	Long	Azim	time	time	corr.				depth	cor	resid
ANMO	87	5	15	13:49:14.2	10.0	5.5	-49.98	-115.23	84.9	-7.56	-110.31	4.7	337.9	335.55	1.19	2.3	0.90	A	-3470.62	-2.17	4.5
ANMO	87	5	19	12:56:25.0	39.0	5.6	-30.33	-71.59	72.8	2.35	-88.53	334.8	283.8	283.26	0.87	0.5	0.58	C	-2236.18	-1.40	1.9
CMB	87	5	19	12:56:25.0	39.0	5.6	-30.33	-71.59	81.9	4.16	-94.76	328.6	326.2	321.68	0.97	4.5	0.88	A	-3385.27	-2.12	6.6
ANMO	87	5	23	5: 1: 8.1	41.0	5.2	-20.19	-70.71	64.5	7.67	-87.29	329.7	264.3	254.17	0.66	10.1	0.54	C	-3300.67	-2.06	12.2
ANMO	87	6	9	22:46:11.7	10.0	5.2	-35.24	-106.68	69.8	-0.58	-106.57	0.2	272.9	271.82	0.92	1.1	0.93	A	-3673.65	-2.30	3.4
CMB	87	6	9	22:46:11.7	10.0	5.2	-35.24	-106.68	74.0	1.40	-113.41	350.8	287.7	287.62	0.98	0.1	0.67	B	-3919.08	-2.45	2.5
GAC	87	6	9	22:46:11.7	10.0	5.2	-35.24	-106.68	85.4	5.42	-92.33	17.4	336.4	337.68	1.16	-1.3	0.72	A	-3583.31	-2.24	1.0
LON	87	6	9	22:46:11.7	10.0	5.2	-35.24	-106.68	82.7	5.79	-113.58	351.4	325.9	325.27	1.15	0.6	0.46	B	-4075.20	-2.55	3.2
ANMO	87	6	11	5: 8:52.8	33.0	5.0	-20.51	-70.61	64.8	7.53	-87.27	329.8	262.9	255.03	0.67	7.9	0.82	B	-3283.72	-2.05	9.9
CMB	87	6	11	5: 8:52.8	33.0	5.0	-20.51	-70.61	74.7	9.59	-93.17	323.5	292.4	290.47	0.74	1.9	0.71	B	-3620.41	-2.26	4.2
CMB	87	6	15	6:23: 8.9	44.0	5.5	-12.46	-76.73	64.8	13.65	-96.04	322.7	256.2	254.94	0.55	1.3	0.27	C	-3864.70	-2.42	3.7
CMB	87	6	19	19: 0: 8.3	119.0	5.4	-21.37	-68.38	76.7	8.92	-91.80	322.9	305.2	300.62	0.78	4.6	0.33	C	-3603.77	-2.25	6.8
CMB	87	6	27	9: 9: 5.5	61.0	5.9	-14.13	-76.08	66.5	12.70	-95.69	323.3	263.7	260.86	0.59	2.8	0.88	B	-4175.51	-2.61	5.4
ANMO	87	7	6	1: 6: 7.5	10.0	6.3	-27.02	-108.25	61.7	3.89	-107.39	1.5	247.8	245.19	0.74	2.6	0.83	B	-3835.92	-2.40	5.0
CMB	87	7	6	1: 6: 7.5	10.0	6.3	-27.02	-108.25	65.7	5.53	-113.94	350.6	257.2	257.64	0.80	-0.4	0.77	B	-4013.04	-2.51	2.1
GAC	87	7	6	1: 6: 7.5	10.0	6.3	-27.02	-108.25	78.3	9.72	-93.90	20.5	306.5	305.10	0.94	1.4	0.95	A	-3619.17	-2.26	3.7
HON	87	7	6	1: 6: 7.5	10.0	6.3	-27.02	-108.25	68.0	-3.14	-133.72	316.7	251.9	265.26	0.64	-13.4	0.55	C	-4517.31	-2.82	-10.5
LON	87	7	6	1: 6: 7.5	10.0	6.3	-27.02	-108.25	74.4	9.92	-114.14	351.3	295.4	289.29	0.93	6.1	0.84	B	-3882.17	-2.43	8.5
ANMO	87	7	8	11:50:14.6	10.0	6.1	-26.97	-108.20	61.6	3.88	-107.37	1.5	247.2	245.05	0.74	2.2	0.75	B	-3832.69	-2.40	4.6
CMB	87	7	8	11:50:14.6	10.0	6.1	-26.97	-108.20	65.7	5.54	-113.91	350.6	257.8	257.50	0.80	0.3	0.65	B	-4013.04	-2.51	2.8
GAC	87	7	8	11:50:14.6	10.0	6.1	-26.97	-108.20	78.2	9.74	-93.88	20.5	305.7	304.83	0.94	0.9	0.96	A	-3619.17	-2.26	3.1
HON	87	7	8	11:50:14.6	10.0	6.1	-26.97	-108.20	68.0	-3.12	-133.69	316.7	251.9	265.27	0.63	-13.4	0.46	B	-4516.87	-2.82	-10.6
LON	87	7	8	11:50:14.6	10.0	6.1	-26.97	-108.20	74.4	9.96	-114.11	351.3	295.9	289.12	0.93	6.8	0.85	B	-3860.46	-2.41	9.2
ANMO	87	7	9	4: 7:34.3	64.0	5.2	-20.48	-68.74	65.7	7.45	-86.18	328.6	263.3	258.62	0.68	4.7	0.85	C	-2643.78	-1.65	6.3
HON	87	7	15	7:16:13.6	67.0	6.0	17.56	-97.18	57.2	22.24	-126.95	274.1	233.6	233.54	0.14	0.1	0.70	C	-4392.33	-2.75	2.8
HON	87	7	17	1:57:38.7	10.0	5.4	1.52	-85.30	73.3	14.07	-120.16	286.8	284.2	284.39	0.33	-0.2	0.52	B	-4069.14	-2.54	2.3
ANMO	87	7	21	13:27:13.2	10.0	5.2	-36.29	-97.24	71.4	-0.68	-101.89	353.6	280.0	277.56	0.94	2.4	0.91	A	-3216.59	-2.01	4.4
CMB	87	7	21	13:27:13.2	10.0	5.2	-36.29	-97.24	77.0	0.88	-108.67	345.1	298.9	299.79	1.02	-0.9	0.73	B	-3622.60	-2.26	1.4
GAC	87	7	21	13:27:13.2	10.0	5.2	-36.29	-97.24	83.9	4.79	-87.15	12.2	335.5	330.92	1.17	4.6	0.86	A	-1684.44	-1.05	5.6
LON	87	7	21	13:27:13.2	10.0	5.2	-36.29	-97.24	85.6	5.34	-108.51	346.5	340.3	338.69	1.19	1.6	0.92	A	-3934.69	-2.46	4.1
SCP	87	7	21	13:27:13.2	10.0	5.2	-36.29	-97.24	78.7	2.28	-87.86	12.0	308.9	307.29	1.07	1.6	0.68	B	-2410.39	-1.51	3.1
AFI	87	7	22	8:23: 3.7	98.0	5.2	15.76	-93.44	82.8	1.32	-132.51	247.4	313.9	327.25	0.55	-13.4	0.41	C	-4414.70	-2.76	-10.6
ANMO	87	7	29	15:22:33.0	141.0	5.4	-28.87	-67.17	73.5	2.82	-85.92	331.5	289.6	288.49	0.87	1.1	0.34	C	-2922.49	-1.83	2.9
ANMO	87	8	4	15: 4:40.4	38.0	5.8	-40.46	-73.10	81.1	-2.94	-90.39	339.5	319.2	318.20	1.07	1.0	0.90	B	-2933.91	-1.83	2.8
HON	87	8	6	15:15:34.7	10.0	5.6	-5.40	-105.02	58.3	8.87	-130.56	298.2	233.0	235.80	0.38	-2.8	0.33	C	-4957.12	-3.10	0.3
ANMO	87	8	8	15:48:57.4	82.0	6.4	-19.19	-70.14	63.9	8.01	-86.80	328.9	259.0	253.24	0.65	5.8	0.80	C	-3194.16	-2.00	7.8
ANMO	87	8	9	8:24:20.0	10.0	5.0	-35.23	-103.95	69.9	-0.18	-105.20	358.2	274.8	271.91	0.91	2.9	0.92	B	-3586.13	-2.24	5.1

Stn	Origin time						Epicenter			Bouncepoint			Obs	Pred	Ellip	Resid	r	Grade	Water	Depth	Dcor
	Yr	Mo	Da	Hr Mn Sec	Dep	m_b	Lat	Long	Dist	Lat	Long	Azim	time	time	corr.				depth	cor	resid
CMB	87	8	9	8:24:20.0	10.0	5.0	-35.23	-103.95	74.5	1.40	-112.01	349.0	290.6	289.48	0.99	1.1	0.79	B	-3873.20	-2.42	3.5
GAC	87	8	9	8:24:20.0	10.0	5.0	-35.23	-103.95	84.6	5.40	-90.85	16.0	336.8	333.87	1.15	2.9	0.68	A	-3512.53	-2.20	5.1
LON	87	8	9	8:24:20.0	10.0	5.0	-35.23	-103.95	83.2	5.82	-112.09	349.9	333.4	327.27	1.15	6.1	0.56	B	-4109.15	-2.57	8.7
ANMO	87	8	13	15:23:11.4	74.0	6.1	-17.83	-71.08	62.3	8.74	-87.26	328.8	257.8	248.13	0.61	9.7	0.82	B	-3171.58	-1.98	11.6
CMB	87	8	13	15:23:11.4	74.0	6.1	-17.83	-71.08	72.3	10.87	-93.08	322.5	280.6	282.14	0.68	-1.5	0.86	B	-3828.21	-2.39	0.9
ANMO	87	8	15	9:34:47.7	104.0	5.1	-23.10	-68.57	68.0	5.88	-86.16	329.8	270.2	267.14	0.74	3.1	0.62	C	-1840.11	-1.15	4.2
ANMO	87	8	15	18: 4:22.1	32.0	6.3	-28.15	-70.89	71.2	3.52	-87.98	333.5	279.1	277.10	0.82	2.0	0.79	B	-1671.11	-1.04	3.0
ZOBO	87	8	21	23: 0:52.5	10.0	5.3	23.85	-108.77	56.3	4.05	-87.94	136.3	229.9	230.83	0.50	-0.9	0.51	C	-1850.08	-1.16	0.2
ANMO	87	8	24	6: 9:43.2	33.0	5.1	-20.15	-70.58	64.5	7.72	-87.23	329.6	263.0	254.11	0.66	8.9	0.80	B	-3297.17	-2.06	10.9
CMB	87	8	24	6: 9:43.2	33.0	5.1	-20.15	-70.58	74.4	9.79	-93.12	323.4	293.2	289.42	0.73	3.8	0.69	C	-3639.00	-2.27	6.1
ANMO	87	8	26	13: 1:23.0	10.0	5.1	-37.27	-95.22	72.6	-1.18	-100.92	352.3	283.6	282.17	0.96	1.4	0.53	C	-3308.11	-2.07	3.5
HON	87	9	8	2:58:52.8	25.0	5.4	6.52	-82.55	74.1	17.39	-118.82	282.5	291.1	287.67	0.26	3.4	0.74	B	-3776.97	-2.36	5.8
ANMO	87	9	11	0:34:51.8	128.0	5.4	-22.32	-68.36	67.5	6.25	-85.96	329.3	268.1	265.76	0.72	2.3	0.86	C	-1996.53	-1.25	3.6
ANMO	87	9	11	4: 2: 3.1	95.0	5.1	-31.46	-70.73	74.1	1.50	-88.07	334.8	290.0	289.82	0.90	0.2	0.27	C	-2565.89	-1.60	1.8
ANMO	87	9	18	8:43:25.9	71.0	5.6	-24.41	-69.10	68.8	5.34	-86.64	330.7	271.8	269.38	0.76	2.4	0.74	C	-1590.54	-0.99	3.4
CMB	87	9	19	9:21:41.7	35.0	5.1	-14.97	-75.66	67.4	12.38	-95.59	323.5	263.3	263.40	0.60	-0.1	0.50	C	-4165.59	-2.60	2.5
CMB	87	9	19	21:18:25.9	69.0	5.7	-9.19	-79.07	60.8	15.16	-97.15	322.4	247.7	243.43	0.47	4.3	0.76	B	-3516.05	-2.20	6.5
HON	87	9	22	13:43:39.7	23.0	6.1	-0.96	-78.09	81.0	13.17	-116.33	287.4	316.1	316.57	0.38	-0.5	0.43	C	-4175.50	-2.61	2.1
HON	87	9	22	16:21:38.5	33.0	5.8	-1.08	-78.11	81.0	13.09	-116.31	287.5	318.5	316.92	0.38	1.6	0.66	C	-4167.02	-2.60	4.2
CMB	87	10	3	3:35: 6.1	119.0	5.8	-18.22	-69.31	73.7	10.60	-92.02	321.8	292.7	288.49	0.70	4.2	0.60	C	-3741.53	-2.34	6.6
HON	87	10	4	8:15:17.8	45.0	5.4	10.74	-85.94	69.6	19.54	-120.76	279.5	272.6	270.87	0.21	1.7	0.73	B	-4152.38	-2.60	4.3
ANMO	87	10	6	14:39:54.6	10.0	5.2	-35.78	-101.02	70.5	-0.42	-103.75	356.1	277.0	274.43	0.92	2.6	0.82	B	-3427.60	-2.14	4.7
LON	87	10	6	14:39:54.6	10.0	5.2	-35.78	-101.02	84.3	5.56	-110.53	348.4	334.7	332.39	1.17	2.3	0.25	C	-3962.53	-2.48	4.8
ANMO	87	10	7	0:51:37.0	117.0	5.6	-23.07	-68.12	68.2	5.87	-85.90	329.5	271.1	268.12	0.74	3.0	0.47	C	-1768.25	-1.11	4.1
CMB	87	10	7	0:51:37.0	117.0	5.6	-23.07	-68.12	78.1	8.00	-91.84	323.6	307.2	306.78	0.82	0.4	0.37	C	-3545.23	-2.22	2.6
HON	87	10	20	21:10:59.9	10.0	5.3	0.91	-87.09	71.9	13.56	-121.10	287.6	283.4	278.92	0.34	4.5	0.54	C	-4187.17	-2.62	7.1
GAC	87	10	21	6:11:33.3	10.0	5.4	-23.10	-114.48	77.1	11.94	-97.76	25.2	301.8	300.08	0.85	1.7	0.62	B	-4004.17	-2.50	4.2
ANMO	87	10	21	23:25:51.7	76.0	5.4	-21.14	-69.69	65.8	7.02	-86.70	329.5	263.3	259.09	0.69	4.2	0.58	C	-2956.92	-1.85	6.1
ANMO	87	10	27	21:58:17.7	616.0	5.9	-28.73	-62.96	75.5	1.46	-82.82	329.1	315.2	311.31	0.96	3.9	0.85	B	-3285.54	-2.05	5.9
CMB	87	10	27	21:58:17.7	616.0	5.9	-28.73	-62.96	85.4	3.35	-88.58	324.0	359.3	356.97	1.05	2.3	0.82	B	-1734.26	-1.08	3.4
ANMO	87	10	31	5:11:17.0	66.0	5.1	-25.88	-69.80	69.7	4.57	-87.14	331.8	276.8	272.54	0.79	4.3	0.50	C	-1632.47	-1.02	5.3
HON	87	10	31	8:52:30.8	33.0	5.4	-6.98	-80.57	80.9	9.14	-117.78	292.1	319.5	316.77	0.47	2.7	0.58	C	-4078.66	-2.55	5.3
ANMO	87	11	6	18:47:34.9	538.0	5.8	-22.84	-63.63	70.4	4.84	-82.64	326.7	289.6	287.57	0.81	2.0	0.81	C	-3186.73	-1.99	4.0
ANMO	87	11	9	17:46:21.0	62.0	5.4	-22.07	-69.47	66.7	6.60	-86.68	329.8	270.4	261.77	0.71	8.6	0.59	B	-2689.41	-1.68	10.3
HON	87	11	17	3:40: 8.9	76.0	5.8	12.57	-86.98	68.0	20.48	-121.24	278.1	268.0	266.08	0.18	1.9	0.89	B	-4112.69	-2.57	4.5
ANMO	87	12	3	11: 4:32.1	60.0	5.6	-21.40	-68.26	66.7	6.99	-85.99	328.7	263.7	261.90	0.70	1.8	0.59	B	-2436.87	-1.52	3.3
CMB	87	12	3	11: 4:32.1	60.0	5.6	-21.40	-68.26	76.8	9.07	-91.86	322.8	298.4	299.61	0.77	-1.2	0.37	C	-3630.57	-2.27	1.1

Stn	Origin time						Epicenter			Bouncepoint			Obs	Pred	Ellip	Resid	r	Grade	Water	Depth	Dcor
	Yr	Mo	Da	Hr Mn Sec	Dep	m_b	Lat	Long	Dist	Lat	Long	Azim	time	time	corr.				depth	cor	resid
ANMO	87	12	8	14:47:59.3	10.0	5.6	-32.59	-112.16	67.4	1.15	-109.35	4.3	265.0	263.28	0.86	1.7	0.68	C	-3691.87	-2.31	4.0
CMB	87	12	28	8:16:21.3	52.0	6.0	-28.08	-70.61	80.6	5.33	-93.89	327.2	320.0	316.22	0.92	3.8	0.54	C	-3510.43	-2.19	6.0
SCZ	88	1	19	7:30:29.7	21.0	6.3	-24.75	-70.60	77.6	6.53	-94.31	324.2	306.1	302.19	0.82	3.9	0.90	A	-3638.76	-2.27	6.2
SCZ	88	2	5	14: 1: 2.2	33.0	6.2	-24.77	-70.37	77.7	6.50	-94.18	324.1	305.3	303.09	0.83	2.2	0.86	B	-3635.20	-2.27	4.5
SCZ	88	2	6	18: 3:53.6	285.0	6.0	-18.04	-66.96	74.8	9.65	-91.04	319.1	300.6	297.00	0.72	3.6	0.74	B	-3737.15	-2.34	5.9
SCZ	88	2	22	19:13:17.4	71.0	5.9	-20.93	-69.80	75.1	8.48	-93.35	321.9	291.2	293.23	0.74	-2.0	0.60	C	-3653.22	-2.28	0.2
SCZ	88	3	28	18:36:26.4	10.0	5.7	-36.03	-102.81	74.3	0.28	-112.07	347.5	285.1	288.77	0.98	-3.7	0.35	C	-3964.06	-2.48	-1.2
SCZ	88	3	30	23:50:56.2	37.0	5.8	-24.91	-70.41	77.8	6.41	-94.20	324.2	307.1	303.55	0.83	3.5	0.73	C	-3623.82	-2.26	5.8
SCZ	88	4	12	23:19:57.3	54.0	6.1	-17.32	-72.40	70.8	10.43	-94.54	321.4	277.1	276.03	0.66	1.1	0.82	B	-3894.04	-2.43	3.5
SCZ	88	5	5	10: 4:13.5	10.0	6.1	-26.91	-113.39	63.6	4.82	-117.18	353.6	248.8	251.04	0.77	-2.2	0.43	C	-4266.47	-2.67	0.4
WFM	88	5	5	10: 4:13.5	10.0	6.1	-26.91	-113.39	79.2	8.39	-94.54	26.9	311.8	309.19	0.92	2.6	0.79	B	-3722.63	-2.33	4.9
KIP	88	5	5	22:32:48.1	10.0	5.5	-26.76	-113.70	64.3	-2.89	-136.34	319.7	248.3	253.03	0.62	-4.7	0.35	C	-4496.37	-2.81	-1.9
SCZ	88	5	5	22:32:48.1	10.0	5.5	-26.76	-113.70	63.4	4.92	-117.35	353.8	248.0	250.48	0.76	-2.5	0.38	C	-4286.14	-2.68	0.2

Abbreviations as in Appendix I.